Generalised modelling of droplet collisions in the frame of Euler/Lagrange calculations

Dissertation
zur Erlangung des akademischen Grades

Doktoringenieur
(Dr.-Ing.)

von **M.Sc. Maohong Sui**
geboren am Januar 12, 1991, in Jilin (China)

genehmigt durch die Fakultät für Verfahrens- und Systemtechnik der Otto-von-Guericke-Universität Magdeburg

Promotionskommission:

Prof. Dr.-Ing. habil. Dominique Thévenin (Vorsitz)

Prof. Dr.-Ing. habil. Martin Sommerfeld (Gutachter)

Prof. Dr.-Ing. Frank Beyrau (Gutachter)

Prof. Dr.-Ing. habil. Udo Fritsching (Gutachter)

Eingereicht am: Juli 04, 2023
Promotionskolloquium am: Oktober 10, 2023

To my wife, family and friends.

Abstract

Spray systems play a crucial role in various technical, industrial, and daily-life processes. Atomisation, achieved through specialised nozzles, is a key step in these systems, as it determines the droplet size distribution. Droplet size distribution is influenced by fundamental processes such as liquid and droplet break-up, as well as droplet collision. Over the past few decades, Computational Fluid Dynamics (CFD) simulations have been widely employed to design and optimise complex two-phase flows in spray systems. In particular, the Euler/Lagrange method has proven effective in numerically simulating spray systems. The objective of this work is essentially to extend droplet collision models, for which both experimental and numerical calculations have been performed.

In order to introduce droplet collisions into Euler/Lagrangian spray simulations, the utilization of collision maps is required. The outcome of binary droplet collisions (bouncing, coalescence, reflexive and stretching separation) depends on many parameters, such as the kinetic and physical properties of the gas and droplets. With the help of the obtained dimensionless numbers, the outcomes of the collision are summarized as a collision map and distinguished by the corresponding boundary lines. The reliability of the boundary lines used to distinguish different collision outcomes is very important. The most widely used bouncing boundary lines are derived from theoretical derivations based on energy balance but neglecting viscous dissipation effects. This paper presents a data-driven model using new assumptions and definitions that take into account the dissipated energy during the collision and the changing shape of the collision complex. Two new parameters are introduced into the model, namely the shape factor and the energy conversion rate, both depending on the impact parameter B. The new bouncing model is thus related to the degree of deformation of the droplet. The dependence on B can be described by a linear correlation between two parameters, namely the slope and the intercept. These parameters are related to the Ohnesorge number (Oh), whose model is $Oh < 0.35$, and they are derived as polynomial fit functions using a large number of existing experiments with different liquids.

In the droplet collision experiments, two droplet chain generators create droplet collisions that are recorded by two synchronised high-speed cameras. Afterwards, an internal image processing script analyses the time-resolved images of the collision sequences. Extensive experimental studies were carried out for water and a maltodextrin solution with different solid concentrations. The focus was on a thorough variation of the droplet size ratio. The effects of size ratio and water quality are studied for water. It is found that water quality does not seem to have a significant effect on collision regimes. As the size ratio decreases, the area of coalescence in the collision map is shown to widen and the area of bouncing is shown to narrow. This also leads to an upward shift of the boundary line between coalescence and stretching separation. For maltodextrin solutions, the effects of size ratio and viscosity were investigated. The critical bouncing point We_{B-C} is affected not only by the properties of the liquid but also by the size ratio. For the same size ratio, We_{B-C} is approximately the same

for different mass concentrations. When the size ratio decreases, We_{B-C} becomes smaller. The critical point (We_C) exists only for solutions with low viscosity and is more sensitive (more coalescence occurs) to smaller droplet diameters than to the size ratio. The collision regimes of maltodextrin solutions show that the triple point (We_T) is not affected by the drop size/size ratio but is sensitive to viscosity. Furthermore, the experimental results are compared with different models from the literature. The model of Sommerfeld and Pasternak (2019) with pure fluid correlation is excellent for predicting collision results with size ratios up to $\Delta = 0.5$. However, the Sui et al. (2023) model gives good results for size ratios of $\Delta = 0.8$ and $\Delta = 1.0$, but fails at $\Delta = 0.5$. Based on the developed boundary lines from theoretical considerations and experiments, numerical spray calculations are carried out using the Euler/Lagrange method. In particular, the sensitivity of the spray calculations (of the obtained size distribution) to the selected boundary lines will be analysed.

In the Euler/Lagrange method, the flow field is calculated by solving the conservation equations for a continuous phase on a given Eulerian grid, taking into account momentum transfer between phases. Modelling dispersed phases requires tracking a large number of droplets through the flow field solving the equations of motion and considering all relevant forces acting on the particles. In this work, the spray is simulated using the Euler/Lagrange approach together with the $k - \varepsilon$ turbulence model which is implemented in the open-source program OpenFOAM®8. In the simulations, the droplets are treated as parcels containing a certain number of real droplets with the same properties. The parcels are tracked taking into account all relevant forces, such as drag and gravity. The stochastic dispersion of particles caused by the turbulence is predicted using the Langevin equation. A stochastic collision model is used to calculate the droplet-droplet interactions, which means the simulations are carried out with four-way coupling. In addition, this model takes into account the impact efficiency for smaller droplets. A key element of the fully stochastic droplet collision model is an accurate description of the collision outcomes using the so-called collision maps. The first spray simulations are performed as a verification case for the fully stochastic collision model. First, different methods for generating fictitious parcels as collision partners are compared. It is shown that the different methods have no significant influence on the profiles of the axial and radial mean droplet velocities, their fluctuation values and the droplet diameters within different measurement ranges. However, the details of the collision model, such as the size distribution of the real and the fictitious particles and the location of the collision event, are affected. Secondly, the simulation results show that most collisions in the spray occur between two droplets of unequal size when the composite model (three boundary lines) of collision regimes is used. The second spray in the simulation is designed for coating tablets with high velocities and turbulence in the pharmaceutical industry. The simulation approaches are the same as for the first spray simulation, which is four-way coupling. It has been shown that particle turbulence dispersion is very important in such high turbulent sprays. It has a direct influence on the simulation results. However, due to the high air velocity of this spray, in such sprays, the results for either the one-way or two-way coupling method are similar.

Zusammenfassung

Sprühsysteme spielen in zahlreichen technischen und industriellen Prozessen sowie im täglichen Leben eine wichtige Rolle. Bei all diesen Techniken ist ein wichtiger Schritt die Zerstäubung der Flüssigkeit unter Verwendung eines bestimmten Düsentyps, um eine bestimmte Sprühnebelform und eine geeignete Tropfengrößenverteilung zu erreichen, Diese wird von grundlegenden Prozessen wie dem Flüssigkeitsaufbruch, dem Tropfenaufbruch und der Tropfenkollision beeinflusst wird. In den letzten Jahrzehnten wurde die numerische Simulation von Sprühsystemen (CFD: Computational Fluid Dynamics) zunehmend für die Auslegung und Optimierung dieser sehr komplexen Zweiphasenströmungen eingesetzt. Insbesondere hat die Anwendung der Euler/Lagrange Methode auf numerische Berechnungen von Sprühsystemen zu fruchtbaren Ergebnissen geführt. Das Ziel dieser Arbeit ist im Wesentlichen die Erweiterung von Tropfenkollisionsmodellen, für die sowohl experimentelle als auch numerische Berechnungen durchgeführt wurden.

Um Tropfenkollisionen in die Euler/Lagrange Simulation von Sprays einzubringen, sind zuverlässige Grenzlinien erforderlich, um zwischen den verschiedenen Ergebnissen von Tropfenkollisionen zu unterscheiden, wie Abprall, Koaleszenz, reflexive und dehnende Separation. Das Ergebnis einer binären Tropfenkollision hängt von vielen Parametern ab, wie den kinetischen und physikalischen Eigenschaften von Gas und Tropfen. Mithilfe von daraus resultierende dimensionslosen Kennzahlen werden die Kollisionsergebnisse durch entsprechende Grenzlinien unterschieden. Die am weitesten verbreitete Grenzlinie für den Abprall wird derzeit aus theoretischen Ableitungen abgeleitet, die auf einer Energiebilanz basieren, aber viskose Dissipationseffekte außer Acht lassen. In diesem Beitrag wird ein datengestütztes Modell vorgestellt, das neue Annahmen und Definitionen verwendet, die die dissipierte Energie während des Abpralls und die sich ändernde Form des Abprallkomplexes berücksichtigen. Es werden zwei neue Parameter in das Modell eingeführt, nämlich der Formfaktor und die Energieumwandlungsrate, die beide vom B abhängen. Das neue Abprallmodell hängt also mit dem Grad der Verformung des Tropfens zusammen. Die Abhängigkeit von B kann durch eine lineare Korrelation zwischen zwei Parametern beschrieben werden, nämlich der Steigung und dem Achsenabschnitt. Diese Parameter hängen mit der Ohnesorge-Zahl zusammen, deren Grenzwert $Oh < 0,35$ beträgt, und sie werden als Polynom-Fit-Funktionen mit Hilfe einer großen Anzahl von bestehenden Experimenten mit verschiedenen Flüssigkeiten abgeleitet. Das Modell wird durch den Vergleich mit vielen vorhandenen experimentellen Ergebnissen validiert.

Zwei Tropfenkettengeneratoren erzeugen Tropfenkollisionen, die von zwei synchronisierten Hochgeschwindigkeitskameras aufgezeichnet werden. Ein internes Bildverarbeitungsskript analysiert die zeitaufgelösten Bilder der Kollisionssequenzen. Zur Ergänzung früherer Arbeiten wurden weitere umfangreiche experimentelle Studie für Wasser und eine Maltodextrinlösung mit unterschiedlichen Feststoffkonzentrationen durchgeführt. Dabei lag der Schwerpunkt auf einer gründlichen Variation des Tropfengrößenverhältnisses. Die Auswirkungen des Größenverhältnisses und der Wasserqualität werden für Wasser untersucht. Es zeigt sich, dass die

Wasserqualität keinen signifikanten Einfluss auf die Kollisionsregimen zu haben scheint. Mit abnehmendem Größenverhältnis, zeigte sich eine Erweiterung des Bereichs der Koaleszenz und seine Vertleinerung des Bereichas Abprall. Dies führt auch dazu, dass sich die Grenzlinie zwischen Koaleszenz und dehnende Separation nach oben verschiebt. Bei Maltodextrinlösungen wurden die Auswirkungen des Größenverhältnisses und der Viskosität untersucht. Der kritische Abprallpunkt We_{B-C} wird nicht nur durch die Eigenschaften der Flüssigkeit, sondern auch durch das Größenverhältnis beeinflusst. Bei gleichem Größenverhältnis ist We_{B-C} bei unterschiedlichen Massenkonzentrationen ungefähr gleich. Wenn das Größenverhältnis abnimmt, wird We_{B-C} kleiner. Der kritische Punkt (We_C) existiert nur für Lösungen mit geringer Viskosität und ist empfindlicher (mehr Koaleszenz tritt auf) für kleinere Tropfendurchmesser als für das Größenverhältnis. Die Kollisionsregimen von Maltodextrinlösungen zeigen, dass der Tripelpunkt (We_T) nicht von der Tropfengröße/dem Größenverhältnis beeinflusst wird, aber empfindlich auf die Viskosität reagiert. Darüber hinaus werden die experimentellen Ergebnisse mit verschiedenen Modellen aus der Literatur verglichen. Das Modell von Sommerfeld and Pasternak (2019) mit reiner Flüssigkeitskorrelation eignet sich hervorragend zur Vorhersage von Kollisionsergebnissen mit Größenverhältnissen bis zu $\Delta = 0,5$. Das Modell von Sui et al. (2023) liefert jedoch gute Ergebnisse für Größenverhältnisse von $\Delta = 0,8$ und $\Delta = 1,0$, versagt jedoch bei $\Delta = 0,5$. Basierend auf den entwickelten Grenzlinien aus theoretischen Betrachtungen und Experimenten werden numerische Sprühnebelberechnungen mithilfe des Euler/Lagrange-Verfahrens durchgeführt. Insbesondere soll die Sensitivität der Sprühnebelberechnungen (der erhaltenen Größenverteilung) auf die gewählten Grenzlinien analysiert werden.

Bei der Euler/Lagrange-Methode wird das Strömungsfeld durch das Lösen der Erhaltungsgleichungen für eine kontinuierliche Phase auf einem gegebenen Eulerschen Gitter berechnet, wobei Impuls-, Wärme- und Massenübertragung zwischen den Phasen berücksichtigt werden. Die Modellierung dispergierter Phasen erfordert die Verfolgung einer großen Anzahl von Tropfen durch das Strömungsfeld, Lösung der Bewegungsgleichungen und Berücksichtigung aller relevanten Kräfte, die auf die Partikel wirken. Bei diesem Ansatz müssen alle Prozesse auf der Tropfenskala in einem geeigneten Modell berücksichtigt werden, einschließlich der Modelle für Tropfenkollisionen. In dieser Arbeit wird der Euler/Lagrange-Ansatz zusammen mit dem $k-\varepsilon$ Turbulenzmodell zur Berechnung von Sprühnebel verwendet. Alle numerischen Simulationen werden mit dem freien Open-Source-Programm OpenFOAM®8 durchgeführt. In den Simulationen werden die Tropfen als Parzellen behandelt, die eine bestimmte Anzahl von realen Tropfen mit gleichen Eigenschaften enthalten. Die Parzellen werden unter Berücksichtigung aller relevanten Kräfte, wie Widerstand und Schwerkraft, verfolgt. Die stochastische Dispersion von Partikeln, die durch Turbulenzen verursacht wird, wird mithilfe der Langevin-Gleichung vorhergesagt. Zur Berechnung der Tropfen-Tropfen-Wechselwirkungen wird ein stochastisches Kollisionsmodell verwendet, d.h. die Simulationen werden mit Vier-Wege-Kopplung durchgeführt. Darüber hinaus wird bei diesem Modell die Auftreffeffizienz für kleinere Tropfen berücksichtigt. Ein Schlüsselelement des vollständig stochastischen Tropfenkollisionsmodells ist eine genaue Beschreibung der Kollisionsergebnisse mithilfe der entwickelten Kollisionsregime. Schlechte Schätzungen dieser Kollisionsregimen können zu einer fehlerhaften Berechnung des endgültigen Tropfengrößenspektrums

führen. Daher werden erste Sprühnebelsimulationen als Verifizierungsfall für das vollständig stochastische Kollisionsmodell durchgeführt. Zunächst werden verschiedene Methoden zur Erzeugung fiktiver Parzellen als Kollisionspartner vergliche. Es zeigt sich, dass die verschiedenen Methoden keinen erheblichen Einfluss auf die Profile der axialen und radialen mittleren Tropfengeschwindigkeiten, deren Schwankungswerte und der Tropfendurchmesser innerhalb verschiedener Messbereiche haben. Allerdings werden die Details des Kollisionsmodells, wie die Größenverteilung der realen und der fiktiven Partikel und der Ort des Kollisionsgeschehens, beeinflusst. Zweitens zeigen die Simulationsergebnisse, dass die meisten Kollisionen im Spray zwischen zwei Tropfen ungleicher Größe stattfinden, wenn das vollständige Modell (drei Grenzlinien) der Kollisionsregime verwendet wird. Der zweite Sprühnebel, der numerisch berechnet wurde, ist für die Beschichtung von Tabletten mit hohen Geschwindigkeiten und Turbulenzen in der Pharmaindustrie konzipiert. Die Simulationsansätze sind die gleichen wie bei der ersten Sprühsimulation. Es hat sich gezeigt, dass die Partikelturbulenzdispersion in solchen hochturbulenten Strahlen sehr wichtig ist. Die Partikelturbulenzdispersion hat einen direkten Einfluss auf die Simulationsergebnisse. Aufgrund der hohen Luftgeschwindigkeit dieses Sprays hat sie jedoch kaum Auswirkungen auf die Berechnungsergebnisse der unidirektionalen und bidirektionalen Kopplungsmethoden.

Stichworte: Mehrphasenströmung, Experiment zur Kollision binärer Tropfen, Kollisionsregime, Grenzlinie, Spray, Euler/Lagrangesche Simulation, Stochastisches Kollisionsmodell.

Contents

Nomenclature

Abbreviations

AMR Adaptive Mesh Refinement

CDF Cumulative Distribution Function

CFD Computational Fluid Dynamic

CMC Critical Micelle Concentration

DNS Direct Numerical Simulations

HPMC Hydroxypropylmethylcellulose

LBM Lattice-Boltzmann method

LES Large Eddy Simulation

LPT Lagrangian Particle Tracking

PDA Phase Doppler Interferometry

PDF Probability Distribution Function

PIMPLE PISO-SIMPLE

PISO Pressure Implicit with Splitting of Operator

PVP Polyvinylpyrrolidone

RANS Reynolds-averaged Navier-Stokes simulation

RMS Root Mean Square

SIMPLE Semi Implicit Method for Pressure-Linked Equations

SMD Sauter Mean Diameter

VOF Volume Of Fluid

Greek formula characters

α Volume fraction

β The conversion rate in Sui model

χ The ratio of the interaction region volume

Δ	Size ratio	
δ	Kronecker delta	
η	Impact efficiency in	
Γ	effective transport tensor	
γ	$1/\Delta$	
κ	Parameter for Ashgriz and Poo (1990) reflexive separation boundary line	
Λ	The width of overlapping interaction in Estrade et al. (1999) model	
λ	Viscous dissipation rate of droplet collision model	
μ	Dynamic Viscosity	mPa·s
ϕ'	Shape parameter	
ψ	Fraction of the volume lost droplets to form the ligament in Kim et al. (2009)	
ρ	Density	kg/m^3
σ	Surface tension	mN/m
τ	Time	s
θ	Angle between collision droplets in relative velocity direction	
ε	The rate of dissipation of turbulent kinetic energy	
φ	Volume fraction in stochastic collision model	
ξ_i	Gaussian distribution with zero mean and unit variance	
ζ	Parameter for Ashgriz and Poo (1990) reflexive separation boundary line	

Dimensionless parameters

B	Impact Parameter
Ca	Capillary Number
Co	Courant number
Oh	Ohnesorge Number
Re	Reynolds Number
St	Stokes number
We	Weber number

We_{B-C} Critical bouncing Weber number in the collision map

We_{C-S} Intersection of C-SS while $B = 1$

We_C Critical Weber number in the collision map

We_T Triple Point in the collision map

Latin formula characters

$\dot{m}$	Mass flux	kg/(m²s)
b	Lateral displacement	m
C	Constant	
d	Diameter	m
E	Energy	
f	Collision frequency	
g	Gravity acceleration factor	m/s^2
I	Turbulence intensity	
k	turbulent kinetic energy	m^2/s^2
$k_{\beta'}$	The slope of conversion rate in the model of Sui et al. (2023)	
$k_{\phi'}$	The slope of shape factor in the model of Sui et al. (2023)	
KE	Kinetic Energy	
L	Length	m
m	Mass	kg
N_k	Number of real particles in the parcel k	
np	Number of particles in a parcel	
P	Probability	
p	Pressure	Pa
r	Radius	m
RE	Rotational energy in Hu model	
RN	Random Number	
S	Source term	

SE	Surface Energy	
t	Time	s
T_L	The integral time scale of turbulence	
u	Velocity	m/s
V	Volume	m^3
VDE	Viscous dissipation Energy	
XX	Random number	
Y_c	Radial distance	
ZZ	Random number	

Subscript

cell	Cell
coll	Stochastic Collision model
cv	Control volume
dissp	Dissipation
f	Fluid phase
in	Initial state
l	Large droplet
p	Particle / dispersed phase
rel	Relative velocity
relax	Relaxation
s	Small droplet
sat	satellite droplet

Chapter 1

Introduction

1.1 Background and overview of the thesis

Spray systems find widespread use in various industrial and technical settings, such as in spray combustion for automobiles and stationary turbines, spray drying of suspensions or solutions, spray cooling of surfaces, and spray painting. A fundamental objective of technical atomisation processes is the creation of a dramatically augmented gas/liquid interface in a dispersed multiphase system (Fritsching (2016), Fritsching and Li (2016)). Numerous factors, such as the viscosity and surface tension of the liquid being sprayed, the spray nozzle design, and operational conditions (such as pressure and flow rate), can impact the size distribution of a spray. Additionally, environmental factors, the distance between the nozzle and the target, as well as the air's turbulence and motion at the point of spray, can break up droplets or lead to their collision or amalgamation, which also affects the size distribution of a spray. Hence, studying droplet collision can not only offer a deeper understanding but can also assist in controlling droplet size across various spray applications, which can enhance the efficacy, quality and safety of several processes, including those employed in agricultural, meteorological, environmental, medical and industrial engineering.

Most of the previous studies of binary droplet collision assume that colliding droplets have identical droplet diameters and liquid properties (e.g. surface tension and viscosity). However, in general spray combustion, the sprayed droplets have a large size distribution and different trajectories. The flow field in the combustion chamber is extremely complex, so the droplets are distributed chaotically throughout the chamber. Furthermore, the droplets may have different temperatures, which results in different liquid properties (viscosity and surface tension). This effect is also evident in spray drying, as the drying chamber is much larger. Droplets with different trajectories are at different stages of drying, resulting in different solid content and liquid properties between each other. Therefore, detailed experimental studies are necessary to quantify the influence of liquid properties and droplet size on the collision outcomes and the collision maps obtained. The collision map, using the non-dimensional number We and the impact parameter B as axes, contains the droplet collision outcomes and the boundary lines between the outcomes. Extending the different boundary lines accounting for the droplet diameter and liquid properties(especially viscosity and surface tension) is essential. Therefore, a generalisation of the collision maps will be possible in this respect.

Computational fluid dynamics (CFD) provides a powerful tool for simulating and analysing spray behaviours in different scenarios. The fundamental expansion of CFD methods over the last few decades owes to rapid technological advances in computing power, the refinement of numerical techniques, and the development of more mathematically accurate models that capture physical processes. CFD can be used to simulate fluid dynamics in a spray, such as

the movement of fluid through the nozzle, the fluid's breakup into droplets, and the transport of these droplets through air. As such, valuable insights can be gained into how various factors, including nozzle design, fluid properties, and operating conditions, affect the size and behaviour of a spray. The Euler/Lagrange approach is often employed to systematise such simulations; it models a spray as a collection of discrete droplets with each droplet acting as a separate entity. In this approach, the fluid is modelled using the Eulerian method, and treated as a continuum. The equations of motion of the fluid are determined at fixed grid points in space, allowing the simulation of fluid flow, pressure, and temperature fields in the continuous medium. However, the motion of discrete droplets is calculated through a Lagrangian approach, where the equations of motion for each droplet are solved, considering the forces acting upon it, such as gravity and drag. The droplet is tracked as it moves through the continuous medium to simulate its behaviour, such as motion, collision, and break-up. Nevertheless, droplet collision is not fully resolved with this approach, requiring accurate collision models to enhance the simulation's accuracy.

This dissertation aims to investigate the effect of droplet collisions on numerical calculations of spray systems by gaining a comprehensive understanding of binary droplet collision mechanisms through experimentation. An optical shadow imaging method captures a sequence of binary droplet collisions, which are then subjected to image processing to construct collision maps. These maps use theoretical boundary lines based on droplet size, velocity, liquid properties, and other factors to aid in understanding the mechanisms of droplet collisions. The collision maps also serve as a guideline for subsequent numerical calculations based on the Euler/Lagrange approach, which simulates two-phase flows in spray systems incorporating variables such as particle turbulence dispersion, the fully stochastic collisions of binary droplets, and forces acting on particles. The reliability of the numerical results is confirmed by comparing them with existing spray experimental data.

1.2 Objective and scope of the thesis

The primary goal of this PhD project is to conduct experiments on binary droplet collisions and carry out a numerical analysis of sprays using the Euler/Lagrange method to gain a better understanding of the impact droplet collisions have on sprays. The following steps were taken to achieve this aim:

- Conduct binary droplet collision studies using the experimental facility to assess the influence of droplet diameter, size ratio, relative velocity, and liquid properties (surface tension and viscosity) on the results of binary droplet collision within identical solutions/pure liquid;

- Create collision maps with non-dimensional numbers that correspond with theoretical boundary lines to distinguish collision outcomes, and generate an empirical correlation of a boundary line within the collision map

- Extend the inter-particle stochastic collision model to consider binary droplet collision outcomes using the collision maps, from gas-solid to gas-liquid (spray) systems.

- Extend a three-dimensional, transient CFD solver, which relies on the Euler/Lagrange method, to account for the following: the corresponding forces that act on the particles, the dispersion of particle turbulence via a Langevin equation, and the fully stochastic collision model.

- Validate the spray simulation using the available experimental data and the extended CFD solver. To statistically analyse the effect of the collision model on the spray, corresponding velocity profiles, the mean size distribution across the entire radius, the local size distribution, and the Sauter Mean Diameter are used.

The numerical calculations and relevant model implementations are undertaken using the OpenFOAM®8 CFD code, which is free and open-source. OpenFOAM®8 allows flexible code modification and new model inclusion to cater to specific project needs, making it an ideal CFD code liaison for this PhD project. Moreover, OpenFOAM® is a widely adopted software solution in academia and scientific research with steadily growing popularity in industrial settings. The OpenFOAM® basic library is maintained and continually upgraded with enhancements furnished by a dynamic community of developers, rendering it the optimal choice for this PhD project.

1.3 Thesis Structure

To improve readability, this dissertation is divided into the following eight chapters:

- Chapter I - This chapter presents background on the topic and describes the purpose and scope of the investigation;

- Chapter II - This chapter is divided into three main sections discussing the theoretical basis of dispersed two-phase flow, basic definitions of binary droplet collision and a literature review of experimental and numerical studies of droplet collision, Euler/Lagrange spray simulation.

- Chapter III - This chapter describes the existing boundary lines in the binary droplet collision maps and the boundary line model developed by the author;

- Chapter IV - This chapter describes the methods and experimental tools used in binary droplet collision studies, including image processing methods and facility setup. In addition, this chapter provides experimental results containing the effects of size ratios on droplet collisions with water, as well as liquid properties and size ratios on binary droplet collision results with maltodextrin solutions;

- Chapter V - This chapter is devoted to summarising the numerical calculation method used in this study, which is based on the transient three-dimensional Euler/Lagrange method. The chapter provides the governing equations that define the flow behaviour of the continuous and dispersed phases and summarises the important forces acting on the particles. The connection between the continuous and dispersed phases and the particle turbulence dispersion model is then presented. Next, details of the completely random collision method used to calculate binary droplet collisions are described;

- Chapter VI - This chapter presents a spray simulation using the Euler/Lagrange method as a validation case for the model mentioned in Chapter V. The simulations are based on experimental data from the literature. In this chapter, numerical settings are presented, as well as a comparison between numerical and experimental results and a discussion of the fully stochastic collision model.;

- Chapter VII - This chapter gives a numerical calculation of a spray having higher velocity and turbulence as a validation of the methods introduced and verified in former chapters;

- Chapter VIII - This chapter presents conclusions and suggestions for future work.

Chapter 2

State of Knowledge

Droplet collisions have significant practical implications in areas related to sprays. Understanding and controlling the effect of droplet collisions on sprays can optimise these processes and improve efficiency. This chapter provides the fundamental principles necessary to understand dispersed two-phase flows and their characteristics. It also presents essential definitions related to binary droplet collision, including dimensionless numbers, followed by a description of collision outcomes and composition of collision maps. The final section provides a comprehensive review of previous experimental and numerical studies on droplet collisions, as well as simulations of sprays using the Euler/Lagrange method.

2.1 Classification of Multi-Phase Flow

Multiphase flows exist in various configurations in numerous industrial applications, as illustrated in Figure 2.1. The types of these flows include transient flows generated by external heating (e.g., heat pipes), separated flows (e.g., stratified, slug, or thin-film flows), and dispersed two-phase flows in which one phase exists as particles and droplets (Sommerfeld et al. (2008)). It is critical to understand the interfacial transport processes of these multiphase flow types. Dispersed two-phase flows are essential in numerous technological and industrial processes, including particle technology (creation and transport of solid particles), chemical engineering, and biotechnology. Two flow regimes (dilute and dense) are often present in dispersed two-phase flows. In dilute dispersion systems, particles are generally far apart from each other, and their movement is primarily controlled by hydrodynamic forces because direct contact between them is rare. In contrast, in dense dispersion systems, the distance between particles is relatively small (less than 10 particle diameters), resulting in particle collisions being the dominant factor that controls the particle movement within a fluid bed.

Dispersed two-phase flows exhibit various overall characteristics, which are briefly summarised below. The interaction mechanism between the fluid and dispersed phase depends on the volume fraction of particles α_p within the control volume V_{cv}, as expressed by the following equation:

$$\alpha_p = \frac{\sum_i N_i V_{p,i}}{V_{cv}} \tag{2.1}$$

Here, N_i denotes the number of particles in the size fraction i with the particle volume given by $V_{p,i} = d_{p_i}^3 \pi / 6$. If multiple phases are present, a volume fraction can be assigned to each of them. As the total volume fraction of the dispersed and continuous phases is 1, the volume fraction of the continuous phase α_f can be calculated as follows:
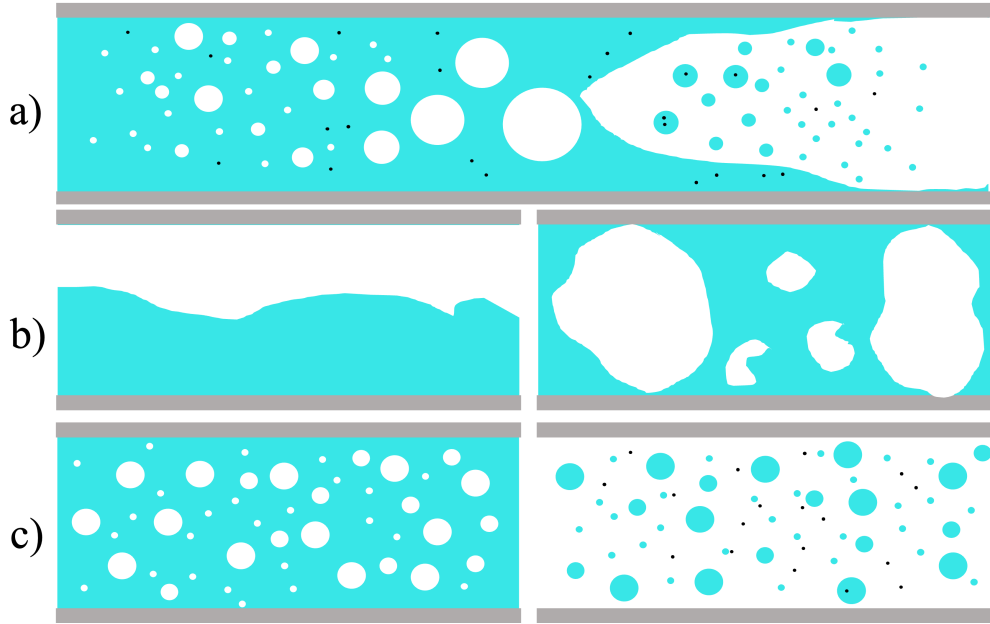
Figure 2.1: Different regimes of two-phase flows, a) transient two-phase flow, b) separated two-phase flow, c) dispersed two-phase flow (Cyan: liquid phase, Transparent: Gas phase, Black: Solid)

$$\alpha_p + \alpha_f = 1 \tag{2.2}$$

$$\alpha_f = \left(1 - \sum_i \alpha_{p,i}\right) \tag{2.3}$$

The bulk density or concentration of the dispersed phase is defined as the mass of particles per unit volume, as shown in Eq. 2.4. In contrast, the bulk density or concentration of the continuous phase is provided by Eq. 2.5, where ρ_p and ρ_f correspond to the densities of the dispersed and fluid phases, respectively. The particle concentration is frequently quantified by the number of particles per unit volume, as reported in Eq. 2.6.

$$\rho_p = c_p = \alpha_p \rho_p \tag{2.4}$$

$$\rho_f = (1 - \alpha_p)\rho_f \tag{2.5}$$

$$n_p = \frac{N_p}{V} \tag{2.6}$$

$$\eta = \frac{\alpha_p \rho_p u_p}{(1 - \alpha_p)\rho_f u_f} = \frac{\dot{m}_p}{\dot{m}_f} \tag{2.7}$$

The mass loading term η is an essential parameter used in gas-solid flow dynamics to quantify the ratio of total mass flux of the dispersed phase and the fluid phase. Mass flux defines the motion of particles and fluid per unit area within a unit of time and is expressed in kg/(sm^2).

The bulk velocities of the dispersed and fluid phases, represented by u_p and u_f, respectively, denote their mean velocities. Mass flux is a vector quantity that allows specifying the movement in any direction and described as a local characteristic. Moreover, Eq. 2.8 calculates the inter-particle distance (L), which is proportional to the volume fraction of the dispersed phase under the cubical arrangement of the particles. Specifically, the spacing is 3.74 diameters for a volume fraction of 1%, whereas it drops to 1.74 diameters for the same arrangement at 10%. It is important to note that due to the significant fluid dynamic interactions, particles with these high volume fractions cannot be considered as moving independently, as noted in Sommerfeld et al. (2008).

$$\frac{L}{d_p} = \left(\frac{\pi}{6\alpha_p}\right)^{\frac{1}{3}} \tag{2.8}$$
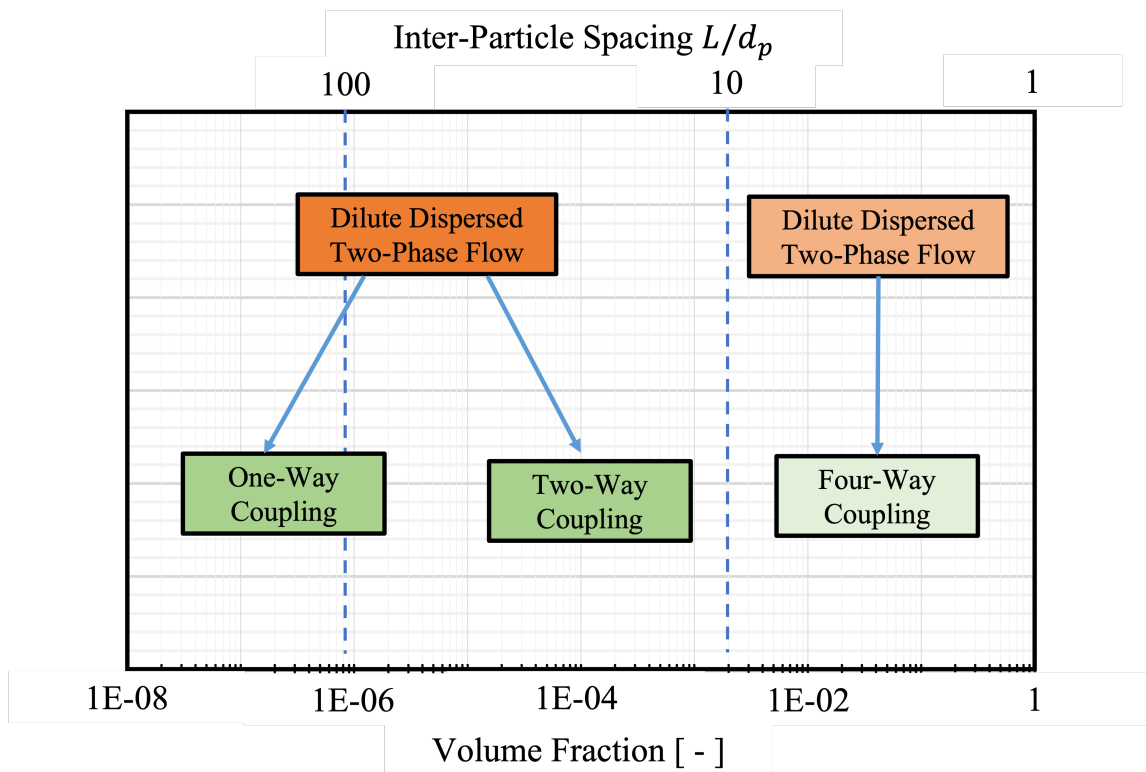

Figure 2.2: Regimes of dispersed two-phase flows as a function of particle volume fraction. (Sommerfeld et al. (2008) and Elghobashi (1994))

Two-phase dispersed flows can be categorised into different regimes based on the extent of interaction between the fluid and dispersed phases, as shown in Figure 2.2 (Elghobashi, 1994; Sommerfeld et al., 2008). Dilute or dense flows of dispersed two-phase systems depend on the volume fraction and inter-particle spacing, and they exhibit various interaction phenomena. A two-phase system is considered dense when the volume fraction α_p exceeds 10^{-3} or the inter-particle spacing L/d_p drops below 8. In the left regime, where $\alpha_p < 10^{-6}$ and $L/d_p > 80$, one-way coupling can be used, ignoring the influence of the dispersed phase on the fluid phase. However, in the middle regime, where $\alpha_p < 10^{-6}$ and $L/d_p > 80$, momentum transfer from the dispersed to the fluid phase alone is not sufficient to modify the flow characteristics, calling

for two-way coupling. The right regime is determined by high volume fractions and short inter-particle spacing ($\alpha_p > 10^{-3}$ and $L/d_p > 8$).

2.2 Binary Droplet Collision

2.2.1 Definition of relevant parameters

Non-dimensional parameters, derived from liquid properties and collision kinematics, are frequently employed to describe and quantify binary droplet collision. First, the relative velocity u_{rel} between the collision pairs is used to calculate the Weber number (We) using Eq. 2.9, in which ρ_p, σ_p, and d_s refer to droplet density, surface tension, and the diameter of the smaller droplet, respectively.

$$We = \frac{\rho_p d_s u_{rel}^2}{\sigma_p} \tag{2.9}$$

The impact parameter B refers to the lateral displacement b of the centroids of the two droplets perpendicular to the relative velocity vector prior to collision (Figure 2.3a), with a value calculated as the average diameter of the colliding droplet pair. Additionally, the sine of the angle of closure, φ, between the relative velocity vector and position vector of the droplet centre points is also equivalent to B. The value of $B = 0$ indicates a head-on collision, and $B = 1$ represents a grazing collision. Based on these two non-dimensional parameters, it is possible to generate the well-known collision map for binary droplet collisions, which depicts $B = f(We)$, as shown in Figure 2.3b. The droplet size ratio, Δ, is another critical geometric parameter defined in Eq. 2.11.

$$B = \frac{2b}{d_s + d_l} = sin\varphi \tag{2.10}$$

$$\Delta = \frac{d_s}{d_l} \tag{2.11}$$

The Ohnesorge number Oh provides a relative evaluation of the surface tension energy and internal viscosity dissipation in droplet collision. This number is expressed as the square root of Weber number divided by the Reynolds number and can be calculated using Eq. 2.12. Additional non-dimensional parameters related to droplet collisions are the capillary number, Ca, and the Reynolds number, Re. Ca represents the ratio of viscous forces to surface tension, and Re represents the ratio of inertial to viscous forces. To account for droplet viscosity, the third parameter introduces the relaxation velocity (u_{relax}), proposed in Sommerfeld and Kuschel (2016), to the model since these parameters hold significant importance.

$$Oh = \frac{\mu_p}{\sqrt{\rho_p \sigma_p d_s}} = \frac{\sqrt{We}}{Re} \tag{2.12}$$

$$Ca = \sqrt{We}Oh = \frac{\mu_p}{\sigma_p}u_{rel} = \frac{u_{rel}}{u_{relax}} \tag{2.13}$$

$$Re = \frac{\sqrt{We}}{Oh} = \frac{\rho d_s u_{rel}}{\mu_p} \tag{2.14}$$
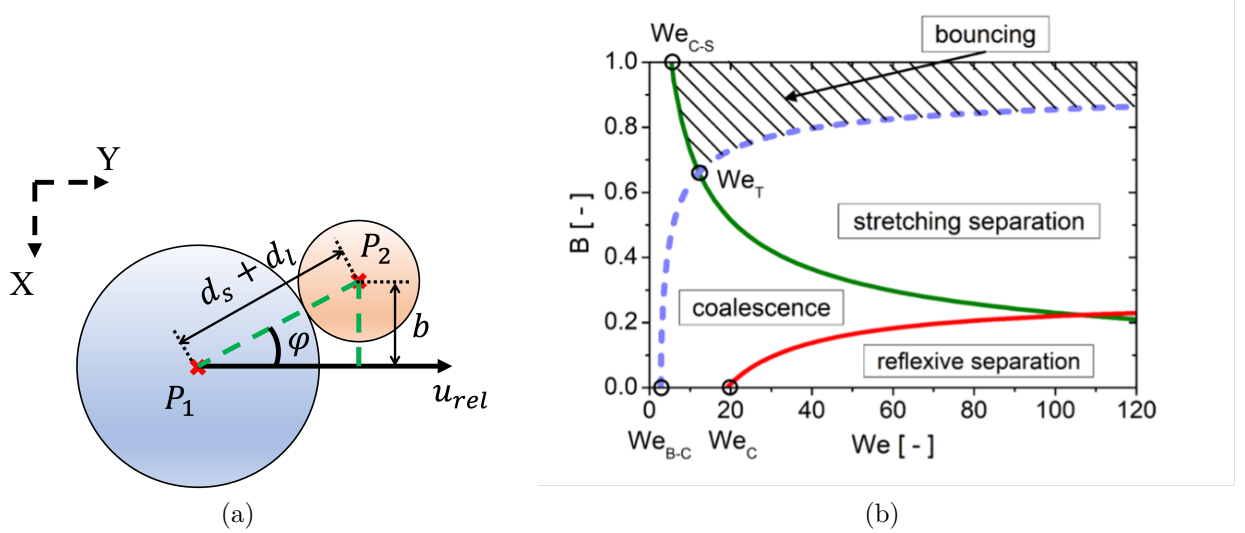

(a)   (b)

Figure 2.3: Typical droplet collision map showing the four droplet collision outcome scenarios and droplet collision geometry for non-equal-sized droplets with a relative velocity vector (Sommerfeld and Pasternak (2019))

2.2.2 Collision outcomes and collision map

Four primary collision outcomes, namely bouncing, coalescence, reflexive separation and stretching separation, have been identified in experiments on binary droplet collisions and documented in collision maps, with an example of a $B = f(We)$ collision map shown in Figure 2.3b. The collision outcomes depend on kinetic properties like droplet velocities, droplet diameter ratio, impact angle, and thermo-physical properties of gas and droplets, such as density, viscosity, surface tension, gas-phase type, pressure, and temperature. Due to this, these collision maps may exhibit varying outcomes while considering different liquids. Brief summaries of the different outcomes for binary droplet collisions are provided below:

1. **Bouncing**: When droplets interact, they flatten and become nearly disk-shaped, separated by a thin gas film at the collision point. This film can prevent droplets from merging if the gas cannot escape quickly enough. However, if the interfaces have small instabilities, they can come into direct contact and merge. Coalescence can occur when the minimum thickness of the film is so small that van der Waals attraction dominates the droplets' approach (Huang and Pan (2021); Pan et al. (2008); Zhang and Law (2011)). Examples of the collision sequences are shown in Figure 2.4a and the resolved example are shown in Figure 2.5a.

2. **Coalescence**: Coalescence occurs when the inter-droplet air film breaks or when short-range forces dominate at significant droplet deformations. Collision pairs then merge, as seen in the solved cases in Figures 2.4b and 2.5b.
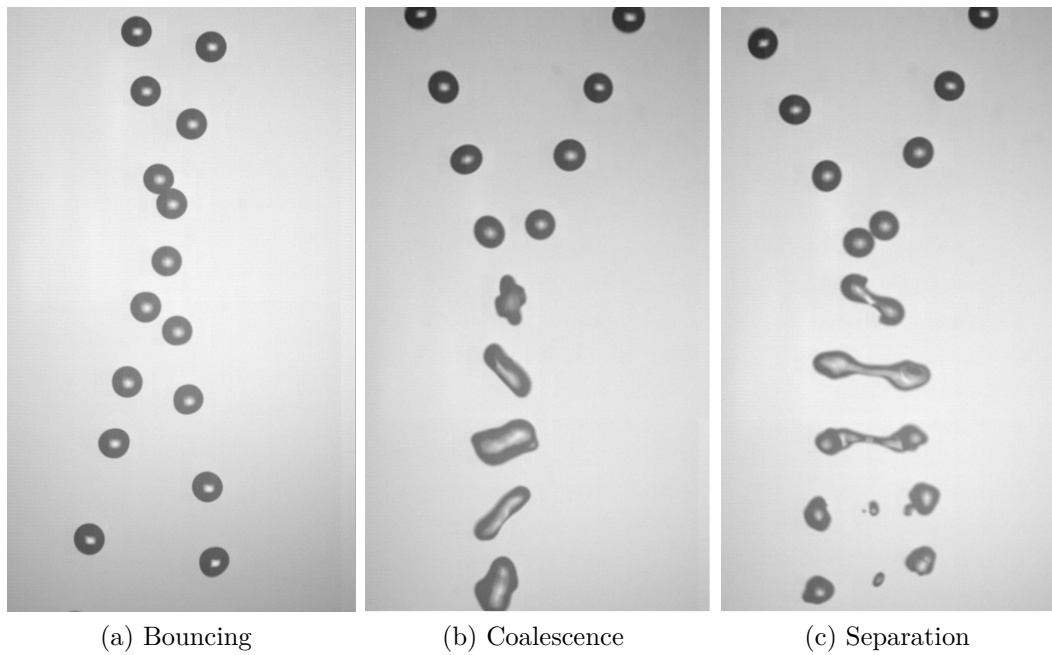
Figure 2.4: Typical droplet collision outcome illustrations (Maltodextrin solution 20Ma% with $\sigma = 57.4$ mN/m, $\mu = 3.12$ mPas, $Oh = 0.0142$)
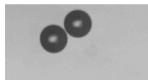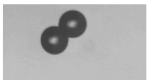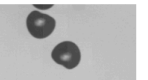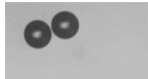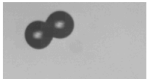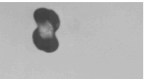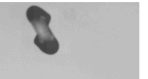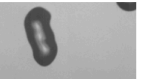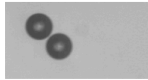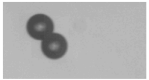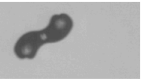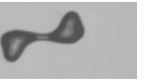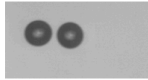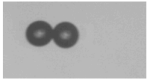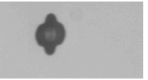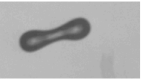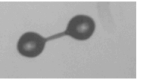

Figure 2.5: Illustrations of resolved droplet collision outcome (Maltodextrin solution 20Ma% with $\sigma = 57.4$ mN/m, $\mu = 3.12$ mPas, $Oh = 0.0142$)
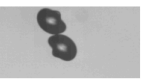
3. **Stretching Separation**: When two droplets collide at high impact parameter B, only a portion of the droplets come into immediate contact, forming an interaction region. Due to the velocity of the non-interacting region of the remaining part of the droplet, the merged region is stretched, creating a ligament between the two colliding droplets, which eventually disintegrates into satellite droplets as shown in Figure 2.4c. Example of separation and examples of resolution are shown in Figure 2.5c.

4. **Reflexive separation**: This outcome occurs only in the region of low impact parameter B. Initially, the droplets combine to form a disc-shaped droplet with a disc and an annular rim at its maximum deformation. It is possible to establish a strong enough internal flow effect to produce a cylindrical droplet with its axis perpendicular to the plane of the disc. This cylinder breaks up into two or more droplets, as shown in Figure 2.5d.

In the collision map as shown in the Figure 2.3b, some characteristic points are introduced for modelling the boundaries between collision outcomes:

- Transition from bouncing to coalescence at $B = 0$, here called critical bouncing point We_{B-C}.

- The critical Weber-number We_C for the transition from coalescence to reflexive separation at $B = 0$ by Qian et al. (1997). This critical point is the onset of reflexive separation.

- The triple point We_T is introduced by Kuschel and Sommerfeld (2013) where bouncing, coalescence, and stretching separation meet.

- The intersection of the boundary line between coalescence and stretching separation with the We-axis at $B = 1.0$, called We_{C-S}.

These distinct regimes are delineated by empirically or theoretically established boundary lines, in Chapter 3, the theoretical calculations for boundary lines are presented and described in depth.

2.3 Literature review

2.3.1 Experimental studies of binary droplet collision

In general, a considerable number of published experimental studies on droplet collisions have been categorised according to their features, including materials, liquid properties such as viscosity (μ) and surface tension (σ), size or size ratio (Δ), and other effects. These studies are summarised in Table 2.1.

This study provides an overview of seminal and widely accepted research on binary droplet collisions. Brazier-Smith et al. (1972) conducted collision experiments with water droplets of varying radii, ranging from 150 to 750 μm, and established boundary lines for coalescence and separation, based on the energy balance. This boundary line was extensively utilised in the collision model suggested by O'Rourke (1981) for spray simulations. Ashgriz and Poo

(1990) further extended this work by considering the size ratio effects on water droplet collision, eventually proposing classical boundary lines of coalescence-stretching separation and reflexive separation on collision maps based on energy balance. Jiang et al. (1992) considered the impact of viscous dissipation energy for the first time in hydrocarbon droplet collision research and established boundary lines for coalescence-stretching separation based on momentum equation. Estrade et al. (1999) conducted collision experiments using ethanol droplets, accounting for size ratios and proposed a boundary line based on the energy balance for bouncing, which became the most commonly used model for bouncing. These classical boundary lines, together with the outcomes of droplet collisions and the characteristic points mentioned above, form the binary droplet collision map. It has the impact parameter B as the vertical coordinate, while the horizontal coordinate is represented by We, as illustrated in Figure 2.3b.

Numerous researchers have conducted experiments on droplet collisions with pure liquids or Newtonian fluid solutions to investigate the impacts of viscosity and surface tension on the outcomes of collisions. For instance, Gotaas et al. (2007) performed experiments with high-viscosity droplets of n-decane, monoethyleneglycol (MEG), diethyleneglycol (DEG), and triethyleneglycol (TEG). Based on these experiments, a modified model for the coalescence-stretching separation boundary line was proposed for high-viscosity droplets. The study also introduced a correlation that can predict the critical We_C for high-viscosity liquids. Kuschel and Sommerfeld (2013) and Sommerfeld and Kuschel (2016) conducted experimental studies with high-viscosity solutions of Polyvinylpyrrolidone (PVP) and sucrose, as well as low surface tension liquids such as FVA oil and alcohols. These experiments were analysed in detail at a size ratio of $\Delta = 1$, and collision maps were presented. Existing collision models were adopted to fit the experimental data, and a boundary between dominant surface tension and viscosity was identified. Furthermore, Pan et al. (2016) investigated the effects of surface tension on collisions by adding surfactant to water and demonstrated a significant improvement in bouncing before reaching the critical micelle concentration (CMC) concentration. Chen et al. (2016) studied the collision behaviour of biodiesel and emulsion diesel at $\Delta = 1$. The study found that emulsion diesel droplets are less likely to present bouncing effects with low impact parameters compared to biodiesel droplets. Furthermore, under similar viscosity conditions, emulsion diesel droplets have a larger coalescence region than biodiesel droplets. Al-Dirawi and Bayly (2019) examined the effect of viscosity on the regime maps of binary droplet collisions of 2%, 4%, and 8% hydroxypropyl methylcellulose (HPMC). A modified model was proposed to predict the boundary of the bouncing regime. Shlegel et al. (2020) conducted experimental research into the influence of viscosity, surface, and interfacial tension on the position of transition boundaries between droplet interaction regimes and the main characteristics (number and dimensions) of child droplets. Finotello et al. (2018b) and Finotello et al. (2018a) investigated the collision behaviour of a shear-thinning non-Newtonian fluid Xanthan at 500 ppm in binary droplet collision experiments. They produced a full $We - B$ collision map of non-Newtonian droplet collisions for the first time, without discovering a reflexive separation. They also investigated collisions of milk droplets affected by shear-thinning, and no bounce was found in the collision maps of milk.

Besides the properties of the liquid, the influence of droplet size or size ratio on the outcome of droplet collisions should not be overlooked. Tang et al. (2012) performed head-on

collisions of droplets with different sizes of tetradecane, decane, and water. The study indicated that We_{B-C} weakly depended on the size ratio, while We_C significantly increased with the size ratio. The energy analysis showed that before the droplets began to stretch apart, viscous dissipation of internal motion of the merged droplets had increased, making stretching separation more difficult to occur in the collisions of non-equal-sized droplets. Huang and Pan (2015, 2021) provided experimental results of equal-sized droplet collisions with varying alcohols viscosity, surface tension, and different sizes (160 μm, 300 μm, 600 μm, and 1000 μm). The studies discovered that with increasing droplet size, bouncing was promoted, and the effects of size could not be simply generalised to existing non-dimensional numbers. In addition, Pasternak and Sommerfeld (2017) noticed that size ratio had no bearing on the triple point and the promotion of bouncing with the increasing droplet diameter in collision maps of PVP solutions with low viscosity, which was consistent with the research of Huang and Pan (2021). Furthermore, Sommerfeld and Pasternak (2019) summarised the experimental and theoretical studies of droplet collisions in detail. The research analysed the effect of size ratio on the collision map of sunflower oil and compared it with the experimental results of PVP. A combined model was proposed for the coalescence-stretching separation boundary lines. Lastly, Sui et al. (2021) conducted droplet collision experiments and showed collision maps of water considering the effect of size ratio.

Several studies have been conducted to investigate the collision of droplets of different materials or containing different liquid properties. Gao et al. (2005) explored the collision between water and ethanol droplets and observed minimal bouncing due to the disequilibrium-surface force effect and the rapid mixing of the two liquids. Chen and Chen (2006) studied immiscible droplets (water and diesel) and found no bouncing in their experiments. Planchette et al. (2011) and Roisman et al. (2012) studied binary collisions of immiscible liquid drops, namely glycerol and silicon oil, and identified three mechanisms: crossing separation, single-reflex separation, and reflexive separation. In addition, they measured the evolution of drop diameter, maximum drop diameter, and corresponding time for various liquids and impact velocities. Kuschel and Sommerfeld (2012) and Focke et al. (2013) focused on the collision of miscible droplets with different viscosity properties. They found that the difference in viscosity of the droplets delayed the initial merging of the droplets. Al-Dirawi and Bayly (2020) extended their research of Al-Dirawi and Bayly (2019) to analyse droplet collision with different viscosity and found that the droplet with lower viscosity deformed more than the other droplet containing higher viscosity during bouncing. Increasing the viscosity of one droplet had a negligible effect on the boundary of the stretching separation regime.

Environmental conditions, such as air pressure and substances contained in the surroundings, can also affect the collision outcome. Qian and Law (1994) observed that bouncing was facilitated as the ambient pressure increased in their experiments with water and hydrocarbons at varying ambient pressures (0.6 - 11.2 atm). Willis and Orme (2000, 2003) conducted experimental studies on the collision of binary viscous droplets in a vacuum environment and found no bouncing. In contrast, hydrocarbon droplets were less likely to bounce and more likely to coalesce when hydrocarbon vapour was added to the environment. Foissac et al. (2010) and Rabe et al. (2010) conducted experiments with clean or dirty environments and water size ratios, respectively. They proposed a new formulation of the Weber number, called

the symmetric Weber number, and two new simple models to describe the boundaries of the coalescence and separation regimes. Foissac showed the bouncing region, whereas Rabe did not.

The aspect of droplet collision has been extensively researched with several areas receiving attention. Menchaca-Rocha et al. (1997) published the first quantitative analysis of droplet collision. Their research provided experimental analysis of the number and size distribution of droplets caused by stretching separation at $\Delta = 1$, and the fragmentation of mercury droplets on a horizontal glass surface caused by collisions. Brenn et al. (2001) studied the number of satellite droplets resulting from the collision of propanol-2 drops. They found that different droplet sizes (i.e. different Oh) affect the number and distribution of droplets after stretching separation, even at the same We and B. Gao and Fritsching (2010) conducted a binary droplet collision experiment on two liquid-liquid states of molten Carnauba wax at $We = 570$. The experiment found stretching and reflexive separation with satellite droplets produced. As the impact parameter increased, the collision process changed from head-on to off-centre collision. After the collision, the droplet rotation was caused by the angular momentum of the droplet, which played a role in the stretching separation and formation of secondary droplets.

As summarised in Table 2.1, it is a collection of main experimental studies on binary droplet collisions during the last 30 years, in which the studied material and effects are presented. It is worth noting that very few studies have been devoted to investigating the effect of size/size ratio and viscosity on binary droplet collisions.

Table 2.1: Review of experimental studies of binary droplet collisions ('x' is the effect studied by the researchers)

Researchers	Material	μ	σ	Δ	Other effects
Ashgriz and Poo (1990)	Water			x	
Jiang et al. (1992)	Hydrocarbons	x			
Qian and Law (1994)	Water Hydrocarbon				Ambient pressure
Menchaca-Rocha et al. (1997)	Mercury	x			
Estrade et al. (1999)	Alcohols		x	x	
Willis and Orme (2000) Willis and Orme (2003)	Hydrocarbon fuels Water	x			Vacuum
Brenn et al. (2001)	Propanol	x	x		Number of satellite droplet formation
Gao et al. (2005) Chen and Chen (2006) Chen (2007)	Water Ethanol Diesel	x	x		Ethanol and water collision
Gotaas et al. (2007)	n-decane MEG DEG	x	x		
Foissac et al. (2010)	Water				Dirty /clean environment
Rabe et al. (2010)	Water			x	

Planchette et al. (2011)	glycerol	x	x		Immiscible droplet
Roisman et al. (2012)	Silicon oil	x	x		collision
Kuschel and Sommerfeld (2012)	PVP				Viscosity ratio
Tang et al. (2012)	Tetradecane Decane Water	x		x	
Focke et al. (2013)	PVP solution Water	x			Viscosity difference droplet collision
Kuschel and Sommerfeld (2013)	PVP Saccharose	x			
Huang and Pan (2015)	Alcohols	x	x		Size effect
Sommerfeld and Kuschel (2016)	FVA Alcohols		x		
Pan et al. (2016)	Water	x			Surfactant
Chen et al. (2016)	Diesel Biodiesel	x	x		Biodiesel emulsion diesel droplet collision
Pasternak and Sommerfeld (2017)	PVP	x		x	
Finotello et al. (2018a)	Xanthan				Non-Newtonain
Finotello et al. (2018b)	Milk Glycerol	x	x		
Al-Dirawi and Bayly (2019)	HPMC	x	x		
Sommerfeld and Pasternak (2019)	Sunflower Oil	x		x	
Al-Dirawi and Bayly (2020)	HPMC	x	x		Viscosity difference
Shlegel et al. (2020)	Water		x		
Sui et al. (2021)	Water			x	
Huang and Pan (2021)	Alcohols	x	x	x	Size effect

2.3.2 Numerical studies of binary droplet collision

Experimental studies can observe the development of complex collision geometries through high-speed cameras. However, monitoring the fluid mechanisms inside droplets is challenging. On the other hand, numerical methods possess the capacity to provide valuable local information, notably relating to velocity and pressure fields inside droplets. Such knowledge is critical in thoroughly characterising the droplet collision process. There are several numerical methods that may be employed to simulate droplet collisions, including the Front-Tracking, Level-Set, Volume of Fluid (VOF), and Lattice Boltzmann Method (LBM). Every methodology has its unique advantages and limitations, the selection of method depends on the specific problem and desired level of accuracy.

The Front-Tracking method, one of the earliest approaches for simulating droplet collisions, directly tracks the position and movement of the interface by identifying and following the points on the interface. Although widely employed in simulating droplet collisions with various

geometries and topologies, this method can be computationally demanding and fail to capture minute features of the droplets. In the study by Pan et al. (2008), collision dynamics between two identical droplets were observed using the Front-Tracking method in both experimental and computational settings. The results indicated that the merging of droplets could be caused by an increased van der Waals force that ruptures their surfaces. The Hamaker constant was determined empirically and consistently retrieved through experimental observations. Using the Front-Tracking method, Zhang and Zhang (2017) performed an analysis of binary droplet collisions of varying sizes. The study focused on the kinetic energy recovery and the interface hysteresis of bouncing droplets. Additionally, Rajkotwala et al. (2018) utilised the local front reconstruction method, a Front-Tracking method without connectivity, to obtain a satisfactory fit of experimental findings in conjunction with a film drainage model. This approach could only achieve a precise forecast of collision dynamics if the impact of film drainage time was accurately predicted.

The Level-Set method involves assigning a continuous function, F, to represent the signed distance between any point within the domain and the interface. At the interface, F equals zero, is positive on one side, and negative on the other (Fritsching and Li (2016)). The zero-level curve of F, in particular, serves to demarcate two distinct areas. This technique is efficient in detecting topological modifications to the interface, such as the merging and breaking of droplets, and has been employed in diverse droplet collision simulations as detailed in Tanguy and Berlemont (2005) and Pan and Suga (2005). However, the Level-Set approach lacks intrinsic liquid mass conservation, leading to liquid volume errors proportional to the underlying grid resolution. Recently, the coupling of Level-Set and Volume of Fluid has produced a hybrid method (CLSVOF) that harnesses the benefits of both methods. The VOF method precludes mass loss, while the Level-Set method preserves the fine representation of interface properties (Fritsching and Li (2016)).

The Volume of Fluid (VOF) method traces the interface by assessing the volume fraction of one liquid phase in each computational cell. This method is easy to implement and is effective at modelling flows with sharp density and viscosity gradients, such as droplet collisions. Hence, VOF stands as the most frequently employed methodology nowadays. The research of Chen et al. (2011), Chen et al. (2012), and Chen and Yang (2012) cantered on water binary droplet collisions with equal and non-equal size ratios across a wide range of We and B. An enhanced version of the VOF algorithm, combined with an adaptive mesh refinement (AMR) algorithm, was utilised to keep track of the liquid/gas interfaces. The study's results were found to agree well with experimental findings. A mass transfer rate model was proposed for the stretching separation of colliding droplets of different sizes based on their geometric relationship. Li and Fritsching (2011) introduced a ghost cell, which is an artificial gas layer between colliding droplets, to prevent immediate numerical coalescence between two approaching droplets, and then combined it with the VOF method to simulate bouncing and head-on coalescence. The authors of Saroka et al. (2012) and Saroka and Ashgriz (2015) employed the VOF method to simulate water, mercury and tetradecane droplet collisions' coalescence process, and water stretching separation process, respectively. They investigated a broad range of droplet sizes (10 μm to 2 mm), relative velocities from 0.5 m/s to 21 m/s, and Weber numbers from 10 to 60. In the research of Saroka et al. (2012), the dissipated energy in different droplets was studied,

and it was discovered that the assumption in the research of Jiang et al. (1992) overestimated the energy dissipation of water and mercury droplets. Subsequently, in the investigation of Saroka and Ashgriz (2015), it was observed that the ligaments anchoring two droplets undergo a pinching process regulated by Rayleigh instability, or they can be pulled until they rupture. Pulling (tearing) ruptures happen when high impact parameters and high Weber numbers are present. In Cong et al. (2020), the authors conducted a numerical investigation of binary unequal-sized ($\Delta = 0.5$) droplet collisions under various high Weber numbers (ranging from 210 to 810) and impact parameters ($B = 0.3$ - 0.9). They employed a combined level-set and VOF method with adaptive mesh refinement technology. The results reveal that during the deformation process, the droplets formed a noticeable hole-like structure, and as the Weber number increased, the rim expanded outwards and upwards. During the breakup process, the droplets exhibited wave-like motion and gave rise to secondary droplets. In contrast to head-on collisions, off-centre collisions resulted in rotational motion. Hu et al. (2017) used VOF with AMR to simulate alumina droplet collisions, achieving bouncing by employing a dual VOF function for the droplet and air film. He et al. (2022) employed the VOF method to probe spin-affected droplet separation following off-centre collisions, which were more conceptually rich and closer to reality than head-on collisions. The key idea behind the phenomenon is that the interplay between the initial spin angular momentum of spinning droplets and the orbital angular momentum determines the collision outcomes. By changing the chirality of droplet spin, the total angular momentum of the system can be augmented or reduced, which affects the stretching separation and reflexive separation differently. In Focke and Bothe (2011), the authors investigated binary collisions of non-Newtonian droplets and compared them to Newtonian rheology while proposing a lamella stabilisation algorithm. A more refined lamella stabilisation algorithm from Liu and Bothe (2016) was used in the simulation conducted by Planchette et al. (2017) to eliminate unphysical lamella rupture observed at higher Weber numbers mentioned in Focke and Bothe (2012).

The Lattice-Boltzmann method (LBM) is an alternative technique employed for simulating droplet collisions that has recently been explored. This method is advantageous for simulating a broad range of Reynolds numbers and can manage complex geometries and boundary conditions. Binary droplet collision dynamics with various diameter ratios ($0.4 < \Delta < 1.0$) were investigated in Yoshino et al. (2018) using a two-phase lattice method scheme based on the smaller droplet's properties and the droplets' diameter ratio. Similarly, in Liu et al. (2022), the LBM was used to examine the bouncing behaviour of equal-sized droplet collisions. The study also discovered that resistance from the gas film between droplets became more significant with lower liquid-to-gas density ratios, resulting in stronger bouncing behaviour.

In summary, implementing numerical methods for simulating droplet collisions enables researchers to gain essential insights into droplet dynamics and behaviour, as well as investigate various variables, including droplet size and velocity, and their impact on collision outcomes. By doing so, better comprehension on how droplets interact can be achieved. The acquired knowledge can help to inform and improve the design of droplet-based systems, rendering them more efficient and effective.

2.3.3 Euler/Lagrange simulation

The Euler/Lagrange approach serves as a productive numerical calculation technique in multiphase flows. This method provides solutions to the standard Euler equations, whilst Lagrangian methods track particles to update positions, velocities, and other properties. As a result, this technique produces a coupling of both gas and liquid phases over time. The Euler/Lagrange approach has been extensively employed to study a multitude of systems such as spray simulation (Ruger et al. (2000), Laín and Sommerfeld (2020), Sommerfeld et al. (2021b)), pneumatic conveying systems (Laín and Sommerfeld (2013)), cyclones (Sgrott and Sommerfeld (2019)), bubble columns (Taborda et al. (2021), Taborda and Sommerfeld (2021)), solid particle erosion (Ricardo and Sommerfeld (2020)), inhalers (Sommerfeld et al. (2021a)), among others.

Euler/Lagrange spray simulations face the challenge of accurately resolving the collision process of liquid droplets, necessitating the use of experiment-based models. By doing so, researchers can establish a connection between droplet collision experiments and their corresponding Euler/Lagrange simulations. Once the We and B of a collision are calculated, its location in the collision map can be established, and the collision outcome is determined based on the region demarcated by the boundary lines in the collision maps. These boundary lines are constructed using experimental data and theoretical analysis based on energy or momentum balance. As such, the development of reliable models for predicting droplet collision outcomes becomes imperative when performing spray simulations using the Euler/Lagrange approach.

Several studies have used the Euler/Lagrange approach to investigate collisions. For instance, in diesel spray simulations, O'Rourke (1981) and Amsden et al. (1989) created models classifying collisions as either coalescence or separation using a single boundary line. In a follow-up study, O'Rourke (1989) then explored the effects of particle turbulence dispersion models, culminating in the development of stochastic-deterministic collision models that continue to see wide use. Later, Post and Abraham (2002) proposed a composite boundary line model that demonstrated better numerical agreement with water collision maps than the popular single-line model by Brazier-Smith et al. (1972), and produced lower rates of coalescence than its previous model. Following this, a further alternative was developed, such as those by Ko and Ryou (2005a,b) and Kim et al. (2009), with considerations of stretching and reflexive separation, post-collision satellite droplets, and other aspects. More recently, Finotello et al. (2019) numerically investigated droplet-droplet collisions in a turbulent sub-grid spray system. To detect droplet collisions, the study employed a stochastic Direct Simulation Monte Carlo (DSMC) alongside large-eddy simulation (LES) to determine droplet movement. Additionally, collision boundary models were developed to examine the effects of various milk concentrates on binary collisions, and they conclusively revealed the profound impact of collision boundaries and turbulence dispersion models on spray particle size distribution.

The findings of Ruger et al. (2000) indicated that Sauter Mean Diameter variation within a spray was primarily due to coalescence and separation, rather than droplet evaporation. In another study, Sommerfeld (2017) used the $k-\varepsilon$ turbulence model, the fully stochastic droplet collision model Sommerfeld (2001), and the impact efficiency effects from Ho and Sommerfeld (2002) to simulate a turbulent water spray. They employed the three-line boundary model for

Euler/Lagrange calculations, which indicated an over-prediction of the collision frequency by 48% when impact efficiency was disregarded. Consequently, coalescence and bouncing were the most common outcomes. Recent research by Laín and Sommerfeld (2020) and Sommerfeld et al. (2021b) revealed that three-line boundary models had a negligible effect on droplet velocity profiles throughout sprays. Additionally, for small size ratios, slight changes in the boundary line size ratio resulted in significant differences in collision outcomes. The absence of collision maps for small size ratios substantively affected spray simulation accuracy.

This literature review only scratches the surface of numerical research on sprays, with further in-depth analysis necessary to understand the influence of droplet collisions accurately.

Chapter 3

Boundary Lines in the Collision Map

The boundary lines between collision outcomes are essential components of the collision maps. In the past few decades, most boundary models have been based on the extrapolation of energy or momentum balances. Experimental data on collisions of water or hydrocarbon droplets under atmospheric pressure conditions typically support these boundary line models, as discussed in the literature review. This chapter briefly introduces the widely recognised boundary lines in the binary droplet collision map. The final section of this chapter provides a thorough explanation of the novel bouncing boundary line proposed in this paper. The boundary lines in collision maps play a significant role in distinguishing collision outcomes in Euler/Lagrange spray simulations.

- For bouncing: Estrade et al. (1999), Hu et al. (2017), Al-Dirawi and Bayly (2019), Sui et al. (2023)

- For coalescence-stretching separation: Ashgriz and Poo (1990), Jiang et al. (1992), Brazier-Smith et al. (1972), Gotaas et al. (2007), Qian and Law (1994), Sommerfeld and Pasternak (2019), Sommerfeld and Kuschel (2016)

- For reflexive separation: Ashgriz and Poo (1990)

3.1 Theory boundary line: Bouncing

3.1.1 Estrade et al. (1999) Model

The bouncing regime boundaries of droplet collisions usually rely on the empirical collision map of ethanol droplets provided in the model by Estrade et al. (1999). The model contains a free constant, the shape factor ϕ', which permits adjustment of the model for different droplet collisions. The energy balance equation for this model is given in Eq. 3.1, and comprises several components, including E_{ce}, the portion of the droplet that does not contribute to deformation; E_{cd}, the kinetic energy that contributes to deformation; E_{si}, the collision surface energy of the droplet before the collision; E_{sf}, the surface energy of the droplet at maximum deformation; and E_{rot}, the rotational kinetic energy. Binary collisions of droplets are calculated using the centre-of-mass coordinates of the smaller droplet.

$$E_{ce} + E_{cd} + E_{si} = E_{sf} + E_{rot} \tag{3.1}$$

This model assumes that one of the colliding droplets is stationary. Thus, the contributing kinetic energy to the deformation is that of the interacting volumes, as illustrated in Figure 3.2. The equation defining this kinetic energy is given in Eq. 3.2. The volume of the interaction
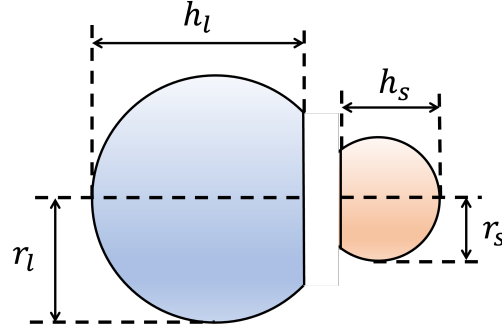
Figure 3.1: The model of deformation during droplet bouncing based on experimental observations.
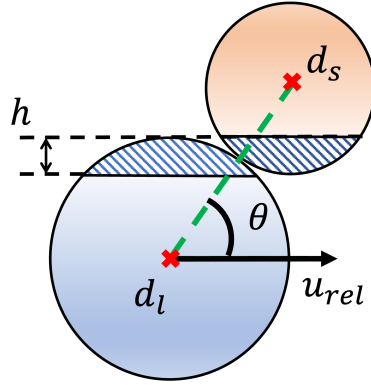
Figure 3.2: Illustrations of overlapping interaction region

region for the larger droplet is denoted by χ_l in Eq. 3.3, where V_{Li} represents the volume of the interaction region, as depicted in Figure 3.2. The width of the overlapping interaction region is represented by Λ in Eq. 3.5, and can be used to compute χ_l using Eq. 3.4.

$$E_{cd} = \frac{1}{2}\rho V_{Li}(u_s cos\theta)^2 \tag{3.2}$$

$$V_{Li} = \chi_l \frac{\pi d_l^3}{6} \tag{3.3}$$

$$\chi_l = \begin{cases} 1 - 0.25(2 - \Lambda)^2(1 + \Lambda) & \Lambda > 1 \\ 0.25\Lambda^2(3 - \Lambda) & \Lambda \leq 1 \end{cases} \tag{3.4}$$

$$\Lambda = (1 - B)(1 + \Delta) \tag{3.5}$$

Eq. 3.6 provides the total contribution of surface energy. At the point of maximum deformation during collision, the kinetic energy of the interaction regions is fully transformed into surface energy, which is defined by Eq. 3.7, with ϕ' indicating the shape parameter. Bouncing is said to occur when $h_s \leq \phi r_s$ and $h_l \leq \phi r_l$, according to Figure 3.1. Here, ϕ represents the ratio h_s/r_s or h_l/r_l, beyond which coalescence or separation occurs. These criteria, along with the mass conservation of the two droplets, result in the relations $h_l \leq d_l^3\sqrt{1 + 3/\phi^2}$ and $h_s \leq d_s^3\sqrt{1 + 3/\phi^2}$. Rotational energy originates from the energy that does not play a role

in deformation, resulting in $E_{rot} = E_{cd}$. When Eqs. 3.2 to 3.7 are inserted into Eq. 3.1, the boundary of the bouncing regime is given by $We = f(B)$ as Eq. 3.8.

$$E_{si} = \sigma\pi(d_s^2 + d_l^2) = \sigma\pi d_l^2 (1 + \Delta^2) \tag{3.6}$$

$$E_{sf} = \frac{1}{3}\sigma\pi d_l^2 \left(1 + \Delta^2\right) \left(2\left(\frac{3}{\phi^2} + 1\right)^{-\frac{2}{3}} + \left(\frac{3}{\phi^2} + 1\right)^{\frac{1}{3}}\right) = \frac{1}{3}\sigma\pi d_l^2 \left(1 + \Delta^2\right)\phi' \tag{3.7}$$

$$We = \frac{\Delta(1 + \Delta^2)(-12 + 4\phi')}{(1 - B^2)\chi_l} \tag{3.8}$$

3.1.2 Hu et al. (2017) Model

Two major modifications have been made to this model in comparison to Estrade et al. (1999):

1) The initial kinetic energy now considers both droplets, as opposed to only the non-moving droplet in the Estrade et al. (1999) model. Therefore, the whole droplet is considered when calculating the kinetic energy rather than just the mass of overlapping interaction.

2) A viscous dissipation energy term is introduced, inspired by the research of Jiang et al. (1992).

As a result, the energy balance of the system is as follows, as shown in Eq. 3.9: KE_{di} represents the initial kinetic energy that contributes to deformation, while the remaining initial kinetic energy is defined as KE_{dni}. SE_{in} represents the initial surface energy, while KE_{dm} and SE_{md} are the kinetic and surface energies at the instant of maximum deformation, respectively. Additionally, VDE denotes the viscous dissipation energy, and RE represents the rotational energy. The complete energy balance equation is as follows:

$$KE_{di} + SE_{in} + KE_{dni} = KE_{dm} + SE_{md} + VDE + RE \tag{3.9}$$

The initial kinetic energy is described in the Eq. 3.10. By combining Eq. 3.11 and Eq. 3.12, the initial kinetic energy can be described as Eq. 3.13. The initial surface energy is calculated as Eq. 3.14.

$$KE_{di} = \frac{1}{2}\rho_l\pi \left(\frac{d_s^3 u_s^2 cos^2\theta}{6} + \frac{d_l^3 u_l^2 cos^2\theta}{6}\right) \tag{3.10}$$

$$u_s = \frac{u_{rel}}{(1 + \Delta)^3} \tag{3.11}$$

$$u_l = \frac{u_{rel}\Delta^3}{(1 + \Delta)^3} \tag{3.12}$$

$$KE_{di} = \frac{\pi d_l^2 \Delta^2 (1 - B^2)}{12(1 + \Delta^3)}\rho_l u_{rel}^2 d_s \tag{3.13}$$

$$SE_{in} = \sigma\pi(d_s^2 + d_l^2) = \sigma\pi d_l^2(1 + \Delta^2) \tag{3.14}$$

The derivation is extended herein to incorporate the impact of viscous dissipation energy, introduced via a viscous dissipation factor, λ. For a head-on collision scenario where the Weber number (We) is 40, the viscous dissipation observed at maximum deformation is $VDE = 0.47KE$, which is consistent with the experimental observations previously documented by Jiang et al. (1992) and Hu et al. (2017) where the value of VDE was recorded as $0.5KE$.

$$VDE = \lambda(KE_{di} + KE_{dni}) \tag{3.15}$$

In this model, the shape factor and viscous dissipation factor are constants dependent solely on the liquid properties. By considering the dissipation effect, the model can effectively handle scenarios of high viscous droplet collisions. Combining Eq. 3.10 to Eq. 3.15 with Eq. 3.9, the boundary line can be described as Eq. 3.16.

$$We = \frac{(1 + \Delta^2)(1 + \Delta^3)(-12 + 4\phi')}{(1 - B^2)(1 - \lambda)\Delta^2} \tag{3.16}$$

3.1.3 Al-Dirawi and Bayly (2019) Model

Compared to the model proposed by Estrade et al. (1999), this model comprises two significant modifications, which are enumerated as follows:

- In this model, the initial kinetic energy considers both droplets, in contrast to the earlier model that only considers the larger droplet. However, it does not adopt the approach utilised by Hu et al. (2017) where the entire droplets are taken into account.

- A new shape factor, $\phi''_{o.s}$, is introduced in this model to consider the oscillating process, and also incorporates the viscous dissipation energy.

The energy balance equation for this model is expressed in Eq. 3.17, where E_{ce} represents the portion of droplet kinetic energy that does not contribute to deformation, while E_{cd} refers to the kinetic energy that contributes to deformation. E_{si} denotes the surface energy of the droplets before the collision, whereas E_{sf} represents the surface energy of the droplets at maximum deformation. E_v represents the viscous loss, and E_{rot} denotes the rotational energy.

$$E_{ce} + E_{cd} + E_{si} = Es_f + E_v + E_{rot} \tag{3.17}$$

The kinetic energy contributing to the deformation is that of the interacting volumes shown in Figure 3.2 which can be described in the Eq. 3.18. Here, χ_s and χ_l represent the ratio of the interaction region volumes of the colliding droplets as Eq. 3.19 from Ashgriz and Poo (1990):

$$E_{cd} = \frac{1}{2}\rho\left(\chi_l\frac{1}{6\Delta^3}\pi d_s^3\left(\frac{u_{rel}}{1 + \Delta^3}cos\theta\right)^2 + \chi_s\frac{1}{6}\pi d_s^3\left(\frac{\Delta^3 u_{rel}}{1 + \Delta^3}cos\theta\right)^2\right) \tag{3.18}$$

$$\chi_s = \begin{cases} 1 - \dfrac{1}{4\Delta^3}(2\Delta - \Lambda)^2(\Delta + \Lambda) & h > 0.5d_s \\[2ex] \dfrac{\Lambda^2}{4\Delta^3}(3\Delta - \Lambda) & h < 0.5d_s \end{cases} \tag{3.19}$$

$$\chi_l = \begin{cases} 1 - \dfrac{1}{4}(2 - \Lambda)^2(1 + \Lambda) & h > 0.5d_l \\[2ex] \dfrac{\Lambda^2}{4}(3 - \Lambda) & h < 0.5d_l \end{cases} \tag{3.20}$$

Λ is defined as Eq. 3.5 and h is:

$$h = \frac{1}{2}(d_l + d_s)(1 - B) \tag{3.21}$$

The initial surface energy is shown as Eq. 3.6 in the model of Estrade et al. (1999), and the surface energy after collision is described as Eq. 3.22.

$$Es_f = \frac{1}{2}\pi\sigma d_l^2 \phi''_{o.s} \tag{3.22}$$

As shown in Figure 12 of Al-Dirawi and Bayly (2019), head-on collision droplets have an approximate oblate spheroid shape. Therefore, this model proposes that the maximum droplet deformation in a head-on collision is closer in shape to an oblate sphere than a spherical cup. To account for this observation, Al-Dirawi and Bayly (2019) proposes a new shape factor, denoted as $\phi''_{o.s}$.

$$\begin{aligned}
\phi''_{o.s} = \frac{1}{2 + 2\Delta^2}\Bigg(&\left(\left(\frac{1}{1 - e_l}\right)^{\frac{1}{3}} + \frac{1}{2}\left(\frac{(1 - e_l)^{\frac{2}{3}}}{e_l}\right)ln\left(\frac{1 + e_l}{1 - e_l}\right)\right) \\
&+ \Delta^2\left(\left(\frac{1}{1 - e_s}\right)^{\frac{1}{3}} + \frac{1}{2}\left(\frac{(1 - e_s)^{\frac{2}{3}}}{e_s}\right)ln\left(\frac{1 + e_s}{1 - e_s}\right)\right)\Bigg)
\end{aligned} \tag{3.23}$$

$$e_l = \left(1 - \frac{\dfrac{c_l^2}{a_l^2}}{1 + \Psi B^\beta}\right)^{\frac{1}{2}} \tag{3.24a}$$

$$e_s = \left(1 - \frac{\dfrac{c_s^2}{a_s^2}}{1 + \Psi B^\beta}\right)^{\frac{1}{2}} \tag{3.24b}$$

Indicators of deformation are represented by e_l and e_s, and the surface area can be related to B by e^2 using the power law correlation proposed in Eq. 3.24, where Ψ and β are positive constants that can be optimised to fit the data. Here, c and a denote the large and small radii of the droplet spheres at maximum deformation before rebound. The empirical parameters

Ψ and β capture the effect of the shape factor on the deformation limit. To determine the viscous losses in the bounce model, Eq. 3.25 is utilized. By assuming that the droplet is viscous and can recover its spherical shape in the absence of oscillations, the aforementioned ratio of energy dissipation is approximately 50%. The empirical parameter, λ, is utilised to account for the effect of the shape factor on the deformation limit.

$$\lambda \sim \frac{0.5E_v}{E_{cd}} \tag{3.25}$$

Based on these assumptions, Al-Dirawi and Bayly (2019) model provides the following boundary line:

$$We = \frac{12\Delta^2(1+\Delta^2)(1+\Delta^3)(\phi''_{o.s} - 1)}{(\chi_s + \Delta^3\chi_l)(1-B^2)(1-\lambda)} \tag{3.26}$$

3.2 Theory boundary lines: Coalescence and Stretching Separation

The boundary line between coalescence and stretching separation has been derived in several studies, including Brazier-Smith et al. (1972), Ashgriz and Poo (1990), Jiang et al. (1992), and the combined model proposed by Sommerfeld and Pasternak (2019).

3.2.1 Brazier-Smith et al. (1972) and O'Rourke (1981) Model

The boundary line suggested by Brazier-Smith et al. (1972) has been widely applied in subsequent studies such as those by O'Rourke (1981) and Amsden et al. (1989) to distinguish between coalescence and stretching separation in collision maps. Based on this model, separation happens when the rotational energy exceeds the surface energy needed to transform two droplets within the radius of the merging pair. This widely used single-line boundary model in droplet collision studies indicates that droplet coalescence occurs when the collision parameter B is less than the critical value, B_{cr}, as defined in Eq. 3.29. If B exceeds B_{cr}, the droplet maintains its size and temperature, but undergoes a change in velocity. The liquid surface tension, $\sigma(\bar{T}_d)$, is assumed to vary linearly between the reference value, σ_0, at the reference temperature, T_0, and zero at the critical temperature, T_{cr}, of the fuel species.

$$\gamma = \frac{1}{\Delta} \tag{3.27}$$

$$b_{cr}^2 = (r_1 + r_2)^2 min\left(1.0, \frac{2.4f(\gamma)}{We(\bar{T}_d)}\right) \tag{3.28}$$

$$B_{cr} = \sqrt{min\left(1.0, \frac{2.4f(\gamma)}{We(\bar{T}_d)}\right)} \tag{3.29}$$

The function $f(\gamma)$ was defined in the Brazier-Smith et al. (1972) as Eq. 3.30. Afterwards, it is simplified as the Eq. 3.31 in the study of O'Rourke (1981). Interestingly, they have the same behavior as shown in Figure 3.3.

$$f(\gamma) = \frac{(1 + \gamma^2 - (1 + \gamma^3)^{\frac{2}{3}})(1 + \gamma^3)^{\frac{11}{3}}}{\gamma^6(1 + \gamma)^2} \tag{3.30}$$

$$f(\gamma) = \gamma^3 - 2.4\gamma^2 + 2.7\gamma \tag{3.31}$$
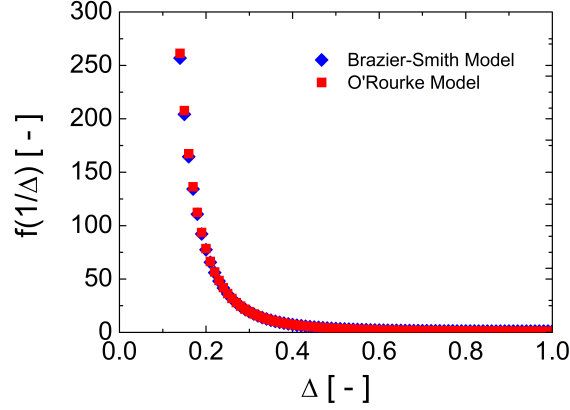
Figure 3.3: The comparison of the correlation in Brazier-Smith et al. (1972) and O'Rourke (1981)

$$We(\bar{T}_d) = \frac{\rho_p u_{rel}^2 d_s}{\sigma(\bar{T}_d)} \tag{3.32}$$

$$\bar{T}_d = \frac{d_s^3 T_{d_s} + d_l^3 T_{d_l}}{d_s^3 + d_l^3} \tag{3.33}$$

In the end, the model can be described as Eq. 3.34. Furthermore, the post-collision velocity calculation is proposed as Eqs. 3.35 and 3.36.

$$We = \frac{2.4}{B^2} f(\gamma) \tag{3.34}$$

$$v_{s,after} = \frac{d_s^3 v_s + d_l^3 v_l + d_l^3 (v_s - v_l)\dfrac{B - B_{cr}}{1 - B_{cr}}}{d_s^3 + d_l^3} \tag{3.35}$$

$$v_{l,after} = \frac{d_s^3 v_s + d_l^3 v_l + d_s^3 (v_l - v_s)\dfrac{B - B_{cr}}{1 - B_{cr}}}{d_s^3 + d_l^3} \tag{3.36}$$

3.2.2 Ashgriz and Poo (1990) Model

The boundary between coalescence and stretching separation in off-centre binary droplet collisions was investigated by Ashgriz and Poo (1990). In stretching separation, a portion of the droplet interacts with the other droplet to form a contact zone that stretches until it breaks off, indicating the occurrence of satellite droplets. The residual region of the droplets that

does not join the interaction zone continue on their original path. In this case, the stretching separation energy includes two parts: the kinetic energy of the interaction region and the remaining kinetic energy. The effective kinetic energy of the contact region is determined using the component of the droplet velocity that is parallel to the direction of droplet separation, as shown in Figure 3.1. The interaction region, in stretching separation, consists of the overlapping regions between the droplets. The breadth of the overlap zone is calculated by subtracting the impact parameter from the total droplet radius, which is determined by Eq. 3.21. The volume of the interaction zone, V_{si} and V_{li}, is then calculated using the Eqs. 3.37 and 3.38, where χ_s and χ_l, are defined as Eqs. 3.19 and 3.20:

$$V_{si} = \chi_s V_s \tag{3.37}$$

$$V_{li} = \chi_l V_l \tag{3.38}$$

The total effective stretching kinetic energy can be expressed as Eq. 3.39. Here, θ denotes the angle between the relative velocity vector and the centre-to-centre line at the time of the collision (see Figure 3.2) with $sin\theta = B$. u_l, u_s, V_l, and V_s represent the velocities and total volumes of the large and small droplets. Then, take Eq. 3.40 and 3.41 into the Eq. 3.39, the total effective stretching kinetic energy can be described as Eq. 3.42.

$$KE_{si} = \frac{1}{2}\rho \left[(V_s - V_{si})u_s^2 + (V_l - V_{li})u_l^2 \right] + \frac{1}{2}\rho \left[V_{si}(u_s sin\theta)^2 + V_{li}(u_l sin\theta)^2 \right] \tag{3.39}$$

$$u_l = \frac{\Delta^3 u_{rel}}{1 + \Delta^3} \tag{3.40}$$

$$u_s = \frac{u_{rel}}{1 + \Delta^3} \tag{3.41}$$

$$KE_{si} = \frac{1}{2}\rho u_{rel}^2 V_l^2 \left\{ \frac{\Delta^3}{(1+\Delta^3)^2} \left[(1+\Delta^3) - (1-B^2)(\chi_s + \Delta^3 \chi_l) \right] \right\} \tag{3.42}$$

The surface energy of the region of interaction is described in the Eq. 3.43.

$$SE_{si} = \sigma \left[2\pi V_l d_l \Lambda (\Delta^3 \chi_s + \chi_l) \right]^{\frac{1}{2}} \tag{3.43}$$

The criterion for stretching separation is assumed to be when the total effective stretching kinetic energy, KE_{si}, is larger than the surface energy of the region of interaction, which is opposing the separation.

$$KE_{si} >= SE_{si} \tag{3.44}$$

Thus, based on the energy balance, the following equation is derived for the boundary between coalescence and stretching separation.:

$$We = \frac{4(1+\Delta^3)^2 \left[3(1+\Delta)(1-B)(\Delta^3 \chi_s + \chi_l) \right]^{\frac{1}{2}}}{\Delta^2 \left[(1+\Delta^3) - (1-B^2)(\chi_s + \chi_l \Delta^3) \right]} \tag{3.45}$$

3.2.3 Jiang et al. (1992) Model

Jiang et al. (1992) posits that droplet collisions involve two processes. The initial collision process leads to a maximum deformation of the joint droplet, similar to a head-on collision. The second process involves a competition between surface tension and the inertial force of transverse velocity, with splitting occurring when the transverse velocity is significantly large. Unlike the model proposed by Ashgriz and Poo (1990), the model of Jiang et al. (1992) relies on momentum conservation and assumes that the merged droplets act like two circular plates sliding against each other. The resistance to the sliding velocity comprises surface tension around the circumference of the plates and the loss of viscosity due to the shear flow layer between the sliding plates (i.e., droplets), as shown in Figure 3.4. The model can be described as Eq. 3.46.

$$B = \frac{C_a}{We^{\frac{1}{2}}} \left[1 + \frac{C_b \mu}{\sigma} \left(\frac{\rho d_s}{\sigma} \right)^{\frac{1}{2}} \right] \tag{3.46}$$
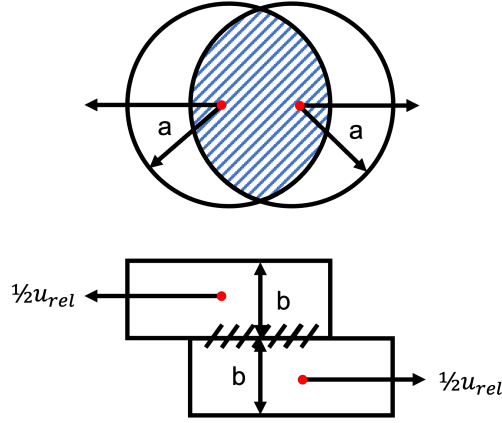
Figure 3.4: Schematic showing the model adopted to analyse droplet breakup during grazing collision by approximating the process as the sliding motion of a merged droplet under the influence of transverse inertia force and restoring surface tension force.(Jiang et al. (1992))

It is worth noting that C_b is expressed in units of $m^2 s^{-2}$ and is not a dimensionless parameter, while C_a is dimensionless. The final equation of the boundary curve contains two model constants, C_a and C_b, which can be adjusted based on experimental data. In the Jiang et al. (1992) model, the default value for C_a is 1, while C_b is a constant. In Gotaas et al. (2007), the adaptation of Jiang et al. (1992) model to a range of viscosities was achieved by adjusting the two parameters included in the model, namely C_a and C_b, to be 2.656 and 0.185 $m^2 s^{-2}$, respectively. In the study by Suo and Jia (2020), a re-derivation of the coalescence-stretching separation criterion is presented, where the value of the model constant C_a is set to 1.0, which has shown no significant effect on the predictions. Furthermore, C_b is corrected to a non-dimensional parameter, and an empirical correlation based on available experimental results is established to determine its value. This approach effectively reduces the uncertainties in applying the Jiang et al. (1992) model. In addition, the improved coalescence-stretching separation model fully considers the effect of the droplet size ratio.

$$We = \left[\frac{1}{B} \left(C_a \frac{h}{d_s} Oh + C_b \right) \right]^2 \tag{3.47}$$

$$\frac{h}{d_s} = \frac{(1-B)(1+\Delta)}{2\Delta} \tag{3.48}$$

The validation of coalescence-stretching separation models involves a comparison between experimental measurements for water droplet collision (with $\Delta = 0.5$) from the study of Rabe et al. (2010) and ethanol droplet collision (with $\Delta = 0.5$) from the study of Estrade et al. (1999), and the boundary proposed by Suo and Jia (2020). The optimal value of C_b is determined from Eq. 3.49 where C_a is fixed at 1. This model is valid for liquid viscosities ranging from 1.0 mPa·s to 47.2 mPa·s at $\Delta = 1$, and for liquid viscosities ranging from 1.0 mPa·s to 1.2 mPa·s at $\Delta < 1$.

$$C_b = (183 - 180\Delta)Oh + 2.58 \tag{3.49}$$

3.2.4 Sommerfeld and Pasternak (2019) Combined Model

The proposed coalescence-stretching separation boundary by Brazier-Smith et al. (1972) fails to account for dissipation effects. However, it offers a relatively simple approach to account for droplet size ratio. On the other hand, the model developed by Jiang et al. (1992) accounts for viscosity effects but neglects droplet size ratio, which requires consideration. By combing those models, Sommerfeld and Pasternak (2019) presented a combined model to overcome these limitations, which incorporates both droplet size ratio and viscosity effects. The model uses $C_b = 1$ and C_a with two empirical equations to account for pure fluids and solutions, respectively. The parameter C_a is experimentally determined and can be optimised with third-order polynomials for either pure liquids or solutions, depending on the liquid properties and droplet size.

$$B = \frac{C_a}{1.14We^{\frac{1}{2}}} \left[1 + \frac{\mu}{\sigma} \left(\frac{\rho d_s}{\sigma} \right)^{\frac{1}{2}} \right] \left[\gamma^3 - 2.4\gamma^2 + 2.7\gamma \right]^{\frac{1}{2}} \tag{3.50}$$

The constant C_a is obtained in a different way for pure fluids and solution droplets:
For pure fluids:

$$C_a = 2.3 - 11.12Oh + 23.74Oh^2 - 18.2Oh^3 \tag{3.51}$$

For solutions:

$$C_a = 2.63 - 7.2Oh + 7.86Oh^2 - 1.4Oh^3 \tag{3.52}$$

3.3 Theory boundary lines: Coalescence and Reflexive Separation boundary line

3.3.1 Ashgriz and Poo (1990) Model for reflexive separation

The model proposed by Ashgriz and Poo (1990) is suitable for reflexive separation in droplet collisions near the head-on ($B = 0$) with low-viscosity liquids. This model is based on an

energy balance equation between the colliding droplets and the merged droplet, where E_r represents the reflected energy, KE_c is the kinetic energy of the reaction flow generated by the directly colliding droplet fraction, KE_e is the kinetic energy of the excess surface-induced flow, and E_s is the stretching energy. Eqs. 3.53 - 3.56 provide the definitions for these energy terms, where V_{sp}, and V_{lp} are the volumes of the prolate regions in the small and large drops, respectively, given by Eq. 3.57 and Eq. 3.58. In cases of off-centre collisions, a portion of the initial drop's kinetic energy will attempt to elongate the fused mass. The stretching flows, created due to elongation, run almost perpendicular to the reflexive flows. These flows, in turn, lower the reflexive energy. The excess kinetic energy of the combined mass is equated to the kinetic energy of the stretching flows.

$$E_r = KE_e + KE_c - E_s \tag{3.53}$$

$$KE_c = \frac{1}{2}\rho \left(V_{lp} u_1^2 + V_{sp} u_s^2 \right) \tag{3.54}$$

$$KE_e = \sigma \pi d_l^2 \left[(1 + \Delta^2) - (1 + \Delta^3)^{\frac{2}{3}} \right] \tag{3.55}$$

$$E_s = \frac{1}{2}\rho \left[(V_l - V_{lp})u_l^2 + (V_s - V_{sp})u_s^2 \right] \tag{3.56}$$

$$V_{sp} = \frac{1}{6}\pi d_l^3 (\Delta - \zeta)^2 (\Delta^2 - \zeta^2)^{\frac{1}{2}} \tag{3.57}$$

$$V_{lp} = \frac{1}{6}\pi d_l^3 (1 - \zeta)^2 (1 - \zeta^2)^{\frac{1}{2}} \tag{3.58}$$

$$\zeta = \frac{1}{2}B(1 + \Delta) \tag{3.59}$$

Based on the equations mentioned above, E_r is shown as Eq. 3.60, where κ_s and κ_l are defined in Eq. 3.61 and 3.62:

$$E_r = \sigma \pi d_l^2 \left[(1 + \Delta^2) - (1 + \Delta^3)^{\frac{2}{3}} + \frac{We}{12\Delta(1 + \Delta^3)^2}(\Delta^6 \kappa_s + \kappa_l) \right] \tag{3.60}$$

$$\kappa_s = 2 (1 - \zeta)^2 \left(1 - \zeta^2 \right)^{\frac{1}{2}} - 1 \tag{3.61}$$

$$\kappa_l = 2 (\Delta - \zeta)^2 \left(\Delta^2 - \zeta^2 \right)^{\frac{1}{2}} - \Delta^3 \tag{3.62}$$

It is assumed that reflexive separation will occur for a nominal spherical combined mass when the effective reflexive kinetic energy is more than 75% of its nominal surface energy.

$$E_r \geq 0.75\sigma \pi (d_s^3 + d_l^3)^{\frac{2}{3}} \tag{3.63}$$

Therefore, the boundary line between coalescence and reflexive separation can be calculated from the following equation:

$$We = 3 \left[7 \left(1 + \Delta^3 \right)^{\frac{2}{3}} - 4(1 + \Delta^2) \right] \frac{\Delta(1 + \Delta^3)^2}{\Delta^6 \, \kappa_s + \kappa_l} \tag{3.64}$$

3.3.2 Critical Weber number model

The boundary between reflexive separation and coalescence is characterised by the critical Weber number, We_C, at $B = 0$, which denotes the onset of reflexive separation. The general form for the correlation between We_C and Oh proposed by Jiang et al. (1992) is given in Eq. 3.65, where $C_1 = 4.816$ m/s and $C_2 = 0.302$ are constants.

$$We_c = C_1 \frac{\mu_d}{\sigma} + C_2 \tag{3.65}$$

According to Qian et al. (1997), for droplet collisions of equal size, there is a rightward shift of We_C as Oh increases. The authors proposed a model with two constants, where C_3 is related to geometrical parameters and C_4 is related to the surface energy of the deformed droplet. Therefore, the correlation between We_C and Oh is given by Eq. 3.66, with C_3 and C_4 values of 15 and $\sqrt{2} \times 480$, respectively, as stated by Qian et al. (1997). Krishnan and Loth (2015) proposed that $C_3 = 12$ and $C_4 = 700$.

$$We_c = C_3 + C_4 Oh \tag{3.66}$$

However, for high viscosity liquids with large Oh, the We_C obtained using Eq. 3.66 is significantly higher than the actual value. Therefore, Willis and Orme (2003) proposed an additional correlation for liquids with $Oh > 0.45$, given by Eq. 3.67. This non-linear correlation fits well with experimental results for high viscosity droplets. Furthermore, Gotaas et al. (2007) examined droplets with viscosity up to 58 mPa·s, corresponding to Oh up to 0.34.

$$We_c = \begin{cases} 14.8 + 643.1 Oh & Oh < 0.04 \\ 9309 Oh^{1.7056} & Oh > 0.04 \end{cases} \tag{3.67}$$

3.4 New Bouncing boundary line: Sui et al. (2023) Model

The bouncing boundary line is based on the model of Estrade et al. (1999) and includes an extension of the model of Hu et al. (2017). A new parameter called the conversion rate β is introduced, which is related to viscous dissipation as described in Sui et al. (2023), which is the percentage of energy that does not convert to surface energy at maximum deformation during droplet collision. In addition, the model assumes that the degree of droplet deformation varies with different relative collision positions and velocities. Therefore, the shape factor ϕ' and the conversion rate β are assumed to be linearly related to the impact parameter B and the degree of deformation. Furthermore, the deformation of the droplet is affected by liquid properties, such as viscosity and surface tension. Therefore, the slope and intercept of ϕ' and β are also related to the liquid properties and can be expressed in terms of Oh. The resulting energy balance equation is shown as Eq. 3.68, where KE_{in} and SE_{in} represent the initial kinetic energy and surface energy, respectively, before the collision, SE_{md} and KE_{md} are the surface energy and kinetic energy at the point of maximum deformation, and VDE denotes the viscous dissipation energy.

$$KE_{in} + SE_{in} = SE_{md} + KE_{md} + VDE \tag{3.68}$$

$$KE_{in} = \frac{1}{2}\rho_l\pi\left(\frac{d_s^3 u_s^2 cos^2\theta}{6} + \frac{d_l^3 u_l^2 cos^2\theta}{6}\right) \tag{3.69}$$

In this model, the initial kinetic energy also considers the whole droplets, as Hu et al. (2017) did. Then, it can be described as Eq. 3.10 considers the entire droplet volume, instead of the assumptions that one droplet is stationary and the interaction region of colliding droplets define in the model of Estrade et al. (1999). The velocities can be calculated as Eqs. 3.11 and 3.12. Therefore, the initial kinetic energy can be described as Eq. 3.70. The initial surface energy SE_{in} is defined as Eq. 3.71. The surface energy at max deformation SE_{md} is defined as Eq. 3.72 with the same definition of shape factor ϕ' in Eq. 3.7 in Estrade et al. (1999). In the end, the model can be described as Eq. 3.73:

$$KE_{in} = \frac{d_l^2\pi\Delta^2(1-B^2)}{12(1+\Delta^3)}\rho_l u_{rel}^2 d_s \tag{3.70}$$

$$SE_{in} = \sigma\pi(d_s^2 + d_l^2) = \sigma\pi d_l^2(1+\Delta^2) \tag{3.71}$$

$$SE_{md} = \frac{1}{3}\sigma\pi d_l^2(1+\Delta^2)\phi' \tag{3.72}$$

$$We = \frac{(1+\Delta^2)(1+\Delta^3)(-12+4\phi')}{(1-B^2)(1-\beta)\Delta^2} \tag{3.73}$$

To complete this model, some assumptions need to be involved. At the moment of maximum deformation, during a head-on collision ($B = 0$), all the initial kinetic energy is converted into surface energy and viscous dissipation energy, resulting in $KE_{md} = 0$. However, as the impact parameter B increases, the degree of droplet deformation decreases compared to that of a head-on collision, leading to a reduction in the viscous dissipation and surface energy at maximum deformation, as shown in Figure 3.5. This figure illustrates the decreasing degree of droplet deformation as the impact parameter B increases. The experimental data was obtained using droplet chain generators and high-speed shadow imaging (see Sui et al. (2021) and Chapter 4). The high-speed camera operated at 10,000 fps, and the upper images are captured one frame before the first contact, so the second images in each row are considered as t = 0 ms. The binary droplet collision sequences shown in Figure 3.5 correspond to $We \approx 8$. During bouncing, the maximum deformation is reached within approximately 0.7 - 1.0 ms (i.e., 7 - 10 frames). The images with added rectangular frames indicate the moment of maximum deformation. Comparing the deformation at low and high impact parameters, one can observe the difference in deformation. Two scenarios may be identified when observing the bouncing droplet collision process. For impact parameters less than 0.3, which are close to head-on collisions, the colliding droplets bounce away from each other and make a specular reflection. However, in the case of bouncing with impact parameters larger than 0.3, the droplets start to move around each other after touching (i.e., the collision complex begins to rotate) and eventually continue almost their original trajectories. The effect of rotational droplets is not included in the energy equation, as in the other models.

As shown in Figure 3.5, the eccentricity and angular velocity of the colliding droplets and
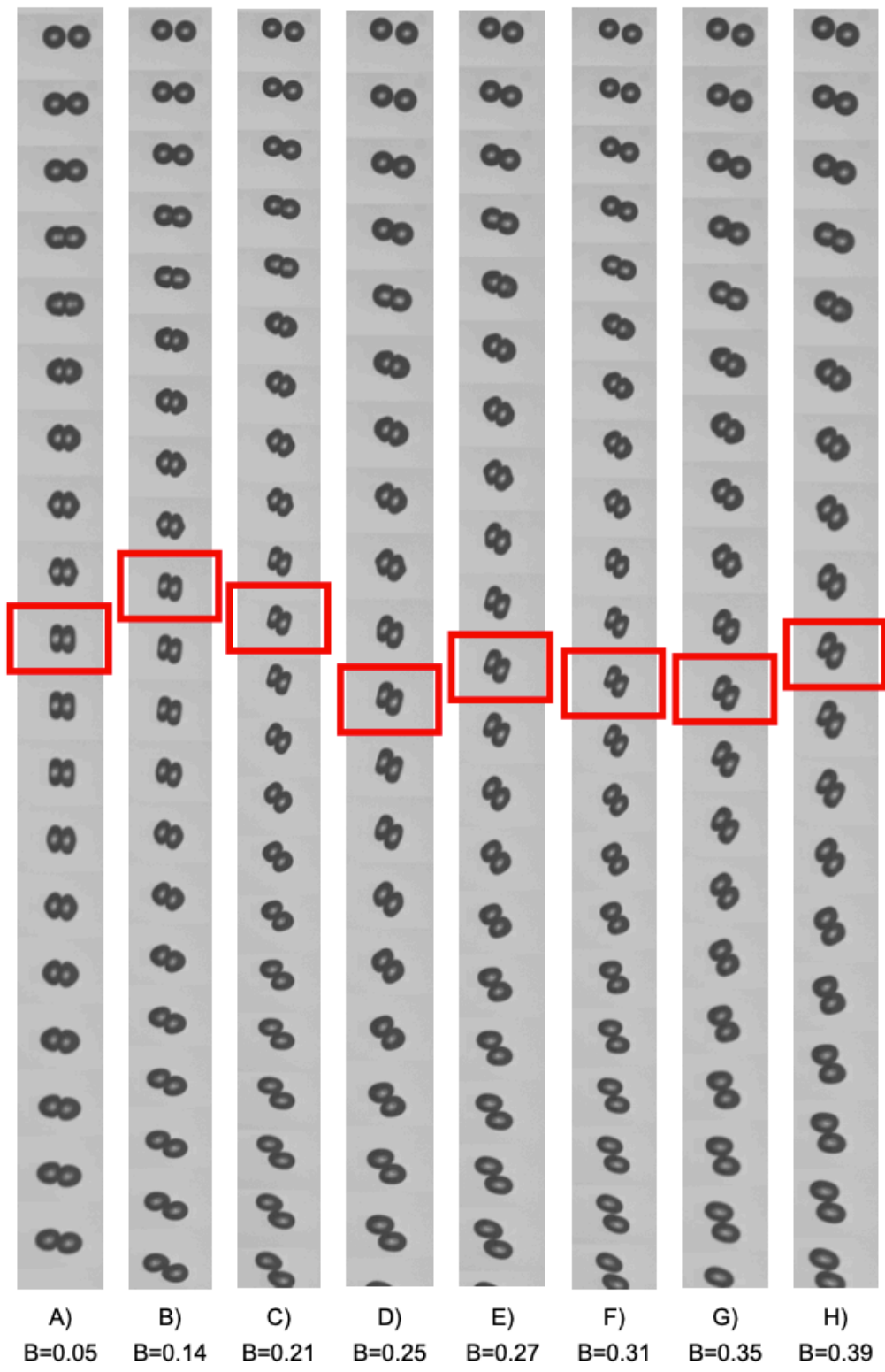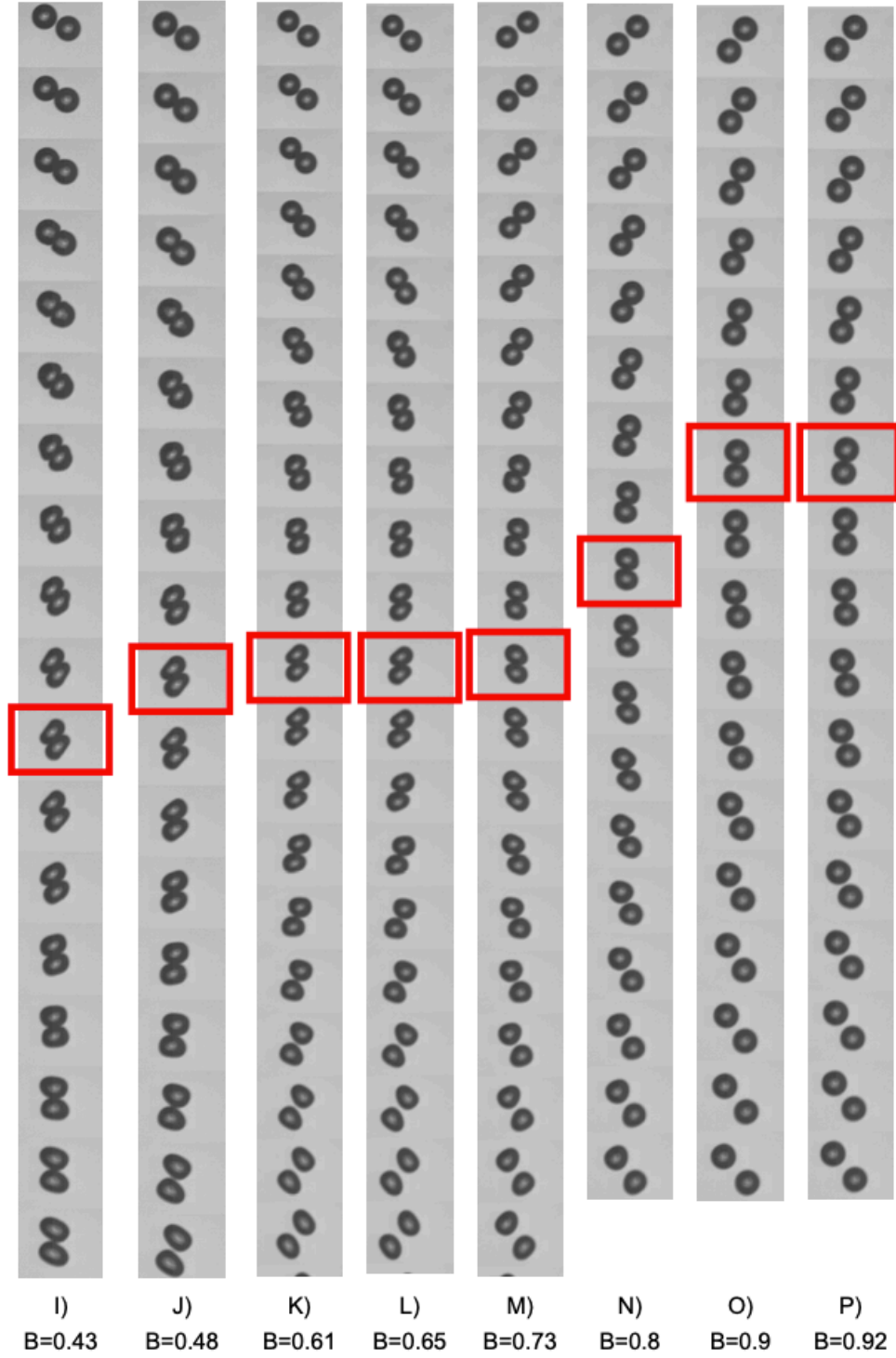
Figure 3.5: Time series of bouncing droplet collisions with a Weber number of $We \approx 8$ and increasing impact parameter B in each of the two graphs from left to right; upper graph: $B = 0.05, 0.14, 0.21, 0.25, 0.27, 0.31, 0.35, 0.39$; lower graph: $B = 0.43, 0.48, 0.61, 0.65, 0.73, 0.80, 0.90, 0.92$; each series of images runs from top to bottom with a time difference of $\Delta t = 0.1$ ms; the images with a rectangular mark corresponds to the moment of maximum deformation in the collision sequences (initial droplet diameter ≈ 770 μm; Maltodextrin solution 20Ma% with σ = 57.4 mN/m, μ = 3.12 mPa·s, $Oh = 0.0142$).

the slowly rotating collision complex can be evaluated for different impact parameters B, as illustrated in Figure 3.6. The eccentricity e of the colliding droplet pair can be calculated by matching each droplet of the collision pair with an equivalent ellipsoid and using its width a and height b. The resulting eccentricity values for both droplets at the point of maximum deformation are plotted in Figure 3.7 as a function of B. The graph shows a nearly linear reduction of the eccentricity with increasing B, indicating that the level of droplet deformation is inversely proportional to the impact parameter for the same liquid.

The angular velocity ω is calculated using the rotational movement of the line connecting the centres of mass of the collision pairs, as shown in Figure 3.6. The angular velocity is equal to the angle difference between frames, or $\omega = \Delta\theta/\Delta t$. As shown in Figure 3.8, the angular velocity behaves similarly for impact parameters between $B = 0.9$ and $B = 0.48$, with relatively small differences for $B > 0.5$. After droplet contact, the linear momentum of the droplets is transferred to rotation, leading to an increase in angular speed. The maximum angular speed is reached at the point of maximum deformation, followed by a continuous decrease until it approaches zero. The angular velocity development has a weak dependence on the impact parameter for $B > 0.5$, with a reduction in torque arm and attained angular speed for smaller B. The time-dependent curves also exhibit stronger fluctuations at smaller B.
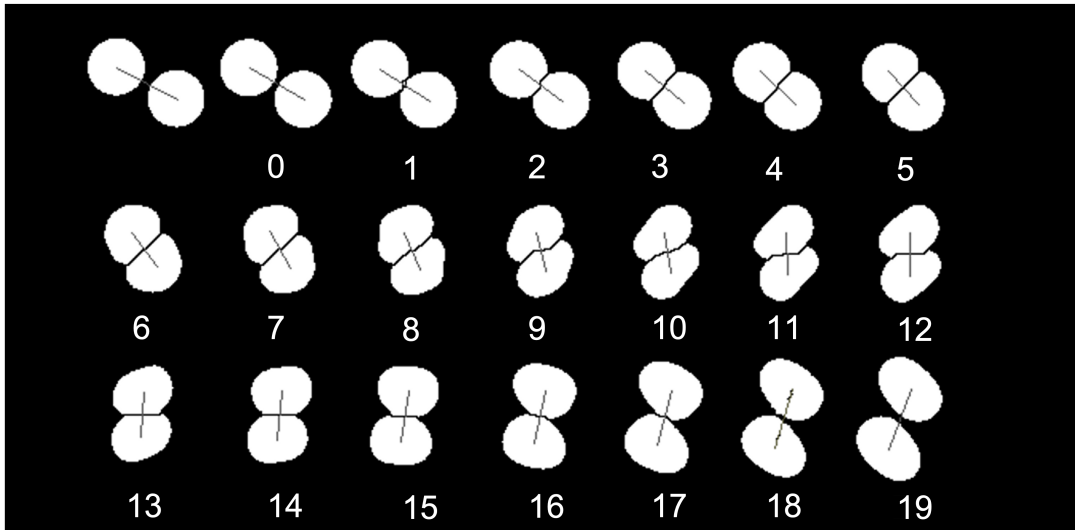
Figure 3.6: Example of eccentricity and angular velocity calculation for colliding Maltodextrin droplets with 20Ma% at $B = 0.48$, marked with number of frame. (Maltodextrin solution 20Ma% with $\sigma = 57.4$mN/m, $\mu = 3.12$ mPa·s, $Oh = 0.0142$, $\Delta t = 1/10000$s)

The bouncing criterion with consideration of the shape factor ϕ' is the same as the model proposed by Estrade et al. (1999). However, it is clear that the shape factor ϕ' varies for different impact parameters B, as discussed above. This also applies to the energy conversion rate β, which comprises the kinetic energy remaining in both droplets and the viscous dissipation energy. In Jiang et al. (1992), it was reported that for head-on collisions at $B = 0$, a maximum of 50% of the initial kinetic energy is transformed, while in Hu et al. (2017), this value was specified as 47%. When the relative velocity becomes zero, there is no remaining kinetic
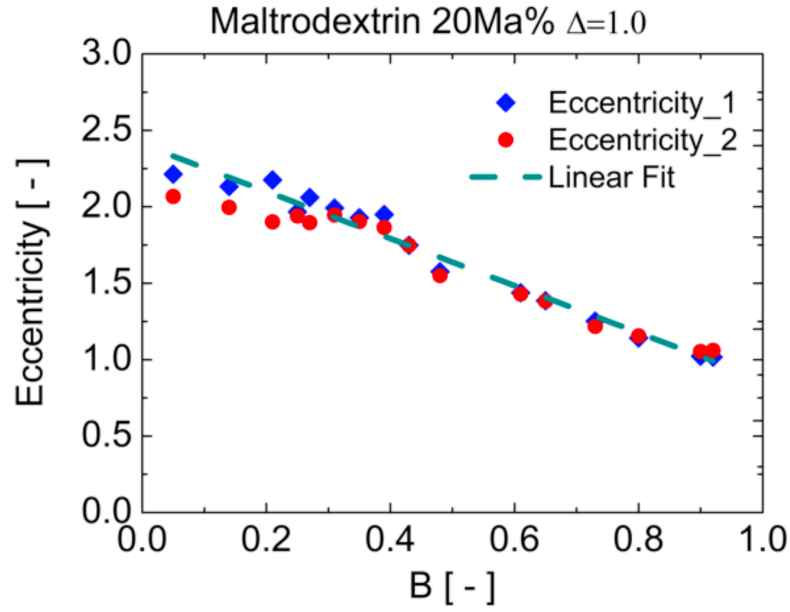
Figure 3.7: Eccentricities at maximum deformation of bouncing droplet collision pairs; eccentricity 1 and 2 correspond to the slightly different values of both droplets (Weber number $We \approx 8$; Maltodextrin solution 20Ma% with $\sigma = 57.4$mN/m, $\mu = 3.12$ mPa·s, $Oh = 0.0142$
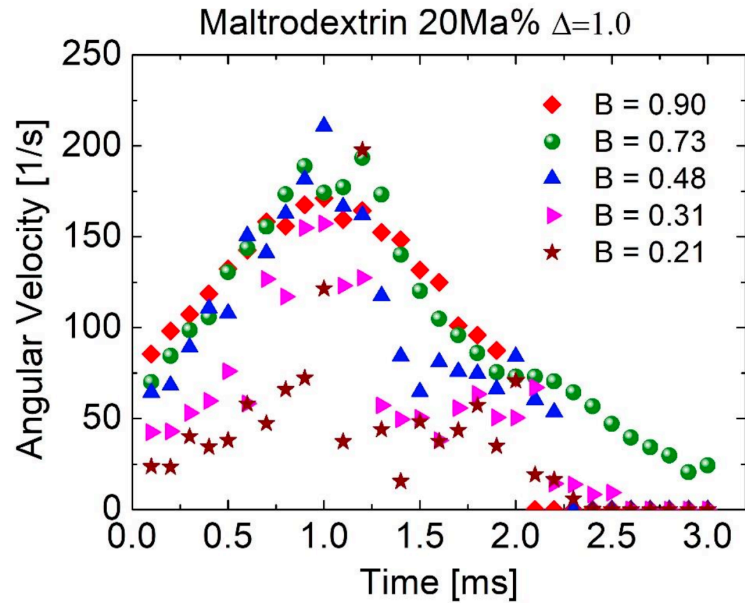
Figure 3.8: Angular velocity of the droplet collision complex (in revolutions per second) in dependence of time with the impact parameter B as a parameter (Maltodextrin solution 20Ma% with $\sigma = 57.4$mN/m, $\mu = 3.12$ mPa·s, $Oh = 0.0142$

energy in the droplets. Therefore, assuming a maximum initial conversion rate ($\beta = 0.5$) for droplets at head-on collision ($B = 0$) is acceptable. As the impact parameter increases to the upper limit ($B = 1$), the two droplets touch each other, and there is no kinetic energy converted to surface energy and viscous dissipation. Hence, the conversion rate approaches a value of $\beta = 1$. According to the definition of β, it cannot exceed unity. Thus, in the graph of β versus B, the curve must pass through two fixed points: $(0, \beta_{in})$ and $(1, 1)$, where β_{in} is the intercept with the vertical axis ($\beta_{in} < 0.5$). However, there may be many possible routes connecting these two points. Previous numerical simulations of droplet collisions (He et al. (2019); He et al. (2020); Chen et al. (2012); Chen and Yang (2012); Chen et al. (2011)) presented an energy analysis for a bouncing process, showing that the dissipated energy behaves in a complex manner throughout the bouncing process, involving three stages: impact, bouncing, and oscillation. Therefore, in this study, the behaviour was simplified by assuming that both model parameters $\phi'(B)$ and $\beta(B)$ have a linear relationship with the impact parameter B, as given by the following equations:

$$\phi'(B) = -k_{\phi'}B + \phi'_{in} \tag{3.74}$$

$$\beta(B) = (1 - \beta_{in})B + \beta_{in} \tag{3.75}$$

The slope for the conversion rate, given by $k_\beta = 1 - \beta_{in}$ and already considered in Eq. 3.75, leads to three unknown dependencies. These include an intercept on the ordinate and a slope of the curve for each of the two model parameters, ϕ' and β, which must be determined through a fitting process using experimental data, if possible. Furthermore, the values of ϕ' and β are also influenced by the liquid properties, making the Ohnesorge number relevant. As shown in Figure 2.3a, the surface tension plays an important role in the bouncing process and the critical bouncing point We_{B-C}. The studies conducted by Pan et al. (2016) and Al-Dirawi and Bayly (2019) have shown that the We_{B-C} of water is significantly impacted by surfactant concentration until it reaches the Critical Micelle Concentration (CMC), and the location of We_{B-C} varies with different HPMC concentration, respectively. Therefore, the Oh number is a relevant parameter for describing the dependence of the four constants in Eqs. 3.74 and 3.75. Ultimately, ϕ'_{in}, $k_{\phi'}$ and β_{in} are correlated with both Oh and B. To determine the three required fitting parameters in Eqs. 3.74 and 3.75, numerous experimental data were considered. However, only those results presenting complete collision maps, including all common regions of collision outcome scenarios and possible characteristic points (as illustrated in Figure 2.3a), were deemed useful for this purpose. These requirements naturally limit the number of useful data. A summary of all the considered datasets is presented in Figure 3.10a and Tables. A.1 and A.2, which include relevant liquid properties. The procedure for evaluating the remaining 3 fitting parameters eventually in Eq. 3.74 and 3.75 are as follows:

- Adapt the lower bouncing boundary to the data points included in the collision maps and determine the associated values for ϕ'_{in} and β based on Eq. 3.72 until the best matching is reached in the $B - We$ collision map, including especially the regions of low and high We. This adaptation is basically done manually modifying the two parameters in the expected range and selecting the best combination. In some experimental results, like sucrose 20%, there is no critical bouncing point We_{B-C} on the horizontal axis

with $B = 0$. This would generate a problem in identifying the bouncing region on the collision map. However, the triple points We_T location Kuschel and Sommerfeld (2013); Sommerfeld and Kuschel (2016) could also give a good solution for this problem. Therefore, two characteristic points are considered, which are We_{B-C} and We_T, working as anchor points to fit the experimental results properly.

- Then, ϕ'_{in}, $k_{\phi'}$ and β_{in} versus Oh were plotted respectively with the value of perfect artificial matching as reference.

- Afterwards, prototype third-order polynomial regression equations are generated, as baselines, to get the tendency of the three parameters as the model described in Sui et al. (2023).

- Afterwards, the third order polynomial regression equations of ϕ'_{in}, $k_{\phi'}$ and β_{in} versus Oh are also updated by adding other experiment results automatically.

- In the end, the chosen parameters calculated by the third-order polynomial regression equations are taken into the Eq. 3.74 and Eq. 3.75. Then the resulting shape factor and conversion rate for the liquid considered are applied in Eq. 3.72 to obtain the bouncing boundary line.

All collected data points of the fitting parameters ϕ'_{in} and $k_{\phi'}$ show a continuous decay over the entire considered Ohnesorge number range up to about 0.35, whereas β_{in} is continuously increasing as shown in Figure 3.9. Unfortunately, there are only a few experimental data with $Oh > 0.35$, hence, in the region of larger Oh the present data fitting is not reliable. Interestingly, the experimental data delivering the intercept value for the shape factor ϕ'_{in} and the slope data $k_{\phi'}$ are both scattered clearly along two lines. Analysing now the properties of the liquids represented by the full symbols, it is obvious that these are mainly alcohols, alkanes and oils having a quite low surface tension between about 20 and 30 mN/m (see Table A.1) and are therefore termed **non-water-like** liquids. There are only two exceptions in this list; the glycol liquids (MEG, DEG and TEG) used by Gotaas et al. (2007) and the HPMC solutions analysed by Al-Dirawi and Bayly (2019). For these liquids, the surface tension is also remarkably lower as for water, namely between 45 and 50 mN/m. The results for the HPMC solution will be further discussed later including a comparison with both the non-water-like and the water-like correlation (see Figure 3.22). Since HPMC is a surface-active substance, expectedly, this should remarkably influence the droplet bouncing process.

On the other hand, all the liquids represented by the half-filled symbols have surface tensions between 63 and 78 mN/m which is in the range of pure water. Therefore, since most of the liquids in this range are water-based solutions, they are summarised as **water-like** fluids. Naturally, the surface tension will have a large influence on bouncing, and one may expect that growing surface tension might reduce the occurrence of bouncing. This will be further discussed below. It should be emphasised that a similar distinction could be made for the parameter C_a in the stretching separation-coalescence boundary described through the Jiang et al. (1992) model Sommerfeld and Pasternak (2019). On the other hand, the intercept β_{in} of the conversion rate β (see Eq. 3.75) shows a continuous increase and the same trend for both kinds of liquids, as shown in Figure 3.9c)).

The eventually obtained third-order polynomial regression curves can be described by Eqs. 3.76 - 3.78 and are shown together with the considered experimental data points in Figure 3.10, for all three parameters.

For Non-water-like liquids:

$$\begin{cases} \phi'_{in} = -19.03Oh^3 + 11.601Oh^2 - 3.4916Oh + 4.0025 \\ k_{\phi'} = -30.318Oh^3 + 19.05Oh^2 - 4.6816Oh + 0.9449 \end{cases} \tag{3.76}$$

For water-like liquids:

$$\begin{cases} \phi'_{in} = 2.4096Oh^3 + 3.2147Oh^2 - 2.7879Oh + 3.6492 \\ k_{\phi'} = -15.019Oh^3 + 12.937Oh^2 - 4.0545Oh + 0.5935 \end{cases} \tag{3.77}$$

For all liquids:

$$\begin{cases} \beta_{in} = 1.695Oh^3 - 3.9157Oh^2 + 2.4281Oh + 0.0619 & Oh \leq 0.35 \\ \qquad\qquad \beta_{in} = 0.5 & Oh > 0.35 \end{cases} \tag{3.78}$$

It is not expected that the general trend of the proposed polynomials will significantly change with additional new data. However, additional data for fluids with high Ohnesorge numbers, especially for non-water-like liquids, could lead to improvements. First, the Estrade et al. (1999) model is considered, and the results are depicted in the collision map, i.e., $B = f(We)$, (Figure 3.10a and 3.10b). The variation of the droplet size ratio (here in the range $0.5 < \Delta < 1.0$) has only a small influence on the location of the boundary line, basically yielding an upward and left shift when decreasing Δ. The shape factor ϕ' has much stronger effects on the boundary line location. The increase of the shape factor results in a downward and right displacement of the boundary line to higher We. It should be noted, that $\phi' = 3.351$ was the original value obtained by Estrade et al. (1999). Actually, this trend is similar to that observed for the intercept of the shape factor ϕ'_{in} and is associated with a decrease of the surface tension (see Figure 3.9a).

In the novel bouncing boundary model proposed here, ϕ'_{in} and Δ are the major parameters that significantly influence the boundary line location and the critical bouncing point We_{B-C} in the collision map. The variation of the slope $k_{\phi'}$ in the shape parameter will of course not change the critical bouncing point We_{B-C}, but the bouncing boundary line is bending downwards with decreasing slope parameter $k_{\phi'}$ (Figure 3.10c). According to Figure 3.9b, this may be linked to an increase of surface tension, namely when going from a non-water-like fluid to a water-like fluid. An increase of the intercept value (i.e. ϕ'_{in}) obviously shifts the critical bouncing point to the right, to higher We (Figure 3.10d), which was also observed for a reduction of liquid viscosity (see Kuschel and Sommerfeld (2013) and Sommerfeld and Kuschel (2016); also becoming obvious from Figure 3.14 and 3.17 below. The right part of the bouncing curve (i.e. at higher We) is bending downwards when increasing ϕ'_{in} (Figure 3.10d). According to Figure 3.9a)) an increase of the intercept ϕ'_{in} is also associated with a reduction of the surface tension (i.e. going from water-like to non-water-like fluids), whereby the bouncing region would be extended. However, there is competition with $k_{\phi'}$, which predicts a constant critical bouncing point and a reduction of the bouncing region with growing surface tension.
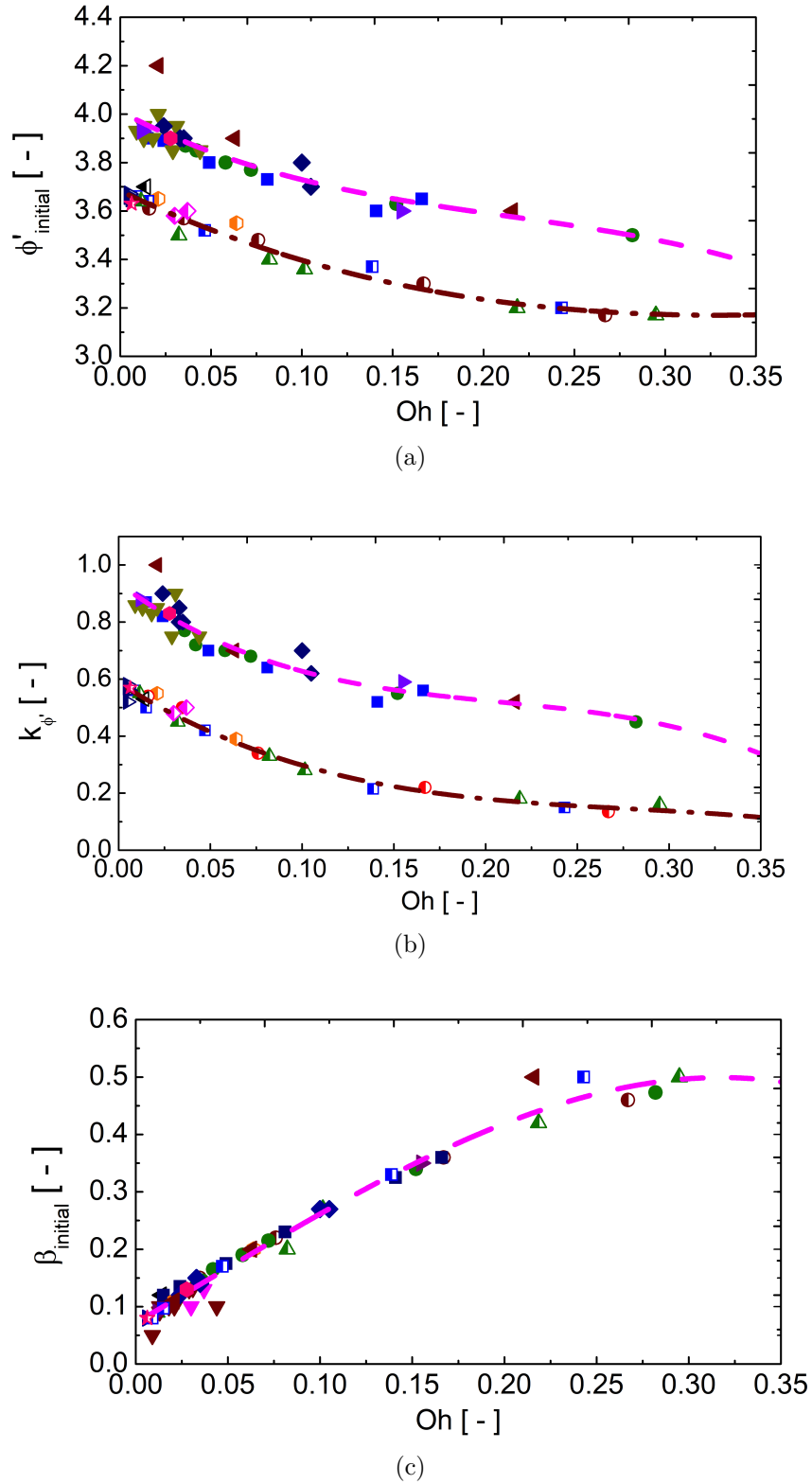
(a)

(b)

(c)

Figure 3.9: Experimental data points for evaluating the three fitting parameters in dependence of liquid properties are summarised in the Ohnesorge number and resulting functions according to Eqn. 3.76 to 3.78; (a) ϕ'_{in},(b) $k_{\phi'}$,(c) β_{in}. (Legend in next page)

Non-Water-Like Group:

- ■ Alcohol (Sommerfeld and Kuschel (2016))
- ● FVA (Sommerfeld and Kuschel (2016))
- ▼ Alkanes (Huang (2015))
- ◆ Diesel (Chen, Wang, and Chen (2016))
- ◀ HPMC (Al-Dirawi and Bayly (2019))
- ▶ MEG/n-decane(Gotaas et al. (2007))
- ⬤ Tetradecane(Qian and Law(1994))
- – – – Fit Curve for Non-water like liquids

Water-Like Gourp:

- ◫ K17 (Kuschel and Sommerfeld (2013))
- ◑ K30 (Kuschel and Sommerfeld (2013))
- ▲ Sucrose (Kuschel and Sommerfeld (2013))
- ◆ PVP (Pasternak and Sommerfeld (2017))
- ◀ Xanthan (Finotello et al. (2018))
- ▶ Waters (Kuschel and Sommerfeld (2013)
        Sui, Sommerfeld, and Pasternak (2019)
        Foissac, Malet, and Mimouni (2010))
- ⬡ Glycerol (Finotello et al. (2018))
- ★ Water (Qian and Law(1994))
- –·–·– Fit Curve for water like liquids

Legend of Figure 3.9

This occurs at a lower rate, so that the trends observed for ϕ'_{in} should be dominating. The increase of the intercept β_{in} in the conversion rate, results in a parallel shift of the bouncing boundary line towards higher We numbers, as shown in Figure 3.10e. With decreasing in the size ratio Δ, the novel model shows a much stronger effect compared to the original Estrade et al. (1999) model and the bouncing boundary moves to a higher We number and the curvature is remarkably growing (Figure 3.10f).

3.4.1 Collision Maps and Validation

To ensure the validity of the proposed novel bouncing boundary line model, several experimental results are taken into consideration. These results consist of full collision maps that incorporate a bouncing region. Most of these datasets are sourced from Kuschel and Sommerfeld (2013); Sommerfeld and Kuschel (2016), which investigate **non-water-like** and **water-like liquids**, respectively. Non-water-like liquids, such as alcohols and FVA reference oil at different temperatures, are examined, while water-like liquids, including PVP (polyvinylpyrrolidone) K30 solution with 5-25Ma% mass concentration, PVP K17 with 5-25Ma% mass concentration, and sucrose with 20-60Ma% mass concentration in water solutions, are analysed. All of these liquids have a dynamic viscosity ranging from 1 to 60 mPa·s. The experiments were conducted at a temperature of approximately $23°C$ and an air pressure of 1 bar. Moreover, a glycerol-water mixture with varying concentrations, which was studied experimentally by Finotello et al. (2018a) in connection with spray dryer applications, is also examined. Additionally, Chen et al. (2016) present additional droplet collision maps for a range of alkanes and diesel mixtures, which include the novel bouncing boundary.

Water is an exception to the bouncing boundary model as it does not exhibit a bouncing region for low B and We Laín and Sommerfeld (2020). As such, the continuous bouncing boundary line that runs from low to high B cannot be directly applied, as shown in Figure 3.11. In experimental studies with a size ratio of one, bouncing is only observed when $B > 0.6$, and it extends over the entire range of Weber numbers. This behaviour may be due to the unique interface characteristics of water and its large surface tension compared to most other liquids in air (see Tables A.1 and A.2). Collision maps of various experiments with different initial droplet diameters are presented in Figure 3.11 and compared with the novel
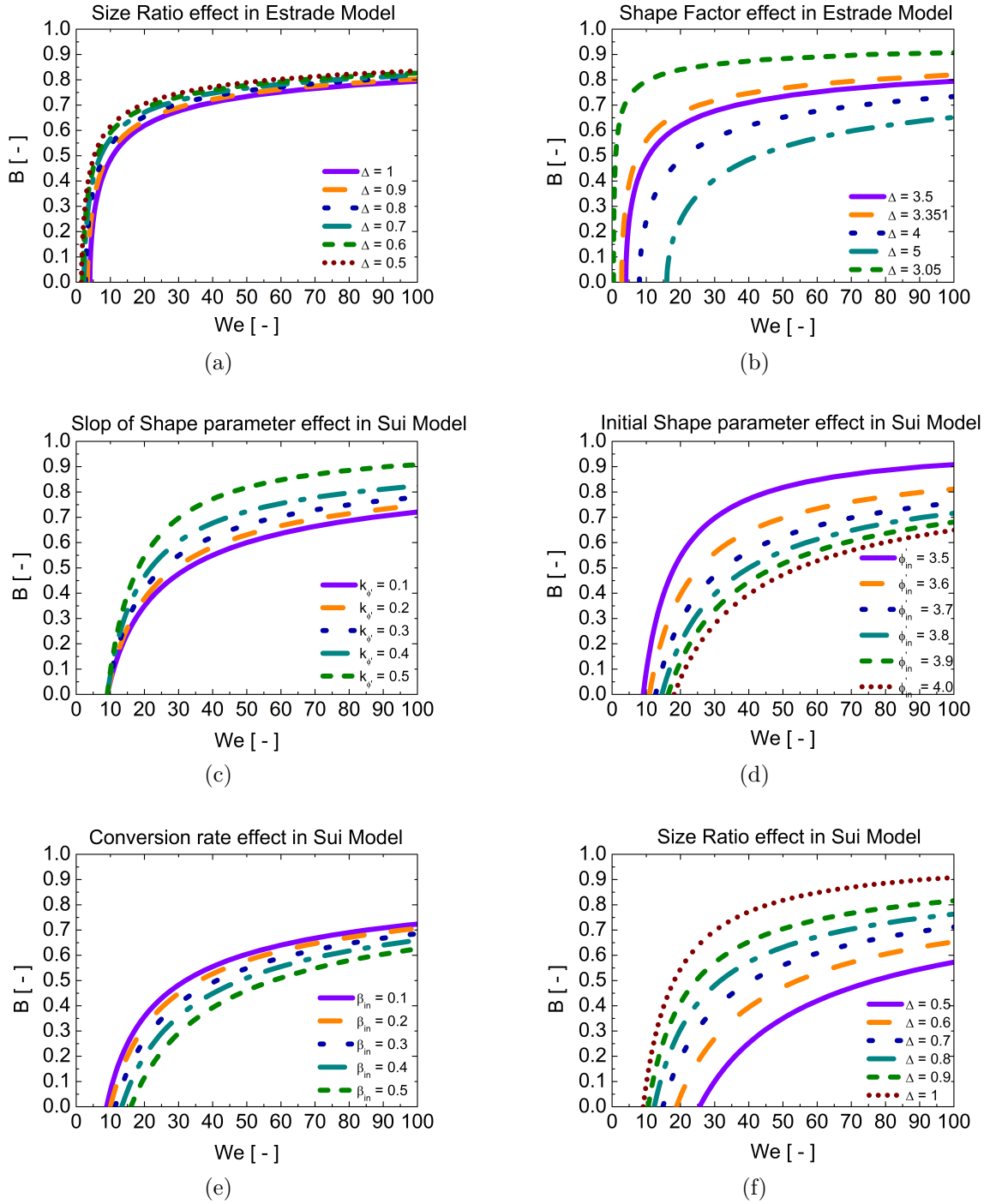
Figure 3.10: Influence of the included model parameters and the droplet size ratio on the lower bouncing boundary, comparison between the Estrade et al. (1999) model and the present new model (Sui et al. (2023)); (a) effect of size ratio Δ and (b) shape factor ϕ' in the Estrade et al. (1999); (c), (d), (e) and (f) influence of $k_{\phi'}$, ϕ'_{in}, β_{in} and size ratio Δ on the proposed bouncing boundary in the $B - We$ collision map.

bouncing boundary model and the model proposed by Estrade et al. (1999). The experiments conducted by Kuschel and Sommerfeld (2013) used 380 μm droplets, and Foissac et al. (2010) used 300 μm droplets. Although the experiments by Sui et al. (2021) used even larger water droplets (405 and 601 μm), the results showed the same droplet collision behaviour and almost identical collision maps. The extension of the bouncing region is comparable for all experiments shown (Figure 3.11). The trend of both bouncing lines is consistent, even for other liquids, as discussed below. The Estrade et al. (1999) boundary is located to the left of the new bouncing boundary line for lower B values (i.e., $B < 0.7$), including dissipation and a parameter dependence on B. For larger impact parameters, the new bouncing boundary is slightly above the Estrade et al. (1999) model, leading to slightly better agreement with the experiments (see Figure 3.11). The new model captures the location of the triple point We_T better, but neither model accurately represents the lower bouncing boundary to the left of the triple point because no bouncing occurs at $B < 0.7$. To simulate spray behaviour numerically, the bouncing boundary should be considered only up to the triple point We_T, and the boundary between bouncing and coalescence should be described using the coalescence-stretching separation boundary Laín and Sommerfeld (2020).

In experiments with droplets of different alcohols (a non-water-like fluid), complete bouncing regions were observed across the entire range of B, from small We to the maximum considered We (Figure 3.12). Unfortunately, experimental data were not collected for the entire bouncing region at that time (Sommerfeld and Kuschel (2016)). However, bouncing was observed for Hexanol and Heptanol at small B. Upon the first inspection of the alcohol collision maps, it became evident that the original bouncing model proposed by Estrade et al. (1999) did not accurately predict the bouncing boundary over the entire range of We considered (Figure 3.12). On the other hand, the proposed novel model that incorporates dissipation performed much better. The critical bouncing points We_{B-C} were relatively well-captured for all four alcohols. Additionally, the improved boundary line captured the transition between the boundaries of bouncing-coalescence (at low We) and bouncing-stretching separation (at higher We) very well. The Estrade et al. (1999) boundary was consistently located to the left of the proposed bouncing boundary in the low We region, and below the new bouncing boundary for higher We, yielding better agreement with the measurements.

Additionally, for the measurements, as shown in the Figure 3.13, with FVA reference oil, a non-water-like fluid, at different temperatures, and properties (see Table A.1 and A.2), unfortunately, not sufficient experiments were conducted in the region below $We < 20$ (Sommerfeld and Kuschel (2016)). Therefore, it is unclear whether bouncing exists in this region and if it does, whether it extends down to $B = 0$ (Figure 3.13). However, in other oils, such as sunflower oil, bouncing has been observed at low impact parameter and low We (Sommerfeld and Pasternak (2019)). When only considering the upper branch of the bouncing boundary, the extended bouncing model shows a slightly better agreement with experimental data than that predicted by the Estrade et al. (1999) model and performs better around the triple point region (Figure 3.13).

The following results pertain to **water-like** liquids, such as solutions and water-miscible fluids, as shown in Figures 3.14 - 3.17. In the detailed experimental studies by Kuschel and Sommerfeld (2013), several solutions with varying solid content were examined. The increase
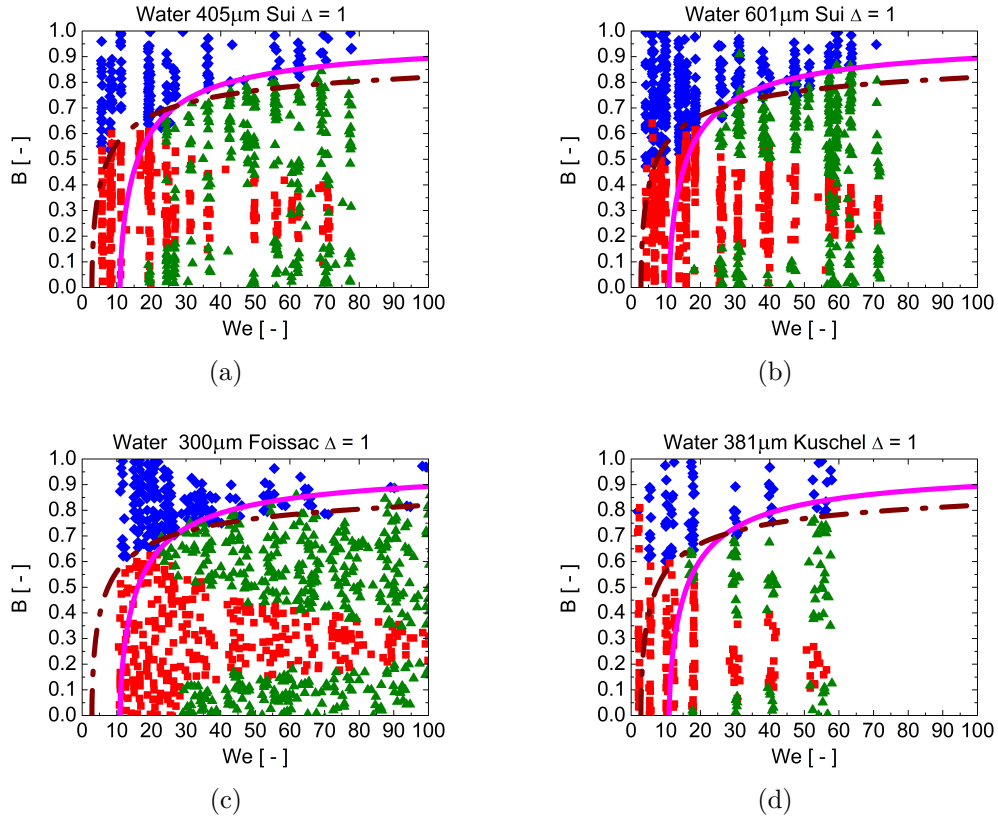
Figure 3.11: Droplet collision maps for water obtained from different research studies and with different initial droplet sizes (Foissac et al. (2010); Kuschel and Sommerfeld (2013); Sui et al. (2021); comparison with theoretical boundary lines; (brown) dash-dot line: model of Estrade et al. (1999) with shape factor $\phi' = 3.351$; (magenta) closed line: Sui et al. (2023) model with water-like correlation; (symbols: (blue) diamonds: bouncing region; (red) squares: coalescence region; (green) triangles: separation regions).

in solid content resulted in a significant increase in dynamic viscosity.

At the lowest solid content, the experiments clearly indicate bouncing occurring down to $B = 0$ (Figure 3.14a). At higher solid content, the region near the critical bouncing point is not adequately resolved in the experiments, and no bouncing is observed near $B = 0$. Nonetheless, with an increase in viscosity, the critical bouncing point We_{B-C} shifts significantly to the left, towards lower Weber numbers; both the model and experiments exhibit this behaviour, implying an increasing tendency of coalescence. The possible reasons for this will be discussed below. The new bouncing model with energy dissipation and a dependence on the impact parameter B seems to accurately capture the location of the triple point and critical bouncing point. Moreover, in the range of large We, the new boundary is positioned above the Estrade et al. (1999) boundary and thus shows a better agreement with the measured boundary location (Figure 3.14). The Estrade et al. (1999) model is observed to go through the region of stretching separation for most cases.

In the experiments of Kuschel and Sommerfeld (2013), PVP K17 solutions with a different molecular chain length were studied as shown in the Figure 3.15, having a much lower dynamic
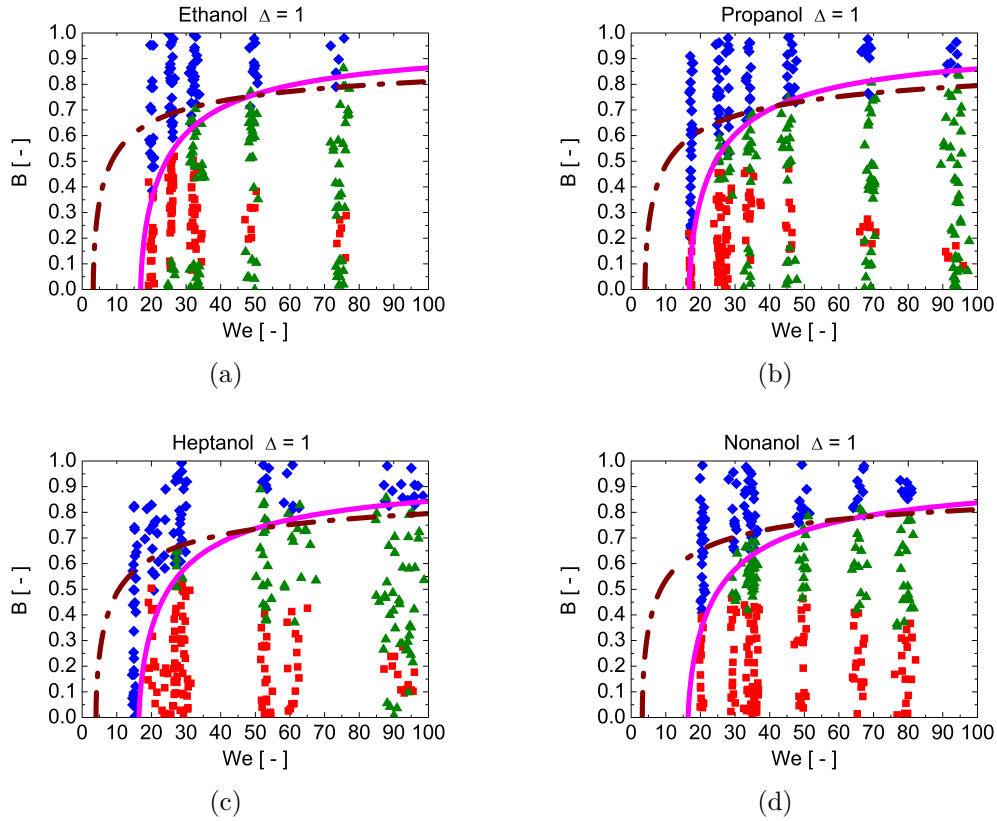
Figure 3.12: Droplet collision maps for the series of alcohols a) Ethanol, b) Propanol, c) Hexanol, d) Heptanol and comparison with theoretical boundary lines; (brown) dash-dot line: model of Estrade et al. (1999) with shape factor $\phi' = 3.351$; (magenta) closed line: Sui et al. (2023) model with non-water-like correlation; (symbols: (blue) diamonds: bouncing region; (red) squares: coalescence region; (green) triangles: separation regions).

viscosity compared to PVP K30 for the same solids content (see Table A.1 and A.2). These results were compared with those obtained by Sommerfeld and Pasternak (2019) for about the same solids content and dynamic viscosity, but using much larger droplets. The comparison suggests that the bouncing region at lower impact parameter B is extended to the right when the initial droplet size increases, resulting in a higher critical bouncing Weber number of around 14.5 instead of 7.0 (Figure 3.15). The same behaviour was observed for hydrocarbon droplets with different initial sizes, as summarised in Figure 3.18. This suggests that a bigger air cushion between the droplets, associated with larger drainage times and reduced coalescence probability, can prevent coalescence for lower We. However, a higher collision velocity is needed to result in coalescence and yield the drainage of the air cushion, as shown in Figure 3.15b). This effect was also confirmed by a scaling analysis presented by Huang and Pan (2021). All introduced bouncing boundary line models only account for the size ratio, not the absolute droplet size, which remains constant in both cases of Figure 3.15 with $\Delta = 1$. Therefore, the shape and location of both bouncing models (i.e., Estrade et al. (1999) and Sui et al. (2023)) do not change when the droplet size increases. The new bouncing model predicts the experimental data well for the lower droplet size, but under-predicts the critical bouncing
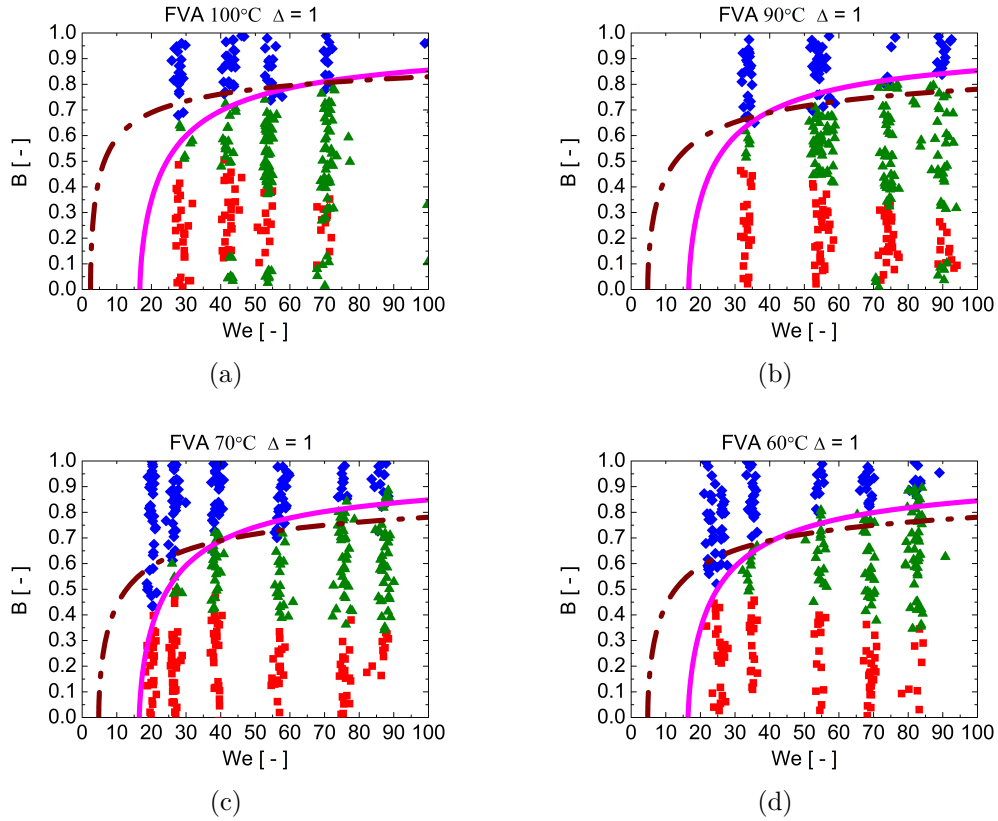
Figure 3.13: Droplet collision outcome maps for FVA reference oil at different temperature a) $100°C$, b) $90°C$, c) $70°C$, d) $60°C$ and comparison with theoretical boundary lines; (brown) dash-dot line: model of Estrade et al. (1999) with shape factor $\phi' = 3.351$; (magenta) closed line: Sui et al. (2023) model with non-water-like correlation; (symbols: (blue) diamonds: bouncing region; (red) squares: coalescence region; (green) triangles: separation regions).

Weber number for the larger droplets (Figure 3.15). However, this prediction is closer to the experimental value than the We_{B-C} value predicted by the Estrade et al. (1999) model.

In the case of sucrose solutions in water (Kuschel and Sommerfeld (2013)), neither theoretical boundary lines match well with the experiments for all cases with different solids content (Figure 3.16). Only for the 40% sucrose solution, the new model seems to be better than the Estrade et al. (1999) model, especially for the regime of large We. However, the available experimental data do not provide clarity as to whether bouncing at low We extends down to $B = 0$. Therefore, the sucrose droplet collision maps are similar to the pure water cases (see Figure 3.11). The experiments suggest that the bouncing boundary at high We moves slightly downward with increasing solids content and then jumps up again at 60% solids content. At this higher solid content, the bouncing model of Estrade et al. (1999) performs better, especially at the lower branch with low B. Additional experiments for low We are necessary to confirm the existence of bouncing in this region at low impact parameter.

The experimental studies of Finotello et al. (2018b) focused on droplet binary collisions in spray dryers, using real milk concentrates with varying solids content. However, bouncing was not observed in milk collision experiments for Weber numbers up to about $We = 100$, which
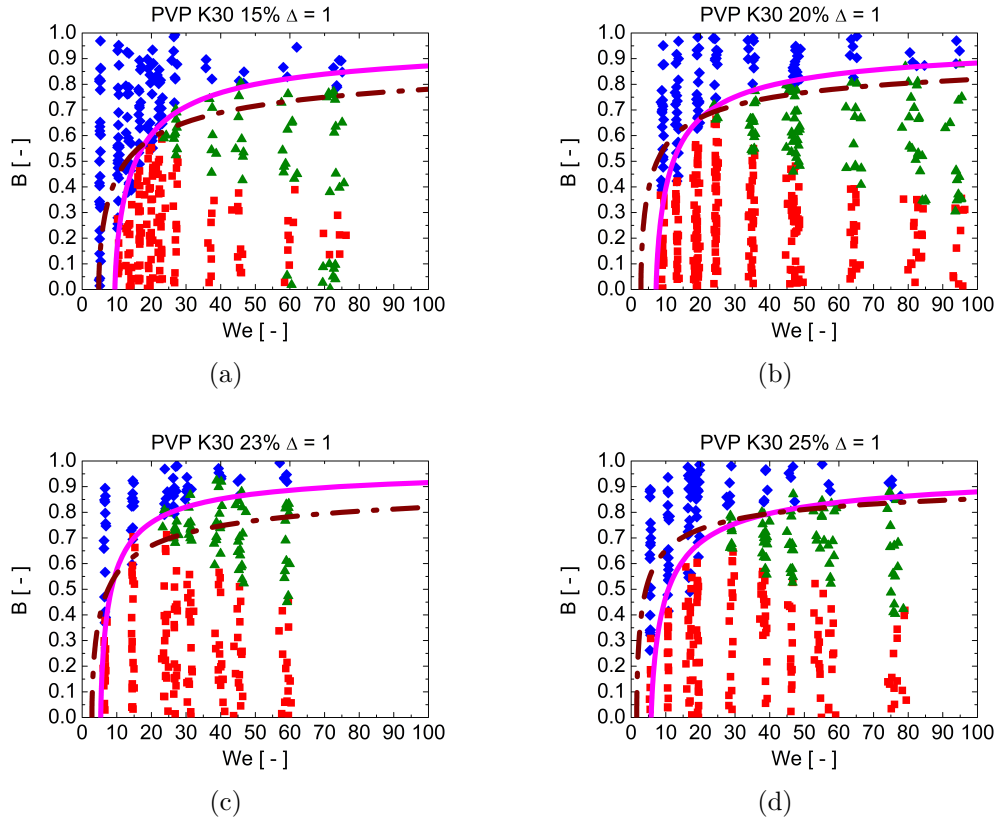
Figure 3.14: Droplet collision maps for a polymer solution PVP (polyvinylpyrrolidone) K30 with different solids content and comparison with theoretical boundary lines; a) 15 Ma%, b) 20 Ma%, c) 23 Ma%, d) 25Ma%; (brown) dash-dot line: model of Estrade et al. (1999) with shape factor $\phi' = 3.351$; (magenta) closed line: Sui et al. (2023) model with water-like correlation; (symbols: (blue) diamonds: bouncing region; (red) squares: coalescence region; (green) triangles: separation regions).

was attributed to the complex surface chemistry of milk concentrates. Instead, coalescence, reflexive separation, and stretching separation were identified. The composite models (Sommerfeld and Pasternak (2019) as presented in Sommerfeld et al. (2021b)) accurately predicted the boundaries between coalescence and both separation regions. Additionally, experiments with fully miscible glycerol-water mixtures were conducted, which yielded complete collision maps with four outcomes. As the volume concentration of glycerol increased, the dynamic viscosity and Ohnesorge number also increased, and reflexive separation shifted to higher We and eventually disappeared (Figure 3.17). Bouncing was observed over the complete range, from small We and small B to the region of large We and large B. As the percentage of glycerol increased, the critical bouncing point (We_{B-C}) was considerably shifted to the left, to smaller values. A similar behaviour was observed in the experimental results from Al-Dirawi and Bayly (2019) with HPMC solution (see also Figure 3.22), where increasing concentration led to a viscosity growth, shifting the critical bouncing We_{B-C} to lower We. Higher viscosity promoted coalescence to occur already at lower Weber number, as the droplet interface became more stable and the internal flow was hindered by the damping effect of viscosity. This may have reduced the occurrence and size of air cushions between head-on colliding droplets,
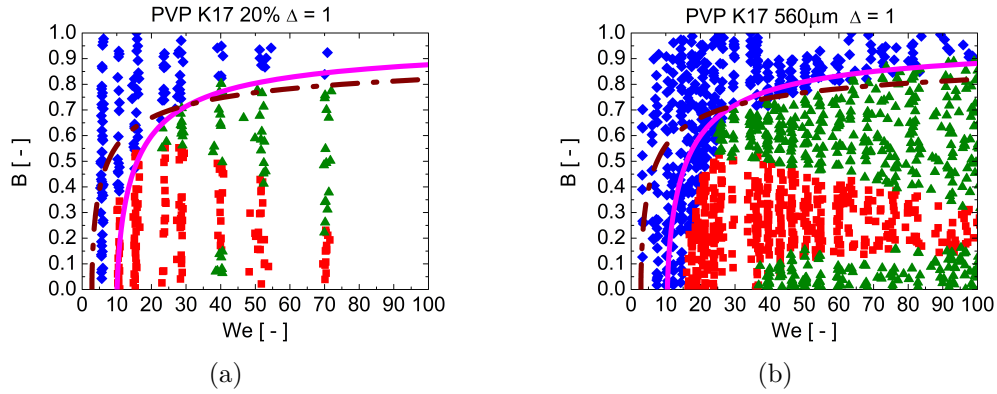
Figure 3.15: Droplet collision maps for the PVP K17 solution with different initial droplet diameter; left: Kuschel and Sommerfeld (2013) with 370 μm droplets and $\mu = 7.6$ mPa·s; right: Sommerfeld and Pasternak (2019) with 560 μm droplets and $\mu = 5.5$ mPa·s; model calculations: (brown) dash-dot line: model of Estrade et al. (1999) with shape factor $\phi' = 3.351$; (magenta) closed line: Sui et al. (2023) model with water-like correlation; (symbols: (blue) diamonds: bouncing region; (red) squares: coalescence region; (green) triangles: separation regions).

leading to easier coalescence. While the surface tension of these water-like fluids (i.e., PVP and glycerol solutions) is quite large, it slightly reduces with growing concentrations. Lower viscous droplets, on the other hand, may deform more easily upon collision (also prior to contact) and promote the occurrence of an air cushion, resulting in higher bouncing probability (Chen and Yang (2020)).

The experimental results for the collision of droplets in glycerol solutions show that the original Estrade et al. (1999) model is not accurate for low glycerol concentrations, but provides a reasonable prediction for the highest concentration. On the other hand, the new model performs well in capturing the general trends, with only a slight under-prediction of the critical bouncing point (We_{B-C}) and incomplete capture of the experimentally estimated triple point for a glycerol concentration of 60%. Nevertheless, the new model accurately predicts the decreasing trend of critical bouncing point with increasing viscosity, which is opposite to the prediction of the Estrade et al. (1999) model that is not observed experimentally (Figure 3.17).

3.4.2 Further Validation

In the studies of Jiang et al. (1992), the boundary between bouncing and stretching separation was not analysed in detail. To further validate the bouncing boundary for alkanes, experimental studies of Huang and Pan (2015) and Huang and Pan (2021) are considered, where the effect of absolute droplet size on binary droplet collisions with $\Delta = 1$ was studied, i.e. the difference between 300 and 600 μm droplets as shown in the Figure 3.18. Unfortunately, these experiments were conducted only for relatively low Weber numbers, i.e., $We < 50$. With respect to the bouncing boundary line (Figure 3.18), a shift of the critical bouncing Weber number We_{B-C} to higher values with increasing droplet diameter is noticed in the experiments. Also, in the research of Pasternak and Sommerfeld (2017), it was found that bouncing for larger droplet collisions occurs at higher Weber numbers (see Figure 3.15). As
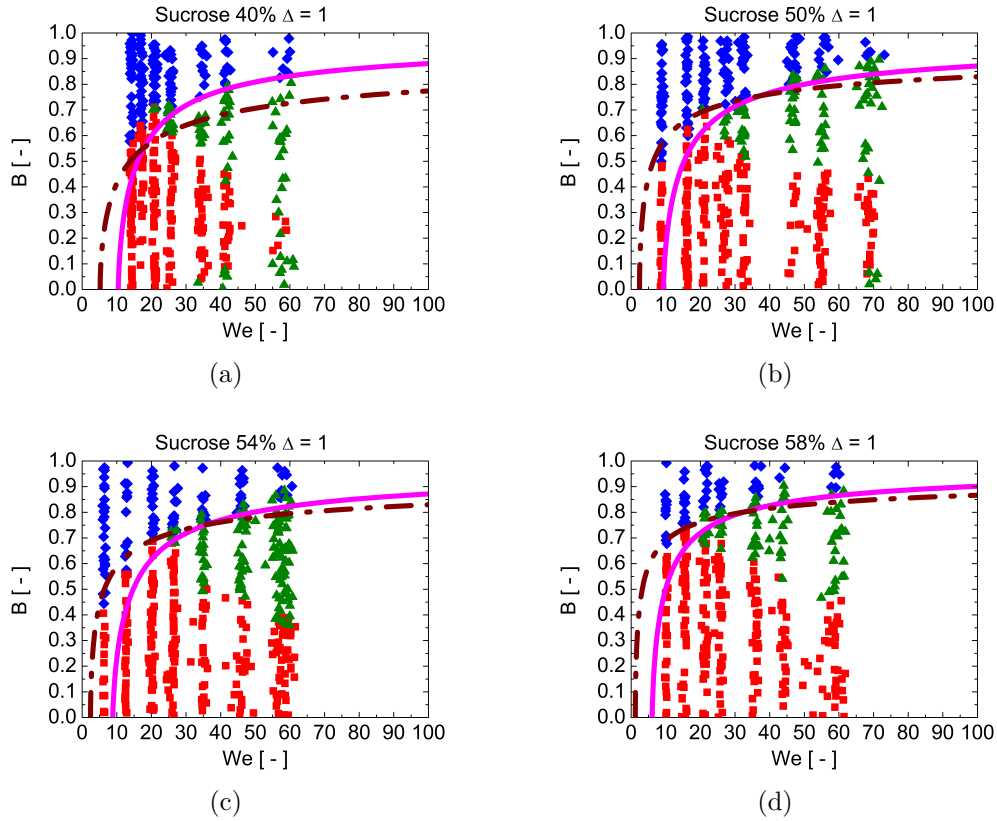
Figure 3.16: Droplet collision maps for sucrose with different solids content and comparison with theoretical boundary lines; a) 40 Ma%, b) 50 Ma%, c) 54 Ma%, d) 60 Ma%; (brown) dash-dot line: model of Estrade et al. (1999) with shape factor $\phi' = 3.351$; (magenta) closed line: Sui et al. (2023) model with water-like correlation; (symbols: (blue) diamonds: bouncing region; (red) squares: coalescence region; (green) triangles: separation regions).

argued above, this may be associated with the formation of bigger air cushions in the case of larger colliding droplets, but also possible initial droplet oscillation. However, the developed bouncing boundary model does not include an absolute size dependence; the droplet diameter is included in the calculation of the non-dimensional numbers like We and Oh. Interestingly, the experimentally reported bouncing boundary (i.e., left-side branch) is generally better predicted for the larger droplets in this case (Figure 3.18). However, good agreement of the new model with the experiments is obtained only for the higher viscous liquids, i.e., Tetradecane and Hexadecane in Figure 3.18. Again, for all different alkanes, the Estrade et al. (1999) boundary line is found to be located too far left, i.e., predicting much smaller We_{B-C}.

A thorough analysis of binary droplet collisions (i.e. for water and tetradecane) was conducted by Qian et al. (1997) focussing on the influence of ambient conditions on the collision outcome. As noted above, the proposed bouncing model accounts for dissipation effect during droplet collisions, but is not able to capture influences of the environment unless the liquid properties are modified thereby; e.g. due to changing environmental temperature. However, the data of Qian et al. (1997) were used to evaluate the parameters in the bouncing model (see Figure 3.9) for the 1 atm ambient pressure condition. To demonstrate how the model
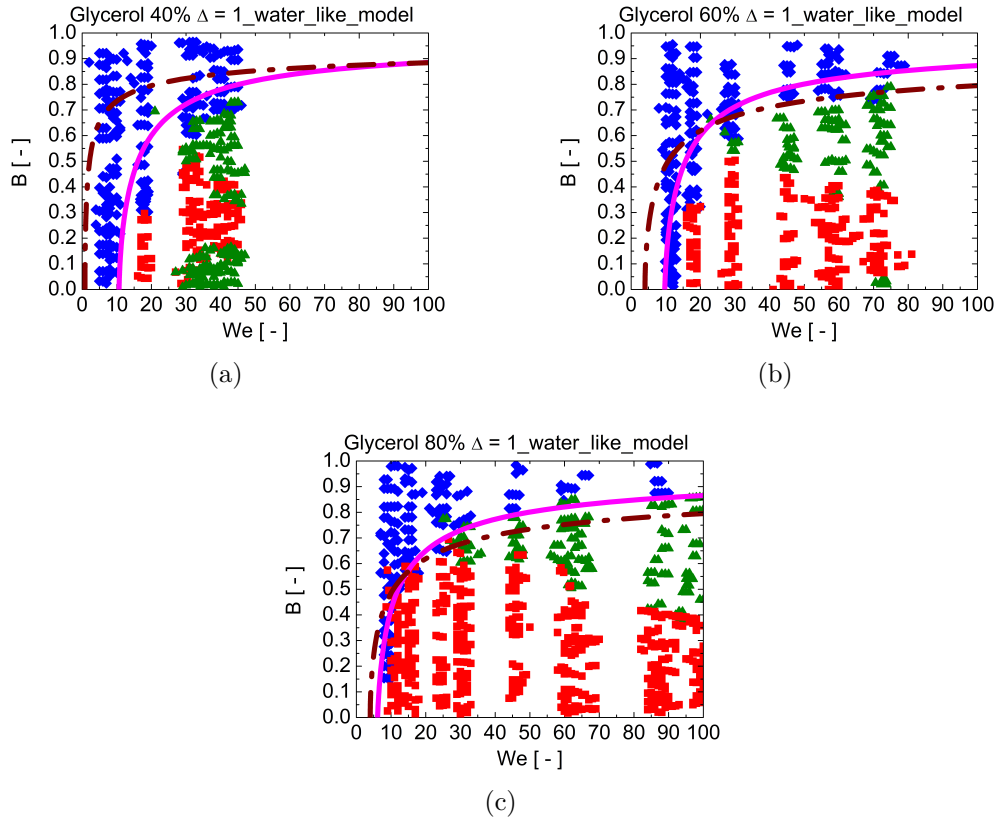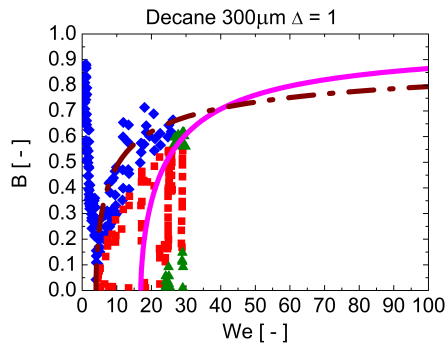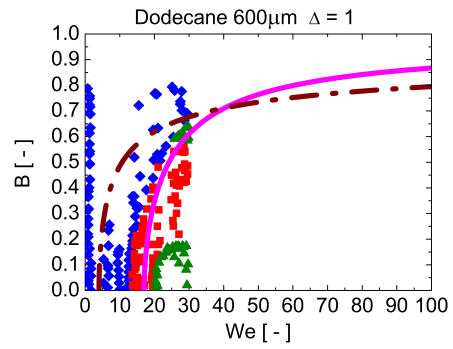
Figure 3.17: Droplet collision maps for Glycerol-water mixtures with different volume concentrations from Finotello et al. (2018b) and comparison with theoretical boundary lines; a) 40 Vol%, b) 60 Vol%, c) 80 Vol%; (brown) dash-dot line: model of Estrade et al. (1999) with shape factor $\phi' = 3.351$; (magenta) closed line: Sui et al. (2023) model with water-like correlation; (symbols: (blue) diamonds: bouncing region; (red) squares: coalescence region; (green) triangles: separation regions).

compares with experimental data for different ambient pressures, the case with tetradecane droplets was considered. The new model captures the bouncing line for 1 bar very well, and a good agreement is also observed for the higher pressure. It should be noted that the We_{B-C} in the experiments is not significantly different for these two pressures. However, reducing the pressure (Figure 3.19a) leads to easier coalescence due to better drainage of any air cushion between the colliding droplets, but this gas-effect is not captured by both models. The Estrade et al. (1999) model happens to provide better agreement with the experiments for the low pressure condition, but it fails to work well at higher pressures.

Experiments by Chen et al. (2016) on diesel and its mixtures with biodiesel and water were examined in detail as shown in Figure 3.20. The addition of water to diesel fuel has been previously investigated as a possible method of reducing emissions, resulting in an emulsion of water droplets in diesel. However, in the novel bouncing model, the liquid was of course considered as non-water-like. The new model accurately predicts both the left and upper branches of the bouncing boundary, as shown in Figure 3.20, especially in the low Weber number regime where the Estrade et al. (1999) model completely fails. However, for cases with a high water content in diesel, the new model slightly deviates from the experimental

(a)

(b)
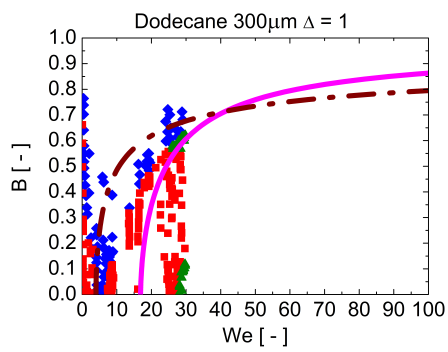
(c)
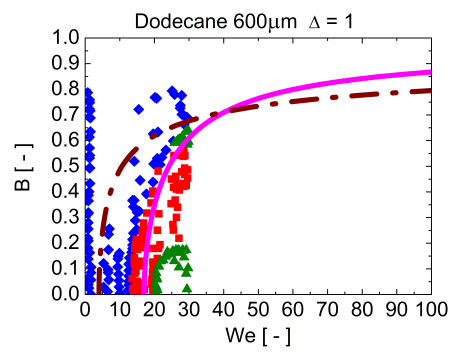
(d)
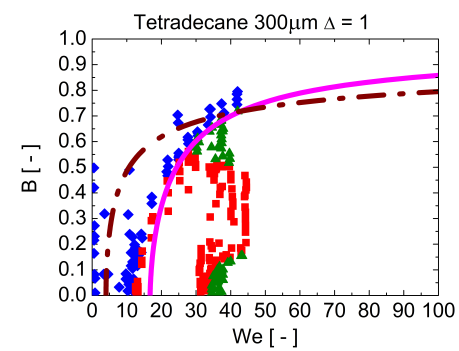
(e)
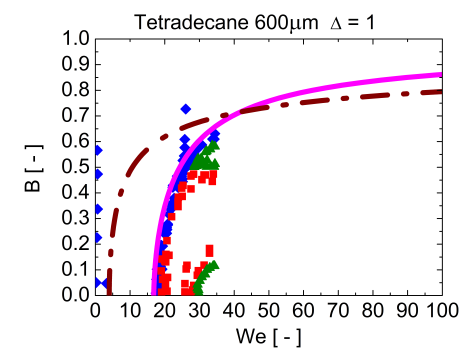
(f)
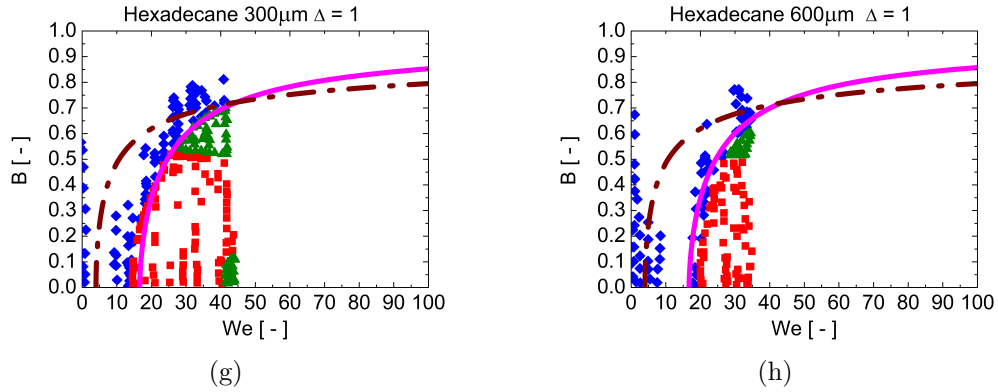
Figure 3.18: Droplet collision maps for the series of alkanes from Huang and Pan (2015), left column with droplet size 300 μm, right column with droplet size 600 μm; a) Decane, b) Dodecane, c) Tetradecane, d) Hexadecane; (brown) dash-dot line: model of Estrade et al. (1999) with shape factor $\phi' = 3.351$; (magenta) closed line: Sui et al. (2023) model non-water-like model; (symbols: (blue) diamonds: bouncing region; (red) squares: coalescence region; (green) triangles: separation regions)

results. Nevertheless, the model is able to reasonably represent the other regime boundaries for equal-sized diesel droplets colliding Sommerfeld et al. (2021b).

In order to clarify the influence of possible non-Newtonian behaviour on the collision process for binary collisions of milk droplets, a droplet collision map of a Xanthan-water solution of 500 ppm was created in Finotello et al. (2018b) as shown in Figure 3.21. However, the experimental results indicate that the boundaries between different collision scenarios are not clearly defined in such a liquid as shown in Figure 3.21, with points for droplet coalescence appearing in the bouncing region and bouncing also happening in the stretching separation region. Nonetheless, the proposed model is able to capture the lower bouncing boundary reasonably well, performing much better than the classical Estrade et al. (1999) model.

The validation of the novel bouncing model for water-like HPMC solutions is presented in Figure 3.22. According to the model parameters, HPMC is categorised as a non-water-like liquid (Figure 3.9). HPMC is a water-based viscoelastic polymer commonly used in the food and pharmaceutical industries. As the HPMC concentration increases, the dynamic viscosity of the solution rapidly increases. Unlike other water-based solutions, the surface tension of the HPMC solution is significantly lower, approximately 45 mN/m, and relatively independent of HPMC concentration within the range considered. This suggests that HPMC behaves like a surfactant. The paper of Pan et al. (2016) mentions the Critical Micelle Concentration (CMC), which is the concentration of surfactants above which micelles form. The CMC is an essential characteristic of a surfactant solution. Before reaching it, the surface tension changes significantly with the concentration of the surfactant. This occurs because particles are unevenly distributed on the surface. After reaching the CMC, the surface tension remains relatively constant, or changes slightly. The value of the CMC depends on temperature, pressure, the presence, and concentration of other surface-active substances and electrolytes.

In the experiments with HPMC solutions considered here, the mixtures all have a similar
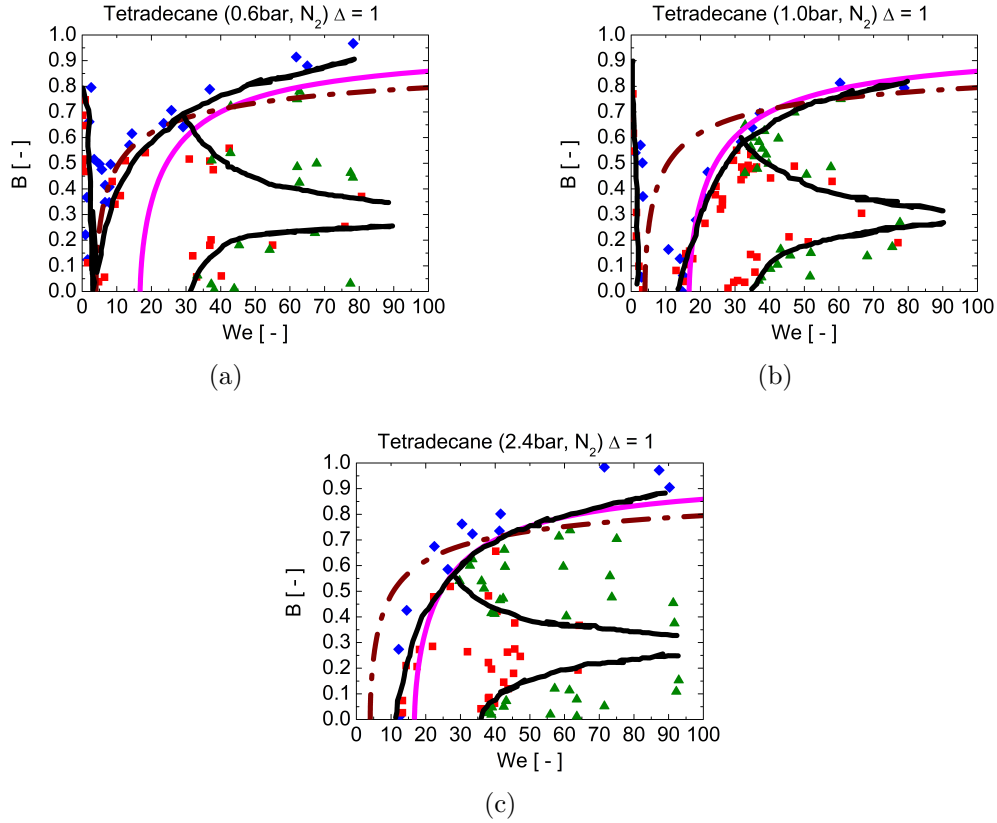
Figure 3.19: Droplet collision maps for tetradecane droplets at different ambient pressure in nitrogen gas from Qian et al. (1997) symbols represent measurement points (blue) diamonds: bouncing region; (red) squares: coalescence region; (green) triangles: separation regions; thin black lines: boundaries extracted from Qian et al. (1997); a) 0.6 bar, b) 1.0 bar, c) 2.4 bar; comparison with model predictions: (brown) dash-dot line: model of Estrade et al. (1999) with shape factor $\phi' = 3.351$; (magenta) closed line: Sui et al. (2023) model with non-water-like correlation.

surface tension, indicating that the critical micelle concentration (CMC) of these solutions has already been reached. The discrepancies in model predictions for solutions with surfactants are not solely due to surface tension variations, as short-range forces between colliding droplets are also affected by surfactants. As a result, the proposed model, like the Estrade et al. (1999) model, may not account for interfacial effects and therefore may not accurately predict the bouncing boundary for HPMC solutions. However, the shape factor parameters evaluated for the HPMC solutions fall within the data for non-water-like fluids, indicating that the proposed model for such fluids should capture the bouncing boundary line properly. This is supported by the excellent matching found with the new model for higher HPMC concentrations. Only for the lowest HPMC concentration (i.e., 2%), is the non-water-like bouncing line slightly to the left of the experimental observations, and the upper branch of the curve is located above the experiments. In all cases, the original Estrade et al. (1999) boundary line is completely off the measurements. For comparison, the present model for water-like liquids is also included in Figure 3.22. Due to the lower values obtained for the intercept of the shape factor ϕ'_{in}, this boundary line is located to the left of the non-water-like boundary. Further studies
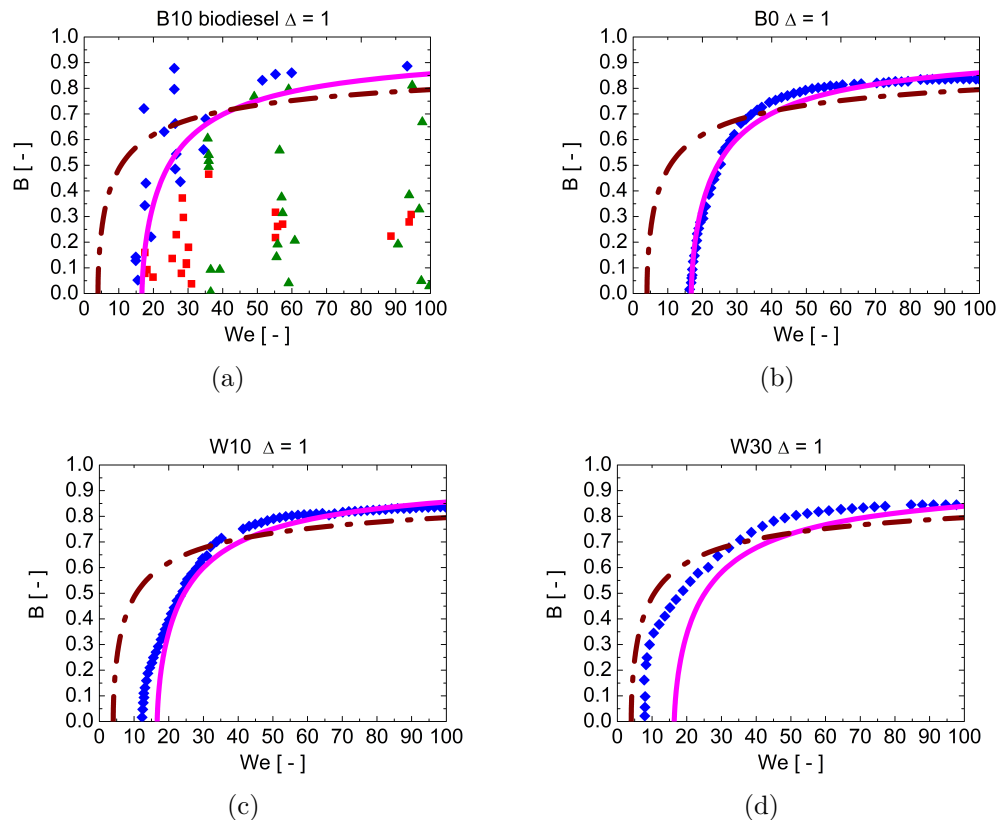
Figure 3.20: Droplet collision maps for Diesel and mixtures with Diesel from Chen et al. (2016) and comparison with theoretical boundary lines; a) Diesel with 10 Ma% biodiesel , b) pure Diesel fuel , c) Diesel with 10 Ma% water, d) Diesel with 30 Ma% water; (brown) dash-dot line: model of Estrade et al. (1999) with shape factor $\phi' = 3.351$; (magenta) closed line: Sui et al. (2023) model with non-water-like correlation ; (symbols: (blue) diamonds: bouncing region; (red) squares: coalescence region; (green) triangles: separation regions; in b) , c) and d) the (blue) diamond symbols follow the experimental bouncing boundary line).)

focusing on the influence of surfactants are required to clarify the deviations at low HPMC concentrations. However, it is acceptable for now to treat liquids with surface tension $\sigma < 50$ mN/m as non-water-like fluids and apply the associated parameters. Failure to consider the model for non-water-like liquids would result in a significant underestimation of bouncing, which is critical for predicting the droplet size distribution of a spray (Laín and Sommerfeld (2020)).

3.5 Conclusions

This chapter focuses on the models of boundary lines in collision maps. Droplet collision maps are crucial for accurately describing the outcome of droplet collisions in numerical simulations of sprays, which are mostly conducted by an Euler/Lagrange parcel concept (Laín and Sommerfeld (2020)). The ultimate goal is to obtain droplet collision maps with boundary lines that are valid for a wide range of liquid properties, as described through correlations with

(a)
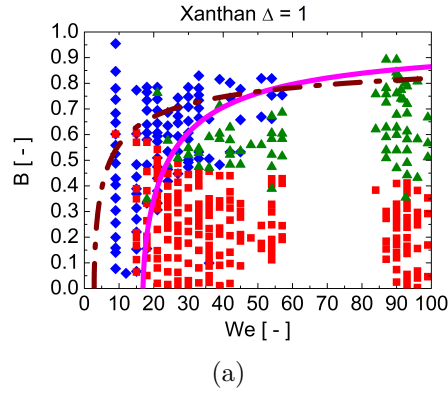
Figure 3.21: Droplet collision maps for non-Newtonian fluid 500 ppm Xanthan-water solution from (Finotello et al. (2018a) b) and comparison with theoretical boundary lines; (brown) dash-dot line: the model of Estrade et al. (1999) with shape factor $\phi' = 3.351$; (magenta) closed line: Sui et al. (2023) model with water-like correlation; (symbols: (blue) diamonds: bouncing region; (red) squares: coalescence region; (green) triangles: separation regions).

(a)

(b)

(c)
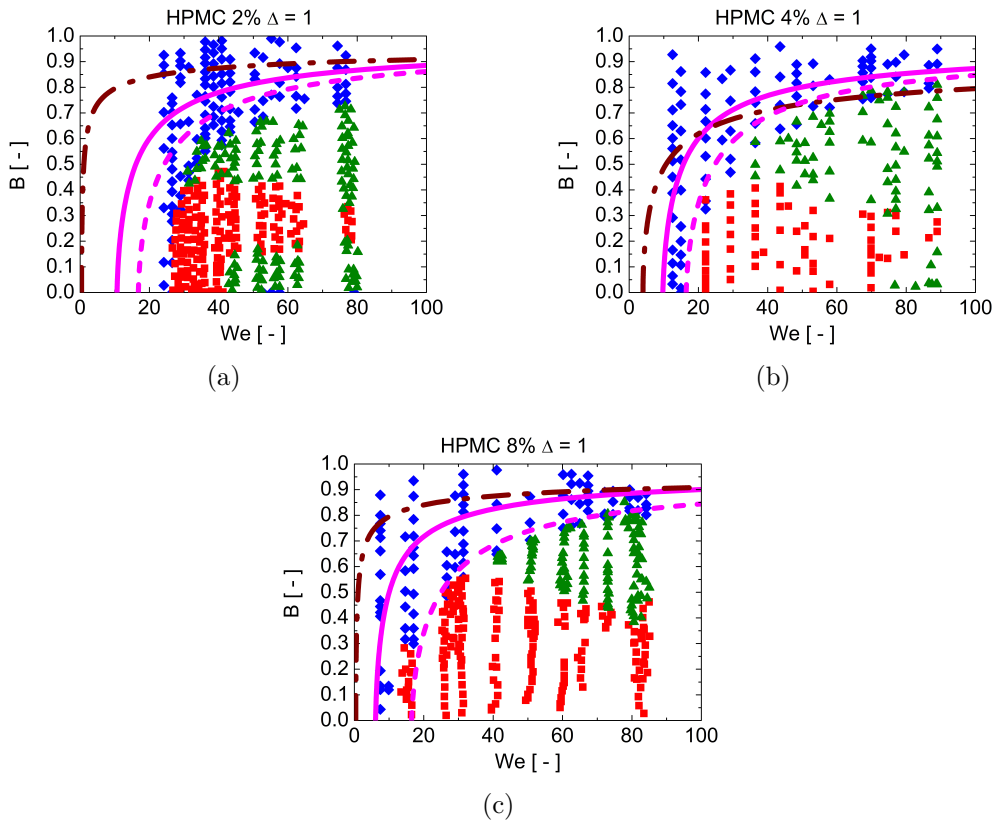
Figure 3.22: Droplet collision maps for the HPMC solutions with different concentrations from Al-Dirawi and Bayly (2019) and comparison with theoretical boundary lines; a) 2Ma%, b) 4Ma%, c) 8Ma%; (brown) dash-dot line: model of Estrade et al. (1999) with shape factor $\phi' = 3.351$; (magenta) closed line: Sui et al. (2023) model with water-like correlation; (magenta) dashed line: proposed novel with non-water-like correlation; (symbols: (blue) diamonds: bouncing region; (red) squares: coalescence region; (green) triangles: separation regions).

the Ohnesorge number. An extended model was developed to predict the bouncing boundary line in the binary droplet collision map $B = f(We)$, which is necessary for determining the droplet collision outcome. The model considers viscous dissipation effects in the energy balance. The new model includes two parameters, the shape parameter ϕ' and the conversion rate β. The model assumes that these parameters are not constant, as previous models, but depend on the impact parameter B, which characterises the degree of droplet deformation during a bouncing process. This assumption was confirmed through detailed shadow imaging experiments. Both model parameters have a linear relationship with the impact parameter B, described through the intercept with the ordinate and a slope value. To determine the slope $k_{\phi'}$ and the initial values of each parameter, ϕ'_{in} and β_{in}, numerous experimental results were evaluated and correlated with the Ohnesorge number, which depends on the liquid properties and droplet size only. It is important to note that the model cannot capture effects due to the variation of environmental conditions (e.g., pressure and type of gas) as long as these do not influence the liquid properties.

The intercept and slope values for the shape parameter show two different trends. Liquids were classified into two categories based on their properties: non-water-like liquids with a surface tension of approximately 25 mN/m and water-like liquids with a higher surface tension of approximately 70 mN/m. Therefore, surface tension appears to be the key property for selecting the model, either water-like or non-water-like. However, the HPMC water solution was an exception since it was classified as a non-water-like fluid, presumably due to its surface activity. On the other hand, the intercept for the conversion rate followed a single correlation for all liquids. Third-order polynomial functions were used to describe the three model parameters, but these are valid for Ohnesorge numbers less than 0.35 due to the lack of experimental data for highly viscous liquids.

The proposed new bouncing boundary was validated against experimentally obtained collision maps for equal-sized droplets ($\Delta = 1$) in a variety of different droplet liquids, including both water-like and non-water-like fluids. The results were compelling, as the proposed model performed considerably better in many regards than the commonly applied model by Estrade et al. (1999). The novel model predicts that the lower branch of the bouncing curve (in the low We and B region) is always to the right of the Estrade et al. (1999) model and therefore yields better agreement with the experimental values of the critical bouncing Weber number (We_{B-C}). The upper branch of the bouncing curve at higher We (i.e., right of the so-called triple point) is mostly above the Estrade et al. (1999) model for most of the liquids, and also matches the experimental observations better. Hence, for droplets with a size ratio of $\Delta = 1$, the proposed model gives acceptable agreement for a range of different liquids. It is worth reiterating that the proposed bouncing model can only capture liquid-side effects because it depends on the liquid Ohnesorge number. Any influences resulting from absolute droplet size, variation in environmental conditions, or interface modification are not considered in the model, unless the liquid properties are changed. A unique behaviour is seen in the case of pure water, where bouncing is not observed experimentally in the low impact parameter and low Weber number region. Therefore, it can be assumed that the bouncing boundary line terminates near the triple point, which connects to the stretching separation-coalescence boundary line. Experimental observations reveal that with increasing viscosity, the critical bouncing

point shifts to lower Weber numbers, which the new model properly captures. This effect is particularly evident in the results for glycerol solutions. Extending the proposed bouncing boundary line to cases with different droplet sizes (i.e., $\Delta < 1$) necessitates further analysis and additional experimental studies, especially for small size ratios ($\Delta < 0.5$).

Chapter 4

Experiments of Droplet Collisions

This chapter provides an overview of the experimental setup and results obtained for droplet collisions. The experimental facility is designed to investigate droplet collision behaviour under controlled conditions, and comprises a droplet generation system and a high-speed imaging system for recording droplet behaviour during collisions. The post-processing involves image processing and calculation methods, leading to collision maps for water and maltodextrin. The results demonstrate that the outcome of droplet collisions is influenced by the impact parameters, such as velocity and droplet size/size ratio, as well as the properties of the liquid, including viscosity and surface tension.

4.1 Experimental setup

As shown in Figure 4.1, the experiments utilising two oscillating membrane droplet generators (Encap BioSystems, model IE-0010H-P) were conducted to generate mono-sized and evenly spaced droplet chains. These generators use membrane vibration to produce a continuous droplet stream with a specific oscillation frequency, achieved by a coil inside the nozzle generating sinusoidal waveforms from a tune generator controlled by a computer. Droplet size relies on liquid properties, flow rate, orifice size, excitation frequency, and amplifier power. The liquid is sourced from a pressure vessel equipped with flow rate control valves, and droplets are generated by forcing the fluid through orifices of 200, 300, or 400 μm in size, generating two chains of droplets with constant spacing and controlled sizes. A new experimental setup is established for droplet collisions with size ratios below 0.3, utilising a spray nozzle to generate smaller droplets while larger droplets are still produced by the droplet generator. The larger droplet chain passes through the spray nozzle in a chance manner, resulting in random droplet collisions. The single-fluid pressure nozzle (SCHLICK-Mod. 553) operates at an air pressure of 2.5 bar, producing a droplet size spectrum ranging from 20 to 280 μm.

To capture droplet-droplet collisions, researchers used the shadow imaging technique, which involves high-resolution imaging with backlight illumination and is ideal for visualising particles, droplets, and other structures. Two LED arrays serve as backlights for illuminating the collision process, and the measurement volume is determined by the imaging system's focal plane and depth of field. To capture the collisions, two synchronised high-speed cameras (Photron FASTCAM SA4) are mounted on the traversing system, with the master camera recording droplet-droplet collision scenarios, paired with a lens (Nikkor 85 mm 1:1.4 lenses) and a 10 mm extension tube. The slave camera operates in synchronised mode to ensure that the two mono-size droplet chains collide in the same collision plane. The cameras have a resolution of 16.6 μm/pixel for water and 21.4 μm/pixel for maltodextrin solutions. They operate

<center>(a)   (b)</center>
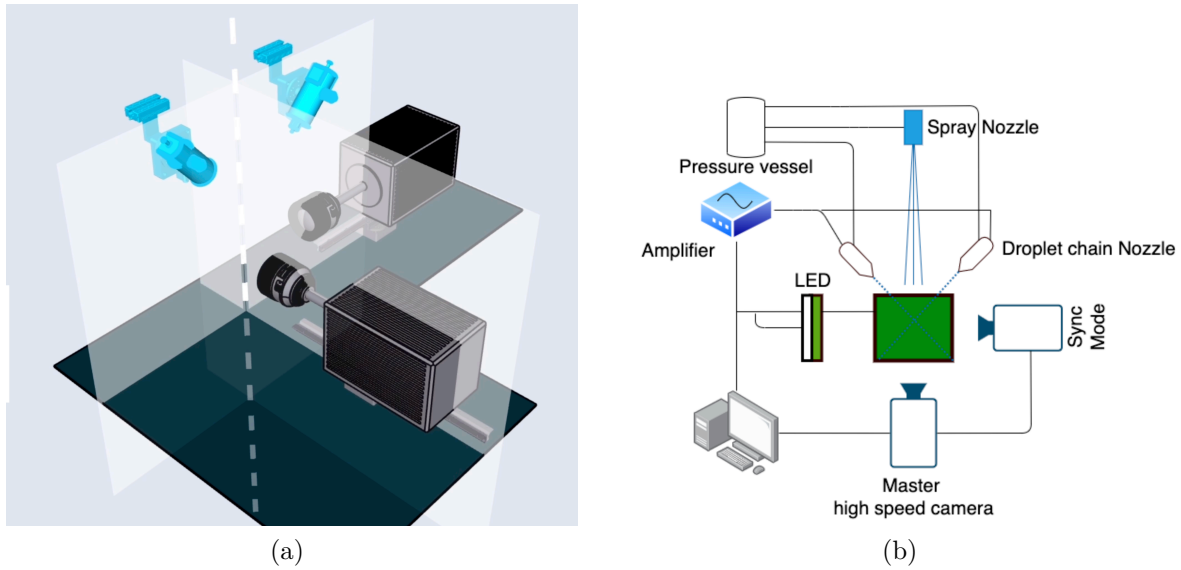
Figure 4.1: Sketch of the experimental setup with droplet chains (spray nozzle only for water), liquid supply from a pressure vessel, LED illumination and high-speed camera recording as well as image recording PC (Sui et al. (2021)).

at 10,000 fps, with an exposure time of 1/10,800 s. Additionally, another synchronised high-speed camera, positioned parallel to the impact plane, records the side view of droplet chains and any eccentric impacts that are excluded from further analysis. The impact parameter B varies, using the aliasing or frequency shifting method.

Figure 4.2: Example of one big droplet colliding with two small droplets

To ensure droplet stability, a higher frequency and smaller orifice are required for the smaller droplet chain, considering the size ratio. Six different size ratios of water and three different size ratios of maltodextrin solutions ($\Delta = 1$, $\Delta = 0.8$, and $\Delta = 0.5$) are studied in this work. For the reference case of maltodextrin at $\Delta = 1$, 300 μm orifices are used in both nozzles. In the $\Delta = 0.8$ case, one of the orifices is changed to 400 μm, and in the $\Delta = 0.5$ case, another 300 μm orifice from the $\Delta = 0.8$ case is changed to 200 μm. Droplet chains of constant spacing and size are generated by controlling the volume flow rate, frequency, and amplifier power. However, in the case of $\Delta = 0.5$, the smaller spacing between droplets and the lower velocity magnitude of the larger droplet chain result in larger droplets colliding with more than one small droplet before the first collision is detectable, as shown in Figure 4.2. This study only considers binary droplet collisions, and as B decreases, obtaining effective binary collisions becomes more challenging.

4.2 Image Processing

The in-house Image Processing script is generated by using the Python-OpenCV package(Bradski (2000)) with the workflow as shown in Figure 4.3.

- S1.1: Background subtraction is applied to all images. This separates the foreground objects in the images from the background. Frame differencing is chosen as the algorithm to calculate the difference between the current frame and a reference frame. Pixels that have changed significantly are considered part of the foreground. A background image is captured before each measurement.

- S1.2: The images are binarised by adjusting thresholding values. This converts the images to binary images, with each pixel being either black or white.

- S1.3: The OpenCV findContours function is used to find the objects (droplets) in the binary images. This function detects and extracts the contours of objects on an image, allowing for shape analysis, object detection, and recognition.

- S2: Well-focused and binarised droplets are tracked and labeled in each frame. Relative objects are connected as candidates by Euclidean distance with a distance threshold in the next frame. Each droplet trajectory generates a position file for further post-processing.

- S3: Collision detection to distinguish the collision outcome is done manually.

- S4: All recorded collision pairs with information on centroids, sizes, and velocities are used to calculate W_e and B using a Python script.

To account for changes in instantaneous velocities, each collision sequence requires a minimum of six photos before the first impact, as demonstrated in Figure 4.4. The mean droplet velocities are calculated from the instantaneous data, and the droplet impact point can be determined by using the velocities and the final droplet position before collision. The impact parameter B is then computed, and the relative velocity u_{rel} is determined using Eq. 4.1.

$$u_{rel} = \sqrt{(u_{l,x} - u_{r,x})^2 + (u_{l,y} - u_{r,y})^2} \tag{4.1}$$

To ensure accurate volume estimation, the droplet must be stabilised as a sphere in three dimensions, appearing as a perfect or nearly perfect circle in the 2D image captured by the master (front) high-speed camera. The circularity value (see Eq. 4.2) is computed to estimate the roundness of the 2D image, where a value of 1.0 represents a perfect circle and is considered a perfect sphere. As the circularity value approaches 0.0, the polygon becomes more elongated. To ensure volume estimation accuracy, droplets with a circularity value less than 0.9 are rejected in this experiment.

$$circularity = 4\pi \frac{area}{perimeter^2} \tag{4.2}$$

To ensure data accuracy, it is crucial to estimate potential errors in the measurement and image processing. The camera's pixel resolution varies with the vertical distance from the

Figure 4.3: Image processing flow chart and illustrations

Figure 4.4: Scheme of calculation of u_{rel}

camera to the collision surface, at 16.6 μm/pixel for water and 21.4 μm/pixel for maltodextrin solutions. As a result, the collision surfac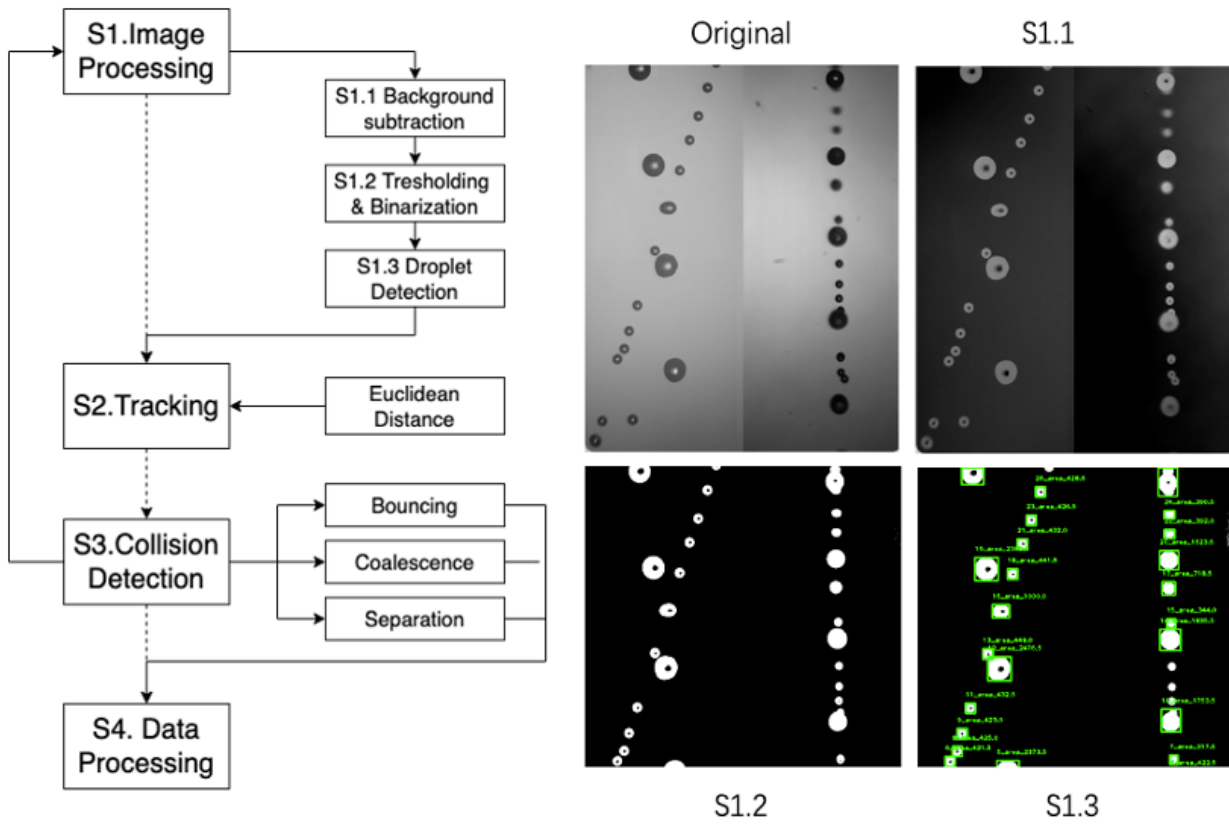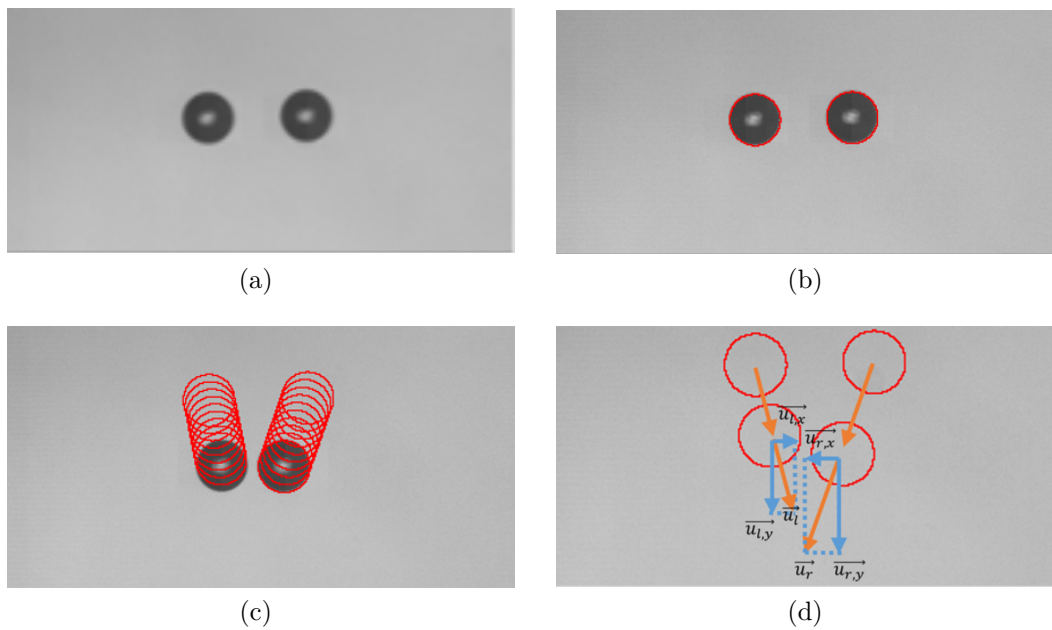e must be adjusted whenever the nozzle angle is changed. A slave (side) high-speed camera is used to align the droplet collision surface, as non-uniform illumination during image processing can lead to errors, particularly with object detection methods. In this study, the post-processing code of Pasternak et al. (2021) is compared with the proposed method, and the error in object area calculation is found to be within 3%.

4.3 Experimental results of water

While water droplet collisions have been well-studied, the effect of size ratios on such collisions remains inadequately explored. This section details the results of experiments on water droplet collisions with varied size ratios, including the influence of water quality (distilled water and tap water) on these collisions.

4.3.1 Liquid properties of water

Table 4.1 summarises the measured properties of distilled and tap water, including their respective densities ($\rho = 998$ kg/m^3 and 997 kg/m^3), surface tensions ($\sigma = 68.8$ mN/m and 65 mN/m), and viscosities ($\mu = 0.735$ mPa·s and 0.755 mPa·s). Additionally, the table presents droplet size, size ratio, and Oh measurements for water droplets.

Water Type	Case	d_s [μm]	d_l [μm]	Δ	Oh_s[$-$]
	Case 1 (Spray)	130$\sim$180	600$\sim$700	$\sim$0.24	0.00717
	Case 2	276	789	0.35	0.00534
	Case 3	388	879	0.44	0.00450
Distilled water	Case 4	410	810	0.51	0.00438
	Case 5	484	739	0.66	0.00403
	Case 6	490	700	0.7	0.00401
	Case 7	567	697	0.81	0.00373
Tap Water	Case 8	473	674	0.7	0.00408
	Case 9	650	713	0.91	0.00348

Table 4.1: The droplet diameters, size ratio and Ohnesorge number of cases for distilled and tab water

4.3.2 Results and discussion of water cases

The collision maps in Figures 4.5 and 4.6 illustrate the effects of variations in absolute droplet size on distilled and tap water, respectively. It is worth highlighting that all water droplet collision experiments were conducted up to a $We \approx 50$ due to spherical droplets being unattainable at higher We values. The oscillating membrane droplet generator was used in the experiments for $\Delta = 0.35$, 0.44, 0.51, 0.66, 0.7, and 0.81 to achieve precise control over the collision pair droplet size. However, for the $\Delta = 0.24$ case, a large droplet chain was used to penetrate

the spray, making it challenging to control the diameter of the small droplets. Hence, this aspect of the calculation was more problematic in subsequent image processing. Theoretical boundaries were considered to classify water collision outcomes, including those established by Estrade et al. (1999), Ashgriz and Poo (1990), and the combined model of Sommerfeld and Pasternak (2019).

This study reveals that water droplet collisions exhibit the bouncing phenomenon at higher values of B for all size ratios and over the entire We range. This finding is consistent with the works of Qian and Law (1994) and Kuschel and Sommerfeld (2013). However, Rabe et al. (2010) did not report any bouncing region. Surprisingly, in some instances, the bouncing phenomenon was observed to extend to lower B values. The results of this study indicate bouncing regimes at $We < 5$ and $B > 0.6$, which differ from the findings of Qian et al. (1997) for water droplet collisions at 1 bar air. Remarkably, even for B as low as approximately 0.4, it is confirmed that bouncing may occur for $\Delta = 0.81$.

As shown in Figure 4.5, the droplet size ratio has an effect on the structure of collision maps. Reflexive separation gradually emerges in the collision maps as the size ratio increases, beginning at $\Delta = 0.51$, while We_C steadily decreases. The stretching separation regime only appears in a small area of high B values for small size ratios ($\Delta < 0.6$). Research conducted by Sommerfeld and Pasternak (2019) reveals that the proportion of stretching separation in collision maps increases as the size ratio becomes larger, with the boundary shifting downwards (i.e., coalescence-stretching separation), which are in line with Rabe et al. (2010). However, in case 1 (the spray case), there is no clear boundary between stretching separation and bouncing. This may be due to the insufficient number of data points. Effective collisions (data points) are extremely difficult to collect when large droplets pass through the spray. Nevertheless, in the same operating conditions, the spray has a reproducible size and velocity distribution, allowing for the reproducibility of the experiment. Although the boundary between coalescence and stretching separation can be identified relatively clearly, more experiments are necessary to determine the boundary's distinctness for this size ratio. Generating smaller droplets through a more productive droplet-generation method would help to control droplet size. Comparing case 1 ($\Delta = 0.24$) with droplet collisions of other size ratios, it is evident that droplets in larger size ratio collisions tend to have more significant deformations than those in smaller size ratio collisions (refer to examples in Sui et al. (2021)). However, smaller droplets are more likely to penetrate the surface of larger droplets, resulting in less pronounced oscillations in the integrated droplet mass that decay rapidly.

The collision maps presented in Figures 4.5 and 4.6 exhibit the boundaries for coalescence, stretching separation, and bouncing for distilled and tap water, respectively, using the Estrade et al. (1999) model with a shape factor of 3.351. While the Estrade et al. (1999) model accurately predicts the coalescence and stretching separation boundaries for low to moderate We, it underperforms in predicting the bouncing region for larger We, as it lies below the experimental boundary. The Ashgriz and Poo (1990) model, however, inaccurately estimates the boundary between coalescence and stretching separation, leading to an incorrect proportion of the collision map captured by separation. Alternatively, the combined model proposed by Sommerfeld and Pasternak (2019) shows a good correlation with experimental measurements for coalescence and stretching separation boundaries, up to a size ratio of 0.5. Nonetheless, it

(a)

(b)

(c)

(d)

(e)

(f)

(g)
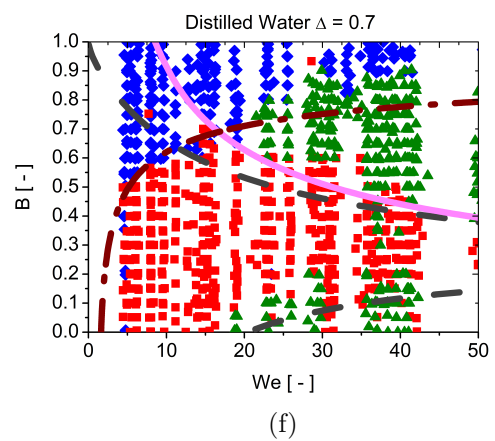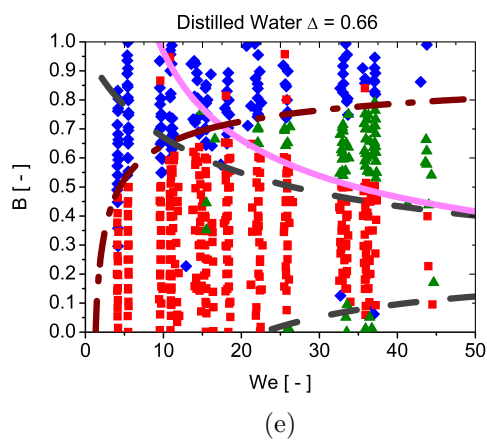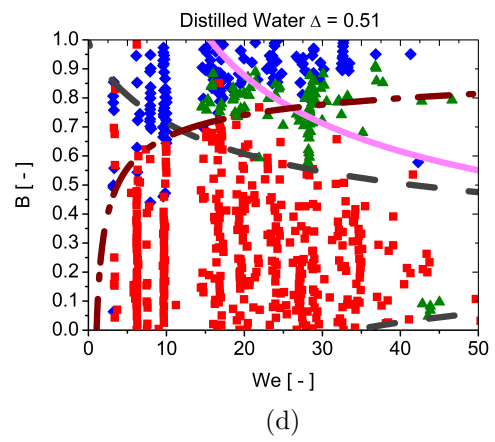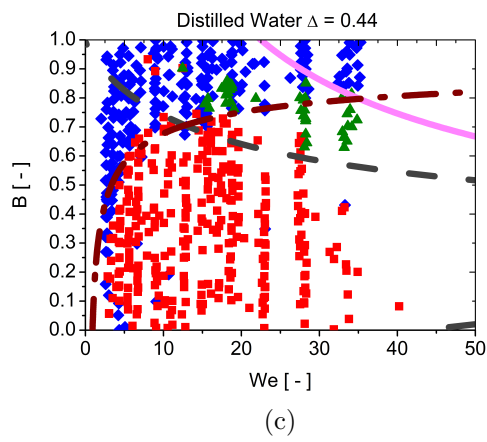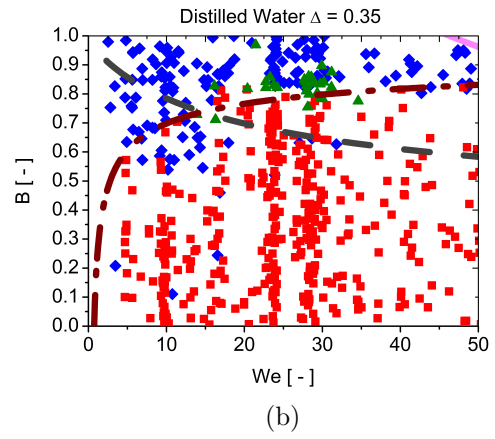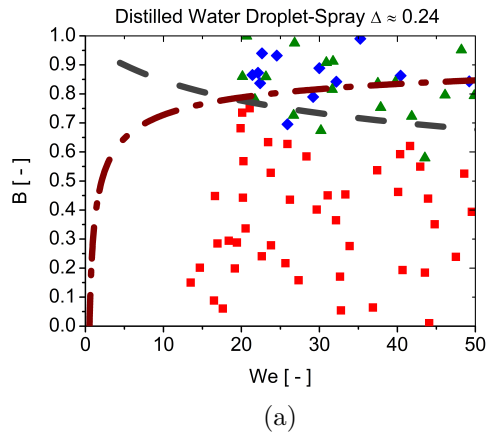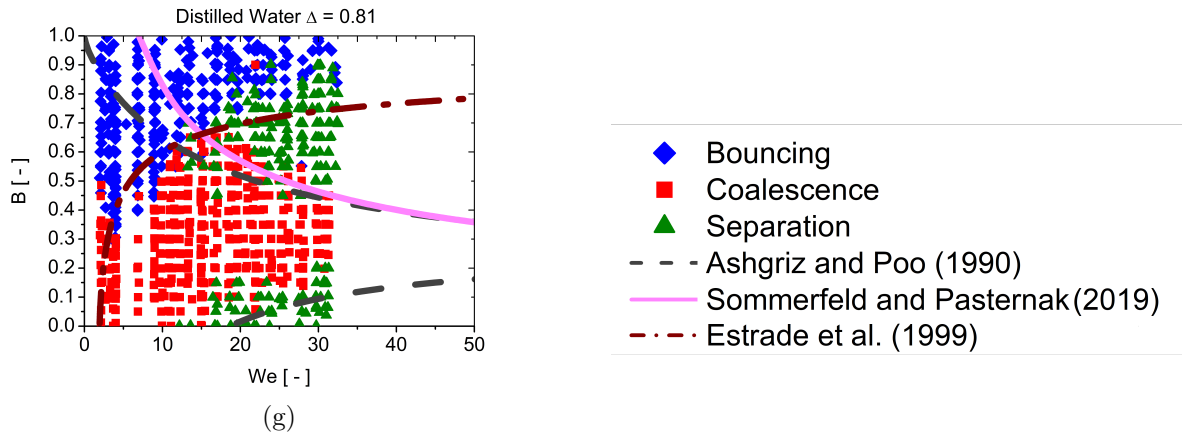
Figure 4.5: Measured collision outcome in the collision maps for distilled water with different size ratios and comparison with model results: (a) $\Delta = 0.24$; (b) $\Delta = 0.35$; (c) $\Delta = 0.44$; (d) $\Delta = 0.51$; (e) $\Delta = 0.66$; (f) $\Delta = 0.70$; (g) $\Delta = 0.81$ (red squares: coalescence; green triangle: separation; blue diamond: bouncing; dash grey lines: model of Ashgriz and Poo (1990); solid magenta line: combined model of Sommerfeld and Pasternak (2019); dash dot wine line: model of Estrade et al. (1999)).

(a)   (b)

Figure 4.6: Measured collision outcome in the collision maps for tap water with different size ratios and comparison with model results: (a) $\Delta = 0.7$; (b) $\Delta = 0.9$ (red squares: coalescence; green triangle: separation; blue diamond: bouncing; dash grey line: model of Ashgriz and Poo (1990); solid magenta line: combined model of Sommerfeld and Pasternak (2019); dash dot wine lines: model of Estrade et al. (1999)).
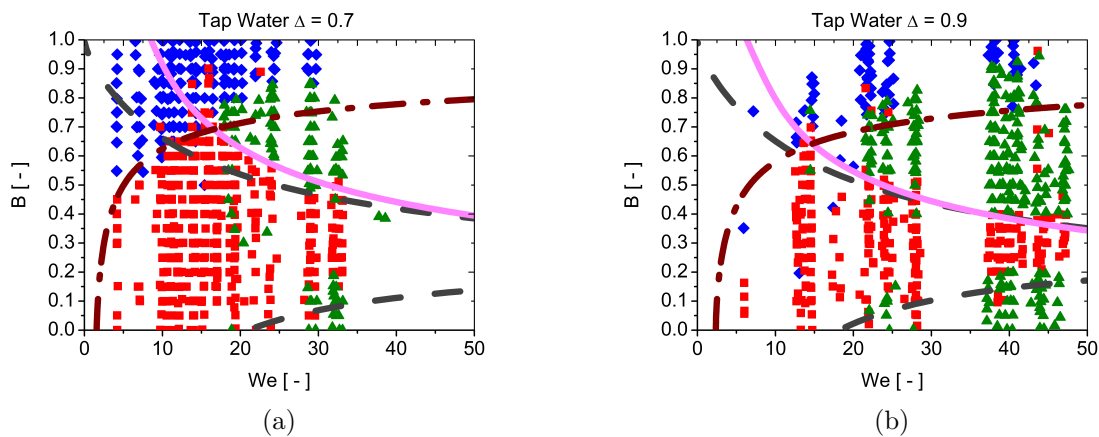
fails to accurately capture the effect of size ratio on collision maps at size ratios less than 0.5. Although the water quality was varied between distilled and tap water, a comparison between case 6 and case 8 in Figures 4.5f and 4.6a indicates that water quality had a minimal impact on the collision maps.

4.4 Experimental results of maltodextrin

Maltodextrin is a mixture of glucose, maltose, oligosaccharides, and polysaccharides, widely used as a versatile food additive in the food industry. It is commonly employed in confectionery, beverages, dried fruit, and as a coating for granules or tablets.

4.4.1 Liquid properties of maltodextrin solution

The maltodextrin powder employed in this study was provided by Arzneimittel Gottfried Herzberg GmbH. Previous work in Sommerfeld and Kuschel (2016) generated collision maps of various sucrose concentrations that were used as a reference in this research. As demonstrated in Figure 4.7, the solution densities of both maltodextrin and sucrose slightly increase with concentration, exhibiting a similar trend. The surface tension of maltodextrin and sucrose does not significantly change with increasing concentration, with maltodextrin serving as a surfactant and reducing the surface tension level to approximately 58 mN/m. While sucrose has little effect on the surface tension of water, maltodextrin's surface tension reduction ability is noteworthy. The dynamic viscosities of maltodextrin solutions, ranging from 20 - 47.5 Ma%, span from 3.12 to 56.91 mPa·s, while sucrose solutions with 20 - 60 Ma% mass fraction exhibit dynamic viscosities between 2 and 57.3 mPa·s. Both solutions undergo a significant increase in dynamic viscosity as the mass fraction increases. Additionally, Tables 4.2 and 4.3 provide a summary of all liquid properties.

4.4.2 Result and discussion

This section presents collision maps for maltodextrin solutions with varying size ratios and mass concentrations. The maps depict the relationship between B and We including the boundary lines used for differentiating collision outcomes. The experiments were carried out up to $We = 70$, encompassing the entire range of B, while other parameters such as ambient pressure were kept constant at atmospheric conditions. The main objective of these experiments was to investigate the influence of viscosity, droplet size, and size ratio on collision outcomes. The proposed collision maps contain the boundary lines of various models (see Table 4.3) for coalescence, stretching separation, and bouncing. These models are detailed in Chapter 3. The measurements provide insight into the expected collision outcomes, including bouncing, coalescence, reflexive separation, and stretching separation.

4.4.2.1 Discussion on viscosity effect

The collision maps of droplet collisions with a size ratio of $\Delta = 1$ are presented in Figure 4.8 to understand the collision outcomes better. In identifying collision outcomes, We_T play a crucial role, especially for higher Weber numbers, where the stretching separation percentage

Table 4.2: Summary of liquid properties in experiments and calculated Ohnesorge number of maltodextrin solutions.

Mass Concentration Ma%	Density ρ [kg/m^3]	Surface tension σ [mN/m]	Viscosity ν [mPa·s]	Size ratio Δ [-]	d_s [μm]	d_l [μm]
20	1078	57.4	3.12	0.496	477.6	962.7
				0.801	763.1	952.9
				0.997	769.3	771.7
35	1120	57.2	13.29	0.499	486.6	975.3
				0.805	781.3	970.4
				0.996	814.2	817.1
40	1146	58.2	19.12	0.485	461.7	952.7
				0.796	781.2	981.6
				0.99	790.4	798.1
45	1196	58.4	40.23	0.496	492.5	993.1
				0.817	796.1	974.1
				0.994	810.3	814.8
47.5	1204	59.1	56.91	0.545	516.9	949.3
				0.8	797.5	997.4
				1.0	809.2	809.3

Table 4.3: Summary of liquid properties in experiments and calculated Ohnesorge number of sucrose.

Mass Concentration Ma%	Density ρ [kg/m^3]	Viscosity ν [mPa·s]	Surface tension σ [mN/m]	Oh [-]
20	1080.9	2	73.7	0.011
40	1176.5	6	75.1	0.0323
50	1229.7	15.5	76	0.822
54	1252	19.4	76.4	0.101
58	1274.9	42.2	76.9	0.219
60	1286.6	57.3	77.1	0.295

(a)

(b)

(c)
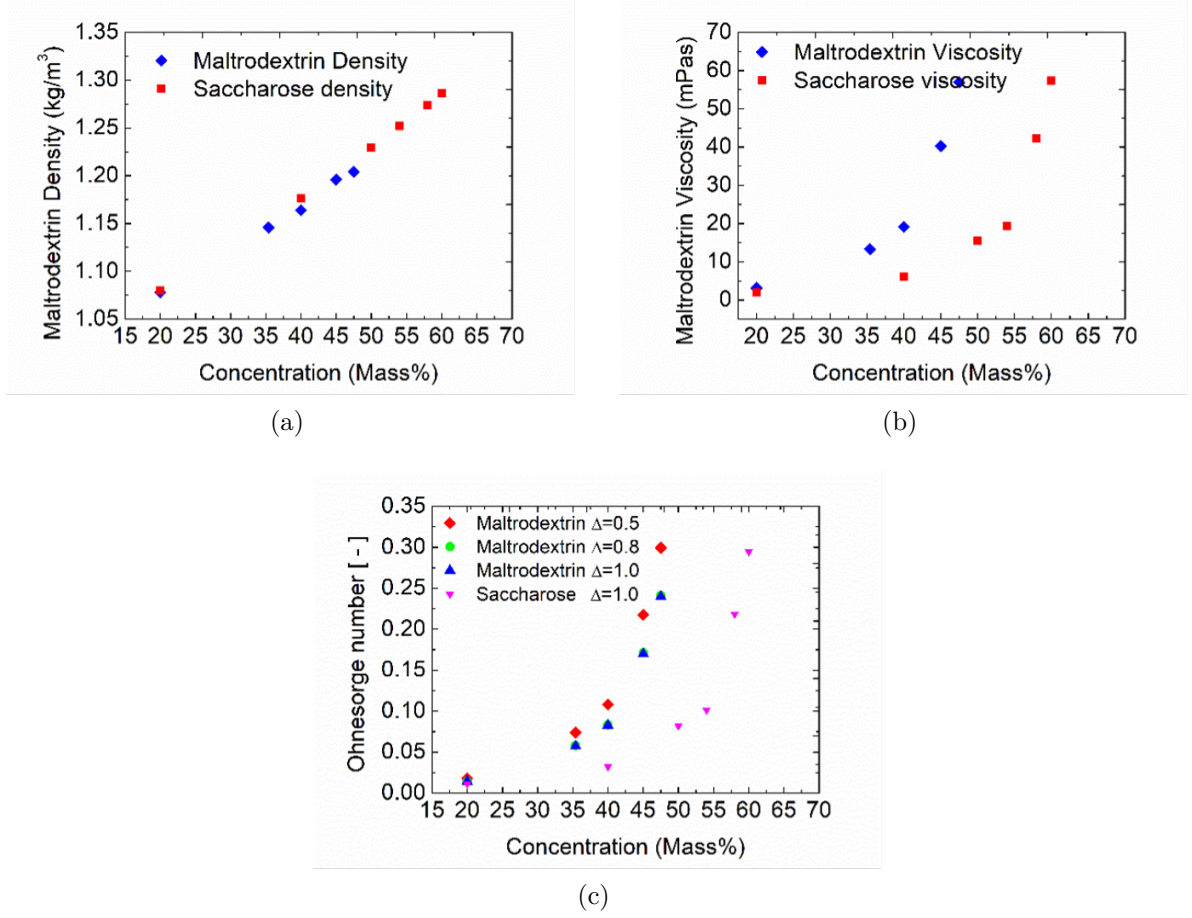
Figure 4.7: (a) Effect of mass fractions on density; (b) Effect of mass fractions on viscosity; (c) Effect of mass fractions on Ohnesorge number with different size ratio

in the collision map increases. Nonetheless, as liquid viscosity increases due to higher mass concentration, the stretching separation percentage decreases. The collision maps show that, with increasing viscosity, the location of triple points We_T moves towards higher Weber numbers. Based on Table 4.4, the critical bouncing points for $\Delta = 1$ cases are approximately at $We_{B-C} = 19$.

Table 4.4: Summary of important points locations of collision map of maltodextrin at $\Delta = 1$

Cases $\Delta = 1$	We_T	We_C	We_{B-C}
Maltodextrin 20 Ma%	$We_T \approx 24$	$We_C \approx 30$	$We_{B-C} = 18$
Maltodextrin 35 Ma%	$We_T \approx 34$	$We_C \approx 60$	$We_{B-C} = 18$
Maltodextrin 35 Ma%	$We_T \approx 37$	Not found	$We_{B-C} = 20$
Maltodextrin 45 Ma%	$We_T \approx 40$	Not found	$We_{B-C} = 19$
Maltodextrin 47.5 Ma%	$We_T \approx 42$	Not found	$We_{B-C} = 17$

The collision behaviour of droplets in solutions of different maltodextrin concentrations has been investigated. It is observed that in the range of 0 and $We < 17$, bouncing occurs for all concentrations (Figures 4.8 to 4.10) in the collision maps. As the impact parameter increases, the bouncing region shifts to larger values and expands over the We range up to

70. With increasing mass concentration, the domain of stretching separation moves towards higher We, in agreement with previous studies Gotaas et al. (2007); Kuschel and Sommerfeld (2013); Sommerfeld and Kuschel (2016). The reflexive separation occurs during near head-on collisions, is observed in the 20Ma% maltodextrin solution and a small region with few points in the 35Ma% maltodextrin solution; however, this regime disappears entirely for solutions with higher maltodextrin concentrations. As a result, an increase in the percentage of coalescence is observed in the collision maps due to the disappearance of reflexive separation and the shrinkage of the stretching separation regime.

The collision behaviour of maltodextrin solutions at $\Delta = 1$ with increasing mass concentration is shown in Figure 4.8, indicating a significant upward shift in the boundary of coalescence-stretching separation and a reduction in the area of stretching separation in the collision maps. The model of Ashgriz and Poo (1990) depicts the boundary curve between stretching separation and coalescence, works well only for 20Ma% solutions with low viscosity. However, with increasing mass concentration, the dominance of the viscous effect over the surface tension effect renders the Ashgriz and Poo (1990) model inadequate for coalescence-stretching separation boundaries. The Sommerfeld and Pasternak (2019) model is a pure liquid correlation model that works well in indicating the higher We direction shift of coalescence-stretching separation boundary lines. However, the combined model with solution does not work as effectively as the pure liquid model in any case. The Suo and Jia (2020) model is less effective than the combined model with pure liquid correlation, but it performs better than the Ashgriz and Poo (1990) and the combined model with solution correlation. In this study, the boundary line from Ashgriz and Poo (1990) for reflexive separation is not considered due to the quick disappearance of the reflexive separation regime in the experiment. The coalescence-stretching separation model of Ashgriz and Poo (1990) is not adequate for maltodextrin solutions with all concentrations, as reported in several previous studies. The experimental results in Kuschel and Sommerfeld (2013) demonstrate that the bouncing behaviour is not observed in sucrose collision maps for small B and We values, which is consistent with the findings in Pan et al. (2016), where reducing surface tension expands the bouncing region. In both sucrose and maltodextrin cases, increasing viscosity results in a smaller reflexive separation behaviour, with the critical point We_C shifting to higher We. However, the reduction in the stretching separation region leads to an upward shift in the coalescence-stretching separation boundary line.

The collision maps of maltodextrin with $\Delta = 0.8$ are presented in Figure 4.9. The We_T locations of maltodextrin are observed to deviate slightly from those in $\Delta = 1.0$ cases, and the locations of We_T for $\Delta = 0.8$ cases increase with increasing viscosity. We_C is observed only in maltodextrin with 20Ma% concentration and not in maltodextrin with 35Ma% concentration. The critical bouncing points are located at approximately $We_{B-C} \approx 16$, as summarised in Table 4.5.

In the collision maps of maltodextrin with different mass concentrations at $\Delta = 0.8$, the overall variation tendencies with increasing viscosity remain unchanged compared to $\Delta = 1.0$ cases, with shrinking stretching and reflexive separations, expanding coalescence regions, and bouncing covering the entire range of B $(0 < B < 1)$ for all mass concentrations when $We < 17$. Interestingly, the collision maps for $\Delta = 0.8$ exhibit little change compared to
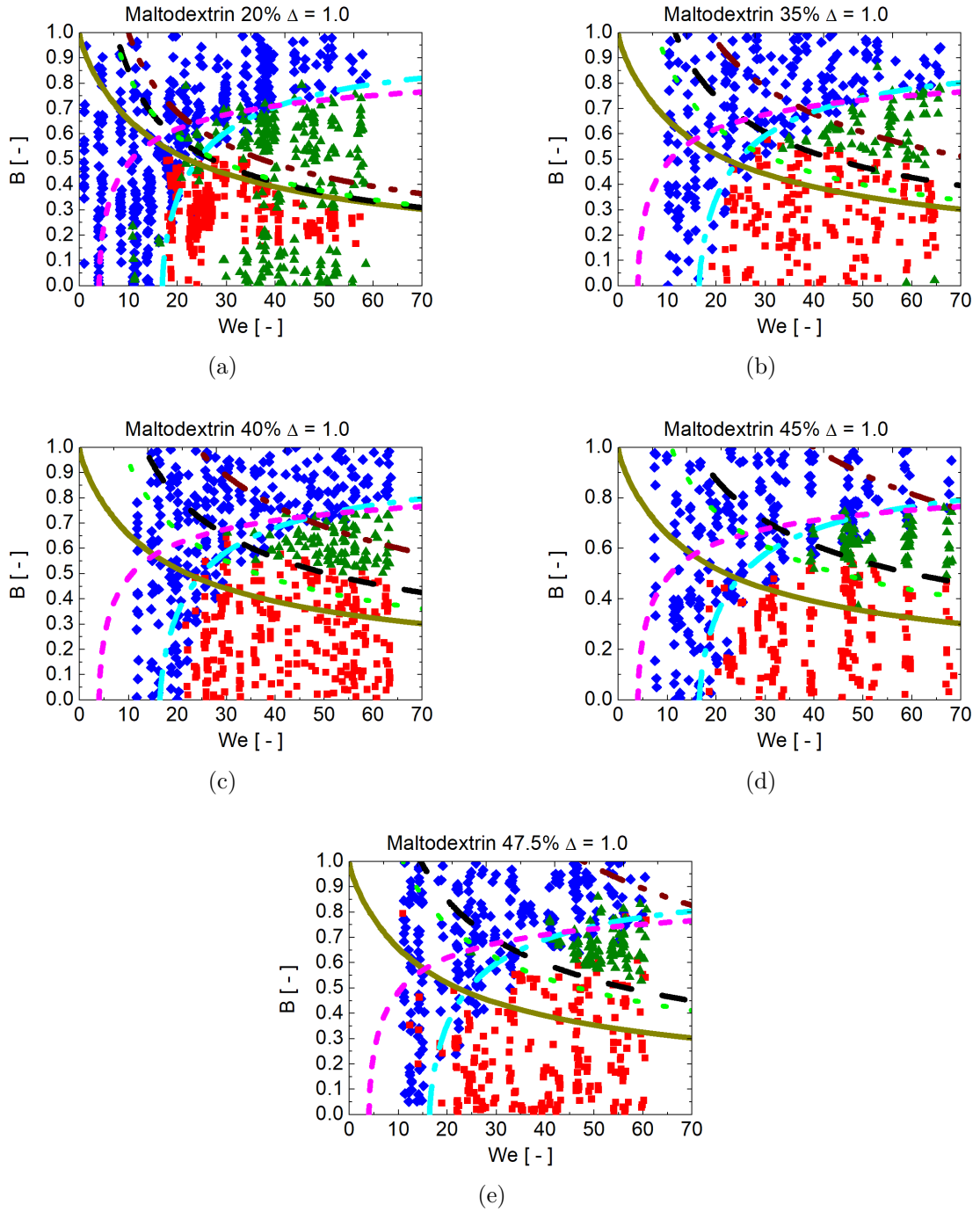
Figure 4.8: Measured collision outcome in the collision maps for maltodextrin $\Delta = 1$ with different mass fractions and comparison with model results: (a) 20 Ma%; (b) 35 Ma%; (c) 40 Ma%; (d) 45 Ma%; (e) 47.5 Ma% (squares: coalescence; triangle: separation; diamond: bouncing; solid dark yellow line: model of Ashgriz and Poo (1990); dash black line: combined model of Sommerfeld and Pasternak (2019) pure liquid correlation; dash dot dot wine line: combined model of Sommerfeld and Pasternak (2019) solution correlation; dot green line: model of Suo and Jia (2020); short dash magenta line: model of Estrade et al. (1999); dash dot cyan line: model of Sui et al. (2023) with non-water-like correlation)).

Table 4.5: Summary of important points locations of collision map of maltodextrin at $\Delta = 0.8$

Case $\Delta = 0.8$	We_T	We_C	We_{B-C}
Maltodextrin 20 Ma%	$We_T \approx 26$	$We_C \approx 30$	$We_{B-C} = 14$
Maltodextrin 35 Ma%	$We_T \approx 33$	Not found	$We_{B-C} = 17$
Maltodextrin 35 Ma%	$We_T \approx 35$	Not found	$We_{B-C} = 17$
Maltodextrin 45 Ma%	$We_T \approx 40$	Not found	$We_{B-C} = 18$
Maltodextrin 47.5 Ma%	$We_T \approx 42$	Not found	$We_{B-C} = 16$

$\Delta = 1.0$. This is due to the We calculation being based on the properties of the smaller droplets, and the characteristic diameter and liquid properties remaining generally the same as for $\Delta = 1.0$ cases, as shown in Table 4.2. Therefore, the Oh_s values are approximately the same for both cases, which is crucial for the boundary line of Sui et al. (2023) and the combined model of Sommerfeld and Pasternak (2019). However, the model of Ashgriz and Poo (1990) and Estrade et al. (1999) do not provide expected results for any of the $\Delta = 0.8$ cases. The model of Suo and Jia (2020) is effective for the 20Ma% maltodextrin solution but not for the other cases. For $\Delta = 0.8$, the combined model of Sommerfeld and Pasternak (2019) with pure liquid correlation performs excellently.

The collision maps of maltodextrin at $\Delta = 0.5$ are presented in Figure 4.10, and unlike the similarity of collision maps of $\Delta = 0.8$ and $\Delta = 1.0$, they exhibit significant changes. As the viscosity increases, the locations of the We_T increase, and the We_C is observed only in the maltodextrin 20Ma% solution. Notably, We_C shows a remarkable increase of approximately 52 at $\Delta = 0.5$, compared to $We_C \approx 30$ in $\Delta = 0.8$ and $\Delta = 1.0$ cases. Additionally, We_{B-C} shifts towards lower We values and is approximately $We_{B-C} \approx 13$, as summarised in Table 4.6. The general tendency of reducing the stretching separation region, expanding the coalescence regime, and bouncing covering the entire We range remains the same as in $\Delta = 0.8$ and $\Delta = 1.0$ cases. However, in the collision maps of $\Delta = 0.5$, the reduction in reflexive and stretching separation regions is more apparent than in the other cases. The remaining area of the collision maps is dominated by coalescence, indicating that coalescence is more likely to occur in these cases. Similar to the other cases, the boundary lines of Ashgriz and Poo (1990) and Estrade et al. (1999) are inadequate for all $\Delta = 0.5$ cases due to their disregard for viscous effects. Furthermore, the model of Sui et al. (2023) is unsuccessful, while the combined model of Sommerfeld and Pasternak (2019) with a pure liquid correlation works exceptionally well, except for the maltodextrin 47.5Ma% solution, which will be discussed later.

Table 4.6: Summary of important points locations of collision map in maltodextrin $\Delta = 0.5$

| Case $\Delta = 0.5$	We_T	We_C	We_{B-C}
Maltodextrin 20 Ma%	$We_T \approx 25$	$We_C \approx 52$	$We_{B-C} = 12$
Maltodextrin 35 Ma%	$We_T \approx 35$	Not found	$We_{B-C} = 16$
Maltodextrin 35 Ma%	$We_T \approx 39$	Not found	$We_{B-C} = 14$
Maltodextrin 45 Ma%	$We_T \approx 40$	Not found	$We_{B-C} = 13$
Maltodextrin 47.5 Ma%	$We_T \approx 43$	Not found	$We_{B-C} = 13$
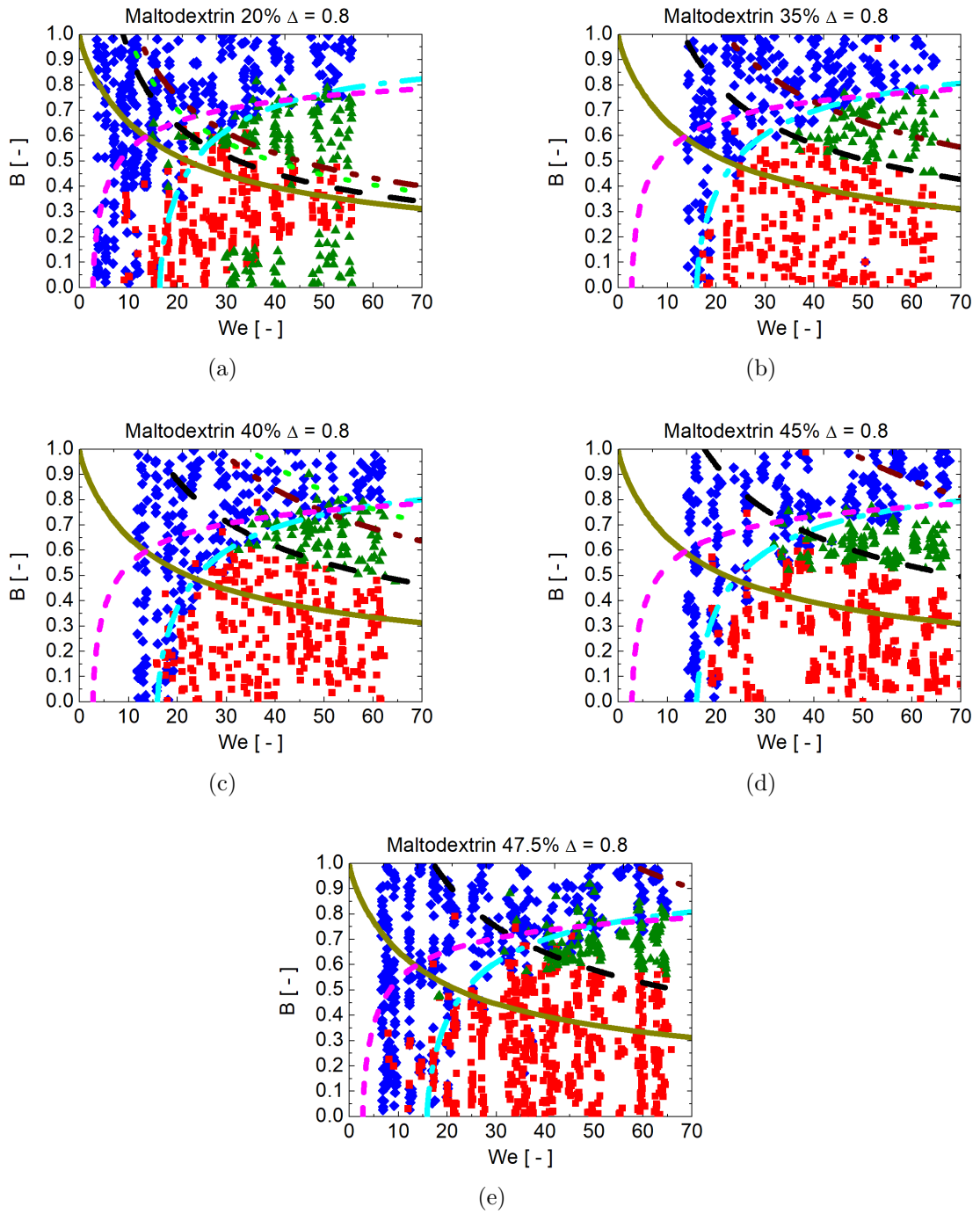
Figure 4.9: Measured collision outcome in the collision maps for maltodextrin $\Delta = 0.8$ with different mass fractions and comparison with model results: (a) 20 Ma%; (b) 35 Ma%; (c) 40 Ma%; (d) 45 Ma%; (e) 47.5 Ma% (squares: coalescence; triangle: separation; diamond: bouncing; solid dark yellow line: model of Ashgriz and Poo (1990); dash black line: combined model of Sommerfeld and Pasternak (2019) pure liquid correlation; dash dot dot wine line: combined model of Sommerfeld and Pasternak (2019) solution correlation; dot green line: model of Suo and Jia (2020); short dash magenta line: model of Estrade et al. (1999); dash dot cyan line: model of Sui et al. (2023) with non-water-like correlation)).

(a)

(b)

(c)

(d)

(e)
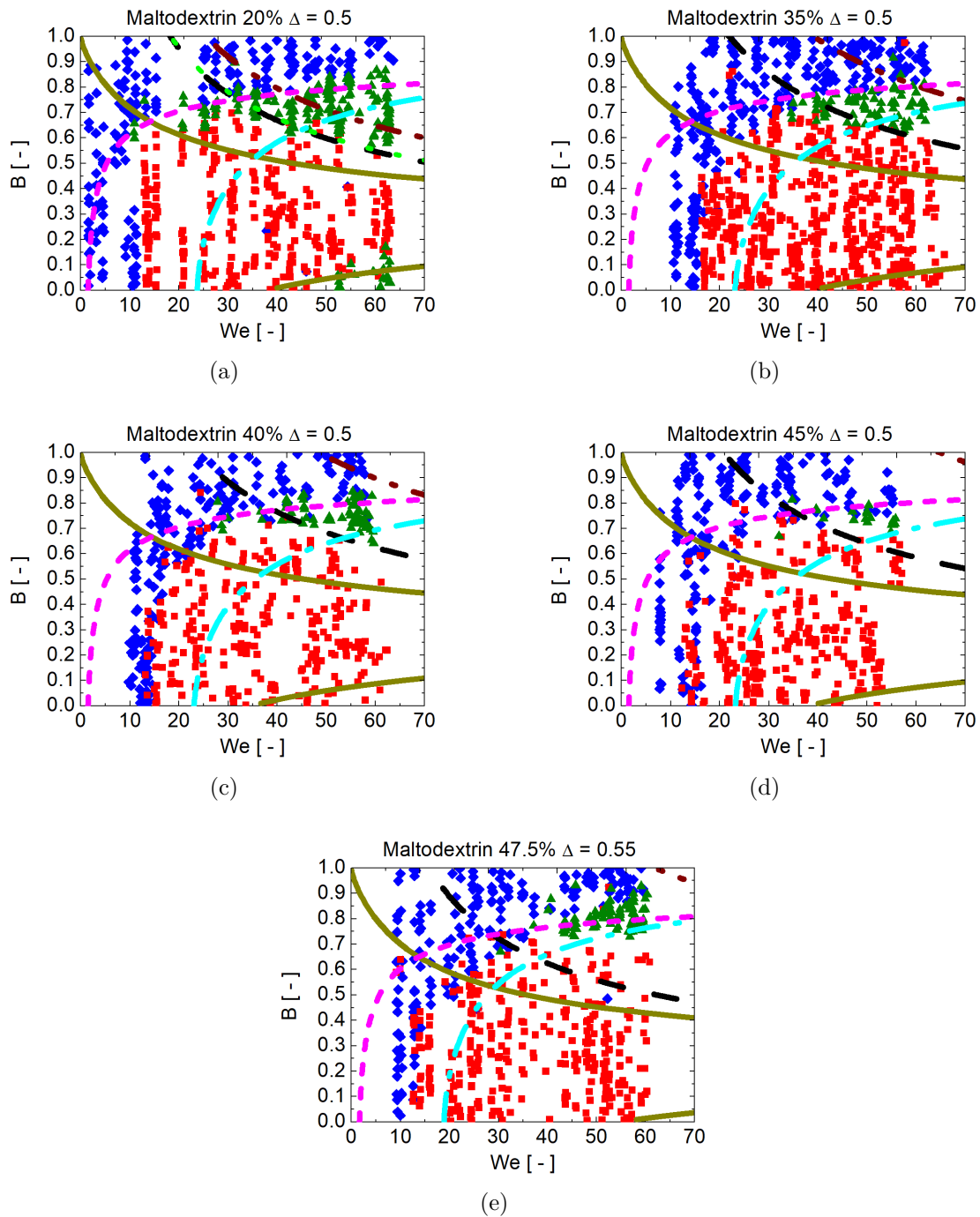
Figure 4.10: Measured collision outcome in the collision maps of maltodextrin at $\Delta = 0.5$ with different mass fractions and comparison with model results: (a) 20 Ma%; (b) 35 Ma%; (c) 40 Ma%; (d) 45 Ma%; (e) 47.5 Ma% (squares: coalescence; triangle: separation; diamond: bouncing; solid dark yellow line: model of Ashgriz and Poo (1990); dash black line: combined model of Sommerfeld and Pasternak (2019) pure liquid correlation; dash dot dot wine line: combined model of Sommerfeld and Pasternak (2019) solution correlation; dot green line: model of Suo and Jia (2020); short dash magenta line: model of Estrade et al. (1999); dash dot cyan line: model of Sui et al. (2023)) with non-water-like correlation).

4.4.2.2 Discussion on size ratio effect

As the size ratio (Δ) decreases, the stretching separation regime shifts to higher We, and its occupancy in the collision maps reduces, as shown in Figures 4.8-4.10. Bouncing covers the entire range of impact parameter B ($0 < B < 1$) for all size ratios in the low We region. The collision maps exhibit a reduction in the bouncing regime, and the We_{B-C} shifts slightly to lower We, while the impact parameter B tends to increase for high We values. For a 40Ma% maltodextrin solution, at $We = 60$, the values of B are 0.75, 0.77, and 0.81 for $\Delta = 1$, $\Delta = 0.8$, and $\Delta = 0.5$ cases, respectively. A reduction in size ratio leads to an increase in the coalescence regime, as both the stretching separation and bouncing regimes lose occupancy on the collision maps for a specific mass concentration.

In summary of the size ratio effect on the characteristic points in the collision maps of maltodextrin, firstly, the We_C is affected by the smaller droplet diameter rather than the size ratio, although the reflexive separation can only be observed in the 20Ma% solution. With the same smaller droplet diameter in $\Delta = 0.8$ and $\Delta = 1.0$ cases, We_C remains at 30, indicating that the size ratio does not affect the critical Weber number. However, in the case of $\Delta = 0.5$, We_C increases to 52, as the diameter of the smaller droplet size decreases to around 477.6 μm compared to 763.1 μm in $\Delta = 0.8$ case and 769.3 μm in the $\Delta = 1.0$ cases. Second, the effect of the size ratio on the location of We_T is less significant than the viscosity. The deviation of locations is not large for the same mass concentration while considering the effect of size ratio, as shown in Tables 4.4-4.6. The deviation for the mentioned size ratios ($\Delta = 0.5$, 0.8, 1) is approximately ± 2.

From the Figure 4.13 to 4.14, the time-resolved collision sequences of the standard four collision outcomes are shown. Each image displays the collision sequence of maltodextrin solution with the same mass concentration and approximately the same We and B, but different size ratios Δ. Figure 4.11 depicts the bouncing sequence of maltodextrin 40Ma% solution at $We \approx 41$ and $B = 0.81$. It is interesting to note that the duration of the bouncing is similar for all size ratios. However, this does not explain why We_{B-C} moves towards lower We. This occurs because bouncing occurs when the film of air trapped between the droplets is unable to drain quickly enough. According to Hicks and Purvis (2010), deformation of the interface generates pressure differences inside the gas film with high pressure at the edge and low pressure at the centre. Therefore, greater deformation results in larger pressure differences between the edge and centre of the air film, making it more difficult for the air film to drain. At impact parameter $B = 0$, as the size ratio decreases, the contact area becomes smaller, reducing the volume of the trapped air film. However, it is difficult to determine whether the pressure difference between the edge and centre of the air film decreases or increases as the size ratio changes. Future studies can verify this through numerical simulations.

Figure 4.12 shows the coalescence sequence of maltodextrin 40Ma% solution at $We \approx 24$ and $B \approx 0.21$. During the process, the merged droplet oscillates and eventually relaxes to a spherical shape, but the oscillation process is not included in the example images. In the case of $\Delta = 0.8$ and $\Delta = 1.0$, an interface merging process is evident after the contact of two droplets. However, in the case of $\Delta = 0.5$, the smaller droplet is completely enveloped by the larger droplet, making it impossible to observe the interfaces in the experiment. However, the shape change of the larger droplet can be clearly observed. Additionally, with decreasing size

ratio and coalescence at low We, the coalescence mechanism seems to shift from breaking the tiny air film at the contact interface of two droplets to small droplets getting directly absorbed by the larger droplet.

Figure 4.13 shows the stretching separation sequence of maltodextrin 40Ma% solution at $We \approx 40$ and $B \approx 0.73$. For the cases of $\Delta = 0.8$ and $\Delta = 1.0$, the main difference is the thickness of the ligament that connects the droplets. In the case of $\Delta = 0.8$, the ligament is thicker on the bigger droplet side due to the unequal droplet diameter, leading to a delay in ligament breakup compared to the case of $\Delta = 1$. Furthermore, the generation of satellite droplets is affected. As for the case of $\Delta = 0.5$, the small droplet participates in the stretching separation to a lesser extent than in the other cases due to the large size difference. As a result, the entire separation process occurs much faster than in the other cases. Interestingly, in the $\Delta = 1$ case, the ligament break-up has the same weight on both sides, leading to simultaneous break-up on both sides. However, for the cases considering size ratio, the break-up first occurs on the small droplet side.

Figure 4.14 shows the reflexive separation sequence of maltodextrin 20Ma% solution at $We \approx 52$ and $B \approx 0$. Reflexive separation can only be observed in maltodextrin solutions with low mass concentration because as viscosity increases, the merged droplet deforms less due to increased viscous dissipation from internal movement. Additionally, with a lower size ratio, the small droplets have less kinetic energy, making it even harder for the ligament to break. With a reducing size ratio, reflexive separation moves to a higher We direction, similar to the results from experiments with pure water by Sui et al. (2021). In that work, the penetration process is clearly observable. In the case of $\Delta = 1$, the two droplets have the same weight, resulting in the ligament staying at the centre of the droplets with almost equal thickness. However, as the size ratio decreases, the larger droplet has a higher weight, causing the ligament to move to the larger droplet side. As a result, the larger droplet affects the trajectories of the smaller droplets and satellite droplets (if they exist).

4.4.2.3 Discussion on the boundary line models

As viscosity increases and size ratio decreases, coalescence occupancy in collision maps increases, while stretching separation and bouncing occupancies decrease. Consequently, the coalescence-stretching separation boundary line shifts significantly upward and toward higher We. This finding is consistent with previous studies Gotaas et al. (2007); Kuschel and Sommerfeld (2013); Sommerfeld and Kuschel (2016).

The model proposed by Ashgriz and Poo (1990) is not effective due to the absence of viscous dissipation. However, the combined model of Sommerfeld and Pasternak (2019) with a pure liquid correlation works well for liquids with different size ratios, except for 47.5 Ma% solution with a size ratio of 0.55, which may be due to missed collision detections in the experiments. Large droplets moving with a higher excitation frequency collide with several small droplets when their spacing is relatively small at a higher velocity, and those collisions are not considered in post-processing, resulting in a gap with fewer spots on the collision map.

According to the definition of the combined model, the maltodextrin solution should use the combined model associated with solution correlation. However, this combination does not work for the maltodextrin collision maps. This is probably related with the balance of the
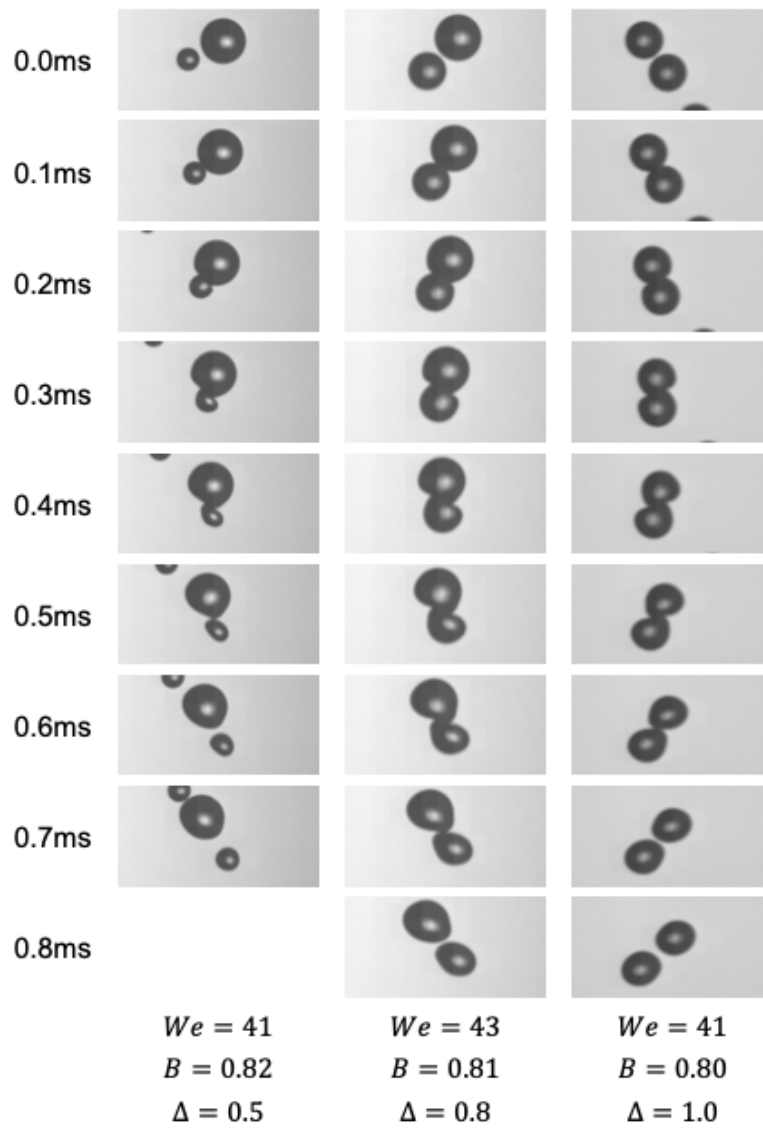
Figure 4.11: Time-resolved collision sequence of bouncing of maltodextrin 40 Ma% ($We \approx 40$, $B \approx 0.81$, size ratio $\Delta = 0.5, 0.8, 1.0$)

Figure 4.12: Time-resolved collision sequence of coalescence of maltodextrin 40 Ma% solution($We \approx 24$, $B \approx 0.21$, size ratio $\Delta = 0.5, 0.8, 1.0$)

Figure 4.13: Time-resolved collision sequence of stretching separation of maltodextrin 40Ma% solution ($We \approx 40$, $B \approx 0.73$, size ratio $\Delta = 0.5, 0.8, 1.0$)
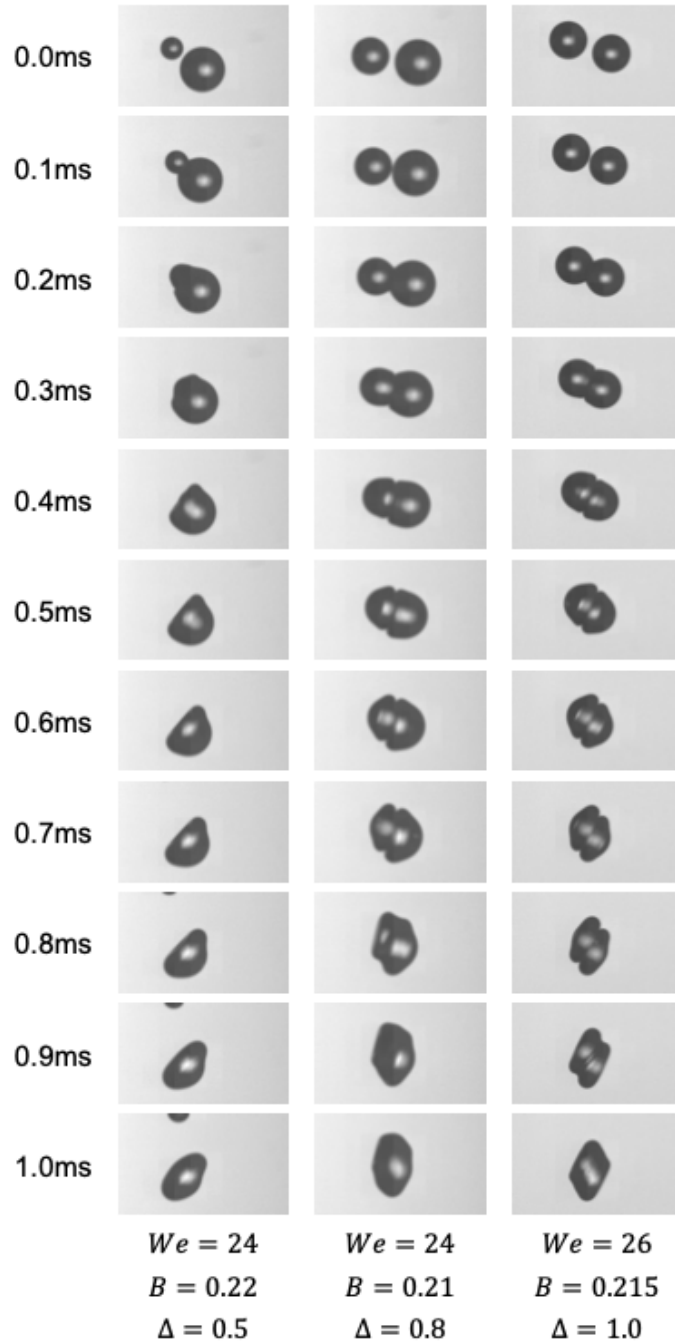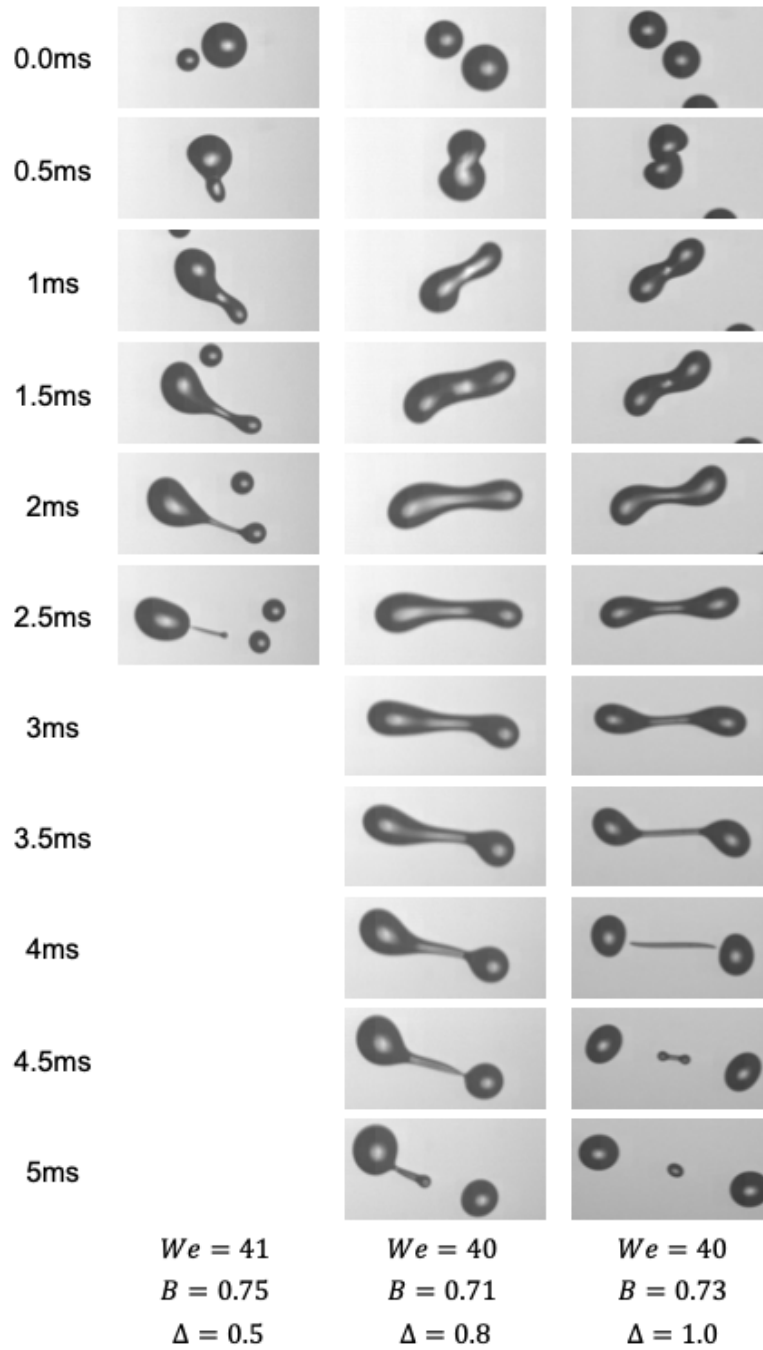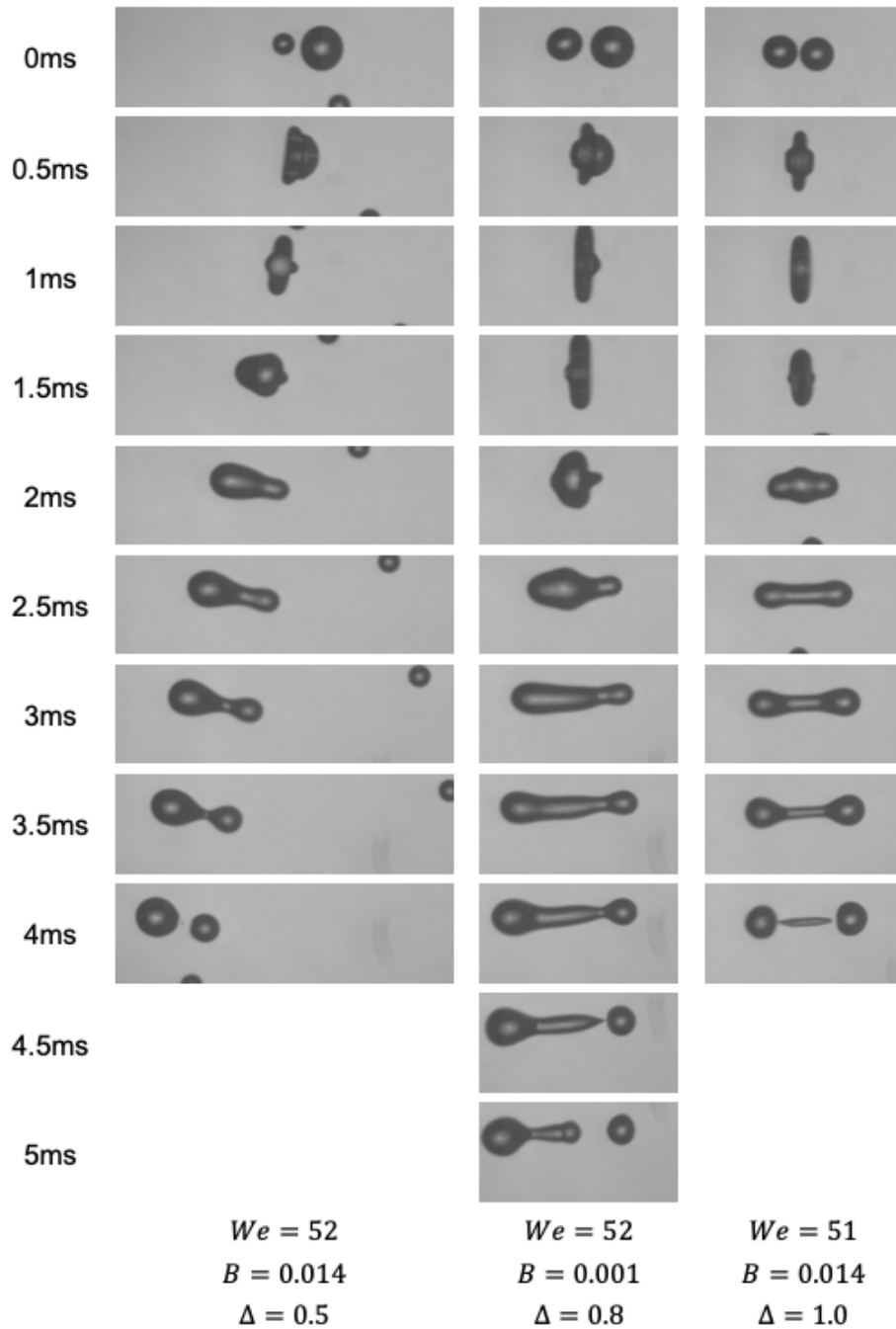
Figure 4.14: Time-resolved collision sequence of reflexive separation of maltodextrin 20 Ma% solution ($We \approx 52$, $B \approx 0.01$, size ratio $\Delta = 0.5, 0.8, 1.0$)

two models in the combined model, where the calculation of the viscosity effect comes from Jiang et al. (1992) and the effect of the size ratio comes from Brazier-Smith et al. (1972). As can be observed from the available collision maps of maltodextrin, the combined model approximates $1/1.14$ times of Jiang et al. (1992) for the same parameters(C_a and C_b) when using the pure liquids correlation and $\Delta = 1$. At this point, it captures the boundary between coalescence and stretching separation relatively well. On the other hand, as the viscosity increases, the solution correlation of the combined model over-predicts the motion of the stretching separation to the higher We. Furthermore, as the size ratio decreases, the change in the combine model originates from the Brazier-Smith et al. (1972) model alone. And it captures the boundary line fairly well. Therefore, based on the experimental results of the maltodextrin solution, improving the combined model's applicability may be more meaningful if better parameters can be chosen for the model part. As mentioned in the paper, the model proposed by Suo and Jia (2020) is valid for liquid viscosity between 1.0 and 47.2 mPa·s at $\Delta = 1$ and liquid viscosity between 1.0 and 1.2 mPa·s at $\Delta < 1$. Therefore, the deviation of the model can be explained.

However, for bouncing boundary lines, neither Estrade et al. (1999) nor Sui et al. (2023) works for all size ratio cases. The collision maps of maltodextrin, PVP, and sunflower oil (Pasternak and Sommerfeld (2017); Sommerfeld and Pasternak (2019)) indicate that the We_{B-C} slightly decreases towards the low We direction as the size ratio Δ decreases. However, the model of Sui et al. (2023) does not go in the lower We direction for $\Delta = 0.5$ cases. Here, the shape parameter and conversion rate are the main factors controlling the We_{B-C} in this model. Third-order polynomial empirical correlations generated from experimental results at $\Delta = 1.0$ by different researchers need further development to adopt them for more size ratios.

4.5 Conclusion

This chapter provides a detailed description of the experimental equipment and image processing methods used, followed by the results of droplet collision experiments with water and maltodextrin. The effect of droplet size ratio on binary collisions of water droplets is explored, and collision maps are presented. All collision maps demonstrate a bouncing collision outcome that spans all We ($We < 50$) at larger impact parameters ($B > 0.8$). This is significant because water sprays are often used as a reference case, without considering the collision outcomes of bouncing. Notably, bouncing is also observed in the region of smaller We ($We < 5 - 10$, $B \approx 0.5$) for distilled water, which is consistent with previous studies. However, further measurements at very low We are needed to fully understand this phenomenon. Additionally, collision maps need to be extended to larger Weber numbers ($We > 50$) to elaborate on the bouncing boundaries. As droplet size ratio decreases, the field of coalescence expands due to reflexive separation moving to higher We. The coalescence-stretching separation boundary moves upward to larger We as the stretching separation also moves slightly to a higher We. Furthermore, it is shown that for water, the combined model proposed by Sommerfeld and Pasternak (2019) predicts the coalescence-stretching separation boundary well up to $\Delta = 0.5$. For smaller size ratios, the model needs to be modified in the Brazier-Smith et al.

(1972) part. Despite of the slightly lower surface tension of tap water, water quality does not appear to have a significant effect on the collision maps.

The effect of viscosity and size ratio on droplet collision outcomes of maltodextrin solutions is also explored, and collision maps are presented. For all cases, critical bouncing point (We_{B-C}), critical point (We_C), and triple point (We_T) are presented. The We_{B-C} is approximately the same for the same size ratio, and it decreases as the size ratio decreases. The We_C occurs only in the lowest two concentrations of maltodextrin solution when We is less than 70, and it is more sensitive to smaller droplet diameter. The We_C is expected to occur in the region of larger We as viscosity increases. The We_T is not affected by droplet size/size ratio but is sensitive to viscosity. The Sommerfeld and Pasternak (2019) model with pure liquid correlation predicts collision outcomes for coalescence-stretching separation boundary excellently for size ratios up to $\Delta = 0.5$. However, the models of Ashgriz and Poo (1990) and Suo and Jia (2020) fail to capture the boundary line due to viscous effect. For bouncing, Estrade et al. (1999) fails without considering the viscosity effect, and Sui et al. (2023) works well for size ratios of $\Delta = 0.8$ and $\Delta = 1.0$, but is significantly off at $\Delta = 0.5$. Further research is needed to understand the bouncing boundary with consideration for the size ratio effect.

Chapter 5

The Euler/Lagrange Approach

This chapter provides detailed descriptions of numerical calculation methods for sprays, based on transient, three-dimensional, and Euler/Lagrange methods. All Euler/Lagrange calculations were performed using OpenFOAM®8, an open-source numerical tool. The chapter starts with a discussion of the governing equations for the fluid phase, as well as the turbulence model's general form. It then proceeds with the discretisation of conservation equations, utilising the finite volume method. Next, the chapter introduces the Lagrangian Particle Tracking (LPT) method to handle discrete phases. This includes considering the forces associated with the parcels in the calculations, along with a particle turbulent dispersion model based on the Langevin equation. Furthermore, the simulation utilises the fully stochastic collision model to evaluate the droplets collision in spray, which involves collision maps determining the collision outcomes.

5.1 Euler phase

The fluid phase is treated as continuum and solved in a computational grid whose transport phenomena are calculated by solving the Reynolds-Averaged Navier-Stokes (RANS) equations associated with the standard $k - \varepsilon$ turbulence model. The governing equations for the continuous phase are incompressible, three-dimensional, and time-dependent, with the general form provided by Eq. 5.1. Eq. 5.1 includes variables such as the fluid density ρ, Reynolds-averaged velocity components u_i, gas viscosity μ, turbulent viscosity μ_T, effective transport tensor Γ_ϕ, source terms of the fluid phase S_ϕ, and particle phase source terms $S_{\phi p}$. Different values of ϕ correspond to the conservation equations for diverse quantities like turbulent kinetic energy k, dissipation rate ε, among others. For instance, when $\phi = 1$, the continuity equation is represented, whereas $\phi = u_i$ results in the momentum equation. Table 5.1 summarises the significance of the quantities for different variables, including the diffusion coefficients, fluid phase source terms S_ϕ, and particle phase source terms $S_{\phi,p}$. Since the dissertation does not address interfacial momentum, heat transfer, and interfacial mass transfer in the simulations, these source terms are not discussed in it. Further information can be found in Sommerfeld (2017).

$$\frac{\partial(\rho\phi)}{\partial t} + \frac{\partial}{\partial x_j}\left(\rho u_i \phi\right) = \frac{\partial}{\partial x_i}\left(\Gamma_\phi \frac{\partial(\phi)}{\partial x_i}\right) + S_\phi + S_{\phi,p} \tag{5.1}$$

By solving Reynolds-Averaged conservation (RANS) equations in conjunction with the standard $k - \varepsilon$ turbulence model equations, the Eulerian phase (flow field) is obtained. The conservation equations are transformed into a set of discrete equations representing the con-

ϕ	Γ_ϕ	S_ϕ	$S_{\phi,p}$
1	0	0	0
u_i	$\mu + \mu_t$	$\dfrac{\partial}{\partial x_i}(\Gamma u_i)\dfrac{\partial u_j}{\partial x_i} - \dfrac{\partial p}{\partial x_i} + \rho g_i$	$S_{u,p}$
k	$\mu + \frac{\mu_t}{\sigma_k}$	$G_k - \rho\varepsilon$	$S_{k,p}$
ε	$\mu + \frac{\mu_t}{\sigma_\varepsilon}$	$\dfrac{\varepsilon}{k}(C_{\sigma 1}G_k - C_{\sigma 2}\rho\varepsilon)$	$S_{\varepsilon,p}$

Where: $G_k = \mu_t\left(\dfrac{\partial u_i}{\partial x_j} + \dfrac{\partial u_j}{\partial x_i}\right)\dfrac{\partial u_i}{\partial x_j}$, $\mu_t = C_\mu\rho\dfrac{k}{\varepsilon}$

$C_\mu = 0.09$	$\sigma_\varepsilon = 1.3$	$C_{\sigma 1} = 1.44$	$C_{\sigma 2} = 1.92$

Table 5.1: Summary of the terms in the general transport equation for different transport variables that describe the fluid phase in connection with the standard $k-\varepsilon$ turbulence model (Sommerfeld (2017)).

servation law for each control volume by applying the finite volume method originally available in OpenFOAM®. These equations are integrated over each control volume in the numerical domain. The gradient and divergence terms are discretised by a Gaussian linear method, with values linearly interpolated from the centre of the cell to the centre of the face. The solution of the discretisation equations is achieved by the PIMPLE algorithm, a combination of PISO and SIMPLE, which relates the momentum and mass conservation equations. The SIMPLE algorithm is used for steady-state calculations, while PISO is used for transient calculations. The main advantage of the PIMPLE (combined PISO-SIMPLE) algorithm over the PISO method is that it allows for larger Courant numbers $Co >> 1$ and increases the time step of the calculation. This is particularly advantageous in cases where complex numerical meshes are required and where local mesh refinement is needed. The PIMPLE method can therefore improve the stability of the solution without drastically reducing the time step. In order to establish a good solution for the flow field, it is crucial to monitor the time scale. Therefore, the PIMPLE method is used to connect the velocity and pressure fields in all calculations of this study.

5.2 Dispersed phase

The Lagrangian approach is employed to simulate the dispersed phase, which involves solving the ordinary differential equation of motion for each particle throughout its journey across the flow domain. However, the computational cost can be reduced using the concept of a computational parcel. To ensure accurate particle mass flow rates, each computational parcel denotes a specific number (np) of particles that have identical properties, including diameter, velocity, and more. The change in linear velocity components of each parcel considers all the significant forces affecting the particles. The equations of motion for the particles are provided in Eq. 5.2 and 5.3, where x_{pi} indicates the particle's location, and u_{pi} denotes its linear velocity component. The mass of each parcel is computed based on the summation of its component particles' mass. The drag and gravity force acting on the particles are represented by F_D and

F_G, respectively.

$$\frac{\partial x_{pi}}{\partial t} = u_{pi} \tag{5.2}$$

$$m_p \frac{\partial u_{pi}}{\partial t} = F_D + F_G \tag{5.3}$$

5.2.1 Forces acting on the particles

In the field of multiphase fluid dynamics using Euler/Lagrange method, the Basset-Boussinesq-Oseen equation (BBO) is utilised to explain the motion of small particles and the forces they encounter in unsteady fluids with low Reynolds numbers. Sommerfeld et al. (2008) provides a comprehensive analysis of the BBO equation, including the varied forces that impact particles and the forces that enable the equation of motion to be extended to higher Reynolds number coefficients. In this study, the drag force F_D and gravitational force F_G are solely considered to determine the parcel's transport. It is because the droplets under examination have relatively small sizes ($d_p < 80 \ \mu$m), and shear-induced lift and slip-rotation lift can be neglected. According to estimates from Sommerfeld (1996), lift becomes significant for particles when the particle size in the air exceeds 80 μm. Likewise, the estimates suggest that shear-induced lift force becomes significant at 30 μm in water and 90 μm in the air. Moreover, to reduce computational costs, other forces are not considered and ignored.

Drag Force: In fluid-particle systems, the drag force is the dominant force governing particle motion. It is expressed as the drag coefficient C_D in Eq. 5.4, as shown by Sommerfeld et al. (2008) and Crowe et al. (2011). The standard correlation by Schiller (1933) presented in Eq. 5.5, can be used to obtain the drag coefficient. The drag coefficient is dictated by the Reynolds number Re_p, as defined in Eq. 5.6. The equation incorporates key parameters such as d_p, particle diameter, m_p, the mass of particle, ρ_f and ρ_p, densities of the fluid and particle, and C_D, the drag coefficient. The instantaneous fluid velocity u_f experienced by the particle is computed by interpolating the mean fluid velocity from the nearby grid points to the particle position and adding a fluctuating component obtained through particle turbulence dispersion (Laín and Sommerfeld (2013)). Additional details are discussed in section 5.2.3.

$$F_D = \frac{3\rho_f m_p}{4\rho_p d_p} C_D (u_f - u_p)|u_f - u_p| \tag{5.4}$$

$$\begin{cases} 0.5 < Re_p < 1000 & C_D = \dfrac{24}{Re_p}\left(1 + 0.15 Re_p^{0.687}\right) \\ Re_p > 1000 & C_D = 0.44 \end{cases} \tag{5.5}$$

$$Re_p = \frac{\rho_f d_p |u_f - u_p|}{\mu_f} \tag{5.6}$$

$$F_G = m_p g \left(1 - \frac{\rho_f}{\rho_p}\right) \tag{5.7}$$

Gravitational Force: The gravitational force acting on the particle can be expressed as shown in Eq. 5.7 by Crowe (2006) and Sommerfeld et al. (2008), where g denotes the

acceleration due to gravity.

5.2.2 Lagrangian time scale

A dynamic Lagrangian time step is adopted for particle tracking to solve the ordinary differential equations of particle motion. It is automatically adjusted based on the local relevant timescales, such as the particle response time, integral time scale of turbulence, and inter-particle collision time. To avoid multiple collisions within a single Lagrangian time step, the time step is kept sufficiently small and determined for the current position under the flow condition. The Lagrangian time step for particle tracking (ΔT_L) is selected as 10% of the shortest among all the locally relevant time scales. Additionally, the time scale for inter-particle collision is limited to $\Delta t_C < 0.05 \ t_{coll}$ to ensure numerical stability, due to the series expansion applied in the collision probability derivation (Zivkovic and Sommerfeld (1992)). Further guidelines related to the determination of particle statistical properties can be found in Laín and Sommerfeld (2020).

$$\Delta t_L = \frac{min(\Delta t_{cv}, T_L, \tau_p, t_{coll})}{10} \tag{5.8}$$

- Δt_{cv} is the Eulerian time step

- $T_L = \frac{c_T \sigma_F^2}{\varepsilon}$ is the integral time scale of turbulence with $C_T = 0.24$ and $\sigma_F^2 = 2/3k$.

- $\tau_p = \frac{\rho_p d_p^2 \mu_f}{18}$ is the particle response time.

- $t_{coll} = \frac{1}{f}$ is the average time for binary particle collisions (f is the collision frequency).
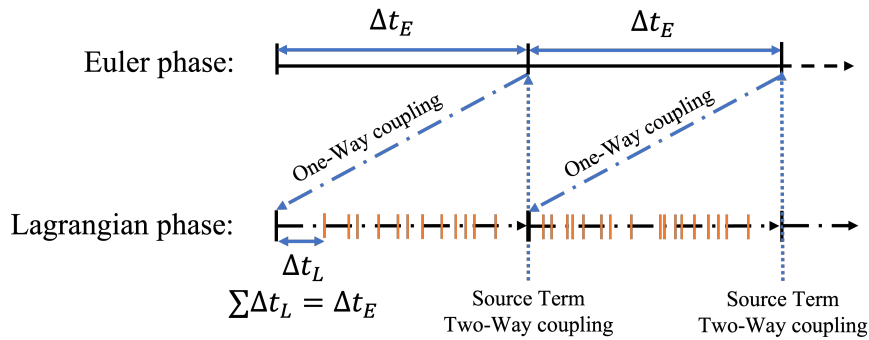
Figure 5.1: Schematic of the solution of the Euler/Lagrange calculation.

After each calculation of the Euler phase with the defined Eulerian time step Δt_E, the calculation of the Lagrangian phase would involve the dynamic Lagrangian time step Δt_L. The computational cost is getting higher with more parcels involved in the computational domain. The Lagrangian particle tracking is the most expensive part of the Euler/Lagrange simulation, no matter whether it is the one-way coupling or two-way coupling. The basic routine of the Euler/Lagrange calculation is shown in Figure 5.1.

- In the first step, the flow field is calculated using Δt_E as the time step. Δt_E determines the time resolution of the flow field, which can be predetermined. And it should be small enough to ensure a reasonable Courant number *Co* for the stability and accuracy of the numerical solutions.

- Thousands of computational parcels are then randomly injected at the end of each Eulerian time step, depending on the mass flow rate of each injector which is calculated by the experiment measurement.

- The parcels are then tracked in this "frozen" flow field. The parcel tracking time step is dynamically adjusted according to the local relevant time scale (see Eq. 5.8).

- If the effect of the parcels in the flow field is not considered, then the so-called one-way coupling is used. Conversely in a two-way coupling condition, the effect of the parcels in the flow field is determined through the source term. Furthermore, the particle phase source terms and the particle properties are averaged over the time sequence Δt_E.

- The new source terms are introduced into the governing equations, which are then solved for the next Eulerian time step.

5.2.3 Particle turbulent dispersion model

When calculating fluid flow using the RANS method, only the mean fluid velocity and non-direct fluctuating components (from the turbulence model) are accessible at the particle location. The RANS solution does not provide information on the instantaneous fluid velocity, which is necessary for the integration of particle trajectories. Therefore, the fluctuating fluid velocity that is seen by the particle has to be estimated by the particle turbulent dispersion model. Consequently, a single-step isotropic Langevin model is utilised to characterise the impact of fluid turbulence on particles, as developed and validated by Sommerfeld (1993) and Lipowsky and Sommerfeld (2005). Based on a correlated contribution from the previous time step and a stochastic influence sampled from a normal distribution function with the standard deviation of the local fluid velocity fluctuation as described in Eq. 5.9, the new instantaneous fluid velocity can be 'seen' by the particle.

$$u_i^{'n+1} = R_{p,i}(\Delta t_L, \Delta r)u_i^{'n} + \sigma_F\sqrt{1 - R_{p,i}^2(\Delta t_L, \Delta r)}\xi_i \tag{5.9}$$

In Eq. 5.9, the time step is indicated by the superscripts and subscripts of the spatial components. Δr represents the distance between the virtual fluid element and the Lagrangian particle during the time step Δt_L. The variable ξ_i corresponds to a Gaussian distribution with zero mean and unit variance in three directions. The first term on the right-hand side of Eq. 5.9 represents the correlated part, while the second term is the random contribution of the local fluid fluctuation velocity. $R_{p,i}(\Delta t_L, \Delta r)$ represents the correlation function predicted by Lagrangian and Eulerian components:

$$R_{p,i}(\Delta t_L, \Delta r) = R_L(\Delta t_L)R_{E,ij}(\Delta r) \tag{5.10}$$

The Lagrangian correlation function $R_L(\Delta t_L)$ describes the instantaneous velocity fluctuation along the way of a virtual fluid element. It depends on the Lagrange integral time scale.

$$R_L(\Delta t_L) = e^{-\frac{\Delta t_L}{T_L}} \tag{5.11}$$

On the other hand, the Eulerian correlation function $R_{E,ij}(\Delta r)$ reflects the deviation of the particle trajectory from the path of the virtual fluid element, the so-called crossing trajectory effect:

$$R_{E,ij}(\Delta r) = (f(\Delta r) - g(\Delta r))\frac{\Delta r_i \Delta r_j}{|\Delta r|^2} + g(\Delta r)\delta_{ij} \tag{5.12}$$

$$f(\Delta r) = exp\left(-\frac{\Delta r}{L_E}\right) \tag{5.13}$$

$$g(\Delta r) = (1 - \frac{\Delta r}{2L_E})exp(-\frac{\Delta r}{L_E}) \tag{5.14}$$

Here, δ_{ij} is the Kronecker delta, $f(\Delta r)$ and $g(\Delta r)$ are the longitudinal and transverse two-point correlation functions (Sommerfeld (1993) and De Karman and Howarth (1938)). The integral length scales $L_E = c_L T_L \sigma_F$ with $c_L = 3.0$.

5.2.4 Influence of droplets on the flow

To incorporate the two-way coupling effects of droplets on the fluid phase in the momentum equation, researchers use a Particle-Source-In-Cell (PSI Cell) approach, as proposed by Crowe et al. (1977), to calculate the additional source term, $S_{u,p}$. By averaging over each parcel passing through a single Lagrangian calculation, the source term represents the momentum exchange resulting from droplet and fluid interchange. The cell volume, V_{cv}, and the mass of the particle, m_k, represent their respective quantities. np_k represents the number of actual particles within the parcel k. The velocities of a parcel before and after the particle tracking during an Eulerian time step are denoted as $u_{k,di}^n$ and $u_{k,di}^{n+1}$, respectively. k_{tot} is calculated as the sum over all parcels that pass via the considered control volume. As a result, obtaining statistically relevant source terms requires an adequate number of parcels to pass through the control volumes, as per Sommerfeld (2017).

$$S_{u,p} = -\frac{1}{V_{cv}\Delta t_E}\sum_k^{k_{tot}} m_k np_k \sum_n \left\{\left(u_{p,k,i}^{n+1} - u_{p,k,i}^n\right) - g_i\left(1 - \frac{\rho_f}{\rho_p}\right)\Delta t_L\right\} \tag{5.15}$$

5.3 The fully stochastic collision model

As shown in Figure 5.2, there are three methods for implementing the collision model in Euler/Lagrange spray simulations, as discussed by Sommerfeld and Pasternak (2019). These include:

  1. A completely deterministic method used for constructing collision trajectories. Each
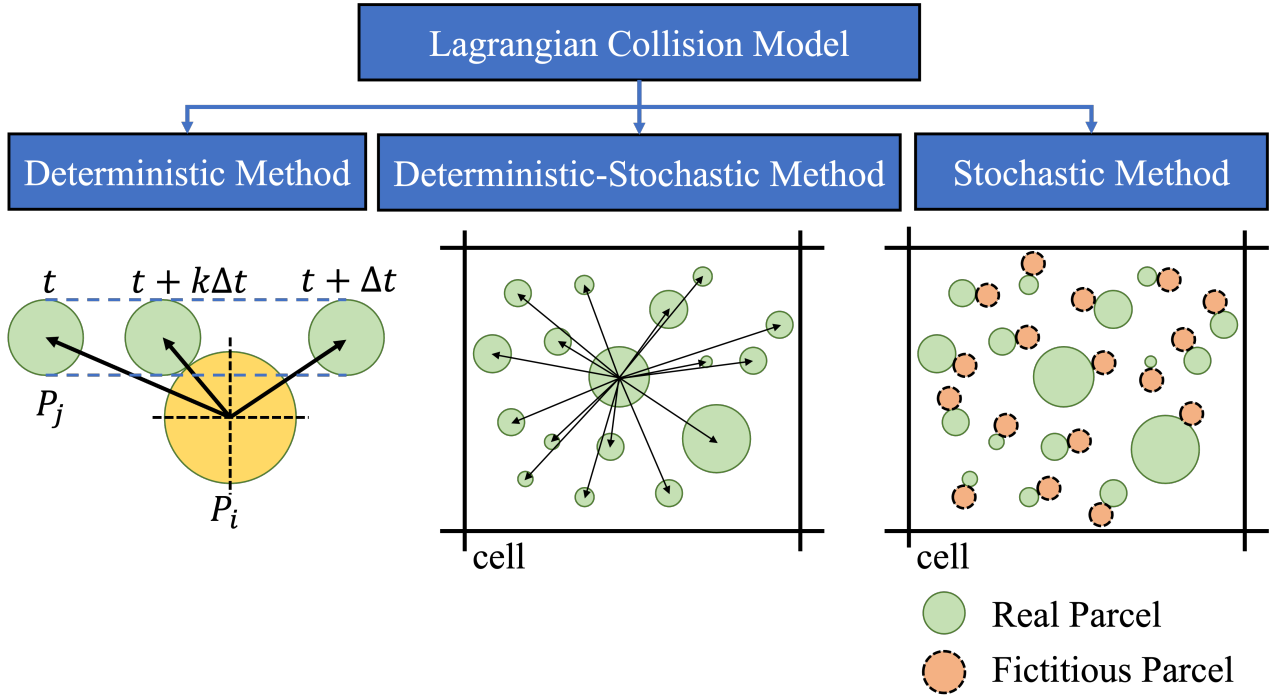
Figure 5.2: Schematic of Lagrangian droplet collision modes: left) (fully deterministic model with geometrical collision detection (Sundaram and Collins (1996); (middle) deterministic-stochastic parcel collision model (O'Rourke (1981)); (right) full stochastic collision model (Sommerfeld (2001), Sommerfeld and Pasternak (2019)

parcel identifies its collision partners within the computational domain. However, this approach is computationally expensive due to a high number of searches that are given by $n(n-1)$ for each time step. It is not practical for simulations that use a considerable number of parcels.

2. The deterministic-stochastic parcel collision model involves identifying the possibility of collision between every couple of real particles in a computational cell. This method was proposed by O'Rourke (1981) and Nordin (2001).

3. The fully stochastic droplet collision model presented in Sommerfeld (2001) combined with the impact efficiency proposed by Ho and Sommerfeld (2002). The fully stochastic model constructs a fictitious collision partner from the local droplet population of the real particle which is accurate and effective.

The fully stochastic collision model, introduced by Sommerfeld (2001), involves generating fictitious collision partners and approximating collision probabilities. An essential advantage of the fully stochastic model is that it does not necessitate position and velocity for all encapsulating real particles, unlike in deterministic models. Instead, the fictitious collision partners are sampled based on statistical information of the particles in each control volume. Beforehand, the droplet population parameters within each computational cell are statistically sampled in the previous Eulerian time step, which will be discussed later. For this study, the number concentration, droplet size distribution, and correlation between droplet size and

the mean (RMS) velocities in each direction are the necessary local properties for the spray. Compared to deterministic models, this approach requires less processing effort to account for the occurrence of droplet collisions.

5.3.1 Sampling of the fictitious collision partner

Sampling fictitious parcels to act as collision partners is a crucial step in the stochastic collision model. The diameter of d_{pj} and velocity of u_{pj} for the fictitious parcel are obtained from the real parcel data, including average droplet diameter, root mean square (RMS) diameter, velocity distribution, and size-velocity and size-RMS velocity correlations within the current control volume. There are four ways to create a fictitious collision partner, which is summarised in Figure 5.3.
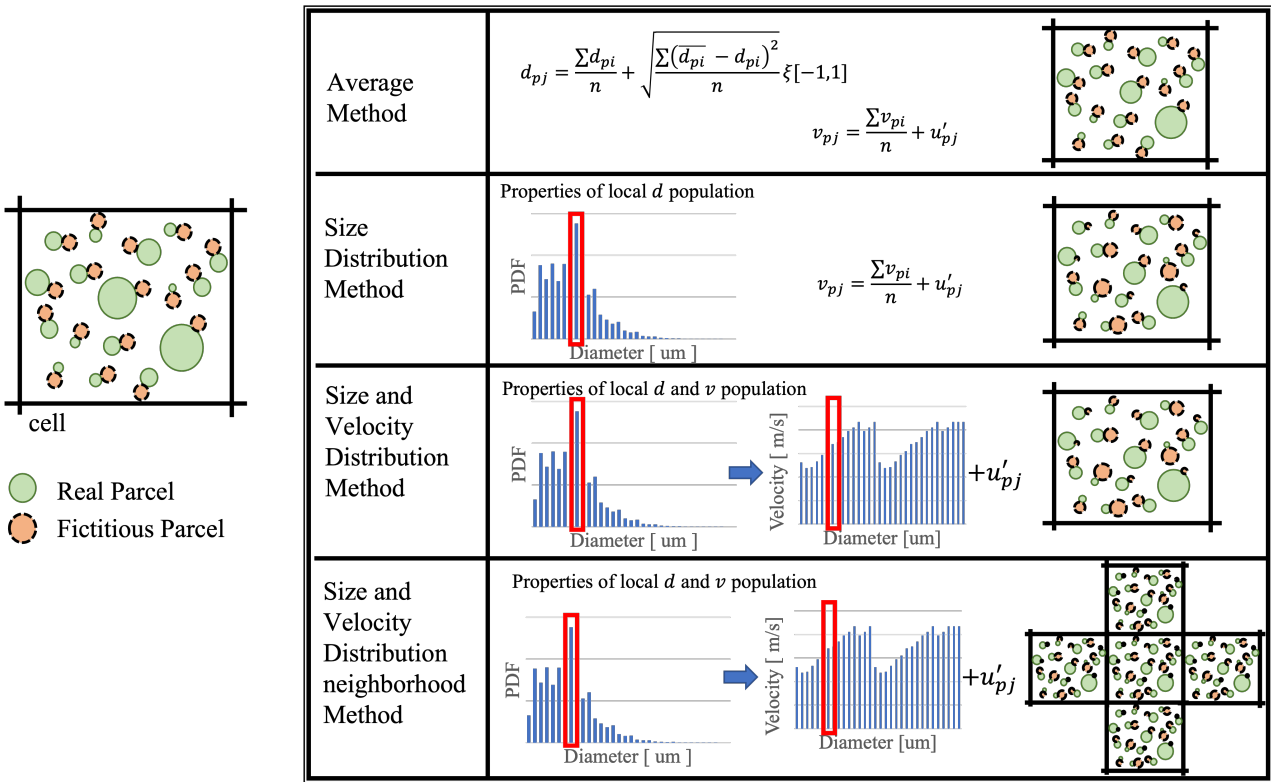
Figure 5.3: Summary of methods to generate diameter and velocity of the fictitious parcel (collision partner) in fully stochastic collision model

5.3.1.1 The diameter of fictitious parcel

In Eq. 5.16, d_{pj} represents the diameter of the fictitious parcel, with $\bar{d}_{pj}$ as the average component and d'_{pj} as the fluctuating component. To introduce stochasticity, a random number ξ_d is selected from the range of $[-1, 1]$. The two methods for computing $\bar{d}_{pj}$ and d'_{pj} are the Average Method and the Distribution Method.

$$d_{pj} = \bar{d}_{pj} + d'_{pj}\,\xi_d \qquad \xi_d \in [-1, 1] \qquad (5.16)$$

Average Method: The average part of the diameter of fictitious parcels $\bar{d}_{pj}$ is calculated as the average droplet diameter of the real particles $\bar{d}_{pi}$ in the cell, as shown in Eq. 5.17. The fluctuating part d'_{pj} is calculated as the root-mean-square (RMS) of the real particles' diameter d'_{pi} in the cell, as shown in Eq. 5.18.

$$\bar{d}_{pj} = \bar{d}_{pi} = \frac{\sum_i d_{pi}^2}{n} \tag{5.17}$$

$$d'_{pj} = d'_{pi} = \sqrt{\frac{\sum_i (\bar{d}_{pi} - d_{pi})^2}{n}} \tag{5.18}$$

Size Distribution Method: $\bar{d}_{pj}$ is randomly sampled from the local real particle size distribution. d'_{pj} is selected from the local real particle size RMS distribution with the same size class as $\bar{d}_{pj}$.

5.3.1.2 The velocity of fictitious parcel

Similar to the method for calculating the diameter of the fictitious parcel, the general form for calculating the velocity of the fictitious parcel is shown in Eq. 5.19, where u_{pj} is the instantaneous velocity of the fictitious parcel that consists of the average part $\bar{u}_{pj}$ and turbulence fluctuating component u'_{pj}. Two methods are available to calculate $\bar{u}_{pj}$, namely the Average Method and the Velocity Distribution Method.

$$u_{pj} = \bar{u}_{pj} + u'_{pj} \tag{5.19}$$

Average method: $\bar{u}_{pj}$ equals to the average velocity of the real parcels $\bar{u}_{pi}$ in the control volume, as shown in Eq. 5.20.

$$\bar{u}_{pj} = \bar{u}_{pi} = \frac{\sum_i u_{pi}}{n} \tag{5.20}$$

Velocity Distribution Method: The Velocity Distribution Method and the Size Distribution Method should be used together. The size-velocity correlations of the real particle generate $\bar{u}_{pj}$, which means that the droplet diameter's size class must be predetermined in the Size Distribution Method. In this case, $\bar{u}_{pj}$ is equal to the average velocity of the selected size class $\bar{u}_{pi,class}$.

$$\bar{u}_{pj} = \bar{u}_{pi,class} \tag{5.21}$$

The determination of the fluctuating velocity components of the fictitious parcel (u'_{pj}) considers the possibility of a correlation with those of the real particle as a consequence of their contact with the same turbulence structure. Therefore, u'_{pj} is composed of both random and correlated contributions. In Eq. 5.22, u'_{pj} is sampled from a Gaussian velocity distribution with the local RMS-value and correlated to the velocity of the considered particle due to turbulence, which depends on the Stokes number St, i.e., the ratio of the particle response time τ_p to the relevant time scale of turbulence τ_t. In the Average Method, σ_{pi} is the local RMS value of the particle velocity in the control volume, while in the Velocity Distribution Method, σ_{pi} is the RMS velocity of the real particle velocity for the selected size class.

$$u'_{pj} = R\left(St\right)u'_{pi} + \sigma_{pi}\sqrt{1 - R\left(St\right)^2}\xi \tag{5.22}$$

$$St = \frac{\tau_p}{\tau_t} = \frac{\tau_p}{T_L} \tag{5.23}$$

$$\tau_p = \frac{\rho_p d_p^2}{18\mu_f f_D} \tag{5.24}$$

$$f_D = \frac{C_D Re_p}{24} \tag{5.25}$$

Increasing the Stokes number St leads to a decrease in the correlated contribution and an increase in the random contribution. To address this issue, Sommerfeld (2001) proposed a correlation function $R(St)$, as shown in Eq. 5.27. This formula was derived by solving the model of Zaichik and Alipchenkov (2003) for the correlation function of drifting particles on velocity. Laín (2010) developed an improved three-parameter profile, as shown in Eq. 5.26, which outperforms the correlation function of Sommerfeld (2001).

$$R(St) = exp(-\frac{0.019St^2}{1 + 0.044St^{1.725}}St^{0.4}) \tag{5.26}$$

$$R(St) = exp(-0.55St^{0.4}) \tag{5.27}$$

By arranging and combining the approaches for calculating the fictitious parcel diameters and velocities, four methods of generating fictitious collision partners are available as shown in Figure 5.3.

- **Average Method:** d_{pj} and u_{pj} of fictitious parcels are calculated using the Average Method.

- **Size Distribution Method:** d_{pj} is determined using the Size Distribution Method, and the velocity is calculated using the Average Method.

- **Size and Velocity Distribution Method:** both d_{pj} and u_{pj} are calculated using the Size Distribution Method and Velocity Distribution Method, respectively.

- **Size and Velocity Distribution Neighbourhood Method:** In the case of core control volumes containing small amounts of parcels and particles, consideration of surrounding neighbouring cells is added to the Size and Velocity Distribution Method.

Once the collision partners have been created for each real particle and their diameters and velocities have been determined, it is necessary to calculate the collision probability P_{coll} .

5.3.2 Collision probability

The calculation of P_{coll} is based on various factors such as the particle concentration, sizes of the real and fictitious parcels, their velocities, and the Lagrangian time step Δt. If the Δt is sufficiently small, the collision frequency f can be approximated as the product of the

Δt and f. A collision between two particles is constrained to occur in a collision cylinder, which is defined by the area $\pi(d_{pi} + d_{pj})^2/4$ and the length $|u_{pi} - u_{pj}|\Delta t$. The probability of collision between the particle being considered and nearby particles can be calculated by multiplying the collision cylinder with the number of particles in the specific control volume n_p/V_{cell}. Figure 5.4 illustrates the collision cylinder.

$$P_{coll} = f\Delta t = \frac{\pi}{4}\left(d_{pi} + d_{pj}\right)^2 \; |u_{pi} - u_{pj}| \; \frac{n_p}{V_{cell}} \; \Delta t \tag{5.28}$$
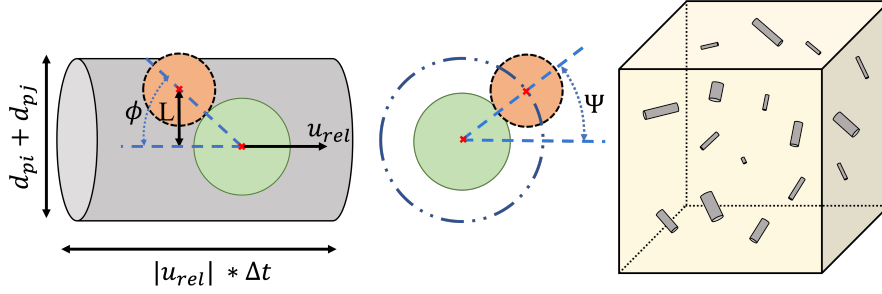

Figure 5.4: Illustration of the collision cylinder (left), collision cross-sectional area (middle) and collision probability (right).

To determine the impact point of collisions, calculations are carried out in a transformed coordinate system, wherein the larger-sized particles remain stationary, and the axes of the colliding cylinder align with the relative velocity vector, as depicted in Figure 5.5. The dimensionless lateral position of the collision point on the cross-section of the colliding cylinder (i.e., the lateral dimensionless displacement L_a) is randomly generated by using two uniformly-distributed random variables, XX and ZZ, in the range $[0, 1]$ using Eq. 5.29. The angle of impact, ϕ, can be calculated as a function of the lateral displacement, L, using the arc sine function. The position of the collision plane across the cross-section of the colliding cylinder (i.e., the angle Ψ in Figure 5.5) is randomly generated from a uniform distribution in the range $[0, 2\pi]$.

$$L_a = \sqrt{XX^2 + ZZ^2} \tag{5.29}$$

$$L = \frac{L_a\left(d_{pc} + d_{ps}\right)}{2} \tag{5.30}$$

After determining the impact point and accounting for the size distribution of the particles as shown in Figure 5.6, it is important to consider the possibility of small droplets colliding with much larger particles, known as collector particles. In such cases, the smaller droplets may move around the larger droplets with the relative velocity field, making it necessary to consider the impact efficiency proposed by Ho and Sommerfeld (2002). Although often neglected in most spray simulations, the impact efficiency η_p is crucial and is defined as the ratio of the circular cross-section from which the small droplets come and hit the larger droplet to the effective collector cross-section, accounting for the so-called blocking effect. The diameter of the collector and the small particles are denoted by d_{pc} and d_{ps}, respectively, as shown in Figure 5.6(Laín and Sommerfeld (2020)). The impact efficiency can also be correlated as a function
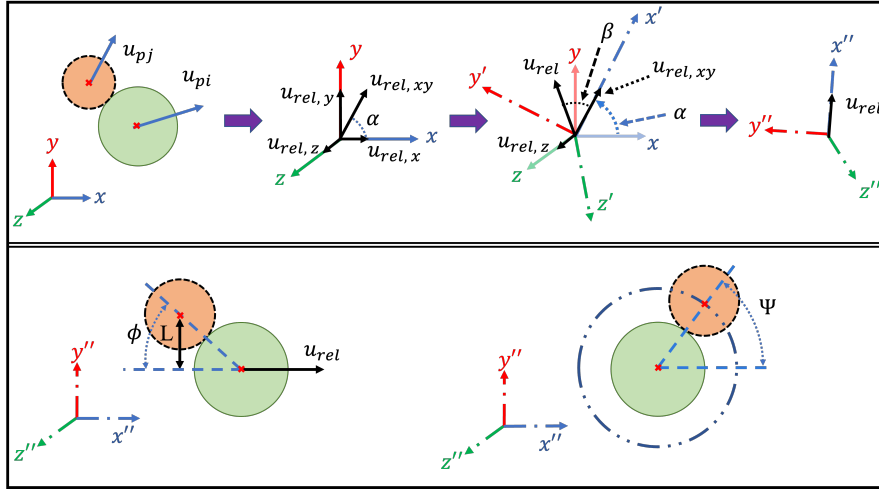
Figure 5.5: Transformation of the coordinate system in order to align the relative velocity with the axis of the collision cylinder (top) and to obtain the point of impact (bottom)
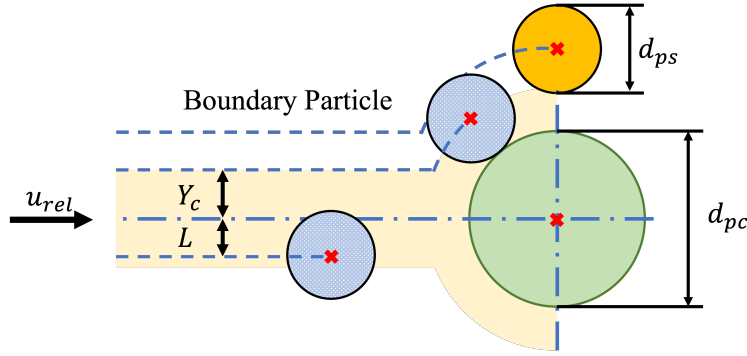

Figure 5.6: Schematic of the impact efficiency for a small particle interacting with a stationary collector (green particle), where the blue particles represent the colliding particles, and the orange one represents the particles that missed the collision.

of the relative Stokes number $St_{rel,i}$ (Schuch and Löffler (1978)), which is the small droplet Stokesian relaxation time to the time it needs to pass the collector droplet, as calculated in Eq. 5.34. The impact efficiency η_p is related to $St_{rel,i}$ using two Reynolds-number-dependent parameters a and b listed in Table 5.2. Here, Re_{pc} is calculated using the relative velocities of the instantaneous fluid velocity and the small particle velocity.

$$\begin{cases} d_{pc} = max\,(d_{pi}, d_{pj}) \\ d_{ps} = min\,(d_{pi}, d_{pj}) \end{cases} \tag{5.31}$$

$$\eta_p = \left(\frac{2Y_c}{d_{pc} + d_{ps}}\right)^2 = \left(\frac{St_{rel,i}}{St_{rel,i} + a}\right)^b \tag{5.32}$$

$$Y_c = \frac{d_{pc} + d_{ps}}{2} \sqrt{\left(\frac{St_{rel,i}}{St_{rel,i} + a}\right)^b} \tag{5.33}$$

$$St_{rel,i} = \frac{\tau_p}{t_{pass}} = \frac{\rho_p u_{rel} d_{ps}^2}{18\mu d_{pc} f_D} \tag{5.34}$$

$$f_D = \frac{C_D Re_{pc}}{24} \tag{5.35}$$

$$Re_{pc} = \frac{\rho_f d_{pc} |u_f - u_{ps}|}{\mu_f} \tag{5.36}$$

Table 5.2: Constants *a* and *b* in the impact efficiency correlation proposed by Schuch and Löffler (1978)

	a	b
$Re_{pc} < 1$	0.65	3.7
$1 < Re_{pc} < 20$	1.24	1.95
$20 < Re_{pc} < 40$	1.03	2.07
$40 < Re_{pc} < 80$	0.506	1.84
$Re_{pc} > 80$	0.25.	2.0

The occurrence of a collision is determined by two conditions, as described in Eq. 5.37. The first condition is that the randomly generated number RN from a uniform distribution over the interval $[0, 1]$ should be less than the calculated collision probability P_{coll}. The second condition is that the lateral displacement L must be smaller than the radial distance of the boundary particle trajectory Y_c.

$$\begin{cases} RN < P_{coll} \\ L <= Y_C + 0.5 + D_S \end{cases} \tag{5.37}$$

5.3.3 Collision outcome determination

Once the collision is confirmed, the collision outcomes (bouncing, coalescence, stretching, and reflexive separation) are determined based on the collision map $B = f(We)$ and theoretical boundary lines introduced in previous chapters. The diameters and velocities of real particles are updated accordingly. Coalescence, stretching, and reflexive separation lead to changes in diameter while bouncing does not have an impact on diameter. Coalescence involves two droplets merging and increasing in size, while stretching and reflexive separation may give rise to secondary droplets, whose production depends on the model (Kim et al. (2009); Ko and Ryou (2005a,b); Munnannur and Reitz (2007); O'Rourke (1989); Zhang et al. (2017)). These outcomes also affect velocity, potentially resulting in a different trajectory. Therefore, collision maps with boundary lines specific to the fluid being studied are necessary for accurate numerical simulations of spray behaviour using the Euler/Lagrange method. In the past, numerical calculations of diesel engine sprays used boundary lines originally created for water, which were inappropriate for fuel droplet collision processes (Post and Abraham (2002)). The models for each of these outcomes are explained in the following sections.

5.3.3.1 Bouncing

For bouncing, the parcels are reflected with the opposite normal velocity component by keeping the lateral component, thereby neglecting momentum loss.

5.3.3.2 Coalescence

Compared to the inter-particle agglomerations model proposed by Sgrott and Sommerfeld (2019), the coalescence of binary droplet collisions is simpler since the merged droplet does not have a porosity as solid particles do. Coalescence results in the direct formation of larger spherical droplets due to surface tension. This treatment is known as the equivalent sphere model, and the diameter of the newly created merged droplet is determined by the sum of the volumes of the relevant parcels. The velocity of the merged droplet is not determined until the coalescence process completes, as shown in Eqs. 5.38 and 5.39. The diameter of the merged droplet d_{coal} is given by the cube root of V_{coal}. Here, V_{coal} is the volume of the merged droplets, d_{pi} and d_{pj} are the diameters of the real and fictitious parcels, respectively, and u_{pi}, m_{pi}, u_{pj}, and m_{pj} denote the velocity and mass of the real and fictitious parcels. Additionally, in binary droplet collision experiments, the merged droplets oscillate for a period of time after impact, and during this process, the droplets are non-spherical. However, in the simulation, the oscillatory motion of the merged droplets is not taken into account, and all merged droplets are treated as spherical directly.

$$V_{coal} = \frac{1}{6}\pi d^3_{coal} = \frac{1}{6}\pi(d^3_{pi} + d^3_{pj}) \tag{5.38}$$

$$u_{coal} = \frac{u_{pi}m_{pi} + u_{pi}m_{pj}}{m_{pi} + m_{pj}} \tag{5.39}$$

The fully stochastic collision model uses one real parcel and one fictitious parcel to form a colliding pair, making it necessary to use two different methods to maintain mass and momentum conservation for coalescence.

- **Method 1**: To maintain mass balance, Ruger et al. (2000), Laín and Sommerfeld (2013), and Sommerfeld et al. (2021a) used a method that reduces the number of particles (number of particles represented by the same properties such as diameter and velocity) in a parcel. Specifically, the mass of the parcel is the sum of the masses of these particles, which makes it possible to decrease the number of particles contained in a parcel. This is shown in Eq. 5.40.

- **Method 2**: In this method, collisions only occur if the volume of the real parcel is greater than that of the fictitious parcel. When the volume of the real parcel is smaller than the fictitious parcel, the newly formed merged droplets disappear. Moreover, the number of particles in the merged parcel after the collision remains the same as the real parcel before the collision.

-

In addition, Method 2 reduces the occurrence of unrealistically large fictitious parcels compared to Method 1. In Method 1, mass balance is maintained by naturally reducing *np* in the parcel. However, after many coalescences, the droplets may become very large and contain very small *np*. In addition, the droplet diameter has a greater influence than the particle concentration in the cell when calculating the collision probability as Eq. 5.28. Therefore, in order to overcome unrealistic collisions and to ensure that such collisions are binary, the time step needs to be smaller and smaller. Ultimately, when using Method 1, this effect leads to an uncontrollable dead loop in the simulation easily. In the end, According to Ruger et al. (2000), the results of both Method 1 and Method 2 are approximately the same. Therefore, Method 2 is used in this study.

$$np_{new} = np \frac{d_{coal}^3}{(d_{pi}^3 + d_{pj}^3)} \tag{5.40}$$

5.3.3.3 Stretching and Reflexive Separation

The droplet collision model proposed by O'Rourke (1981) has been widely utilised in numerous numerical simulations of sprays. Nevertheless, while determining the collision outcomes, this single-line model only considers coalescence and separation outcomes and is insufficient for simulating processes that associate with reflexive and stretching separation and satellite droplet generation. It is also not compatible with other liquids as it is developed based on water droplet collision.

This study employs the model proposed by several authors, Ko and Ryou (2005b), Ko and Ryou (2005a), Ko et al. (2007), Munnannur and Reitz (2007), and Kim et al. (2009), to determine collision outcomes related to stretching and reflexive separation, as well as the satellite droplet generation. This model considers the droplet collision process, including the break-up of droplets and the generation of satellite droplets. By applying the conservation of droplet mass, momentum, and energy before and after impact, the equation derives for characterising the droplets and satellite droplets after the collision. The equations also predict the number, size, and velocity of satellite droplets analytically. While there are differences between the models proposed by each author, they all use a similar parameter C_{vs}, known as the separation volume efficiency, that determines the temporal evolution of a ligament composed of parts of the interacting volumes of the two colliding droplets. Eq. 5.41 shows this process, where $E_{stretch}$ denotes the total effective stretching kinematic energy, E_{surten} denotes the surface energy in the interaction region derived from Ashgriz and Poo (1990), and E_{dissip} denotes the viscous dissipation in the interaction region. The empirical constant λ is set to 30% of the total initial kinetic energy of the droplets Munnannur and Reitz (2007).

$$C_{vs} = \frac{E_{stretch} - E_{surten} - E_{dissip}}{E_{stretch} + E_{surten} + E_{dissip}} \tag{5.41}$$

$$E_{stretch} = \frac{1}{2}\rho_p v^2 \left(\frac{1}{6}\pi d_l^3\right) \frac{\Delta^3}{(1+\Delta^3)^2} \left[(1+\Delta^3) - (1-B^2)(\chi_s + \Delta^3\chi_l)\right] \tag{5.42}$$

$$E_{surten} = \sigma_p \left[2\pi \left(\frac{1}{6}\pi d_l^3\right) d_l \Lambda \left(\Delta^3\chi_s + \chi_l\right)\right]^{\frac{1}{2}} \tag{5.43}$$
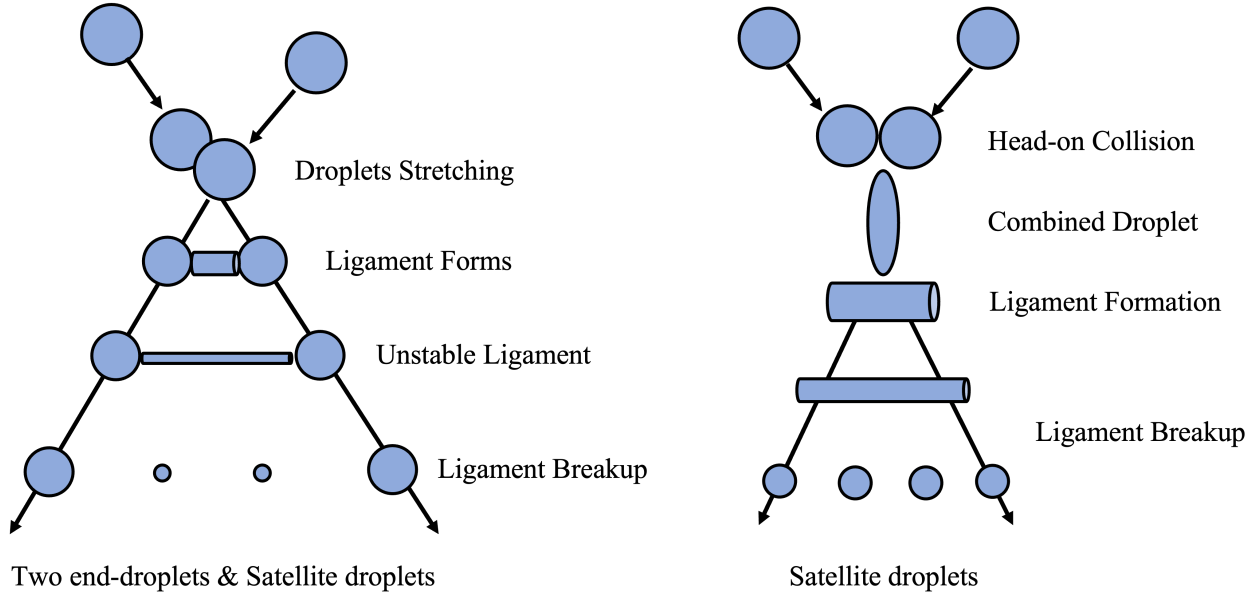
Figure 5.7: Schematic of ligament formation and breakup (left: stretching separation; right: reflexive separation)

$$E_{dissip} = \lambda \frac{1}{2} \rho_d \left[\left(\frac{1}{6} \pi d_l^3 \right) |v_l|^2 + \left(\frac{1}{6} \pi d_s^3 \right) |v_s|^2 \right] \tag{5.44}$$

Stretching separation: According to experimental studies by Kuschel and Sommerfeld (2013) and Sommerfeld and Kuschel (2016), the stretching-separation process can result in the generation of satellite droplets. Ashgriz and Poo (1990) modelled the volume ratio of small and large droplets lost during separation due to ligament formation, which can be represented by ψ_s and ψ_l, respectively. χ_s and χ_l are the separate volume fractions, with the same definitions as in Eq. 3.19 and 3.20.

$$\psi_s = C_{vs} \chi_s \tag{5.45}$$

$$\psi_l = C_{vs} \chi_l \tag{5.46}$$

In this model, fragmentation is prevented when $C_{vs} < 0$, allowing elongated ligaments to be derived from the separated volumes. The connecting mass between the end droplets is assumed to have a uniform cylinder shape, with length equal to its radius. Thus, the initial radius r_0 of the ligament can be calculated by multiplying the length by the radius as Eq. 5.47.

$$r_0 = \sqrt[3]{\frac{4}{3} \left(\psi_s r_s^3 + \psi_l r_l^3 \right)} \tag{5.47}$$

The radius of each satellite droplet can be calculated non-dimensionally using We_0 and $\bar{r}_{bu}$, as shown in Eqs. 5.48 and 5.49. The non-dimensional ligament radius at breakup (r_{bu}) is determined by solving Eq. 5.48 - 5.50 with $k_1 = 11.5$ and $k_2 = 0.45$ as described in Kim et al. (2009). The Newton-Raphson iteration approach is used with a residual of 10^{-5} to solve Eq. 5.50.

$$We_0 = \frac{\rho_d \left(2r_0 v^2\right)}{\sigma} \tag{5.48}$$

$$\bar{r}_{bu} = \frac{r_{bu}}{r_0} \tag{5.49}$$

$$\frac{0.75}{\sqrt{2}} \left(k_1 k_2\right) We_0^{\frac{1}{2}} \bar{r}_{bu}^{\frac{7}{2}} + \bar{r}_{bu}^2 - 1 = 0 \tag{5.50}$$

After that, it is assumed that ligament rupture is dominated by the Plateau-Rayleigh instability. Therefore, the radius of the satellite droplet r_{sat} produced by ligament rupture can be calculated as follows:

$$r_{sat} = 1.89 r_{bu} \tag{5.51}$$

In this model, a significant time scale T is proposed as Eq. 5.52, and the modelling of fragmentation in the stretching separation will be described in terms of this time scale.

$$T = \frac{3}{4} k_2 \sqrt{We_0} \tag{5.52}$$

In the case of stretching separation in Munnannur and Reitz (2007) model, under the circumstance when $C_{vs} \leq 0$, there is no fragmentation in the stretching separation and no effect on the velocity of the droplets. If $C_{vs} \geq 0$ and $T \leq 2$, the ligament is considered to compress into a single satellite with the same radius as the initial radius r_0 of the ligament. If $C_{vs} \geq 0$ and $T > 2$, the ligament is considered to be stretched and broken up. The number of satellite droplets N_{sat} is calculated as Eq. 5.53. It is determined based on the mass conservation of the ligament assuming satellites of uniform size. The velocity of the satellite droplet u_{sat} is calculated as Eq. 5.54.

$$N_{sat} = \frac{3}{4} \left(\frac{r_0}{r_{sat}}\right)^3 \tag{5.53}$$

$$u_{sat} = \frac{\Delta^3 \chi_s u_s + \chi_l u_l}{\Delta^3 \chi_s + \chi_l} \tag{5.54}$$

Criterion	Physical Process	Radius of Satellite drops	Number of satellite droplets
$C_{vs} \leq 0$	Collision without fragmentation	0	0
$C_{vs} > 0, T \leq 2$	Ligament contraction into a single satellite	r_0	1
$C_{vs} > 0, T > 2$	Ligament stretching and capillary break-up	$r_{sat} = 1.89 r_{bu}$	$N_{sat} = \frac{3}{4} \left(\frac{r_0}{r_{sat}}\right)^3$

Table 5.3: Summary of the calculation of satellite droplets for stretching separation

In the fully stochastic collision model, the velocity after stretching separation is calculated only for the real particle by coupling a fictitious collision partner and transforming the droplet velocity into the local coordinate system. If $C_{vs} < 0$, the real droplet velocity after stretching

separation remains unchanged. If $C_{vs} > 0$, z represents the fraction of energy dissipated during the collision and is determined using the stochastic collision model. Here, B_{cr} is defined in Eq. 3.29 from the O'Rourke (1989) model.

$$z = \frac{B - \sqrt{B_{cr}}}{1 - \sqrt{B_{cr}}} \tag{5.55}$$

In the local coordinate system, the larger droplet is considered stationary. Thus, the velocity after stretching separation (u_{after}) is only calculated for the real particle when $C_{vs} > 0$, and is determined using Eq. 5.56 and 5.57. These equations are derived from Eqs. 3.35 and 3.36, as only the velocity of the real parcel is taken into account.

In the case of the bigger droplet is the real particle:

$$u_{after} = \frac{\Delta^3 (1 - z) u_{rel}}{1 + \Delta^3} \tag{5.56}$$

In the case of the smaller droplet is the real particle:

$$u_{after} = \frac{(\Delta^3 + z) u_{rel}}{1 + \Delta^3} \tag{5.57}$$

Reflexive separation:

Figure 5.7 indicates that during reflexive separation, two droplets briefly unite to form a cylindrical ligament with a volume that matches the total volume of the droplets. Therefore, the initial radius r_0 of the ligament can be calculated using Eq. 5.58. The number of satellite droplets is determined by Eq. 5.59 in the model proposed by Kim et al. (2009).

$$r_0 = \sqrt[3]{r_s^3 + r_l^3} \tag{5.58}$$

$$N_{sat} = \frac{3}{4} \left(\frac{r_0}{r_{sat}} \right)^3 - 2 \tag{5.59}$$

If $N_{sat} \leq 0$, it is assumed that the ligament breaks up without forming any satellite droplet, and both end-droplets retain their initial radii. On the other hand, if $0 < N_{sat} < 1$, it is expected that a single satellite droplet with a radius r_{sat}, smaller than the two end-droplets, is formed. Finally, if $N_{sat} > 1$, the ligament is expected to disintegrate into droplets of the same radius r_{sat} for both end-droplets and satellite droplets (Kim et al. (2009)).

	Number of satellite droplets	Satellite droplet diameter
$N_{sat}<0$	0	-
$0<N_{sat}<1$	1	r_{sat}
$N_{sat}>1$	$|N_{sat}|$	r_{sat}

Table 5.4: Summary of the calculation of satellite droplets for reflexive separation

During the process of reflexive separation, the velocity of the real particle is affected by

the kinetic energy loss that the two major droplets experience due to viscous dissipation throughout the collision process. As a result, the velocities of the two major droplets are calculated using Eq. 5.60 with $\lambda = 0.3$ (Ko and Ryou (2005b)). On the other hand, the velocity of a satellite droplet is determined by the conservation of momentum, which is represented by Eq. 5.61.

$$u_{after} = u_{rel}\sqrt{1 - \lambda} \tag{5.60}$$

$$u_{sat} = \frac{\Delta^3 u_s + u_l}{1 + \Delta^3} \tag{5.61}$$

In the fully stochastic collision model, the collision partner is represented by fictitious parcels rather than actual parcels, as opposed to the deterministic approach. Maintaining parcel mass balance requires the number of particles in the parcel (np), along with the parcel concept. The original number of particles in the real parcel in bouncing remains unchanged since the parcels are not combined. Coalescence only considers collisions where the diameter of the real parcel exceeds that of the fictitious parcel, with the number of particles in the real parcel remaining the same. Additionally, stretching and reflexive separations preserve mass balance with the aid of np, utilising Eq. 5.62.

$$np_{after} = \frac{m_{before}}{m_{after}} np \tag{5.62}$$

5.4 Summary of the Euler/Lagrange approach

This chapter offers an overview of the Euler/Lagrange approach utilised in this dissertation. First, a brief introduction to the Eulerian phase calculations is provided, followed by an explanation of the Lagrangian phase calculation, including particle forces, dynamic Lagrangian time steps, particle turbulence dispersion models, and fully stochastic collision models. In order to enhance the comprehension of the Euler/Lagrange numerical computation process in OpenFOAM®, the flowchart depicted in Figure 5.8 and 5.9 is presented.

A Lagrangian library is implemented at the solver level, based on the standard solver for the Eulerian phase. The Figure 5.8 is mainly based on **kinematicCloud** and **kinematicParcel**, which are the foundation for all other cloud and parcel models. In the computations, Lagrangian particles act as units of the "cloud," and the associated control equations are superimposed layer by layer. The cloud layer comprises fundamental definitions in Lagrangian calculations while models in thermo-related and chemical reaction processes are added to higher levels, such as the thermoCloud and reactingCloud. The preEvolve() function initialises necessary fields, while the evolveCloud() function is central to the Lagrangian calculation, including parcel injection and motion calculations, performed in the Parcel Level loop for all parcels in the computational domain. The computational power required increases with the number of parcels in the mesh. Once the computation at the parcel level is over, the solver returns to the cloud level to determine how to couple with the Eulerian phase, depending on the coupling method settings. Any associated temporary data is cleared in readiness for the next round of calculations.
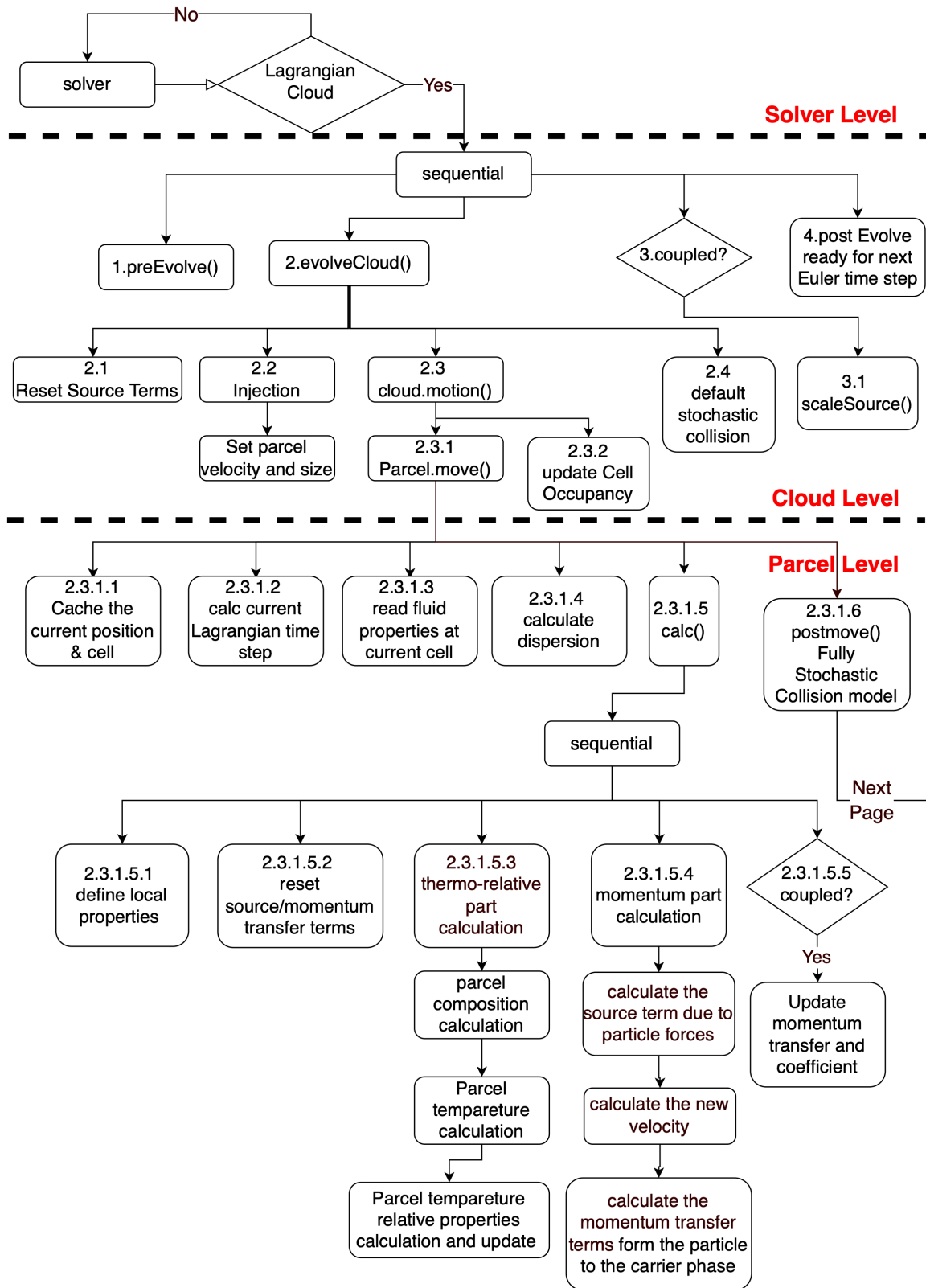
Figure 5.8: The general flow chart of Euler/Lagrange simulation process in OpenFOAM®
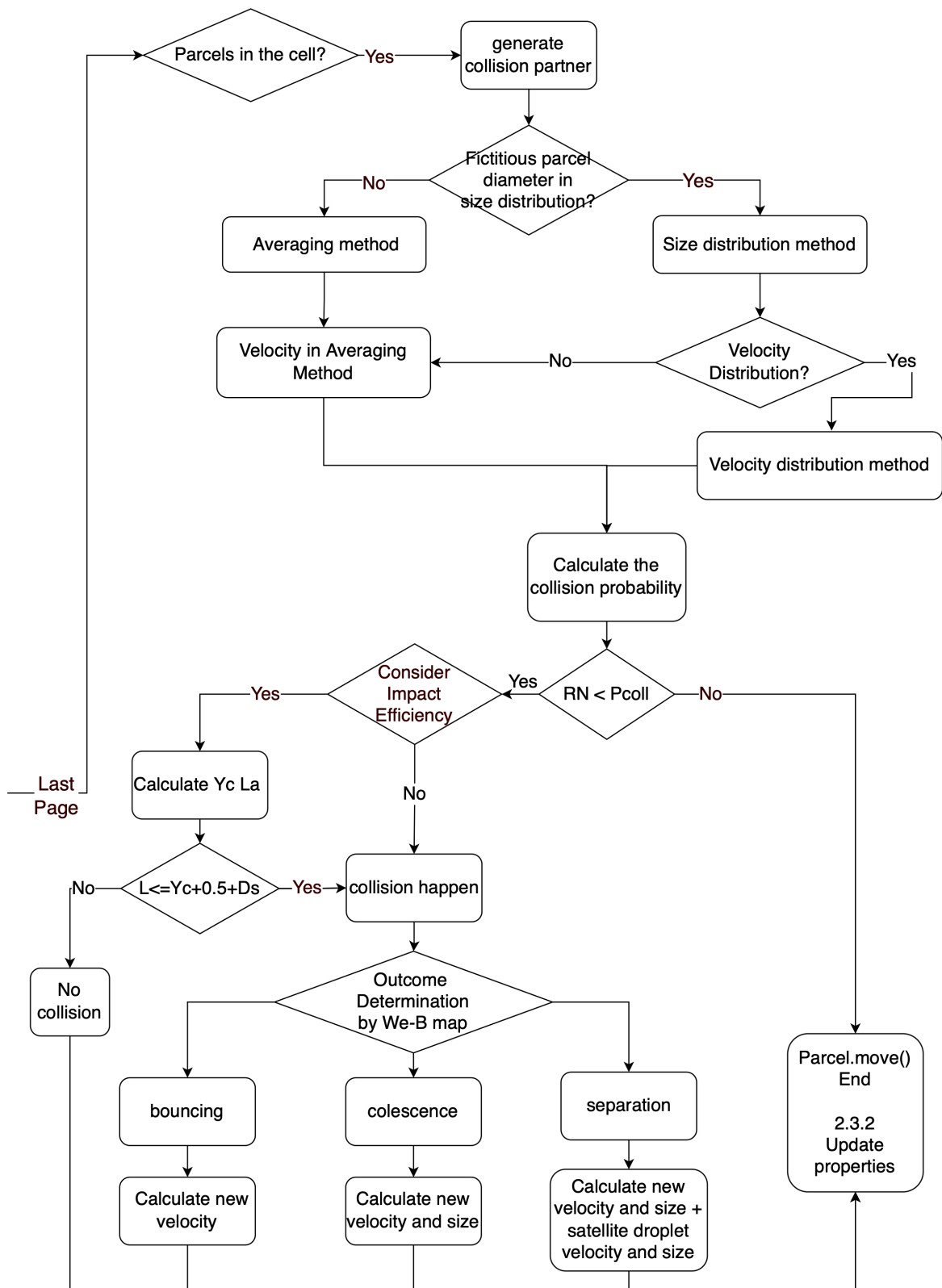(part1)

Figure 5.9: The general flow chart of Euler/Lagrange simulation process in OpenFOAM®
(part2)

Chapter 6

Verification of Euler/Lagrange Approach

This chapter thoroughly discusses the numerical simulation and analysis of the spray using thenumerical methods explained in detail in the Chapter 5. The chapter begins by introducing the geometry and mesh, followed by the setup of the numerical method. Finally, the simulation results are presented and compared to the experimental data.

6.1 Case of Ruger et al. (2000)

The experimental setup, as presented by Ruger et al. (2000), employed a 45-degree hollow-cone nozzle located at the top-centre of a 400 mm diameter pipe, with a test section length of 1 m, as shown in Figure 6.1. A suction blower generated a low-velocity, homogenised airflow within the pipe, assisted by a honeycomb positioned above the nozzle. The nozzle operated at a water flow rate of 0.135 L/min. To determine the air velocity and droplet size distribution, alongside the droplet size-velocity correlation, a two-component phase Doppler anemometer (PDA) was positioned 25 mm downstream of the nozzle outlet, where the primary break-up of liquid was completed, eliminating the need for a complex primary breakup model. Local droplet size distributions and size-velocity correlations were obtained as injection rings at 1 mm intervals from r = 0 mm to r = 30 mm from the centre. Hence, in addition to the droplet size distribution, size-velocity correlations of axial and radial components served as the inlet condition for the Lagrangian phase. The mean component of tangential velocity was zero. Furthermore, droplets with diameters less than 2.5 μm acted as tracer particles to measure gas velocity and turbulence kinetic energy in the measurement plane. Figure 6.2 illustrates the 3D numerical grid used in the simulation process. The structured O-grid employed in the simulation process was separated into three blocks, extending from the inlet plane, 25 mm downstream of the nozzle, to the outlet plane, 1025 mm downstream of the nozzle exit, with a total of 700,000 control volumes. To determine the injection zone, the grid underwent considerable refinement.

6.2 Boundary condition

Inlet: For the velocity of the gas inlet, the inlet boundary conditions is specified by experimental data with the provided measured velocity profile. The boundary condition for the pressure is defined as zeroGradient. The boundary condition for the turbulent kinetic energy of the gas phase comes from the OpenFOAM® 8 turbulentIntensityKineticEnergyInlet. It is based on the turbulence intensity that the user supplies, which is defined as Eq. 6.1.
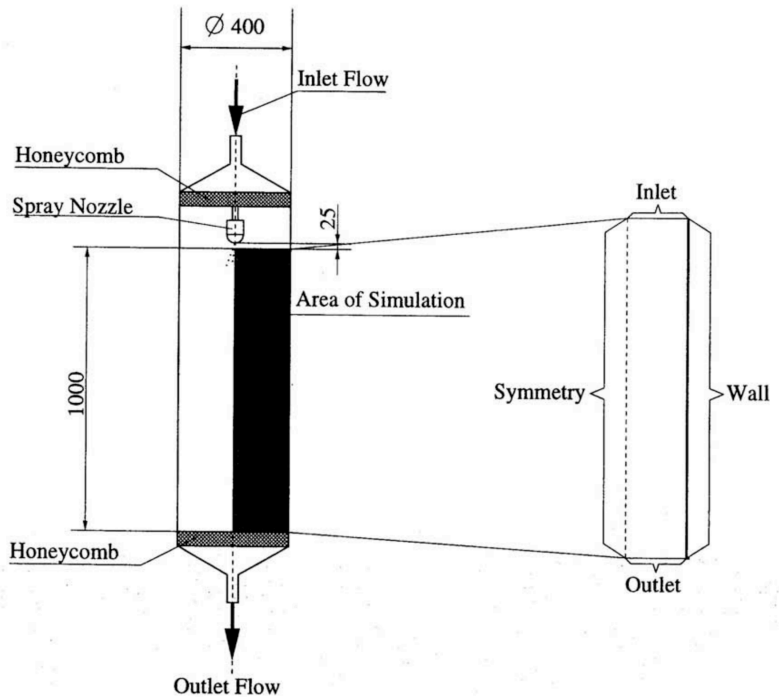
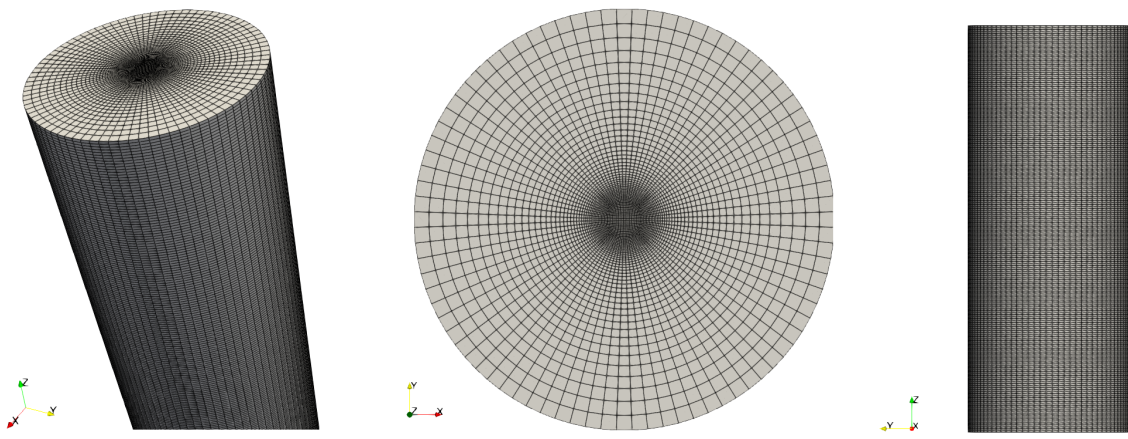Figure 6.1: Experimental facility in the case of the spray of Ruger et al. (2000).

Figure 6.2: The numerical grid of the verification case from Ruger et al. (2000)

$$k = \frac{3}{2} \left(I \left| u \right| \right)^2 \tag{6.1}$$

The local velocity of the inlet is represented by u, while k symbolises the turbulent kinetic energy, with the turbulence intensity set to 0.15, denoted as I. As illustrated in Figure 6.3, the difference between the turbulent kinetic energy of the gas phase, as obtained from the RMS values of the two components under the assumption that $v'^2 = w'^2$, and the specified boundary condition is negligible.

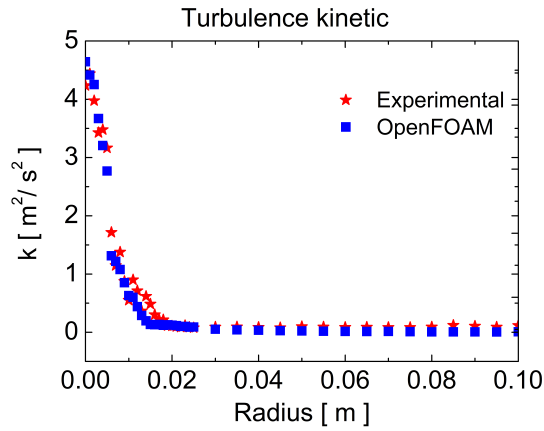$$k_{exp} = \frac{1}{2}(u'^2 + v'^2 + w'^2) = \frac{1}{2}(u'^2 + 2v'^2) \tag{6.2}$$

Figure 6.3: The comparison of different turbulence kinetic energy different model between Ruger et al. (2000) and OpenFOAM® 8.

At the inlet, the boundary condition for ε is set as turbulentMixingLengthDissipation-RateInlet, as specified in Eq. 6.3 and supported by the original OpenFOAM® 8 boundary condition, where C_μ is the constant parameter from $k - \varepsilon$ model, which is 0.09 and L is the characteristic length scale as the nozzle diameter 5×10^{-4} as provided in the Ruger et al. (2000).

$$\varepsilon = \frac{C_\mu^{0.75} k^{1.5}}{L} \tag{6.3}$$

Outlet: The gas outlet boundary condition for velocity, k, and ε is defined as InletOutlet in OpenFOAM® 8. The pressure boundary condition for the outlet uses the totalpressure as shown in Eq. 6.4, where p is the pressure at boundary, p_0 is the total pressure.

$$p = p_0 - 0.5\rho u^2 \tag{6.4}$$

Walls: Wall has a no-slip boundary condition for the velocity and zeroGradient for the pressure. The ε boundary condition is set using epsilonWallFunction, while kqRWallFunction is employed for the k.

6.3 Lagrangian phase setup

Euler/Lagrange spray simulations consider droplets as parcels, which are collections of particles(real droplet) having the same properties such as diameter and velocity. The exploitation of parcels reduces computational expenses. Following, the Lagrangian phase settings for parcel injection are described below:

- Parcel injection begins when the flow field without Lagrangian phases reaches a sufficiently developed state that permits stable solutions using the initial condition.

- Afterwards, a defining number of individual parcels are introduced using an injection model based on droplet size distribution and size-velocity correlations as established by experiments. The injection model follows these steps:

  - Experimental measurements provide droplet size distributions in the range of $0 - 160\mu m$ at a resolution of 32 size classes, along with the mean and fluctuating velocities of droplets corresponding to each size class.

  - To determine the diameter of the injected parcel, it is randomly selected from the provided droplet size distribution profile.

  - After selecting the droplet size, the droplet mean and root-mean-square (RMS) velocities are decided based on the size-(RMS)velocity correlations.

  - Afterwards, the instantaneous parcel velocity is calculated as the sum of mean velocity and RMS velocity multiplied by a Gaussian distributed random number with 0 mean and 1 variance.

  - The number of parcels to be injected in each injection ring (31 measurement rings in the PDA) is calculated from the mass flow rate using experimental results. Initially, each parcel represents three particles. At the end of the calculation, there are 9.3 million parcels in the field. During the simulation, 22 million parcels are injected every second.

- After the parcels have been injected into the computational domain, they are tracked as they pass through the flow field. The interactions between parcels and the flow field are done by the coupling through the source terms, which are sampled for each Euler time step as described in the section 5.2.4.

- In the meantime, the interactions between parcels were also considered, which is binary droplet collision by the fully stochastic collision method proposed by Sommerfeld (2001).

Chapter 5 has described all the related models. Section 5.2.1 explains the drag model, section 5.2.3 discusses the particle turbulence dispersion model, and section 5.2.4 describes the coupling method. Additionally, the section 5.3 presents the fully stochastic collision model, and the determination of collision outcomes is explained in section 5.3.3. The collision outcomes of stretching and reflexive separation are considered with satellite droplet generation as described. The boundary line models applied in the collision maps are the bouncing boundary line model of Estrade et al. (1999), the coalescence and stretching separation boundary line model of

Ashgriz and Poo (1990) and its reflexive separation boundary line model. The other models were not considered as they have their own limitations.

6.4 Results and discussion

6.4.1 Global behaviour

The mass flux profiles at heights of 50, 100, and 200 mm below the injection plane are shown in Figure 6.4. Agreement between simulation and experiment is evident. A typical hollow cone spray shows a droplet mass flux profile presenting a local minimum in the core region and two maxima at the edges. The droplets' air entrainment from the edges of the spray towards the core region increases the droplet mass flux, thereby increasing flow in the core region. As the spray approaches the centre, the number of droplets grows, with the maximum appearing downstream of the nozzle exit in the core region, as shown in Figure 6.5.
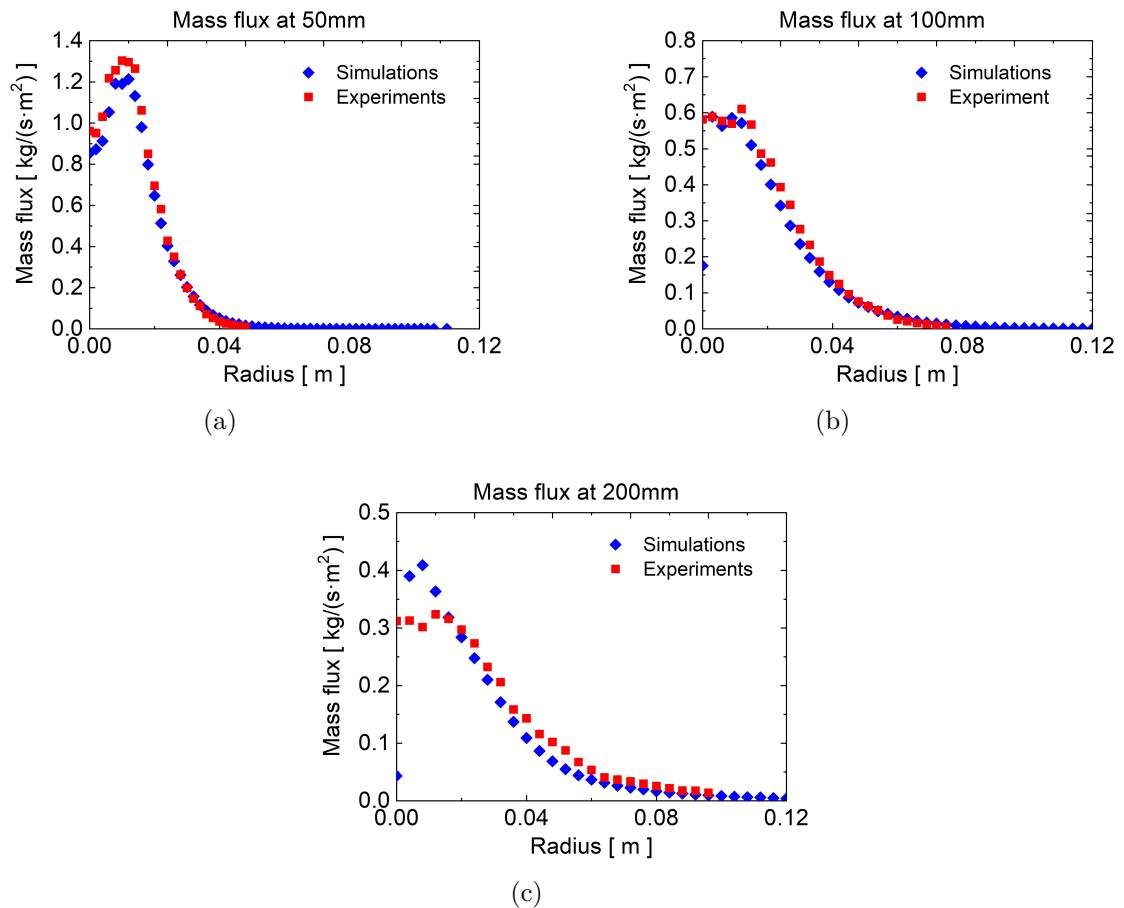

(a)

(b)

(c)

Figure 6.4: The comparison of the mass flux in experiment and simulation (red square: experimental result of Ruger et al. (2000); blue diamond: simulation result).

Ruger et al. (2000) and Laín and Sommerfeld (2020) present research that highlights the significant influence of droplet collisions on the characteristics of spray. The Sauter Mean Diameter (d_{32}) profiles evaluated and calculated along the spray testify to this effect. Without droplet collision considerations, numerical calculations show that d_{32} stays nearly constant
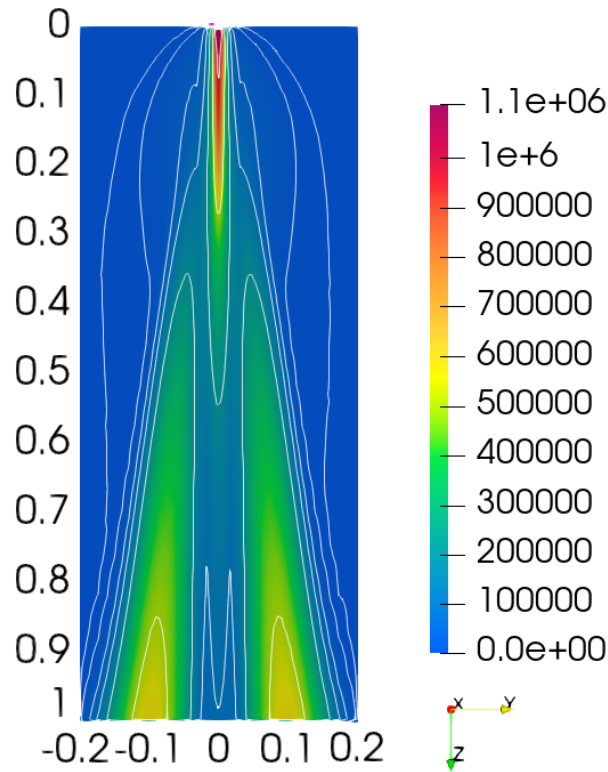
Figure 6.5: Contour of the droplet distribution at cross-section.

along the spray (Ruger et al. (2000)). However, the method employed to generate collision partners has noticeable implications for d_{32} along the spray, as depicted in Figure 6.6. An in-depth discussion of this topic will follow in this chapter.

Figures 6.7 to 6.8 illustrate the axial and radial averaged velocity profiles of the droplets, and the corresponding velocity fluctuations expressed by the RMS velocity of the droplets. The velocity profiles are determined by averaging over the collected droplets, which locate at z = 50 mm, 100 mm and 200 mm below the measurement plane. Most droplets experience high axial velocity close to the nozzle's centre, which drops abruptly with growing measurement radius before reaching a stable zone. Afterwards, the axial velocities decrease slowly. The axial RMS velocity of droplets also follows a similar pattern; it rises sharply to reach a maximum velocity and then drops continuously. While $r > 100$ mm, it fluctuates due to insufficient data samples. The average radial velocity and its RMS velocity continue to increase until $r = 50$ mm, and then both decrease. At $z = 100$ mm, the axial mean velocity considerably decreases in comparison to $z = 50$ mm. The stability zone expands from $r = 15$ - 35 mm to $r = 20$ - 60 mm, with a significant drop in droplet velocity from 6.5 m/s to 3.5 m/s. The spray widens at $r = 100$ mm. Compared to the experimental results, the axial RMS velocity is lower in the middle region of the spray, and the radial and RMS velocities at $z = 100$ mm are relatively consistent with the experimental results. Nonetheless, at the far-field measurement plane ($z = 200$ mm), the axial mean velocity profile overestimates in the central region, whereas underestimating in the spray edge region. Within $r = 50$ mm, the axial RMS velocity is under predicted, then it becomes over-predicted for $r > 50$ mm. The radial velocities are significantly underestimated, whereas they are overestimated beyond $r = 80$ mm In the centre region. The
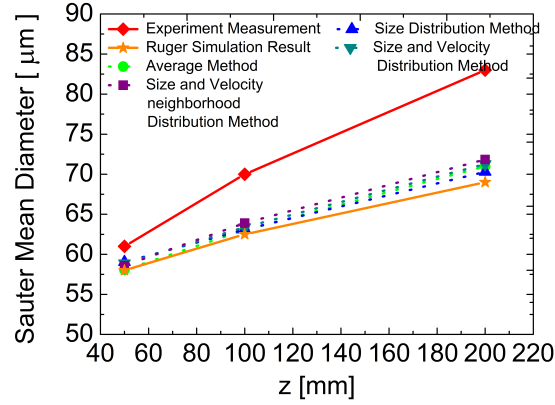
Figure 6.6: Sauter Mean Diameter d_{32} at the cross-section (Red diamond: experiment result of Ruger et al. (2000); Orange star: simulation result of Ruger et al. (2000); Green circle: simulation result of using the Average Method for the fictitious parcel; Blue up triangle: simulation result of using the Size Distribution Method for the fictitious parcel; Green down triangle: simulation result of using the Size and Velocity Distribution Method for the fictitious parcel; Purple square: simulation result of using Size and Velocity Distribution neighbourhood Method for fictitious parcel).

radial RMS velocity aligns well with the experimental data at the centre and falls below it before exceeding it after $r = 60$ mm.

In summary, the simulations yield precise droplet axial and radial average and RMS velociy at $z = 50$ mm and $z = 100$ mm planes but fail at $z = 200$ mm, which could be attributed to the turbulence model, as discussed in Ruger et al. (2000).

Figures 6.9 and 6.10 display the mean gas velocity in the axial and radial directions, as well as the turbulence kinematic energy, respectively. The mean gas velocity in the axial direction is accurately predicted in all three measurement planes. However, the radial mean gas velocity results from the experiment and simulation do not align, which is consistent with Ruger et al. (2000) simulation. The turbulence kinematic energy, calculated using Eq. 6.2 by taking half the sum of the variances of the velocity components, is consistent with the experimental results at the $z = 50$ mm plane of measurement, but slightly lower than the experimental results at the $z = 200$ mm plane.

Figure 6.11 displays the droplet size distribution throughout the measurement planes below the injection plane, at $z = 50$ mm, 100 mm, and 200 mm. The experiment and simulation show excellent agreement at $z = 50$ mm and 100 mm, with a slight overestimation of droplet size at $z = 200$ mm. This could be attributed to the underestimation of radial diffusion of the spray, as evidenced in Figures 6.8e and 6.8f. In hollow cone sprays, the central region has a narrow droplet size distribution, while the outer perimeter of the spray has a wider distribution of larger droplets. The smallest droplets are located in the centre of the spray, and the average droplet size increases towards the outer perimeter. This further supports the idea that the average droplet size gradually increases downstream. The local size distribution of droplets is shown in Figure 6.12.

To gain a more detailed assessment of the spray flow's physical models, examining the local
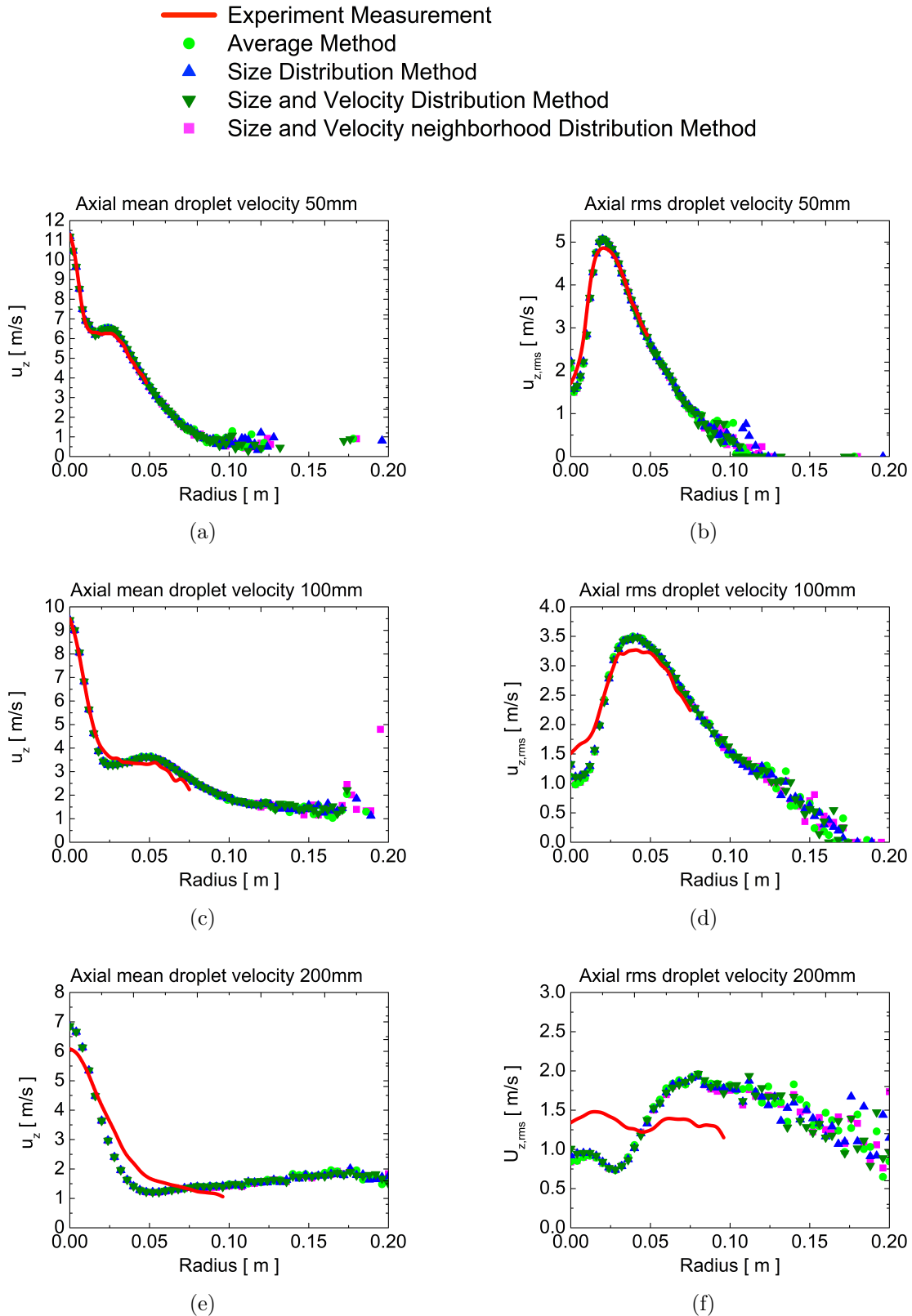
Figure 6.7: The comparison of the droplet velocity profile of u_z and $u_{z,rms}$ in experiment and simulation (red line: the experimental result of Ruger et al. (2000); green circle: simulation result with Average Method in collision model; navy up triangle: simulation result with Size distribution method in collision model; green down triangle: Simulation result with Size and Velocity distribution method in collision model; magenta square: Simulation result with Size and Velocity distribution method in collision model).

Figure 6.8: The comparison of the droplet velocity profile of u_r and $u_{r,rms}$ in experiment and simulation (red line: the experimental result of Ruger et al. (2000); green circle: simulation result with Average Method in collision model; navy up triangle: simulation result with Size distribution method in collision model; green down triangle: Simulation result with Size and Velocity distribution method in collision model; magenta square: Simulation result with Size and Velocity distribution method in collision model).
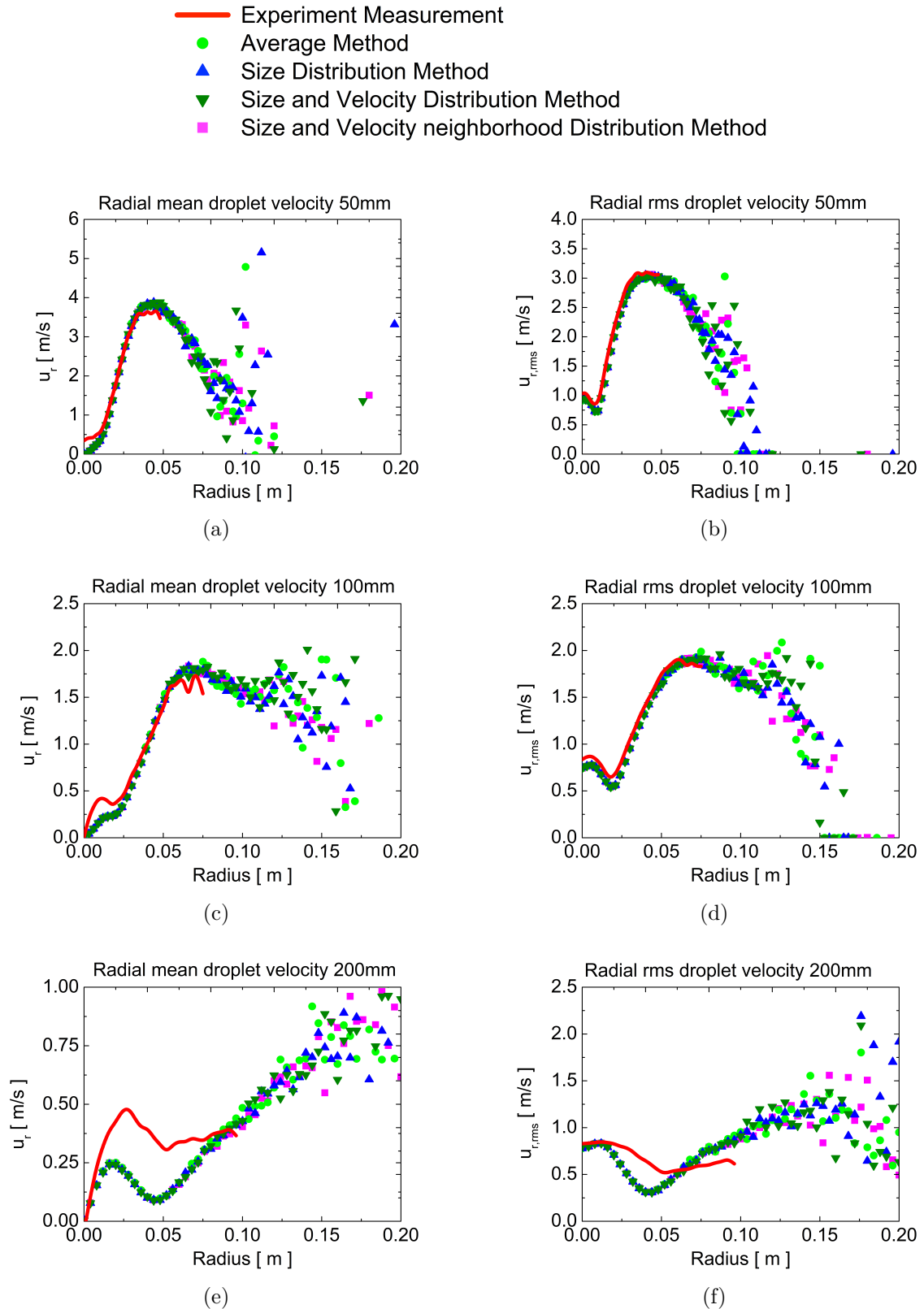
Figure 6.9: The comparison of the gas velocity profile of u_r and u_z in experiment and simulation (red line: the experimental result of Ruger et al. (2000); green circle: simulation result with Average Method in collision model; navy up triangle: simulation result with Size distribution method in collision model; green down triangle: Simulation result with Size and Velocity distribution method in collision model; magenta square: Simulation result with Size and Velocity distribution method in collision model).
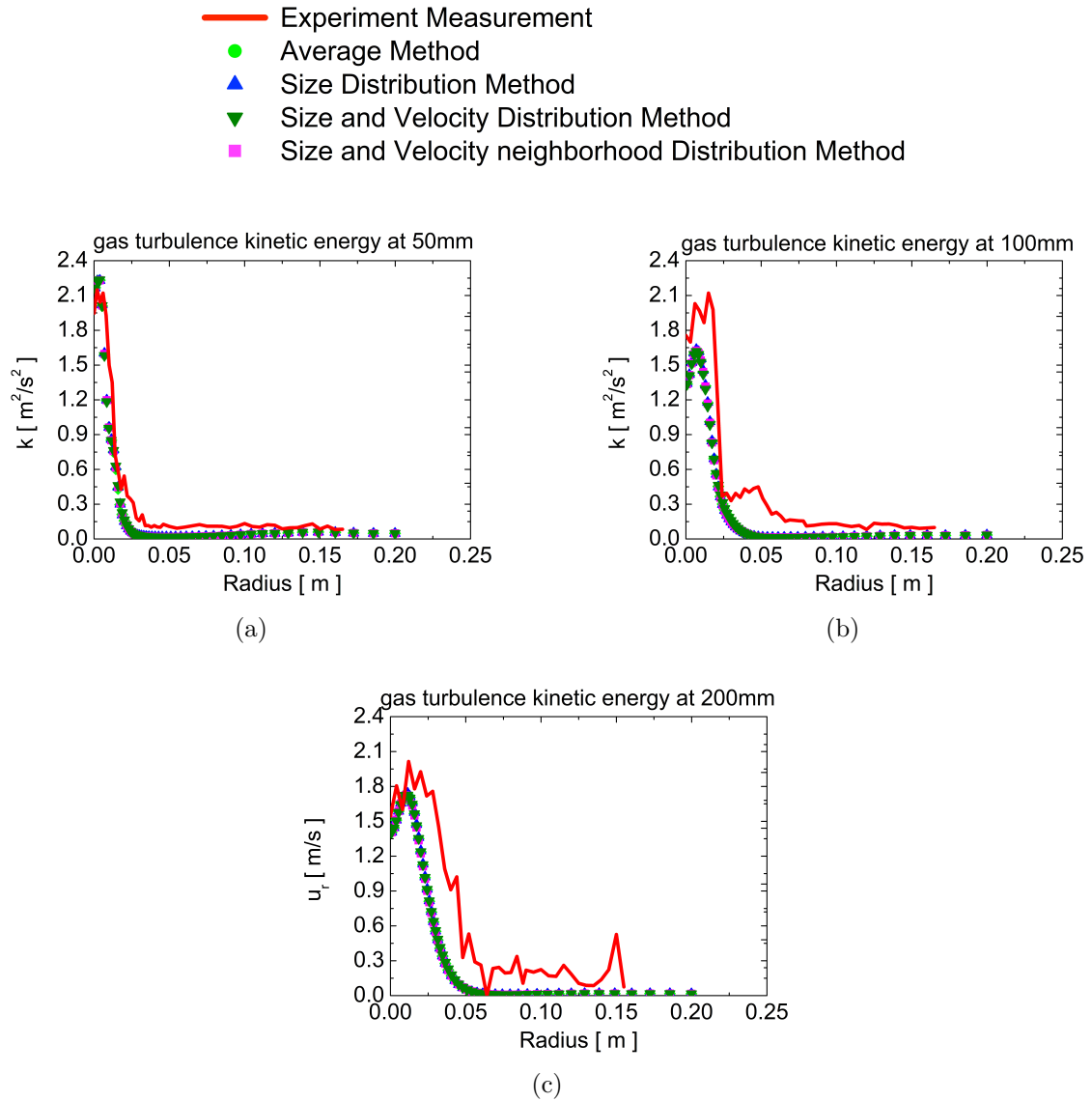
Figure 6.10: The comparison of the gas turbulence kinetic energy profile of k in experiment and simulation (red line: the experimental result of Ruger et al. (2000); green circle: simulation result with Average Method in collision model; navy up triangle: simulation result with Size distribution method in collision model; green down triangle: Simulation result with Size and Velocity distribution method in collision model; magenta square: Simulation result with Size and Velocity distribution method in collision model).
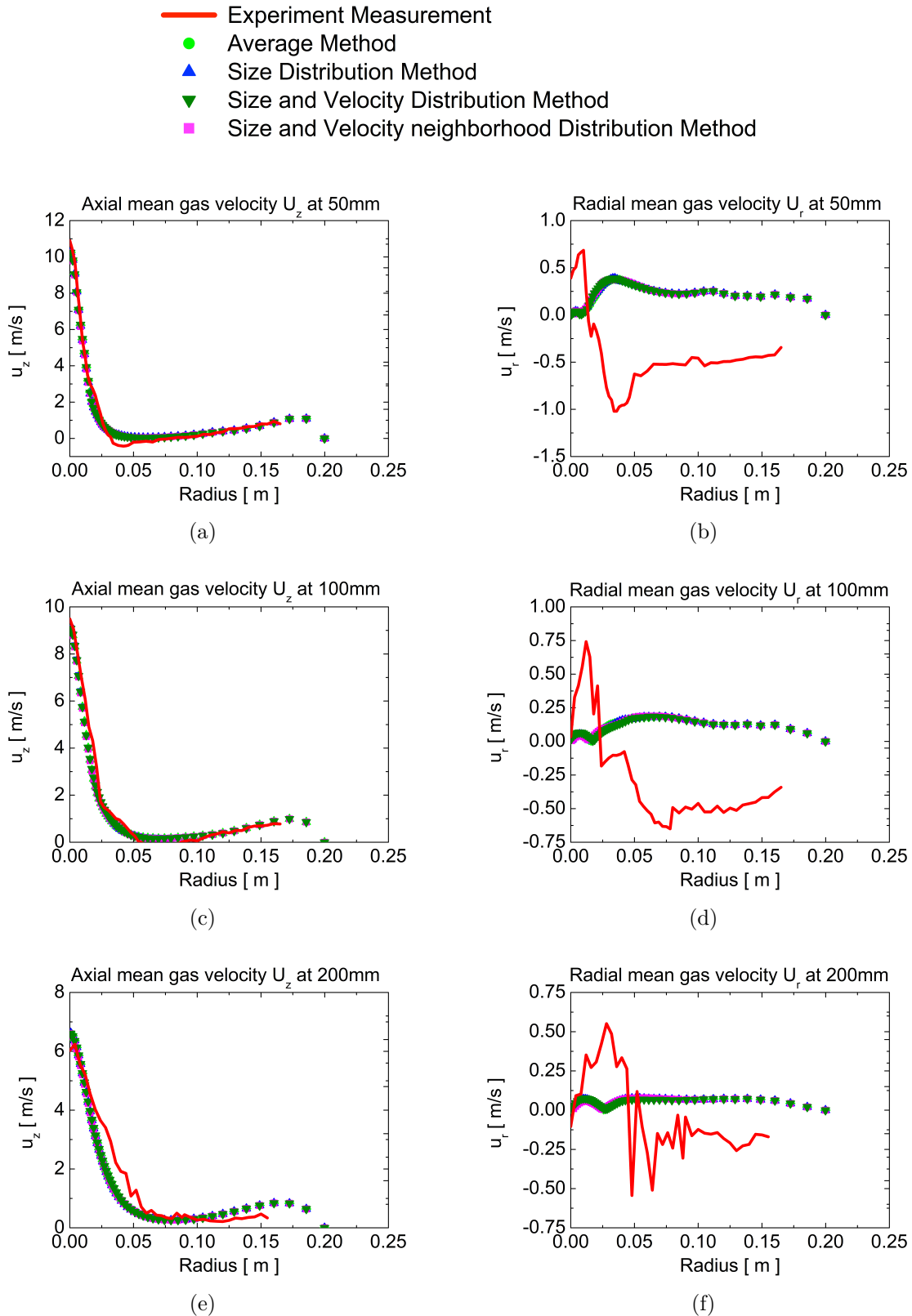
Figure 6.11: The comparison of droplet size profile of d_p in experiment and simulation (red line: the experimental result of Ruger et al. (2000); green circle: simulation result with Average Method in collision model; navy up triangle: simulation result with Size distribution method in collision model; green down triangle: Simulation result with Size and Velocity distribution method in collision model; magenta square: Simulation result with Size and Velocity distribution method in collision model).
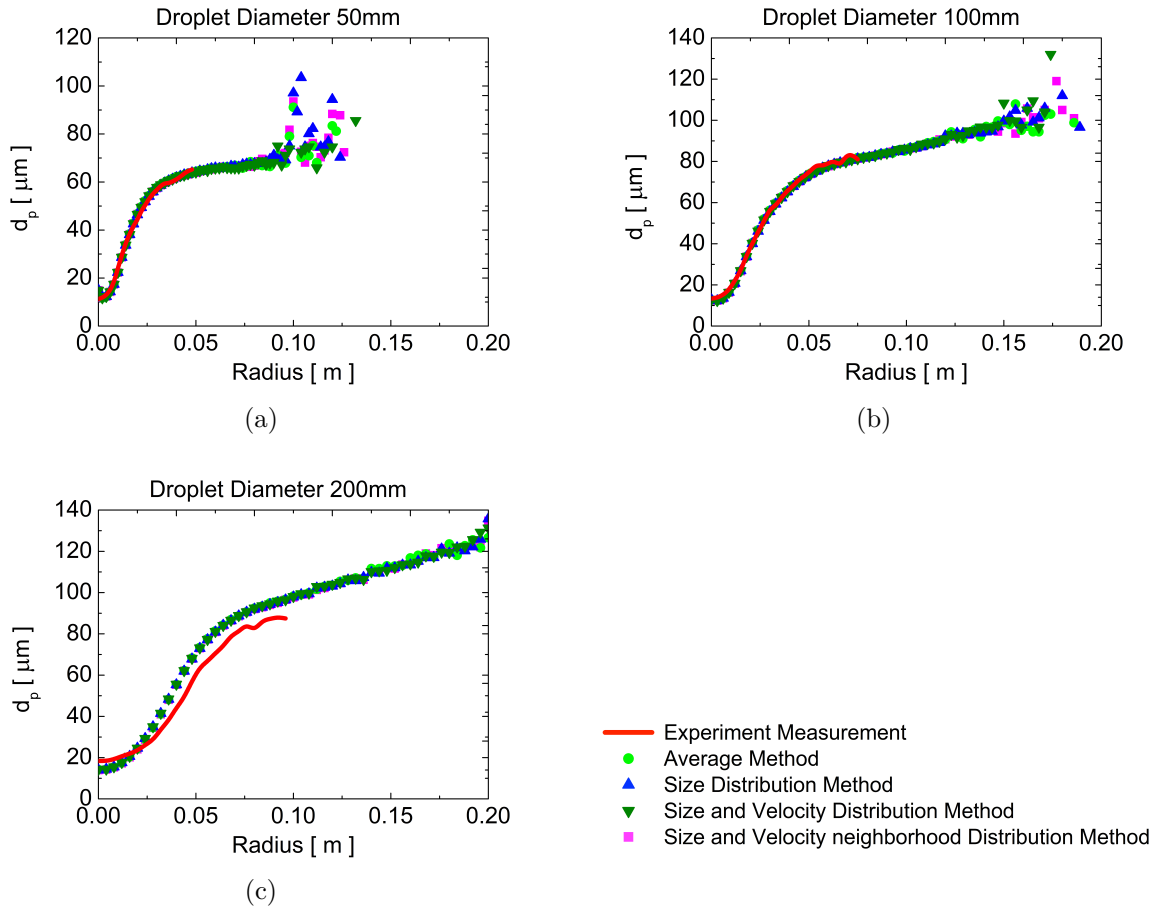
size distributions offers further insight. At the $z = 50$ mm measurement plane, displayed in Figure 6.12a, there is an increase in droplet count in the range of 10 - 35 μm, causing a peak in the droplet size distribution around 20 μm. The simulation results match well with the experimental results for droplets larger than 25 μm, due to the incorporation of stretching and reflexive separation in the collision model. At the $z = 100$ μm plane of measurement, displayed in Figure 6.12b, the PDF peak is located at 20 μm instead of 10 μm, suggesting poor agreement with the experimental results. At the $z = 200$ mm plane of measurement further downstream, the calculated droplet size distributions and the PDA measurements have reasonably good agreement, as shown in Figure 6.12c. A comparison shows that coalescence leads to a slight increase in droplets sized 45 - 100 μm while decreasing the number of droplets in the 20-45 μm range.
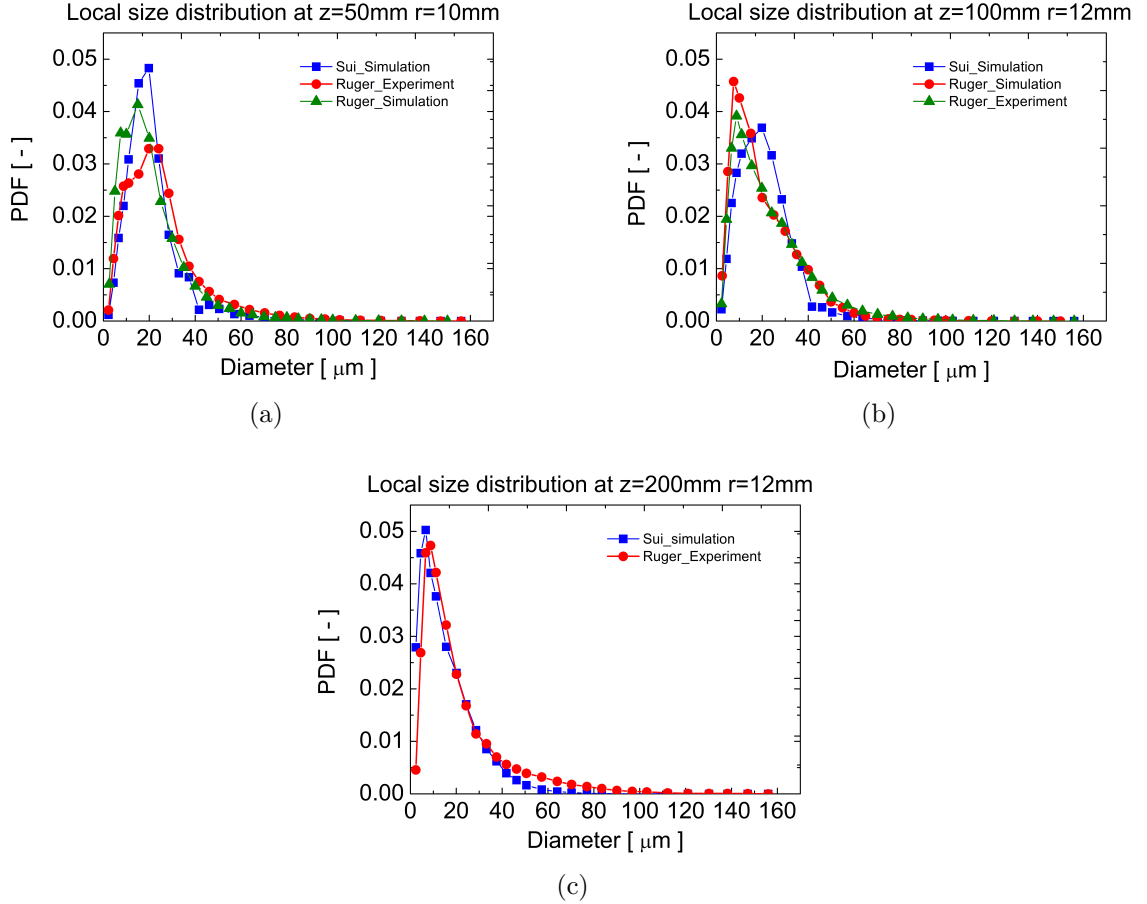
Figure 6.12: The comparison of local size distribution in experiment and simulation (green triangle: simulation result of Ruger et al. (2000); red circle: experiment result of Ruger et al. (2000); blue square: simulation result in this dissertation).

6.4.2 Collision model

Although the spray in the simulation is relatively dilute, droplet collisions still have a significant impact. The main objective of the numerical simulations is to investigate the fully stochastic collision model and the impact of the collision model with previously defined collision maps on the predicted spray. Based on previous studies (See Foissac et al. (2010); Kuschel and Sommerfeld (2013); Qian et al. (1997); Sui et al. (2019)) utilising water as a fundamental template, the collision map is configured. To facilitate the configuration, the boundary lines are classified into three categories: bouncing, coalescence-stretching separation, and reflexive separation. These lines make up a composite, or three-line model, which has been researched in Laín and Sommerfeld (2020) and Sommerfeld et al. (2021b), instead of the single-line model introduced by O'Rourke (1981).

This collision map for water is highly exceptional, as bouncing is only observed for big impact parameters B. The well-known correlation in Eq. 3.8 by Estrade et al. (1999) characterises the bouncing boundary. The boundary between stretching separation and coalescence is significantly better characterised by the Ashgriz and Poo (1990) in Eq. 3.45 than Brazier-Smith et al. (1972) model. The Sommerfeld and Pasternak (2019) correlation (Eq. 3.51) is

superior when evaluating the behaviour with decreasing size ratio till 0.5. It is also observed when $\Delta < 0.5$, this model's deviance is significantly greater than expected. Consequently, this model is excluded from this study. The boundary line for reflexive separation-coalescence is defined using the Ashgriz and Poo (1990) correlation specified in Eq. 3.64, which is the most widely used correlation. Numerous simulations have been conducted with only a single boundary line between coalescence and grazing, where grazing comprises bouncing and separation stretching, primarily utilising the Brazier-Smith et al. (1972) equation (e.g. O'Rourke (1981)). This method, however, completely disregards the observation of reflexive separation for small B and larger We and the satellite droplets produced by the collision.

Figure 6.13 displays the binary droplet collision outcomes considered in this study, including bouncing, coalescence, stretching, and reflexive separation, with collision maps dynamically computed from theoretical boundary lines rather than pre-determined maps. Despite potential minor differences between boundary lines of two collision pairs, neither should result in being identical in theory. When We is large, the boundary lines of stretching separation and reflexive separation may cross. In this study, the upper boundary where reflexive separation occurs is limited to $B = 0.25$. Therefore, if the two intersect at a certain position in the collision maps and $B > 0.25$, the collision outcome is considered to be a stretching separation. Furthermore, as described in the section 5.3, the method to generate fictitious collision partner is very important. Therefore, the primary focus of the coming section is to analyse the effect of different methods used to generate fictitious parcels on the simulation's results. Although coalescence is typically produced by collisions, the different methods generate subtle differences in the fictitious parcels, as shown in Figure 6.15.

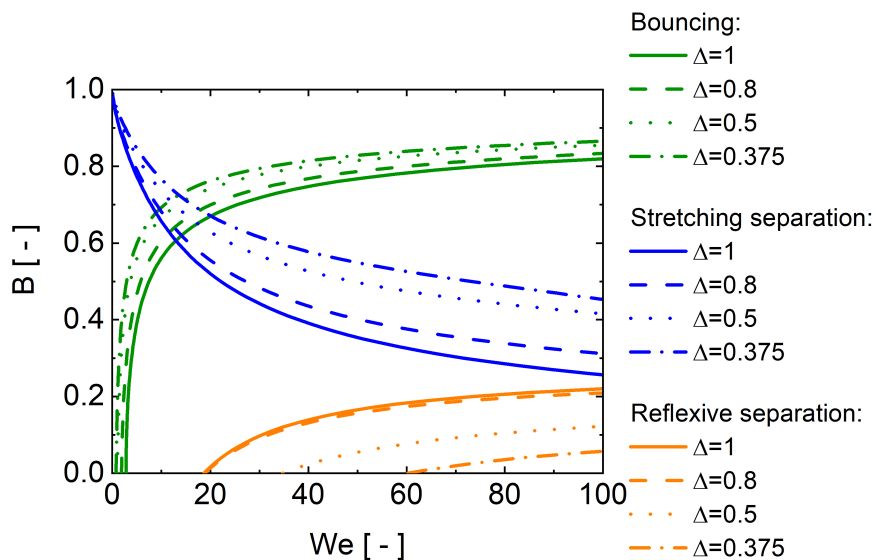Figure 6.13: Examples of collision maps applied in the simulation for all size ratios (green: bouncing boundary line using Estrade et al. (1999); blue: coalescence-stretching separation boundary line using Ashgriz and Poo (1990); orange: reflexive separation boundary line Ashgriz and Poo (1990). Solid line: $\Delta = 1$, dash line: $\Delta = 0.8$, dot line: $\Delta = 0.5$ and dash dot line: $\Delta = 0.375$).

6.4.2.1 The effect of the fictitious parcel generation method

As shown in Figure 6.14a using the **Average Method**, it shows some differences in the size distribution of the real and fictitious parcels. The size distributions of the collision pairs should be the same, as the information from the real small parcels is used to generate the sizes of the fictitious parcels. However, for example, in a local cell using averaging in the fully stochastic collision model, if 90% of the total amount are small parcels and the remaining 10% of the large parcels are randomly distributed, then information on the large parcels in that cell will be omitted, although the fluctuating diameters component would help to reduce the error while calculating the fictitious collision partner. Thus, this approach would produce an over-predicted size distribution in the classes of small diameter and an under-predicted PDF in the classes of big diameter, as shown in Figure 6.14a. Furthermore, as demonstrated in Figure 6.15, it is clear that 99.2% of the droplet collision outcome is coalescence. The bouncing accounts for 0.6% and stretching separation takes 0.2%. In addition, as demonstrated in Figures 6.14b and 6.14c, coalescence occurs throughout the whole computational domain, whereas bouncing and stretching separation occurs close to the inlet up to $z = 400$ mm below the injection plane. And reflexive separation (near head-on collision) is rare and mainly happens close to the injection plane.

By using the **Size Distribution Method**, the size distribution of real and fictitious parcels is almost identical, which makes more sense than the results obtained by the Average Method, as shown in Figure 6.16a. Large droplets can be captured correctly and even very large droplets are not spared. This performance satisfies the requirement that the size distribution of the fictitious particles is the same as the size distribution of the real particles. In this method, coalescence is also the main collision outcome as well. The difference between the Average Method and Size Distribution Method has a very tiny effect on coalescence, resulting in a decrease in the percentage of coalescence from 99.2% to 98.9%. In contrast, the percentage of bouncing increases, from 0.6% to 0.8%. Almost all of the decrease in coalescence translate into an increase in bouncing. The percentages of the stretching and reflexive separation do not change. Both methods use the same approach to calculate the velocity of the fictitious parcels. However, the diameter of the fictitious parcels can be correctly predicted when the method of calculating the size of the fictitious parcel is changed to the Size Distribution Method. This results in droplet collisions that are originally shown as coalescence in the collision maps, changing from coalescence to bouncing due to the change in size ratio. The collision maps previously provided show that the proportion of bouncing increases with increasing size ratio. It is also possible that coalescence is slightly reduced due to impact efficiency while calculating the collision probability, but there is no evidence to prove it. Similar to the collision locations in the Average Method, as shown in Figure 6.16c, the bouncing and stretching separation occurs until $z = 400$ mm below the injection plain, and the reflexive separation occurs until $z = 200$ mm.

In the method of **Size and Velocity Distribution Method**, the size and velocity of the fictitious parcels are generated by the size distribution in the cell and the size - (RMS) velocity correlation. In this method, the size distribution of both real and fictitious parcels is as same as the Size Distribution Method because it is calculated in the same way. And the calculation method for the velocity of fictitious parcels does not affect the size distribution. As for the
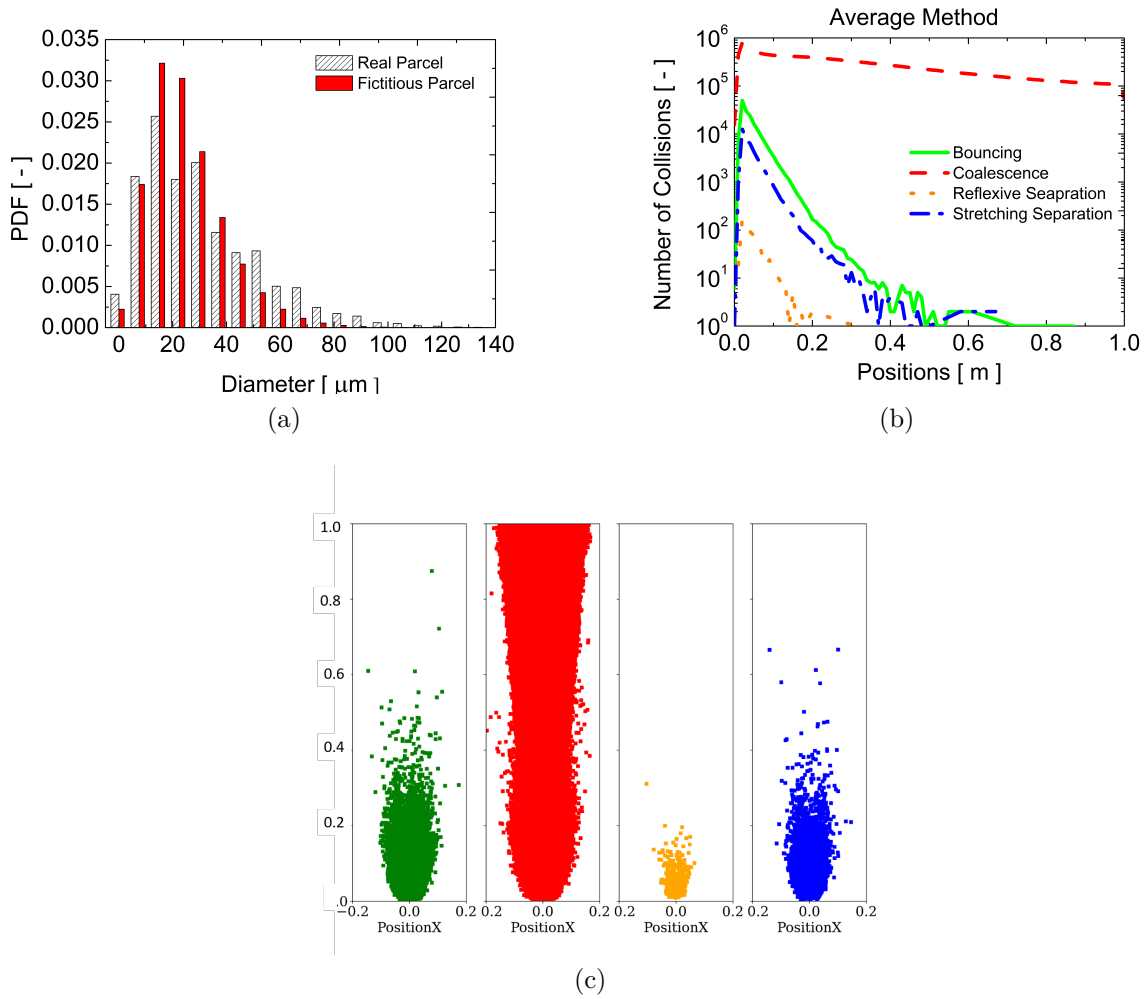
Figure 6.14: General statistic result of Ruger spray by using stochastic collision model with Average Method: (a) The size distribution of real and fictitious parcel; b) The count of collision outcomes along the spray; c) The collision positions in the spray, from left to right, green: bouncing; red: coalescence; orange: reflexive separation; blue: stretching separation).

collision outcomes in Figure 6.15, coalescence is equally dominant, but as the proportion of bouncing and stretching separation increases, the contribution of coalescence decreases from approximately 99% in the first two methods to 96.3%. The reduction in coalescence leads to other collision outcomes getting increasing, some of which translate into bouncing and stretching separation. The different calculation methods of the fictitious parcel increase the probability of bouncing and stretching separation. As shown in Figure 6.17c, the differences between the Averaging Method, Size Distribution Method and Size and Velocity Distribution Method mainly affect the variation of collision locations within the calculated region. In the first two methods, bouncing and stretching separations occur within approximately $z = 400$ mm, however in the Size and Velocity Distribution Method, bouncing and stretching separations occur along the centreline of the spray. Even in the far-field below the injection plain, there are some collisions in the centre of the far-field. For coalescence, the throat, which can be clearly observed in the first two methods, becomes less obvious in this method
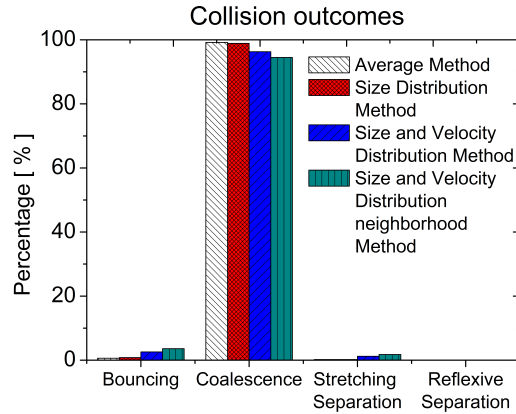
Figure 6.15: Percentage of collision outcomes in different methods (bouncing, coalescence, reflexive separation, stretching separation) a) Average Method: 0.6%, 99.2%, 0.2%, 0% b)Size Distribution Method: 0.8%, 98.9%, 0.2%, 0% c)Size and Velocity Distribution Method: 2.5%, 96.3%, 1.2%, 0% d)Size and Velocity Neighborhood Distribution Method: 3.6%, 94.5%, 1.8%, 0.1%

as more coalescence occurs at the edges of the spray. This is due to the change in calculating the fictitious parcels' velocity. The averaging method uses data for the whole cell, whereas the velocity distribution method uses data for that size class, so the resulting calculation of the fluctuating component is different. In the first two methods, in the far field, all droplets are slowed down to terminal velocity. Since the kinetic energy of the air turbulence is very low at this location, the effect of the turbulence is negligible, so the average velocities of the small parcels are similar. In addition, the RMS velocity between particles in the terminal velocity cell is thus relatively low. Therefore, during the calculation, most collision pairs have similar velocities, which leads to the low collision probabilities described in Eq. 5.28. However, in this approach, the average and fluctuating components required to calculate the instantaneous velocity are determined in a randomly chosen size-velocity as well as size-RMS velocity correlation. As a result, the fluctuations in velocity can be large, leading to more collisions in the far field as well.

The difference between the **Size and Velocity Distribution Neighbourhood Method** and the former is that when a cell contains a small number of parcels or particles, particle information from neighbourhood cells is considered in order to reduce statistical errors due to the small number of samples. If the number of parcels or particles in the cell is less than, for example, 20 in this work, then the information from the particles is obtained from the neighbourhood cells with cell faces connected. If one layer of cells surrounding the core cell still does not satisfy the condition, it is extended to a maximum of four layers surrounding the core cell. The size distribution and size-velocity correlations are established by all selected cells. As seen in Figure 6.18a, the size distributions of the real and fictitious parcels still match well. Like the other methods, coalescence still dominates, but the coalescence keeps dropping to 94.5%. On the other hand, the percentage of bouncing increases to 3.6% and the stretching separation rises to 1.8%. The initial idea of using neighbourhood information is to increase the sample quantity to ensure the statistics are correct in order to better calculate the size and

(a)

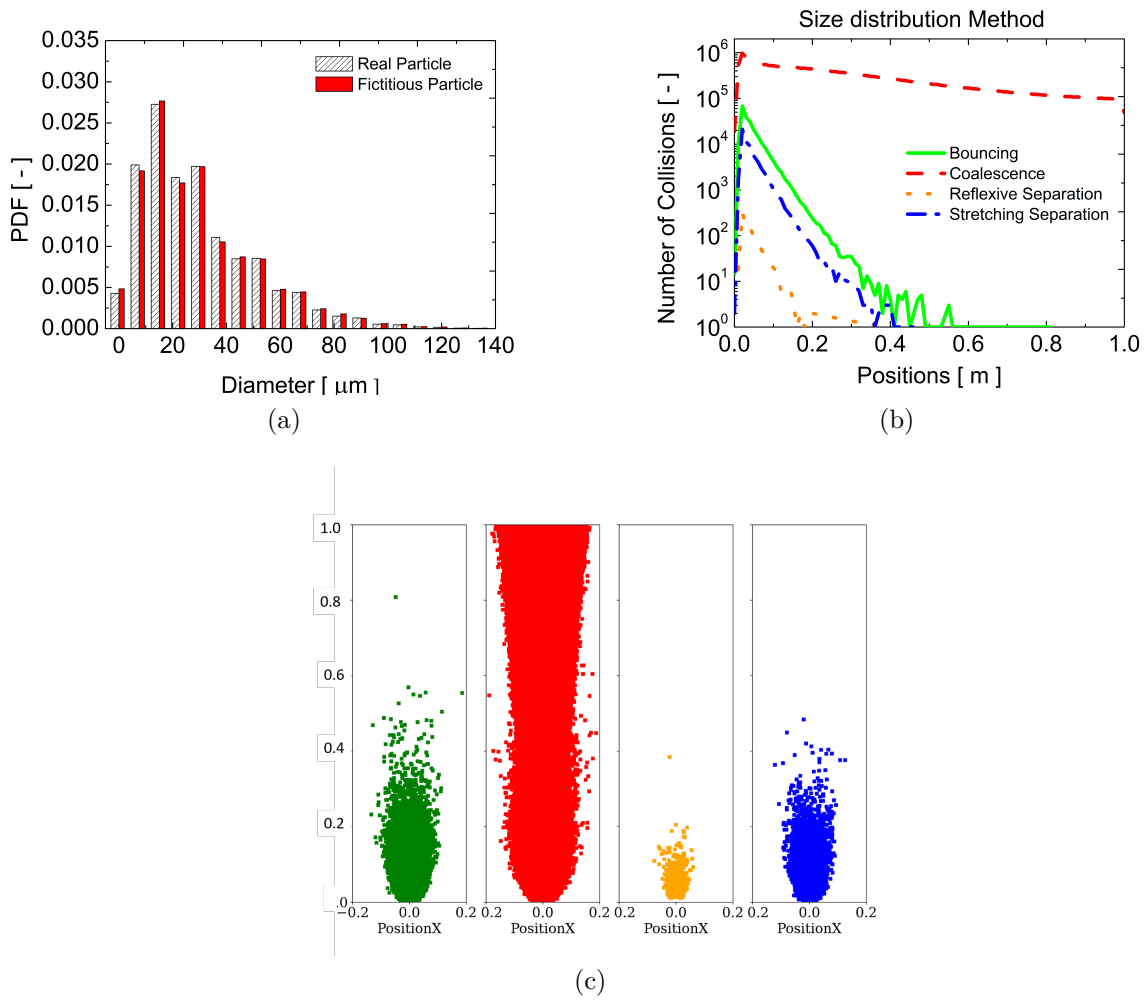(b)

(c)

Figure 6.16: General statistic result of Ruger spray by using stochastic collision model with Size Distribution Method: (a) The size distribution of real and fictitious parcel; b) The count of collision outcomes along the spray; c) The collision positions in the spray, from left to right, green: bouncing; red: coalescence; orange: reflexive separation; blue: stretching separation).
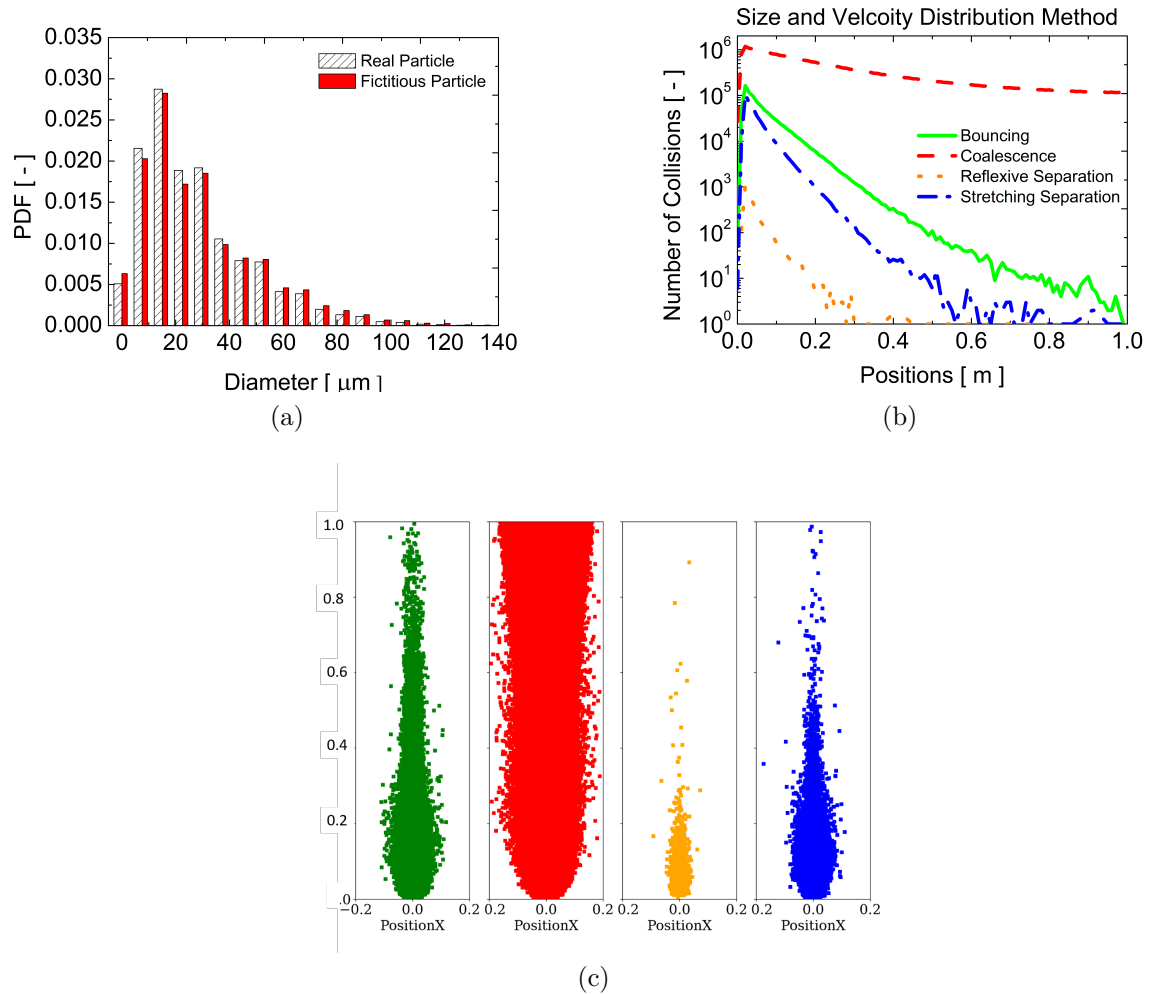
(a)

(b)

(c)

Figure 6.17: General statistic result of Ruger spray by using stochastic collision model with Size and velocity distribution Method: (a) The size distribution of real and fictitious parcel; b) The count of collision outcomes along the spray; c) The collision positions in the spray, from left to right, green: bouncing; red: coalescence; orange: reflexive separation; blue: stretching separation).

velocities of fictitious parcels, particularly at the upper edges of the spray, where there are fewer parcels than in the central region. However, Figure 6.5 shows that the number of parcels in the far-field centre region is similarly low, with both the Size and Velocity Distribution Method and the Size and Velocity Distribution neighbourhood Method increasing the collision probability in this region. In general, however, the increase in the number of collisions in the non-core region does not significantly affect the total number of collisions and their distribution, and the vast majority of collisions remain coalescence.

6.4.2.2 Size ratio distributions

In Figure 6.19, the overall size ratio distribution is depicted, illustrating the size ratio distribution of collision pairs (real and fictitious particles) by number of particles. Figure 6.19a, which employs the Average Method, displays the highest probability of collision occurrence
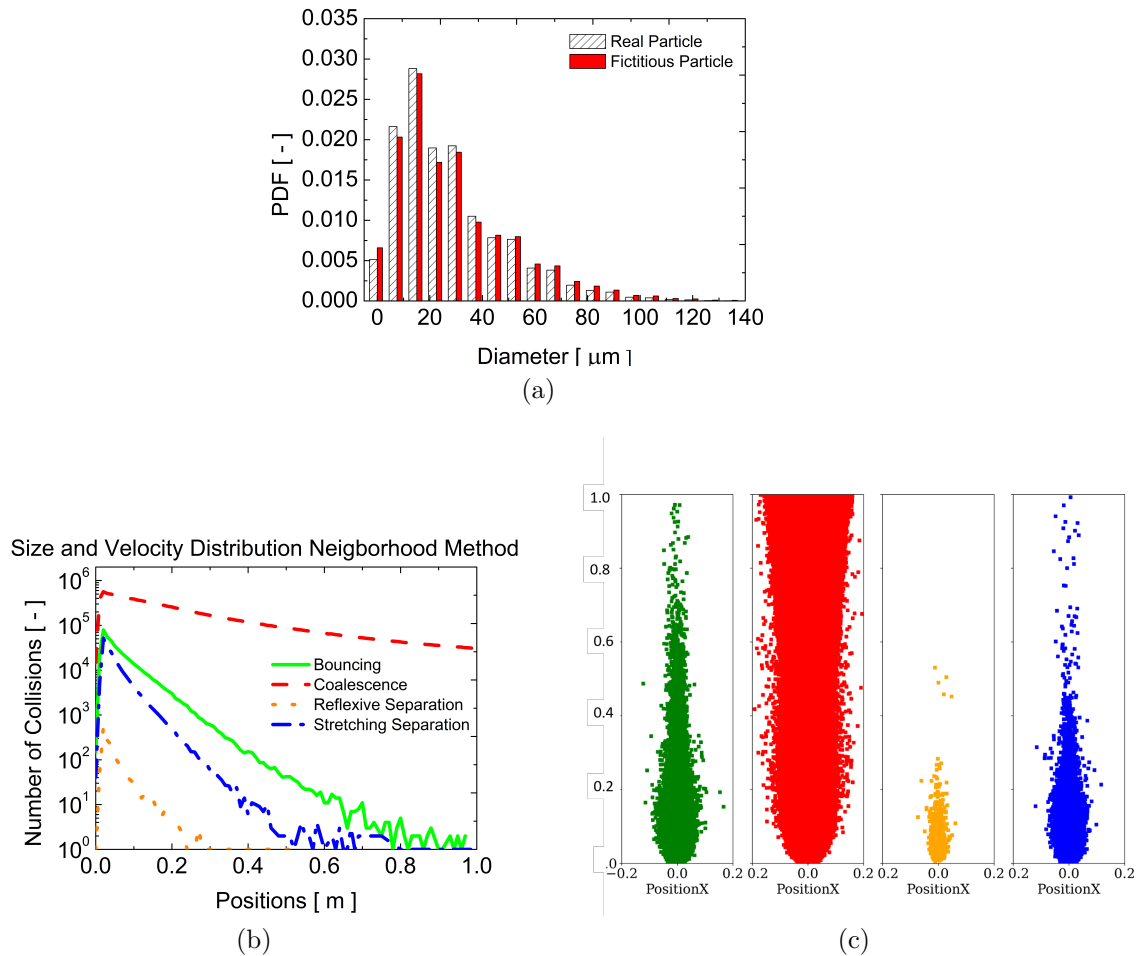
Figure 6.18: General statistic result of Ruger spray by using stochastic collision model with Size and velocity distribution with neighbourhood Method: (a) The size distribution of real and fictitious parcel; b) The count of collision outcomes along the spray; c) The collision positions in the spray, from left to right, green: bouncing; red: coalescence; orange: reflexive separation; blue: stretching separation).

with a higher size ratio near the inlet, where most collisions occur with a high size ratio. At planes $z = 50$ mm and 100 mm, there is a linear increase in the collision probability with a higher size ratio. Conversely, at planes $z = 200$ mm and $z = 300$ mm, there is a peak in the size ratio distribution around $\Delta = 0.45$, indicating that more collisions occur with a smaller size ratio. With the Size Distribution Method, there is also an approximately linear increase in performance at planes $z = 50$ mm and 100 mm, but the overall trend fluctuates slightly. Unlike the Average Method, there is still a clear peak in the size ratio distribution at planes $z = 200$ mm and $z = 300$ mm, with the possibility of the peak moving to $\Delta \approx 0.3$ being 0.0125 (Figure 6.19b). The size ratio distributions in Figures 6.19c and 6.19d are nearly identical for the other two methods, but at planes $z = 50$ mm and $z = 100$ mm, the collision probability is relatively the same for size ratios of 0.4 to 0.9. Then, it decreases for size ratios less than 0.3. However, irrespective of the method used, there are more collisions with smaller size ratios in the far field beneath the injection plane.

The size ratio distribution depicted in Figure 6.20 shows that the Average Method and Size

Distribution Method experience difficulty in detecting bouncing at $z = 200$ mm and $z = 300$ mm planes, therefore pooling no bouncing size ratio distributions for these planes. However, the Size and Velocity Distribution Method and its neighbourhood methods detect much more bouncing, including in the far-field, as demonstrated in Figures 6.17c and 6.18c. Bouncing can be considered noise when coalescence is the dominant collision outcome. Interestingly, the bouncing size ratio distribution in the Size and Velocity Distribution Method and its neighbourhood method reveals that most bouncing occurs at a size ratio of 0.45 at $z = 50$ mm and 100 mm measurement plane. As coalescence is the primary collision outcome, the coalescence size ratio distribution in Figure 6.21 mirrors the overall size ratio distribution in Figure 6.19. The reflexive separation size ratio distributions in Figure 6.22 display messy behaviour due to the scarcity of reflexive separation. At $z = 100$ mm, the size ratio distributions for stretching separation in Figure 6.23 demonstrate slightly noisy behaviour in the Average Method and Size Distribution Method. However, the Average Method exhibits more stretching separation with a large size ratio, whereas the Size Ratio Distribution Method detects more stretching separation with a small size ratio. For the Size and Velocity Distribution Method and its neighbourhood method, most of the stretching separation is observed with a small size ratio, with the peak at around 0.3 in the measurement planes of $z = 50$ mm, 100 mm, and 200 mm.

In summary, collisions with an extremely small size ratio are rare in this spray simulation, in contrast to the findings of Laín and Sommerfeld (2020) that suggested most collisions occurred with a small size ratio around 0.1. This disparity is attributed to the use of the parcel and particle concept in the numerical calculation. The parcel concept reduces the computational effort in spray simulations, leading to collisions occurring primarily when a large parcel collides with a small one. However, in assessing the number of collisions and their properties, counting the number of parcels alone is inadequate. Relevant droplet properties should be evaluated based on real particles rather than parcels, which represent a group of particles. For instance, assuming a situation where the spray is injected under the same mass flow rate, one parcel corresponds to three particles. If the number of particles in a parcel is fixed throughout the spray, the particle and parcel have the same size distribution in the computational domain, which is the most straightforward method. However, in a situation where there are many small droplets, using the parcel concept to reduce the computational effort may lead to one small parcel representing 1000 small particles and one large parcel representing only three big particles, even though both have the same mass flow rate and particle size distribution. In the fully stochastic collision model, the collision probability is based on the concentration of real particles in the cell, but the collision partner will have the same number of particles in the parcel as the real one. Thus, if the parcel and particle size distributions differ, the statistics would be incorrect. Therefore, in the full stochastic collision model, it is essential to compute all statistical results based on the number of particles, rather than the number of parcels.

6.5 Conclusions

In this chapter, the Euler/Lagrange approach is utilised for spray calculations, incorporating four-way coupling, including gas-liquid two-way coupling and droplet collisions. Droplet collisions are implemented via the fully stochastic collision model, which takes into account
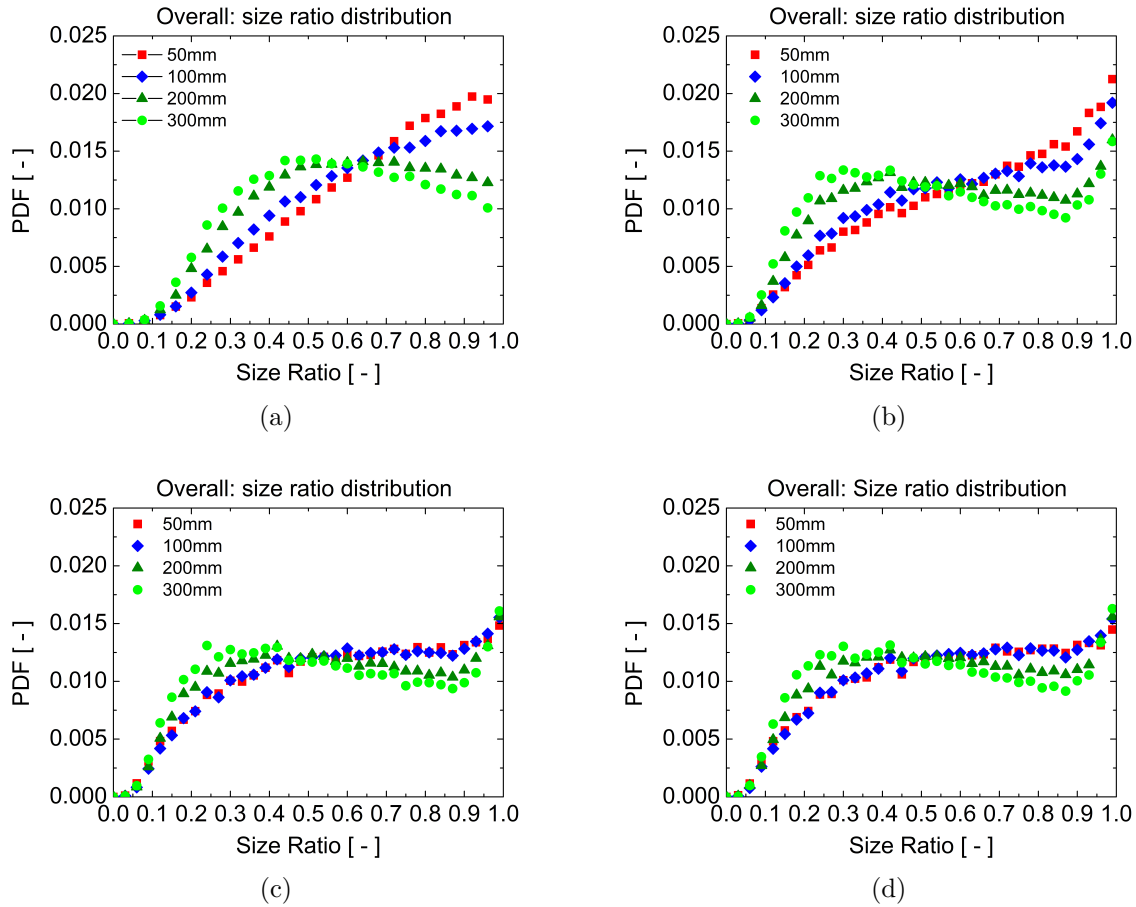
Figure 6.19: The overall collision size ratio distribution along the spray: a) Average Method; b) Size distribution Method; c) Size and velocity distribution Method; d) Size and velocity distribution neighbourhood Method (red square: $z = 50$ mm; blue diamond: $z = 100$ mm; Olive triangle: $z = 200$ mm, green circle: $z = 300$ mm).

all collision outcomes, namely bouncing, coalescence, stretching, and reflexive separation. Detailed experimental data on turbulent sprays are employed as a reference to validate the numerical calculations. PDA measurements provide flow characteristics, such as gas velocity at the measurement planes, droplet size, size-velocity correlation, etc.

This chapter provides a detailed study of various methods for generating coupled indefinite particle properties, such as diameter and velocity. The different methods were found to have no impact on the average profiles of the measurement surface. However, they significantly affect the scaling of the different collision outcomes in the collision model and the location of the collisions. The calculated droplet mass flow rate, droplet mean diameter, droplet velocity, and gas velocity characteristics agree well with the measurement surface of z = 50 mm and 100 mm below the injection plane. Although droplet collisions and coalescence have only a minor effect on the profile of the mean diameter of the droplet number in the relatively dilute spray considered, this effect can be critical for the evolution of the overall Sauter Mean Diameter along the spray.

It has been found that for hollow cone sprays, most collisions occur in hollow cone sprays and size ratios $\Delta > 0.3$ is obtained by weighing the actual number of particles within the

Figure 6.20: The collision size ratio distribution along the spray of bouncing. a) Average Method; b) Size distribution Method; c) Size and velocity distribution Method; d) Size and velocity distribution neighbourhood Method (red square: $z = 50$ mm; blue diamond: $z = 100$ mm; Olive triangle: $z = 200$ mm, green circle: $z = 300$ mm).

parcels. A discussion of the concepts of parcels and particles in Euler/Lagrange simulations shows that the size distribution of parcels is crucial when considering particle-to-particle effects in Euler/Lagrange simulations. The concept of the parcel does help to reduce the computed effort, but at least the size distributions of the parcel and particle should be the same to avoid errors in statistical calculations. All statistical calculations related to post-processing should be particle-based, not parcel-based.
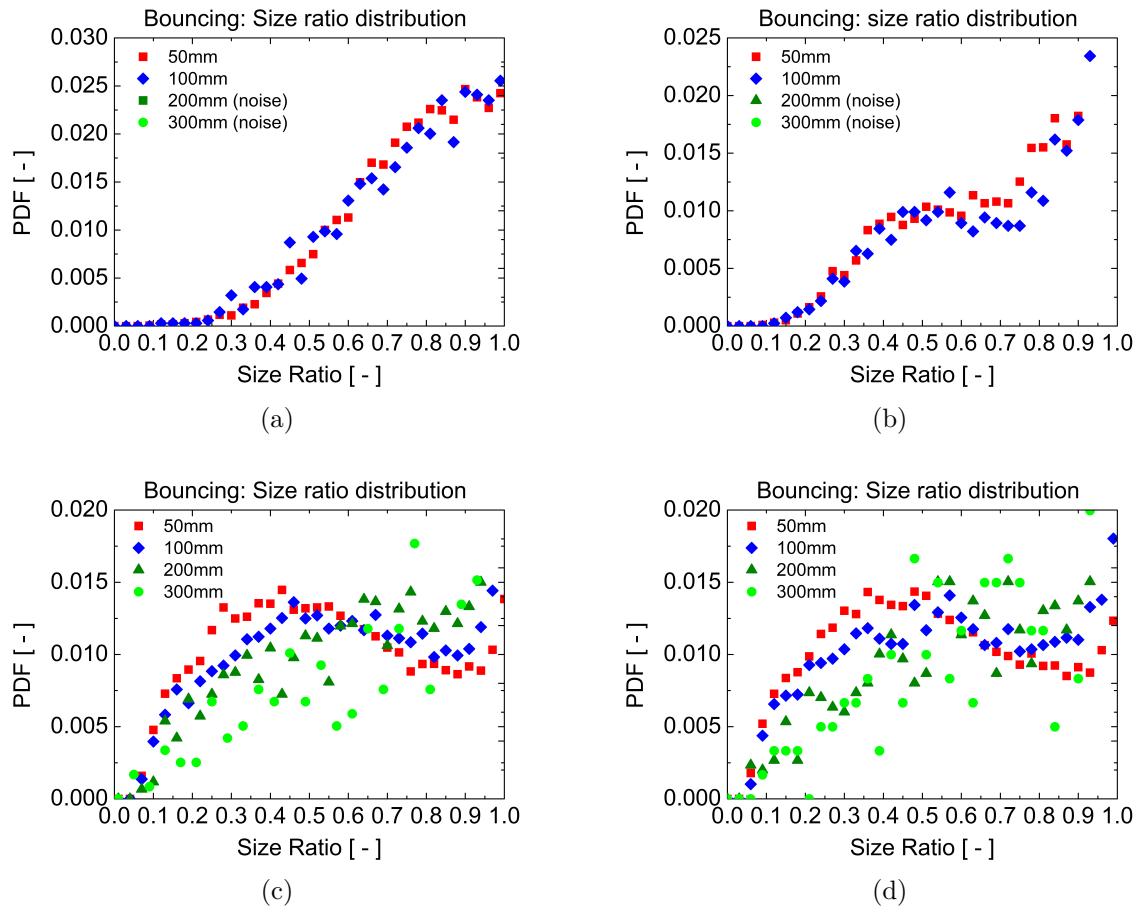
Figure 6.21: The collision size ratio distribution along the spray of coalescence a) Average Method; b) Size distribution Method; c) Size and velocity distribution Method; d) Size and velocity distribution neighbourhood Method (red square: $z = 50$ mm; blue diamond: $z = 100$ mm; Olive triangle: $z = 200$ mm, green circle: $z = 300$ mm).
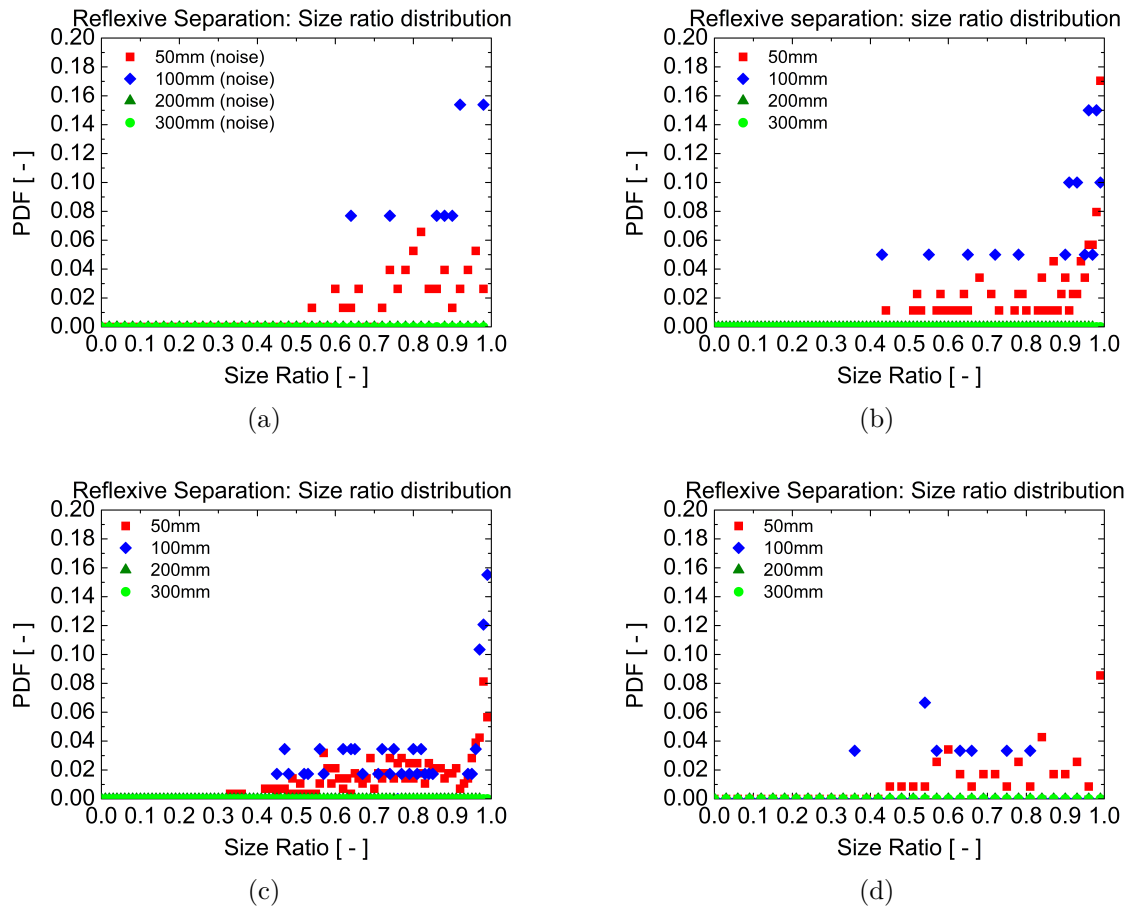
Figure 6.22: The collision size ratio distribution along the spray of reflexive separation. a) Average Method; b) Size distribution Method; c) Size and velocity distribution Method; d) Size and velocity distribution neighbourhood Method (red square: $z = 50$ mm; blue diamond: $z = 100$ mm; Olive triangle: $z = 200$ mm, green circle: $z = 300$ mm).
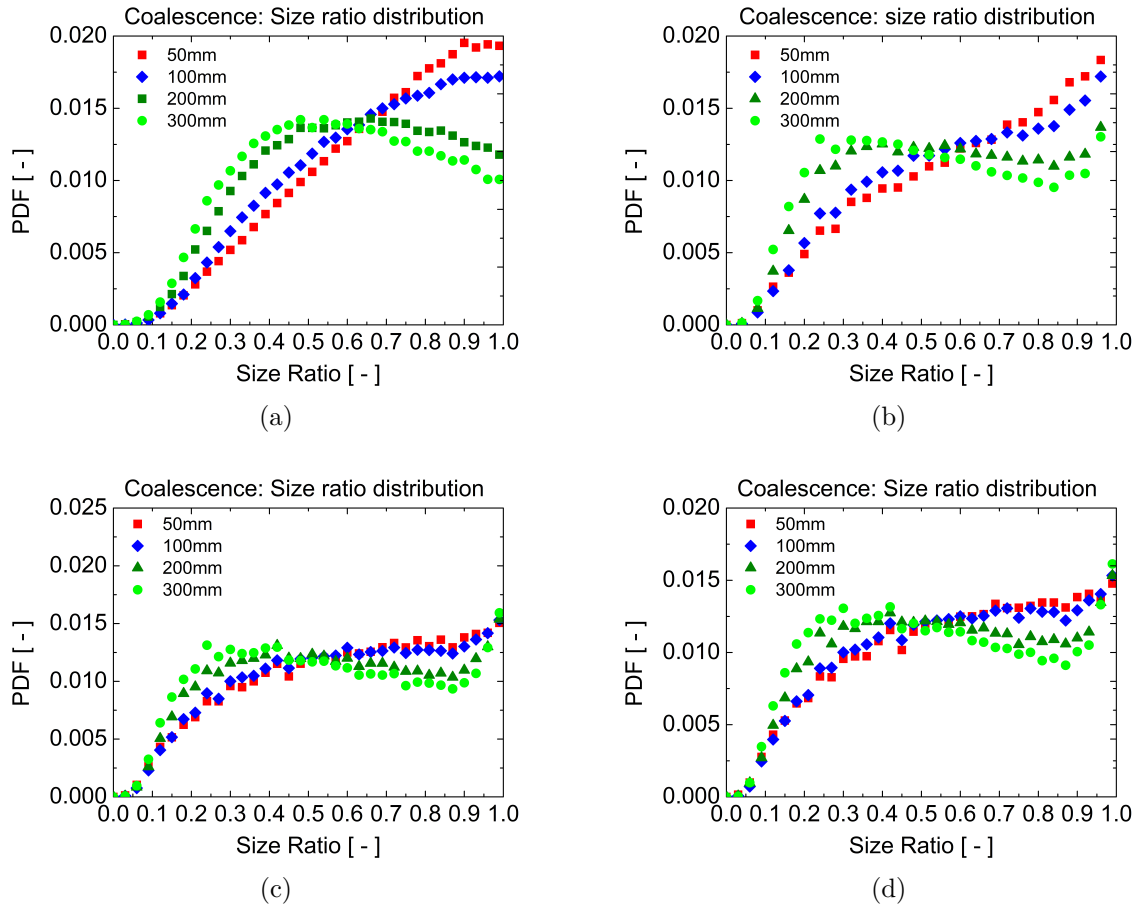
Figure 6.23: The collision size ratio distribution along the spray of stretching separation a) Average Method; b) Size distribution Method; c) Size and velocity distribution Method; d) Size and velocity distribution neighbourhood Method (red square: z = 50 mm; blue diamond: z = 100 mm; Olive triangle: z = 200 mm, green circle: z = 300 mm).
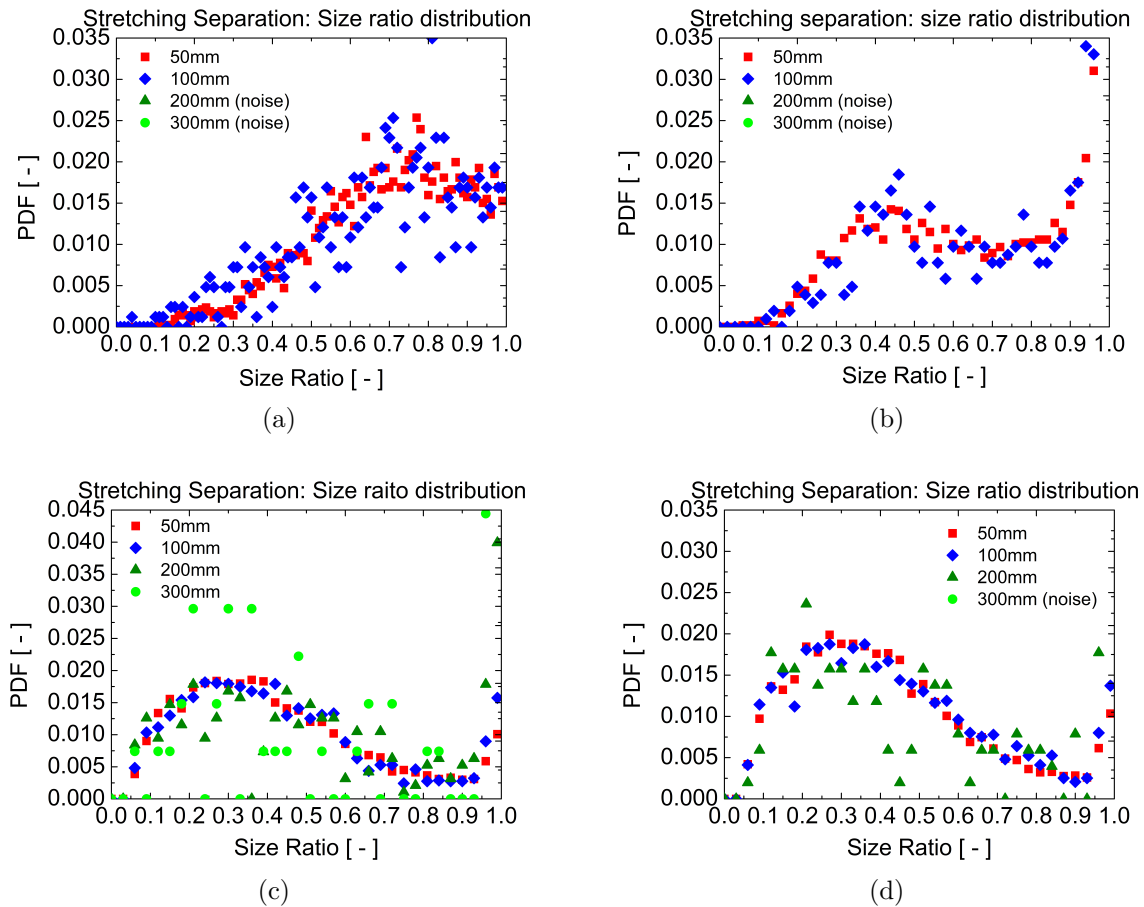
Chapter 7

Validation Spray for Tablet Coating

Following, this chapter presents another Euler/Lagrangian simulation of a spray with high-speed and high turbulence. This spray is designed for tablet coating process and is treated as the validation case of the numerical method described in the former chapters.

7.1 Introduction of the spray

The spray as the validation case was produced by a two-fluid atomizer (model: Schlick 970 S75 ABC), as shown in Figure 7.1, which was used in a tablet coating process (Pasternak and Sommerfeld (2021)). In order to analyse the droplet characteristics inside the spray and the collision of the droplets on the surface of the moving tablet bed, an experimental facility was set up in the institute(see Figure 7.1 left). The nozzle was mounted centrally in the facility without walls around them. The cross-section of the nozzle is shown in Figure 7.1 right. There were two pattern air outlets, a circular outlet for atomised air and another circular outlet for the sprayed liquid. The coating liquid can be controlled by withdrawing the control needle from the nozzle and adjusting the control air pressure. Since there were no tracer particles in the atomised air and the pattern air, they cannot be measured separately to determine the gas velocity. Therefore, the gas velocity can only be derived from instantaneous data for droplets smaller than 2 μm, but the droplet size and velocities encompassed the entire range. In this simulation, the injection liquid is water instead of the HPMC solution.
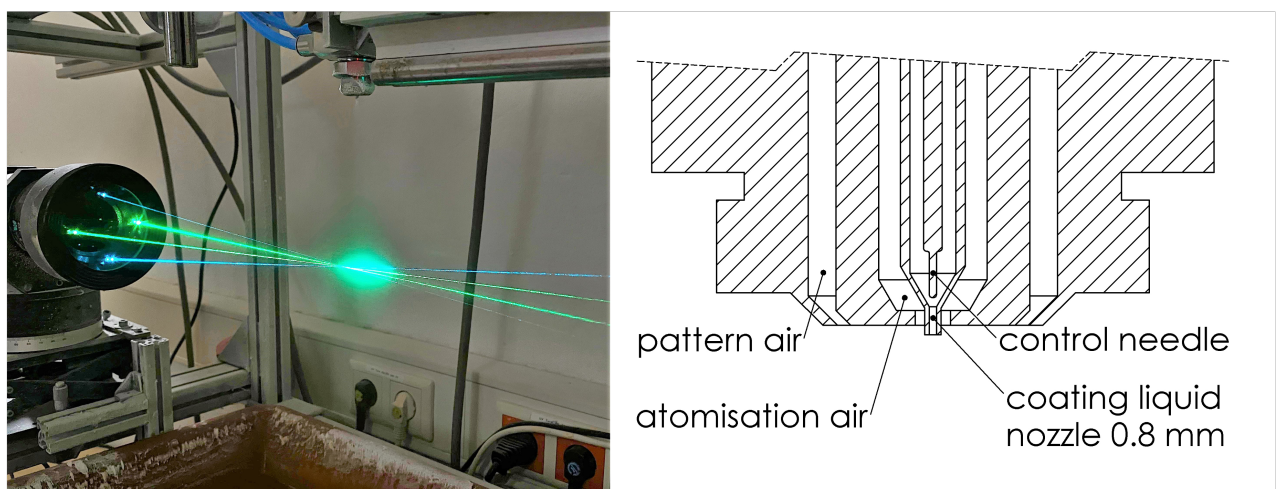
Figure 7.1: (left) The photo of the measurement facility with PDA and Nozzle; (right) The cross-section of the nozzle.
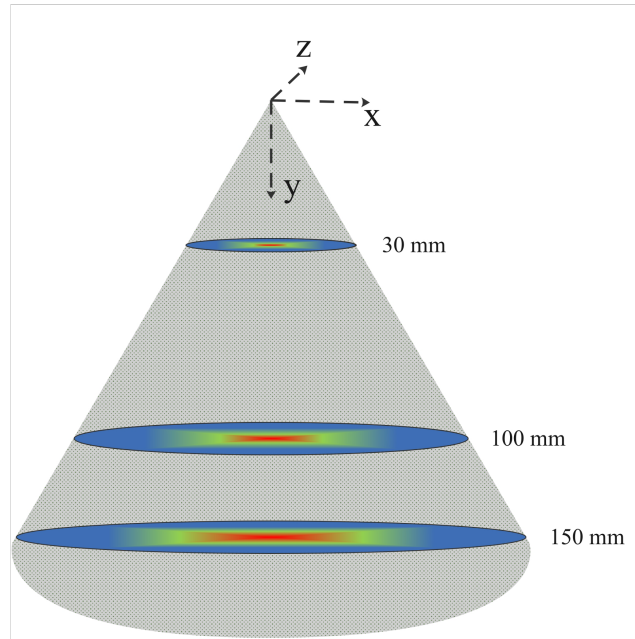
Figure 7.2: Spray geometry and measurement plane setup
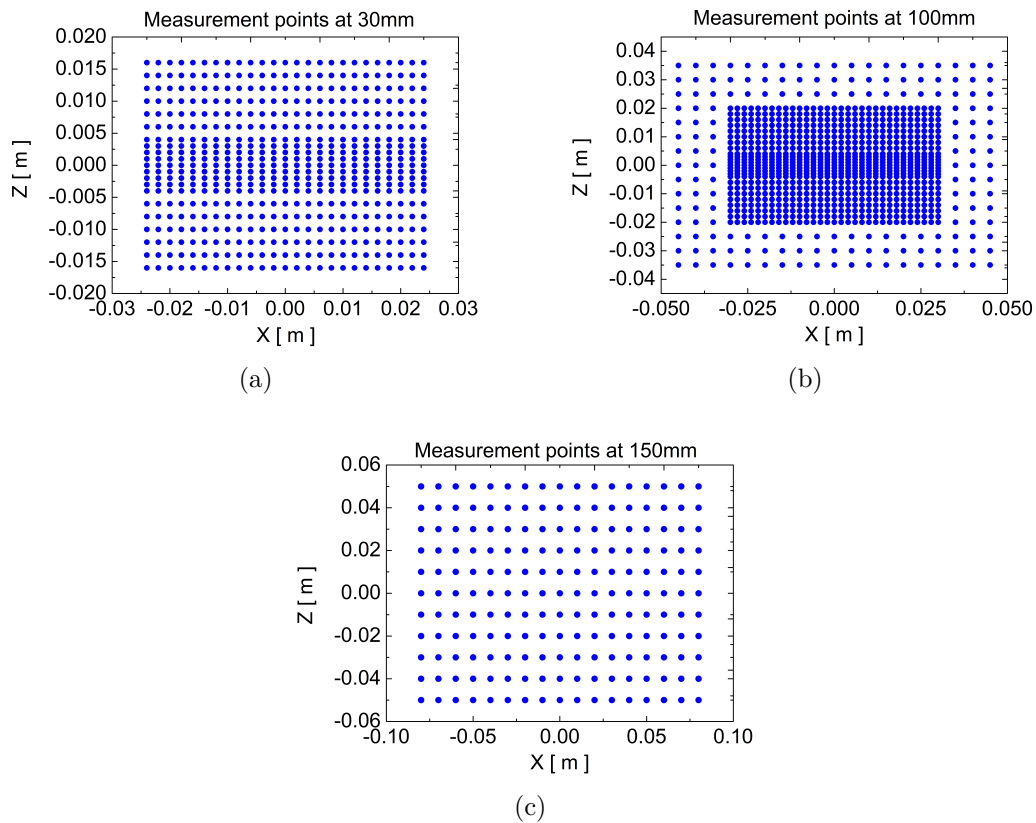

(a)

(b)

(c)

Figure 7.3: Measurement planes and points below the nozzle: a) 525 points at 30 mm below the nozzle (the same settings as the injection points in the simulation); b) 943 points at 100 mm below the nozzle; c) 187 points 150 mm below the nozzle.

The locations of the measurement plane are illustrated in Figure 7.2. The measurement plains contain several measurement points. The position of each measuring point for the cross-section is shown in Figure 7.3, where the total number of measurements and measuring points for each cross-section are also presented. The Dantec Dynamics PDA was used for simultaneous droplet size and velocity measurements based on light-scattering interferometry. Due to the required coupling between droplet size and velocity components, each measurement point was measured three times by repositioning using PDA and nozzle. In total, 525 measurement points were distributed in the first plane located at $y = 30$ mm below the nozzle injector, as shown in Figure 7.3a. Each measurement point collected 50,000 samples or with a collection time of 1 min. The $y = 30$ mm measurement plane is the injection plane of the validation case and applies the same injection method as the verification case described in Chapter 6.

7.2 Simulation setup

The overall droplet size distribution and size-velocity correlation can be determined by post-processing the raw experimental data separately, as illustrated in Figure 7.4. Furthermore, in addition to the droplet size distribution, the size-velocity correlation in the axial y direction as well as in the x and z directions can be used as inlet conditions for the Lagrangian phase, which is also crucial for the jet model.

The computational domain for this spray simulation is a 800 mm $\times$ 300 mm $\times$ 600 mm cubic volume. The reference structured mesh comprises $135 \times 100 \times 101$ nodes in x, y, and z directions, resulting in 1,363,500 hexahedral cells in the domain. Unlike the verification case described in Chapter 6, the injection model for this spray simulation employs a Cartesian coordinate system with the y-direction as the axial direction. To accurately capture the spray jet's central region, the cells have to be non-uniformly distributed in 9 blocks in x and z directions, each block containing 20%, 60%, and 20% of the total cells in x and z directions. The domain borders do not require refinement as there is no wall boundary condition. Thus, an expansion ratio of 10 is used in x and z directions. The mesh in y-direction is not divided into more blocks, but the expansion ratio in y-direction is 10, which is discussed in Section 7.3.1. As shown in Figure 7.5a, the blue square cutout on the grey surface is defined as the inlet, the grey surface is defined as the surroundings, and the entire bottom surface is as the outlet. The boundary conditions are determined as follows:

- **Inlet:** The inlet conditions are specified by experimental data. Each point in Figure 7.3a contains the measurement result of the gas velocity, which is set in the injection plain (the blue cutout) in the domain. Furthermore, the gas velocity and turbulent kinetic energy k at the inlet are interpolated according to the coordinate of the measurement points. The boundary condition of ε is calculated by turbulentMixingLengthDissipationRateInlet method as described in Eq. 6.3. The boundary condition of pressure is set as zeroGradient.

- **Outlet:** The boundary condition of gas velocity is pressureInletOutletVelocity. The

(a)

(b)

(c)

(d)

(e)

(f)

(g)
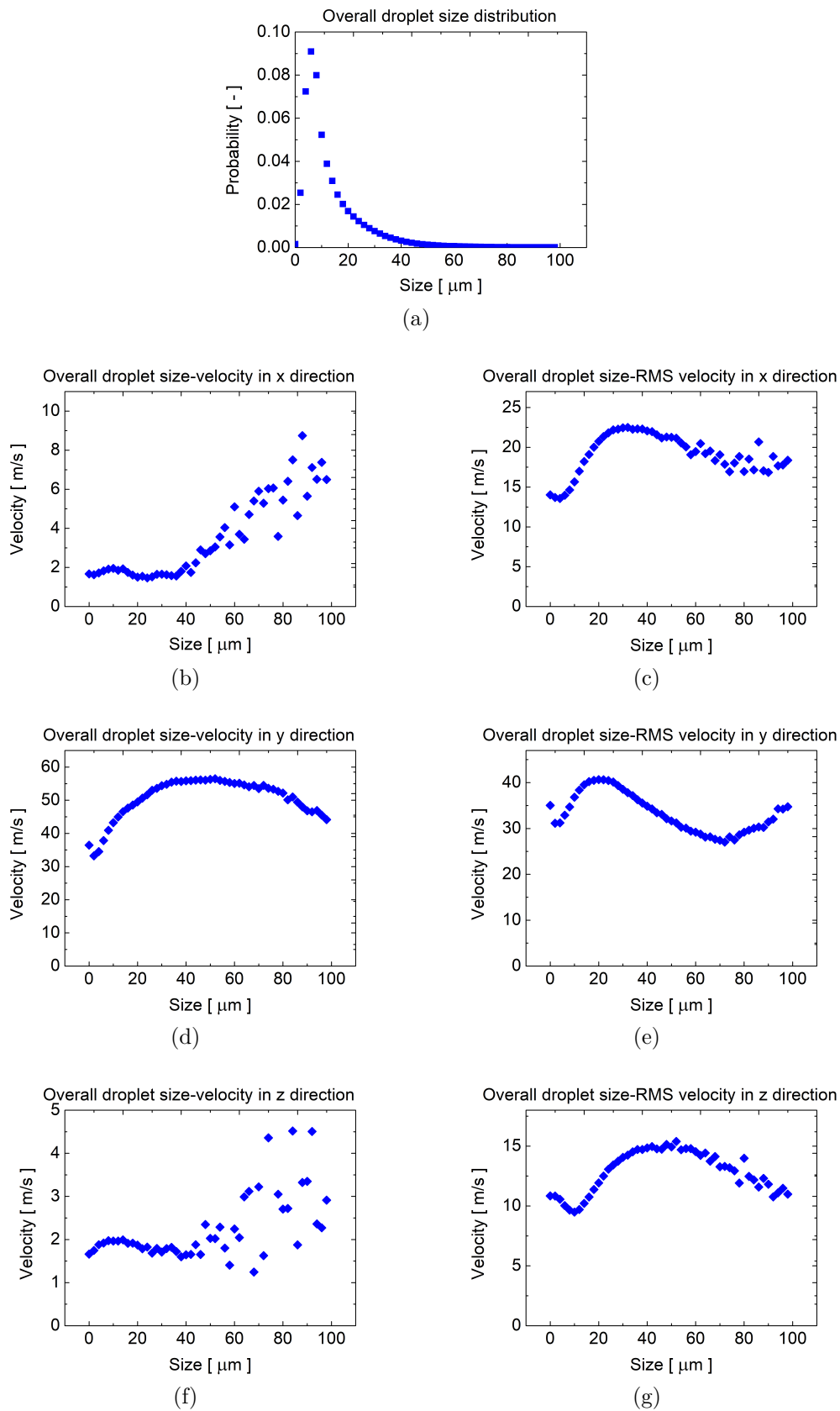
Figure 7.4: Overall droplet size PDF and size-velocity correlations of the injection plain.

(a)

(b)
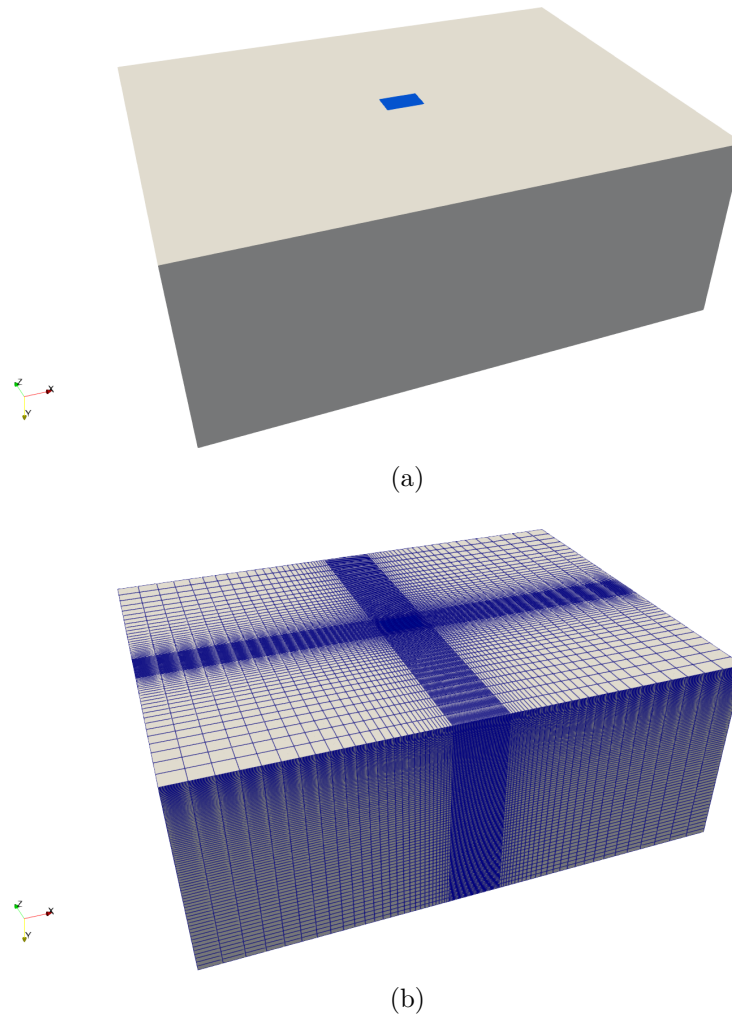
Figure 7.5: General computational domain

boundary condition of k and ε are zeroGradient. For the pressure, the boundary condition of totalPressure is chosen for gas as described in Eq. 6.4.

- **Surroundings**: The absence of walls in the experiments results in the pressureInletOutletVelocity with default setup as the velocity boundary condition for the surroundings. The zeroGradient is set as the boundary condition for k and ε. The pressure boundary condition is the totalPressure.

The injection method for parcels is the same as described in Chapter 6. Each measurement point has a set of local droplet size distribution and size-velocity correlation curves, similar to Figure 7.4 but local profile instead. For the injection model, particle diameter is randomly selected, and the droplet mean and fluctuating velocities in three directions are determined based on size-velocity correlation to calculate the droplet's instantaneous velocity. Each parcel contains three real droplets, and the number of injected parcels is calculated using the mass flow rate calculated by PDA measurement results. The forces acting on the parcels, including drag and gravitational forces, are considered as described in Section 5.2.1. Other forces are neglected because the number average particle size is approximately 12 μm. As for the fully stochastic collision model in this case, the water boundary lines used in the collision maps are

the same as those used in the spray simulations in Chapter. 6, i.e., the bouncing boundary line model of Estrade et al. (1999), the coalescence-stretching separating boundary line model of Ashgriz and Poo (1990), and the reflexive separating boundary line model. In the simulations, the collision maps take into account all We ranges and the droplet size ratios are calculated dynamically.

7.3 Results and discussions

7.3.1 Mesh independence study

A mesh independence study is to investigate whether the simulation results are independent of the underlying mesh. In spray simulations, the Lagrangian particle tracking approach is commonly used due to its simplicity. However, several studies have shown that the grid size can significantly impact the accuracy of Euler/Lagrange spray simulations (Lucchini et al., 2011; Senecal et al., 2013; Wehrfritz et al., 2013). To ensure mesh independence, simulations are conducted with various mesh resolutions. The reference mesh used in this study is described in Section 7.2. Mesh independence study cases were carried out in the $x-$ and $z-$directions with 25%, 50%, 75%, and 125% relative to the reference case, resulting in 346,800, 691,200, 1,009,200, and 1,747,872 cells, respectively (Figure 7.6). To confirm sufficient resolution in the $y-$direction, the reference case's $x-$ and $z-$directions are used with 100 layers raised to 125 or 150 in the $y-$direction. By measuring the velocity at a certain point in the domain, as shown in Figure 7.8, it is confirmed that the reference case already has a good resolution of this case.

7.3.2 Coupling method and particle turbulence dispersion model

The impact of the coupling method and particle turbulence dispersion model on the simulation is significant and is essential to investigate, as explained in sections 2.1 and 5.2.4 for the coupling approach and in section 5.2.3 for the particle turbulence dispersion model.

As shown in Figure 7.9, the simulation results at the centre line of the measurement plain can roughly follow the trend of the experiment result of droplet diameter. Surprisingly, the match between the simulations and measurements shows that the results are better if the particle turbulence dispersion model is disabled. The simulated spray is more widely distributed when the particle turbulence dispersion model is enabled. Figure 7.10b and 7.10d show that the average size distribution at the $y = 100$ mm plane has a moustache shape when the dispersion model is disabled, which is entirely different from the measured results in Figure 7.10a. Although the profile of droplet size on the centre line is in good agreement, the general distribution of droplets at the $y = 100$ mm measurement plane is entirely wrong in these cases. Therefore, the particle turbulence dispersion model is crucial in Euler/Lagrange spray simulations with high turbulent kinetic energy. It significantly affects the RMS velocity profiles shown in Figures 7.11b, 7.11d, and 7.11f. When the particle turbulence dispersion model is disabled, the RMS droplet velocity profiles are incompatible with the measurement data in the $x-$ and $z-$directions since the particles cannot get the correct instantaneous fluid velocity. On the other hand, the one-way or two-way coupling has few or no effects on the mean droplet

(a)

(b)

(c)

(d)

(e)

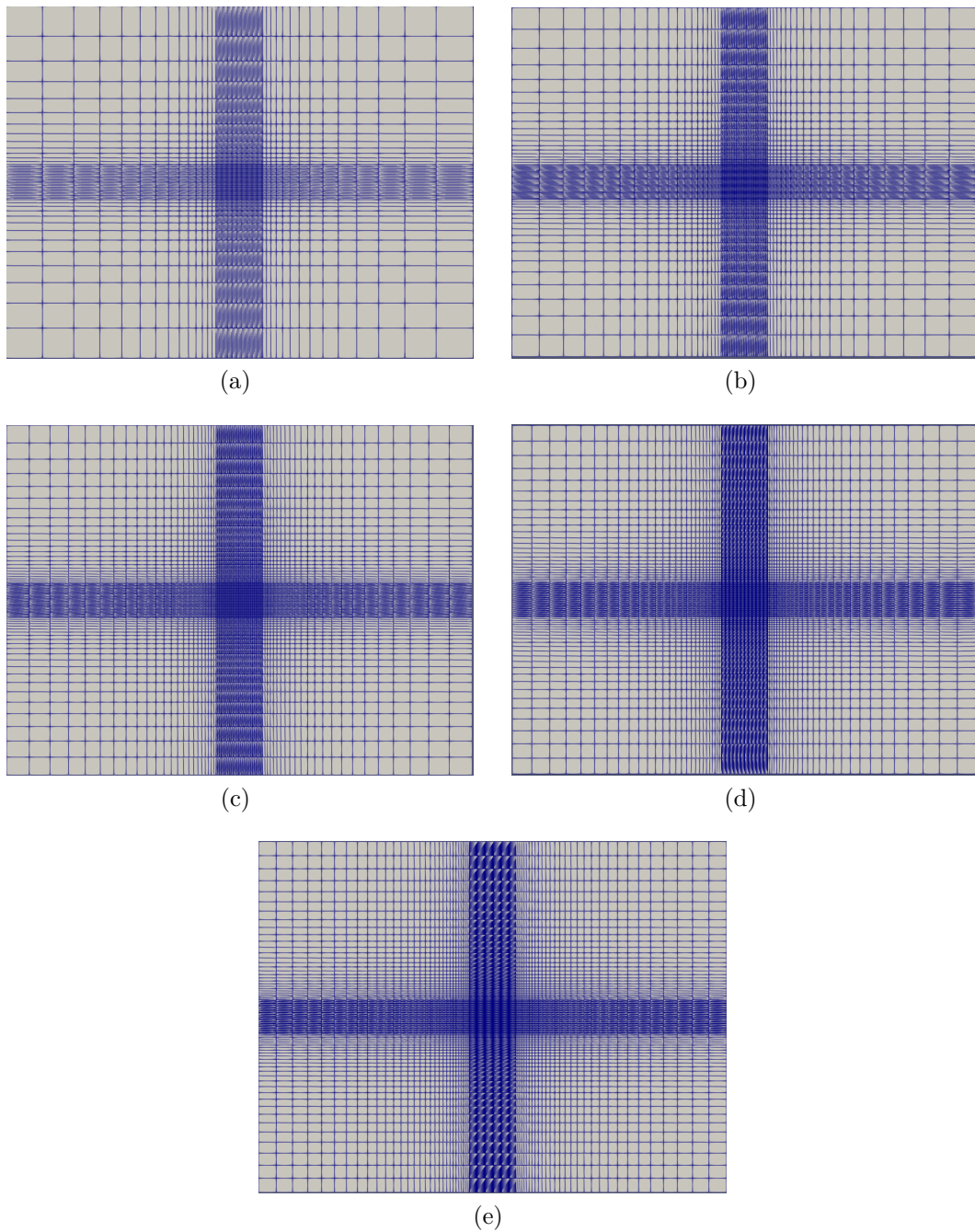Figure 7.6: Mesh independency study in $x-, z-$directions, a) case with 25% cells; b) case with 50% cells; c) case with 75% cells; d) case with 100% cells (reference case); e) case with 125% cells.
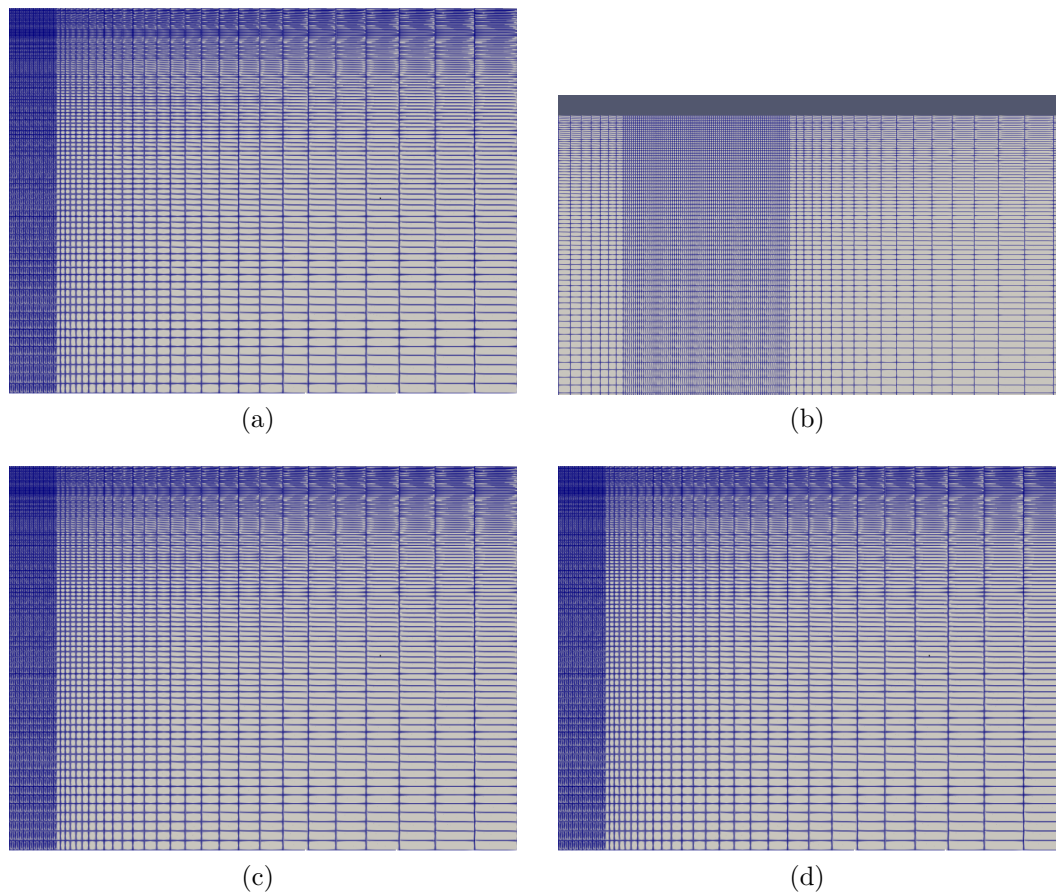
Figure 7.7: Mesh dependency study in $y-direction$, a) reference case with 100 layers; b) zoom of the reference case centre; c) case with 125 layers; b) case with 150 layers.
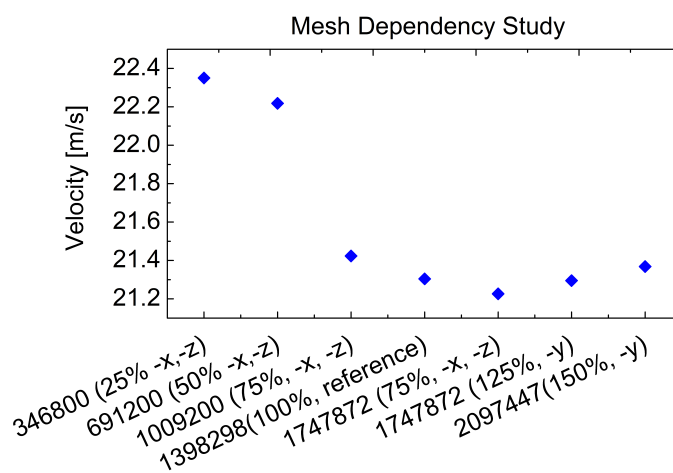

Figure 7.8: Mesh independency study

velocity profiles in the $x-$ and $y-$directions, as shown in Figures 7.11a, 7.11c, and 7.11e. Only when the coupling method changes from one-way to two-way, the profile of droplet mean velocity exhibits completely different behaviour in the centre between -20 mm and 20 mm in the $z-$direction.

Additionally, as illustrated in Figure 7.12, it is crucial to display the gas velocity and turbulence kinetic energy profiles. The simulation results are a good fit to the measurements from $x =$ -20 mm to $x =$ 20 mm in the x-direction, as shown in Figure 7.12a, but outside this range, the agreement is poor. The y-direction of the calculated gas velocity has two high peaks around $x =$ -30 mm and 30 mm. While the simulation results are generally higher than the measured values, the middle region ($x =$ -15 mm to 15 mm) has smaller values than the measurements. The calculated values match the measured values on the left side at $x =$ -25 mm in the z-direction, but the calculated values are lower than the measurements in the middle region ($x =$ -25 mm to 25 mm) and overestimate the measurements on the right side beyond $x =$ 25 mm. The calculated values for turbulence kinetic energy are always lower than the measured values, with significant errors at both ends. Since the PDA does not directly measure the turbulent kinetic energy of the gas, this measurement is obtained by using droplets below 2 μm as tracer particles and calculating the RMS value of these collected particles using Eq. 6.2. The measurements may have errors because they collect only 50,000 samples or for 1 minute, which may be insufficient at the edge of the spray, leading to statistical errors. However, the difference in the coupling method does not affect the mean gas velocity profile, as shown in Figure 7.12. Since the average droplet size d_0 is small and carries extremely little momentum energy, the coupling approach has minimal effects on the gas velocity and turbulence kinetic energy profiles. As a result, there is little feedback to the flow field for two-way coupling simulations.

Figure 7.9: Droplet diameter at the centre line in y = 100 mm plain: (red square: PDA measurement result; blue up triangle: 1-way coupling, particle turbulence dispersion model enable; green circle: 2-way coupling, particle turbulence dispersion enable; magenta down triangle: 1-way coupling, particle turbulence dispersion disabled; navy diamond: 2-way coupling, particle turbulence dispersion disabled ;).
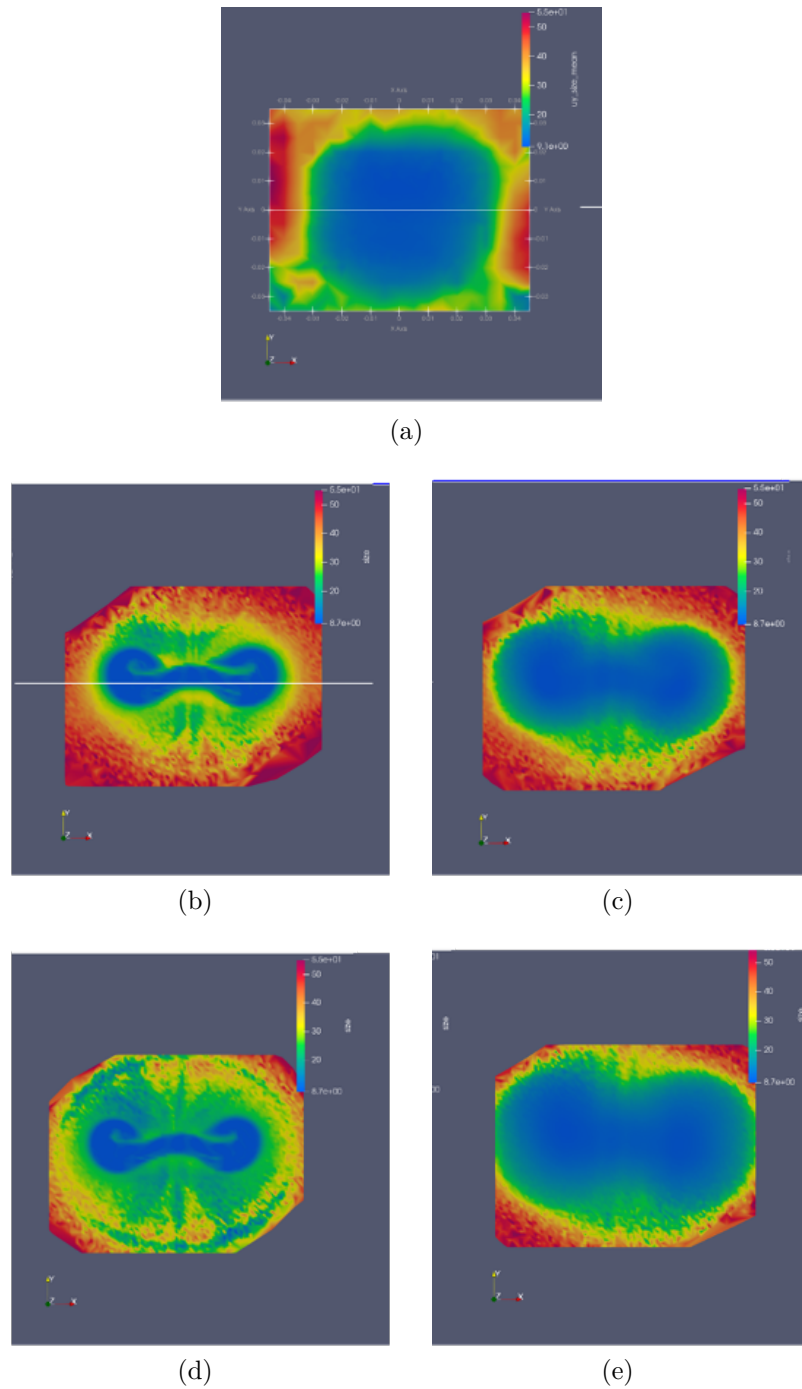
Figure 7.10: Droplet size distribution on the plane y = 100mm: a) PDA measurement result; b) 1-way coupling, particle turbulence dispersion disabled; c) 1-way coupling, particle turbulence dispersion enable; d) 2-way coupling, particle turbulence dispersion disabled; e) 2-way coupling, particle turbulence dispersion enable
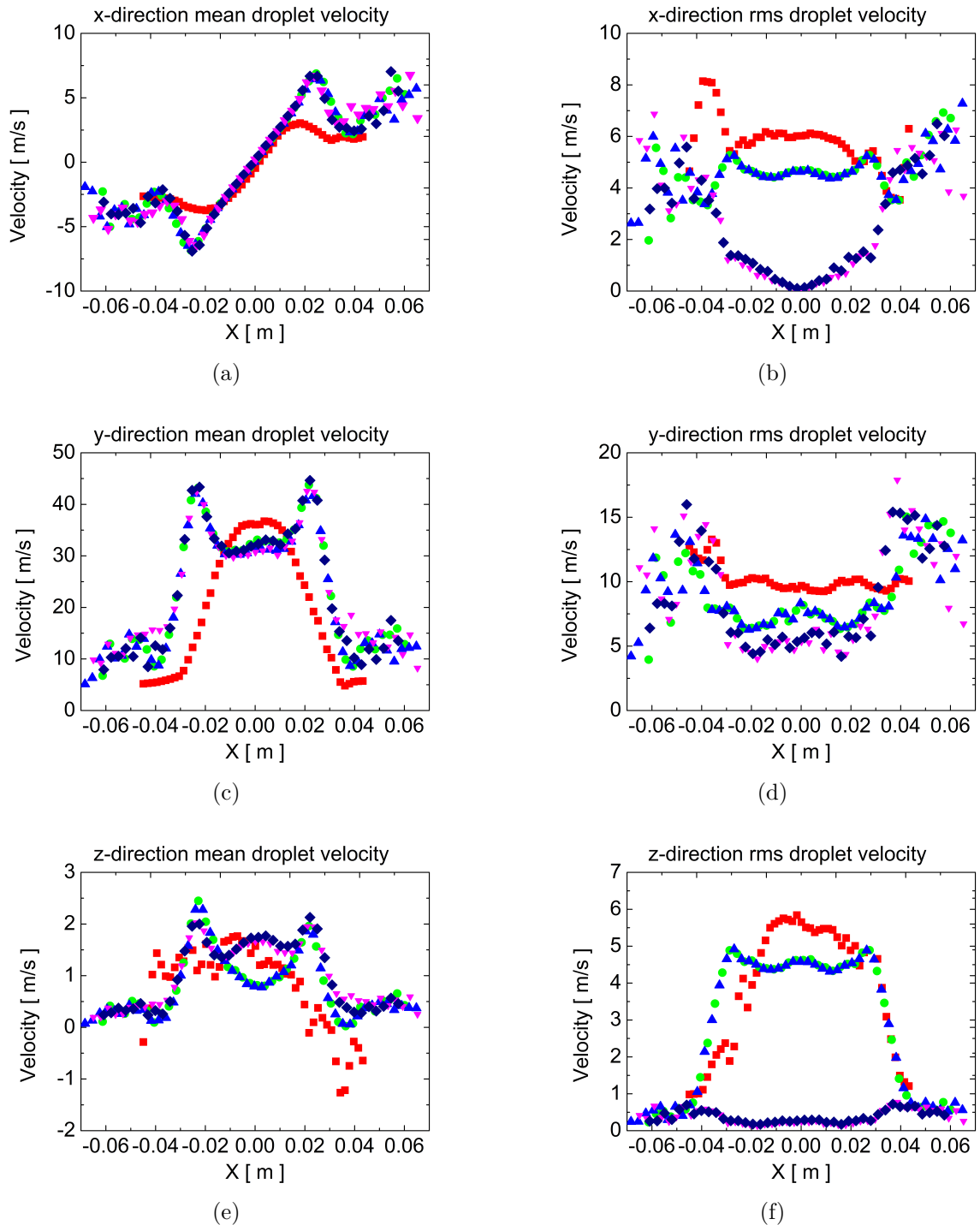
Figure 7.11: Droplet mean and RMS velocity at the centre line in y = 100 mm plain: (red square: PDA measurement result; blue up triangle: 1-way coupling, particle turbulence dispersion model enable; green circle: 2-way coupling, particle turbulence dispersion enable; magenta down triangle: 1-way coupling, particle turbulence dispersion disabled; navy diamond: 2-way coupling, particle turbulence dispersion disabled;).

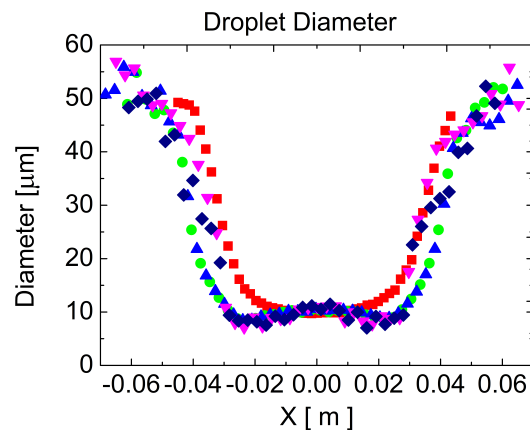Figure 7.12: Gas mean velocity and turbulence kinetic energy at the centre line in y = 100 mm plain: (red square: PDA measurement result; blue up triangle: 1-way coupling, particle turbulence dispersion model enable; green circle: 2-way coupling, particle turbulence dispersion enable; magenta down triangle: 1-way coupling, particle turbulence dispersion disabled; navy diamond: 2-way coupling, particle turbulence dispersion disabled ;).
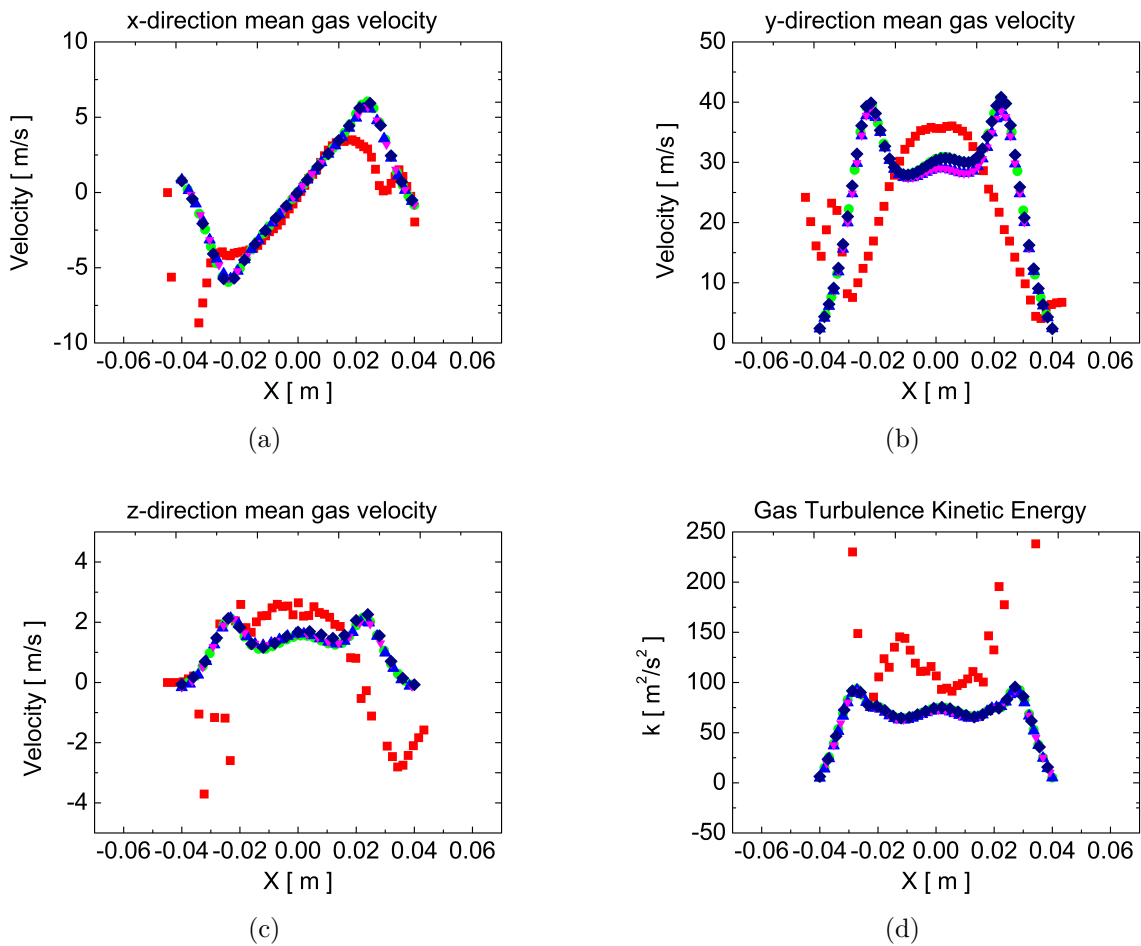
7.3.3 Collision model study

The fully stochastic collision model uses the same models of boundary lines in the collision map as the verification case in Chapter 6. In the spray being studied, coalescence remains the primary droplet collision outcome, accounting for 73.3% of collisions, while bouncing and stretching separation account for 15% and 11.1%, respectively, reflexive separation has the smallest proportion, as presented in Figure 7.8 in the Average Method. In this simulation, the Size Distribution Method yields almost the same results as the Average Method.

Figure 7.14a demonstrates that the real and fictitious droplet size distributions differ from each other, unlike in the validation case using the Average Method. As shown in Figure 7.15a, the size distributions of real and fictitious particles are nearly identical when the Size Distribution Method is used, even capturing anomalous peaks at a size class of 50 μm. Validation case has a shorter domain, and collisions and all types of collision outcomes can be found throughout the whole domain, as shown in Figures 7.14b and 7.15b. Similar to the verification case, most collisions occur with the size ratios at the peak of the size ratio distribution $\Delta = 0.5$ in the Average Method, as demonstrated in Figure 7.14d. In contrast, when the Size Distribution Method is used, the peak of the size ratio distribution is approximately $\Delta = 0.3$. This change in the method causes a shift in the size ratio distribution towards a smaller size ratio, as also seen in the verification case.

The size ratio distribution of bouncing with the Average Method shows a linear increase up to 0.015 when $\Delta = 0$ - 0.6, after which the probability of bouncing for different size ratios is almost the same. The coalescence probability increases to 0.015 at a size ratio of approximately $\Delta = 0.5$, after which it decreases as the size ratio increases, and the probability of stretching separation behaves similarly. In contrast, using the Size Distribution Method, the probability of bouncing increases up to 0.01 at $\Delta = 0$ - 0.3, then stabilises until $\Delta \approx 0.85$ and increases again from $\Delta = 0.85$ to 1. The coalescence probability sharply increases up to 0.015 until $\Delta = 0.3$, then decreases to 0.01 until $\Delta = 0.9$, and then increases again to 0.015. The probability of stretching separation has a noisy behaviour at $\Delta < 0.3$ and slowly decreases from 0.01 to 0.007 until $\Delta = 1$, after which it increases again. The small proportion of reflexive separation outcomes results in a noisy behaviour in the size ratio distribution for this collision type. The Size and Velocity Distribution Method and its neighbourhood method are unavailable in this case because there is still a need to discuss and investigate whether bouncing and stretching separation should exist on the centreline of the far field in the verification case. Additionally, there is no explicit far-field since the domain is not long enough. Therefore, to save effort, a comparison of the Size and Velocity Distribution Method and its neighbourhood method is not included in this study.

7.4 Conclusion

In this chapter, the Euler/Lagrange method is employed to simulate high velocity and turbulent spray, considering four-way coupling and all possible collision outcomes of droplet collisions, including bouncing, coalescence, stretching, and reflexive separation. The numerical calculations are validated using detailed experimental data on turbulent spray obtained from PDA measurements in Pasternak and Sommerfeld (2021). Inlet conditions for droplet
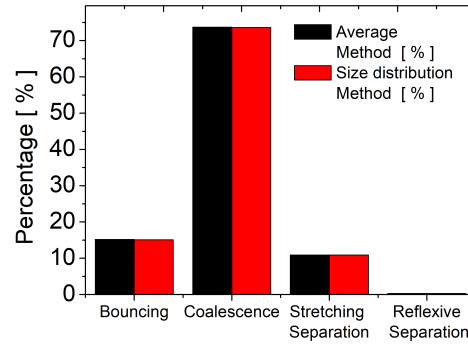
Figure 7.13: Percentage of collision outcomes in different methods (bouncing, coalescence, reflexive separation, stretching separation) black bar: Average Method: 15%, 73.3%, 11.1%, 0.6%; red bar: Size Distribution Method: 15.1%, 73.2%, 11.1%, 0.6%

size distribution and size-velocity dependence are determined using measurements, and gas velocities of the inlet plane are also obtained from measurements. The fully stochastic collision model is used to simulate collisions, which is validated in Laín and Sommerfeld (2020) and Sommerfeld et al. (2021a). The influence of the coupling method and the turbulent dispersion model on the calculation of this spray is also demonstrated. Although the calculated average droplet diameter and velocity agree with the measurements, the particle turbulence dispersion model is essential to obtain the correct RMS velocity of the particles in the highly turbulent flow. The coupling method of particles and flow has a weak effect on the highly turbulent flow. The Lagrangian calculations agree reasonably well with the experiments, but the Euler phase calculations still deviate significantly due to the high velocities and turbulence of the flow.
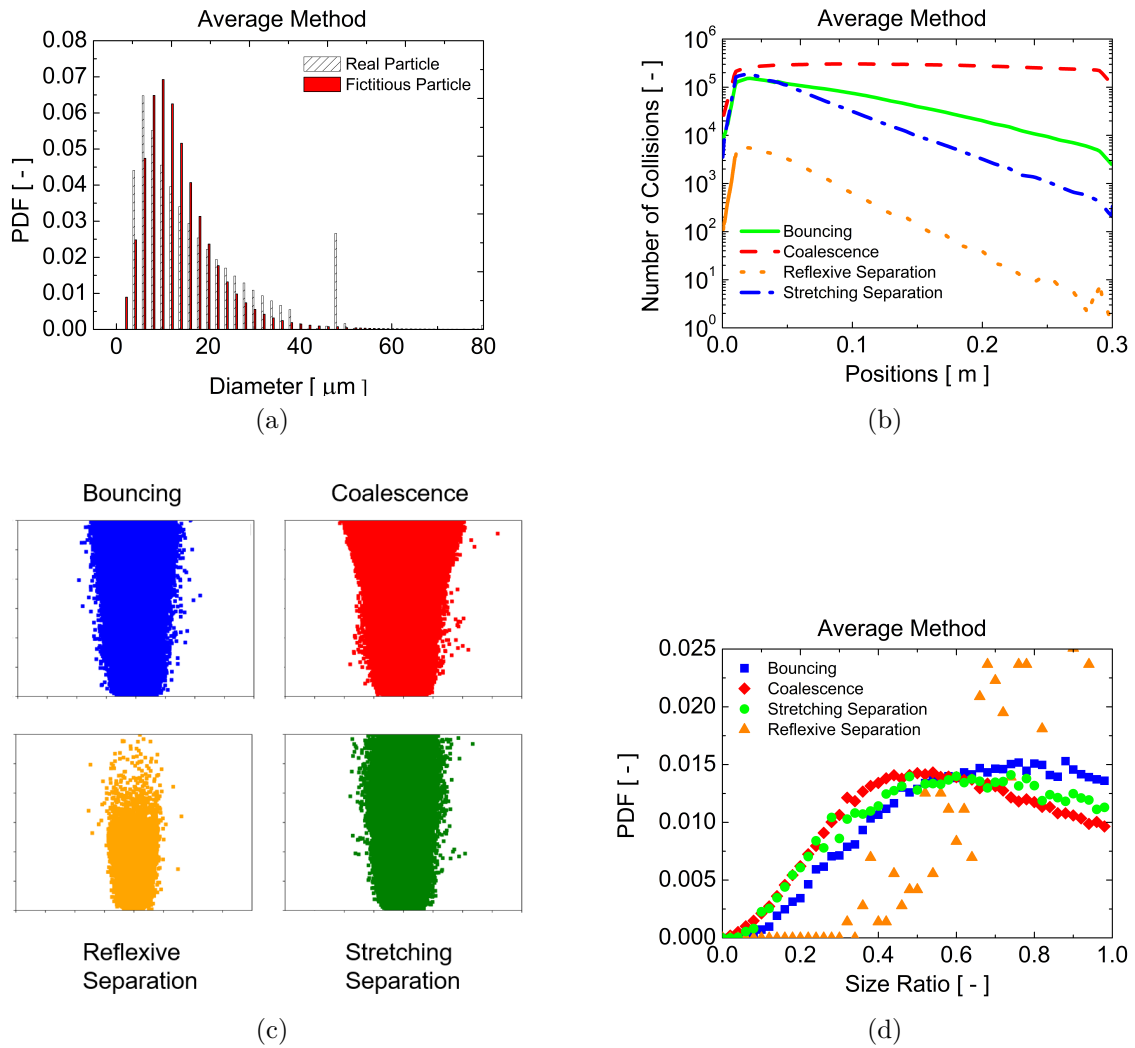
Figure 7.14: General result of validation spray by using stochastic collision model with Average Method at 100 mm plane below the nozzle: a) The size distribution of real and fictitious particles; b) The count of collision outcomes along the spray; c) The collision positions in the spray; d) The size ratio distribution of all outcomes in the spray.
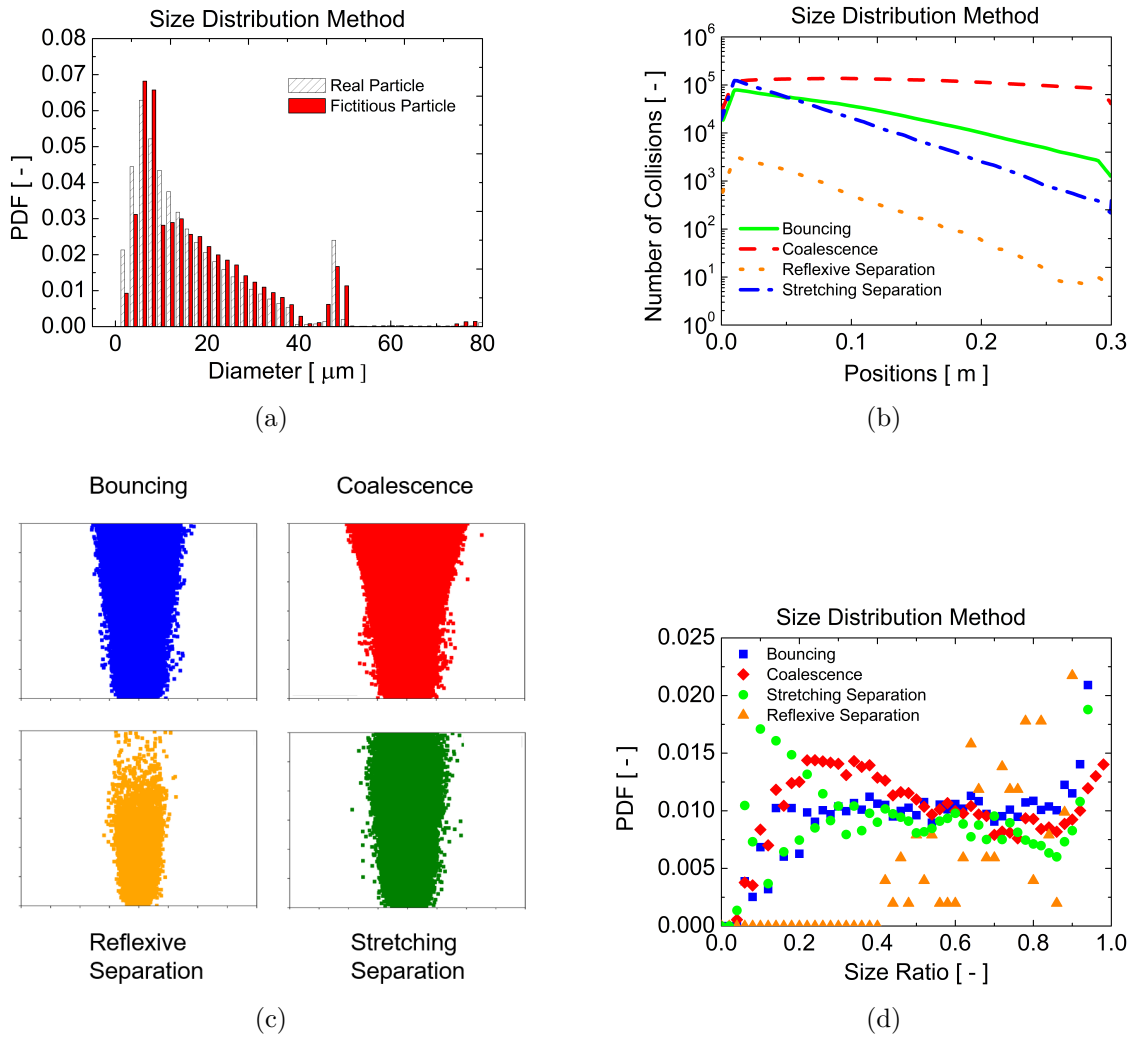
Figure 7.15: General result of validation spray by using stochastic collision model with Size Distribution Method at 100 mm plain below the nozzle: a) The size distribution of real and fictitious parcel; b) The count of collision outcomes along the spray; c) The collision positions in the spray; d) The size ratio distribution of all outcomes in the spray.

Chapter 8

Conclusion and Outlook

This dissertation presents both experimental research and numerical simulations. Binary droplet collision experiments were carried out on two different droplets, with related collision maps generated, the effects of size ratio and viscosity considered, and extended boundary line models investigated. Furthermore, the standard Lagrangian library of OpenFOAM® 8 has also been extended to a fully stochastic collision model, from inter-particle collisions in the gas-solid system to binary droplet collisions of spray, where correlated collision maps determine the droplet collision outcomes. The impact of different generated fictitious collision partners on the collision model is also analysed. This chapter presents the general conclusions of this work, and the outlook is given at the end.

8.1 Conclusions

In Chapter 3, an extended model is developed to predict the boundary line of bouncing binary droplets. The model, referred to as $B = f(We)$, accounts for viscous dissipation effects in the energy balance. Unlike prior models, the proposed bouncing model incorporates the shape parameter ϕ' and the conversion rate β, both of which are dependent on the impact parameter B. The impact parameter B is linearly proportional to the degree of deformation of the droplet during bouncing, and the slope and the intercept values represent the two model parameters. The slope $k_{\phi'}$, as well as the initial values of ϕ_{in} and β_{in}, are obtained by correlating several experimental data with the Ohnesorge number. Depending on their surface tension, liquids are grouped into two categories: water-like liquids with a surface tension of around 70 mN/m and non-water-like liquids with a surface tension of about 25 mN/m. The newly developed model has third-order polynomial functions with Oh which represent the three required parameters. The intercepts of conversion rates for all liquid types follow a single correlation, but they are only valid for $Oh < 0.35$, primarily due to the lack of experimental evidence for more viscous liquids. Additionally, environmental variables are not considered in the model unless they affect the properties of the liquid. After validation, the proposed model is compared with the widely used model Estrade et al. (1999) using numerous droplet collision experiments for water-like and non-water-like liquids. The proposed model outperforms the widely used model in several aspects.

Chapter 4 reports the details of the experiments. At the beginning, the experimental setup is described in detail, including the image processing and post-processing methods. Following, the droplet collision experiments using distilled and tap water to investigate the effects of size ratio and water quality. The results show that the quality of water used has no significant effect on the collision maps, despite tap water having slightly lower surface tension. Two

experimental methods are used to investigate the size ratio effect. The first method involves water droplets passing through a spray to obtain as small a size ratio as possible; however, due to the low sample collection rate and large number of invalid collisions, this method is not investigated further. The other experiments use two droplet generators, and it is found that bouncing occurs regardless of the size ratio. As the size ratio decreases, stretching and reflexive separation decrease, while coalescence occurs more frequently. While the boundary line models proposed in Estrade et al. (1999) and Ashgriz and Poo (1990) capture only part of the information, the former performs better overall. Sommerfeld and Pasternak (2019) captures the coalescence-stretching separation boundary well, but only works when the size ratio is less than 0.5. Later, the maltodextrin solution experiments investigate the effect of viscosity and size ratio on collision outcomes. As the size ratio decreases, bouncing, stretching, and reflexive separation occupy a smaller portion of the collision map, while coalescence occupies a larger proportion. Several characteristic Weber number patterns are identified, including the movement of We_{B-C} towards the lower We region as the size ratio decreases. The critical point (We_C) can only be found at the lowest two concentrations of maltodextrin solution and is more sensitive to size for the 20Ma% solution. We_C may move to the larger We region with increasing viscosity, but the range of We measured in this experiment is not large enough to determine whether reflexive separation occurs for larger We. The triple point (We_T) is unaffected by the droplet size and size ratio but is sensitive to viscosity. The boundary line models are analysed, and the model of Sommerfeld and Pasternak (2019) with pure liquid correlation performs well for coalescence-stretching separation in maltodextrin solutions with size ratios up to $\Delta = 0.5$. There are still some space to discover the effect of the contants in the model. While the model of Sui et al. (2023) works well for bouncing at size ratios of $\Delta = 0.8$ and $\Delta = 1.0$, but deviates significantly for $\Delta = 0.5$. The models of Ashgriz and Poo (1990) and Estrade et al. (1999) do not apply to collision outcomes for maltodextrin solutions, with the former overestimating the proportion of stretching separation and the latter underestimating the proportion accounted for by bouncing. Modelling studies of boundary lines require further investigation.

In the last chapters, the simulation related content is introduced. Transient, three-dimensional Euler/Lagrange methods and the standard $k - \varepsilon$ model are used for all numerical analyses involved in this work. The numerical implementation of other mathematical models is derived from the standard code base in OpenFOAM® 8. In Chapters 6 and 7, two examples of low and high turbulent spray calculations with four-way coupling, encompassing all feasible outcomes of droplet collisions (such as bouncing, coalescence, stretching, and reflexive separation), are presented. Experimental data from previous studies on turbulent sprays Ruger et al. (2000) and Pasternak and Sommerfeld (2021) are used as a reference to validate the numerical calculations. To obtain the flow characteristics of the spray, PDA experiments are conducted. As it is unnecessary to simulate the primary break-up of the liquid, the droplet size distribution and size-velocity correlation measured in a 25/30 mm plane downstream of the nozzle outlet serve as the inlet conditions for the simulations. In the simulations, a fully stochastic collision model based on kinematic theory is utilised. The model calculates the collision probabilities between real and fictitious particles and determines the impact efficiency to decide on a collision in a fully stochastic manner for binary droplet collisions. Compared to other colli-

sion methods, which require traversing all real particles, the fully stochastic collision model is significantly more efficient. The generation of fictitious collision partners is a crucial step in the fully stochastic collision model. Hence, various methods are investigated to generate such collision partners, including the Average Method, Size Distribution Method, Size and Velocity Distribution Method, and Size and Velocity Distribution Neighbourhood Method, in detail. The collision outcomes are determined using collision maps and their boundary lines, and in this dissertation, a combined three-line model is used to incorporate boundary lines that are widely used and consider dynamic size ratios.

In the verification case presented in Chapter 6, simulation results at the measurement planes agree reasonably well with experimental results. The simulations produce good agreement with measured results for droplet mass flow rate, number averaged droplet diameter, droplet velocity, and axial gas velocity profiles. The Size Distribution Method is found to result in a better size distribution when calculating fictitious collision partners in the fully stochastic collision model, which is crucial for accurate collision outcomes. The use of the Velocity Distribution Method to calculate the velocity of the fictitious particle increases the collision probability in the far field, which requires further confirmation through future research. It is important to note that the initial size distribution of the parcel and particle should be the same to avoid errors in the statistical calculations required by the stochastic collision model. Furthermore, all statistical calculations should be particle-based, not parcel-based. Coalescence of droplet collisions has only a small effect on the droplet number mean diameter profile in the relatively dilute spray, but it significantly affects the overall evolution of the Sauter Mean Diameter along the spray. Coalescence leads to an increase in the overall Sauter Mean Diameter along the spray and a decrease in the required droplet number flow rate, consistent with experimental observations. After verification in Chapter 7, it is evident that the particle turbulence dispersion model plays a crucial role in obtaining the correct RMS velocity of the particles in high turbulent spray simulations. Although the way particles and flow are coupled has little effect on the flow field of a high turbulent spray, it is observed that using only one-way coupling results in a relatively smaller area of particle distribution, as seen from the contour plots of the cross sections. The Euler phase calculations, on the other hand, exhibit significant deviations in both simulations, potentially due to the turbulence model. Furthermore, the dispersion of the droplets in the spray is affected due to the four-phase coupling. The particle turbulence dispersion model is also affected since the droplets do not correctly receive their corresponding instantaneous gas velocities. More in-depth research is required to explore this area further.

8.2 Outlook

This section aims to outline potential areas for improvement and further research within the current scope of the study. The authors present a proposed model for bouncing boundary lines in the collision map, utilising past experimental findings regarding the collision outcomes of different liquids under atmospheric pressure and room temperature. However, the existing model is a crude classification based on surface tension intervals and requires refinement. The maltodextrin model has a tendency to mis-predict small size ratios, indicating further

adjustment and research is necessary.

While numerous experimental and numerical studies have contributed to the understanding of binary droplet collisions, several areas are still unclear. For instance, the generation and verification of rotating binary droplet collisions require further investigation. Additionally, accurate models of collision boundaries and reliable theoretical support for the size effect are currently lacking. Some studies explores the effect of short-range forces on bouncing and introduces the two-phase Ohnesorge number to discuss the impact of the surrounding environment on bouncing. Investigating short-range forces is a potential area for future research into droplet collision, whether using experimental or numerical approaches.

The collision of droplets with ultra-small size ratios ($\Delta < 0.2$) is not extensively studied, and experimental verification of collision maps for ultra-small droplets is needed. Additionally, droplet collisions can occur at higher Weber numbers, and the number of satellite droplets generated in stretching separations requires further exploration. Generating more detailed collision maps that incorporate additional information, such as the number of satellite droplets produced, would facilitate direct calculation of droplet generation in Euler/Lagrange simulations.

As computational power continues to increase, Euler/Lagrange methods are becoming increasingly popular for simulating dispersed multiphase gases. However, simulating hundreds of thousands of droplets and considering multiple computational grids remains computationally intensive. Therefore, machine learning and deep learning techniques hold the potential to train models to predict particle motion instead of performing time-consuming calculations, significantly increasing Lagrangian particle calculation speed and reducing computational power requirements. Additionally, developing a Lagrangian calculation method less sensitive to grid size remains challenging, as the density of the grid imposes restrictions on the computation of traditional Lagrangian methods in three-phase calculations involving Lagrangian hybrid VOF.

Bibliography

K. H. Al-Dirawi and A. E Bayly. A new model for the bouncing regime boundary in binary droplet collisions. *Physics of Fluids*, 31(2):027105, 2019.

K. H. Al-Dirawi and A. E Bayly. An experimental study of binary collisions of miscible droplets with non-identical viscosities. *Experiments in Fluids*, 61(2):50, 2020.

A. A. Amsden, P. J. O'Rourke, and T. D. Butler. KIVA-II: A computer program for chemically reactive flows with sprays. Technical report, 1989.

N. Ashgriz and J. Y. Poo. Coalescence and separation in binary collisions of liquid drops. *Journal of Fluid Mechanics*, 221:183–204, 1990.

G. Bradski. The OpenCV Library. *Dr. Dobb's Journal: Software Tools for the Professional Programmer*, 25(11), 2000.

P. R. Brazier-Smith, S. G. Jennings, and J. Latham. The interaction of falling water drops: coalescence. *Proceedings of the Royal Society of London. A. Mathematical and Physical Sciences*, 326(1566):393–408, 1972.

G. Brenn, D. Valkovska, and K. D. Danov. The formation of satellite droplets by unstable binary drop collisions. *Physics of Fluids*, 13(9):2463–2477, 2001.

R. H. Chen. Diesel–diesel and diesel–ethanol drop collisions. *Applied Thermal Engineering*, 27(2):604–610, 2007.

R. H. Chen and C. T. Chen. Collision between immiscible drops with large surface tension difference: diesel oil and water. *Experiments in Fluids*, 41(3):453–461, 2006.

R. H. Chen, W. C. Wang, and Y. W. Chen. Like-drop collisions of biodiesel and emulsion diesel. *European Journal of Mechanics - B/Fluids*, 60:62–69, 2016.

X. D. Chen and V. Yang. A Multi-Scale Study of Droplet Collision Dynamics: From Gas Film Lubrication to Liquid Phase Mixing. In *24th Annual Conference on Liquid Atomization and Spray Systems, ILASS2012-64, ILASS Americas, San Antonio, TX*, pages 1–18, 2012.

X. D Chen and V. Yang. Direct numerical simulation of multiscale flow physics of binary droplet collision. *Physics of Fluids*, 32(6):062103, 2020.

X. D. Chen, D. J. Ma, P. Khare, and V. Yang. Energy and Mass Transfer during Binary Droplet Collision. In *49th AIAA Aerospace Sciences Meeting including the New Horizons Forum and Aerospace Exposition*, pages 1–17, 2011.

X. D. Chen, D. J. Ma, and V. Yang. Collision Outcome and Mass Transfer of Unequal-sized Droplet Collision. In *50th AIAA Aerospace Sciences Meeting including the New Horizons Forum and Aerospace Exposition*, pages 1–19. American Institute of Aeronautics and Astronautics, 2012.

H. C. Cong, L. J. Qian, Y. T. Wang, and J. Z. Lin. Numerical simulation of the collision behaviors of binary unequal-sized droplets at high Weber number. *Physics of Fluids*, 32 (10):103307, 2020.

C. T. Crowe, editor. *Multiphase flow handbook*. CRC press, 2006.

C. T. Crowe, M. P. Sharma, and D. E. Stock. The particle-source-in cell (PSI-CELL) model for gas-droplet flows. *Journal of Fluids Engineering*, 99(2):325–332, 1977.

C. T. Crowe, J. D. Schwarzkopf, M. Sommerfeld, and Y. Tsuji. *Multiphase Flows with Droplets and Particles*. CRC Press, 2011.

T. De Karman and L. Howarth. On the Statistical Theory of Isotropic Turbulence. *Proceedings of the Royal Society of London. Series A-Mathematical and Physical Sciences*, 164(917): 192–215, 1938.

S. Elghobashi. On predicting particle-laden turbulent flows. *Applied Scientific Research*, 52 (4):309–329, 1994.

J. P. Estrade, H. Carentz, G. Lavergne, and Y. Biscos. Experimental investigation of dynamic binary collision of ethanol droplets – a model for droplet coalescence and bouncing. *International Journal of Heat and Fluid Flow*, 20(5):486–491, 1999.

G. Finotello, S. De, J. C. Vrouwenvelder, J. T. Padding, K Buist, A., A. Jongsma, F. Innings, and J. A. M. Kuipers. Experimental investigation of non-Newtonian droplet collisions: the role of extensional viscosity. *Experiments in Fluids*, 59(7):113, 2018a.

G. Finotello, R. F. Kooiman, J. T. Padding, K. A. Buist, A. Jongsma, F. Innings, and J. A. M. Kuipers. The dynamics of milk droplet–droplet collisions. *Experiments in Fluids*, 59(1):17, 2018b.

G. Finotello, J. T. Padding, K. A Buist, A. Jongsma, F. Innings, and J.A.M. Kuipers. Droplet collisions of water and milk in a spray with Langevin turbulence dispersion. *International Journal of Multiphase Flow*, 114:154–167, 2019.

C. Focke and D. Bothe. Computational analysis of binary collisions of shear-thinning droplets. *Journal of Non-Newtonian Fluid Mechanics*, 166(14-15):799–810, 2011.

C. Focke and D. Bothe. Direct numerical simulation of binary off-center collisions of shear thinning droplets at high Weber numbers. *Physics of Fluids*, 24(7):073105, 2012.

C. Focke, M. Kuschel, M. Sommerfeld, and D. Bothe. Collision between high and low viscosity droplets: Direct Numerical Simulations and experiments. *International Journal of Multiphase Flow*, 56:81–92, 2013.

A. Foissac, J. Malet, S. Mimouni, and F. Feuillebois. Binary water droplet collision study in presence of solid aerosols in air. In *7th International Conference on Multiphase Flow (ICMF)*, 2010.

U. Fritsching. *Process-spray: functional particles produced in spray processes.* Springer, 2016.

U. Fritsching and X. G. Li. Spray Systems. In *Multiphase Flow Handbook*, pages 1091–1250. CRC Press, 2016.

S. Gao and U. Fritsching. Study of binary in-flight melt droplet collisions. *Materialwissenschaft und Werkstofftechnik*, 41(7):547–554, 2010.

T. C. Gao, R. H. Chen, J. Y. Pu, and T. H. Lin. Collision between an ethanol drop and a water drop. *Experiments in Fluids*, 38(6):731–738, 2005.

C. Gotaas, P. Havelka, H. A. Jakobsen, H. F. Svendsen, M. Hase, N. Roth, and B. Weigand. Effect of viscosity on droplet-droplet collision outcome: Experimental study and numerical comparison. *Physics of Fluids*, 19(10):102106, 2007.

C. He, X. Xia, and P. Zhang. Non-monotonic viscous dissipation of bouncing droplets undergoing off-center collision. *Physics of Fluids*, 31(5):052004, 2019.

C. He, X. Xia, and P. Zhang. Vortex-dynamical implications of nonmonotonic viscous dissipation of off-center droplet bouncing. *Physics of Fluids*, 32(3):032004, 2020.

C. He, L. Yue, and P. Zhang. Spin-affected reflexive and stretching separation of off-center droplet collision. *Physical review fluids*, 7(1):013603, 2022.

P. D Hicks and R. Purvis. Air cushioning and bubble entrapment in three-dimensional droplet impacts. *Journal of Fluid Mechanics*, 649:135–163, 2010.

C. A. Ho and M Sommerfeld. Modelling of micro-particle agglomeration in turbulent ows. *Chemical Engineering Science*, 57(15):3073–3084, 2002.

C. Hu, S. Xia, C. Li, and G. Wu. Three-dimensional numerical investigation and modeling of binary alumina droplet collisions. *International Journal of Heat and Mass Transfer*, 113: 569–588, 2017.

K. L. Huang and K. L. Pan. Size effect on the transition from coalescence to bouncing regime in binary droplet. In *In 13th Triennial International Conference on Liquid Atomization and Spray Systems, ICLASS, Tainan*, volume 27, 2015.

K. L. Huang and K. L. Pan. Transitions of bouncing and coalescence in binary droplet collisions. *Journal of Fluid Mechanics*, 928:A7, 2021.

Y. J. Jiang, A. Umemura, and C. K. Law. An experimental investigation on the collision behaviour of hydrocarbon droplets. *Journal of Fluid Mechanics*, 234:171–190, 1992.

S. Kim, D. J. Lee, and C. S. Lee. Modeling of binary droplet collisions for application to inter-impingement sprays. *International Journal of Multiphase Flow*, 35(6):533–549, 2009.

G. H. Ko and H. S. Ryou. Droplet collision processes in an inter-spray impingement system. *Journal of Aerosol Science*, 36(11):1300–1321, 2005a.

G. H. Ko and H. S. Ryou. Modeling of droplet collision-induced breakup process. *International Journal of Multiphase Flow*, 31(6):723–738, 2005b.

G. H. Ko, H. S. Ryou, N. K. Hur, S. W. Ko, and M. O. Youn. Numerical study on bouncing and separation collision between two droplets considering the collision-induced breakup. *Journal of Mechanical Science and Technology*, 21(4):585–592, 2007.

K. G. Krishnan and E. Loth. Effects of gas and droplet characteristics on drop-drop collision outcome regimes. *International Journal of Multiphase Flow*, 77:171–186, 2015.

M. Kuschel and M. Sommerfeld. Visualisation of time-resolved mixing and penetration processes during droplet collisions using PLIF. In *16th Int. Symposium on applications of Laser Techniques to fluid mechanics*, Lissabon, 2012.

M. Kuschel and M. Sommerfeld. Investigation of droplet collisions for solutions with different solids content. *Experiments in Fluids*, 54(2), 2013.

S. Laín. *On modeling and numerical computation of industrial disperse two-phase flow with the Euler-Lagrange approach.* Shaker, 2010.

S. Laín and M. Sommerfeld. Characterisation of pneumatic conveying systems using the Euler/Lagrange approach. *Powder Technology*, 235:764–782, 2013.

S. Laín and M. Sommerfeld. Influence of droplet collision modelling in Euler/Lagrange calculations of spray evolution. *International Journal of Multiphase Flow*, 132:103392, 2020.

X. G. Li and U. Fritsching. Numerical Investigation of Binary Droplet Collisions in All Relevant Collision Regimes. *The Journal of Computational Multiphase Flows*, 3(4):207–224, 2011.

J. Lipowsky and M. Sommerfeld. Time-Dependent Simulation of a Swirling Two Phase Flow Using an Anisotropic Turbulent Dispersion Model. In *Proceedings of the ASME Fluids Engineering Summer Conference*, volume 41987, pages 677–686, 2005.

L. Liu, Y. Xing, and R. Huang. A lattice Boltzmann study on the bouncing behavior of equal-sized droplet collision. *Physics of Fluids*, 34(4):043318, 2022.

M. Liu and D. Bothe. Numerical study of head-on droplet collisions at high Weber numbers. *Journal of Fluid Mechanics*, 789:785–805, 2016.

T. Lucchini, G. D'Errico, and D. Ettorre. Numerical investigation of the spray mesh turbulence interactions for high-pressure, evaporating sprays at engine conditions. *International Journal of Heat and Fluid Flow*, 32(1):285–297, 2011.

A. Menchaca-Rocha, F. Huidobro, A. Martinez-Davalos, K. Michaelian, A. Perez, V. Rodriguez, and N. Cârjan. Coalescence and fragmentation of colliding mercury drops. *Journal of Fluid Mechanics*, 346:291–318, 1997.

A. Munnannur and R. D. Reitz. A new predictive model for fragmenting and non-fragmenting binary droplet collisions. *International Journal of Multiphase Flow*, 33(8):873–896, 2007.

P. N. Nordin. 2001. *Complex Chemistry Modeling of Diesel Spray Combustion*. PhD thesis, Chalmers University, 2001.

P. J. O'Rourke. 1981. *Collective drop effects on vaporizing liquid sprays*. PhD thesis, Princeton University, 1981. 1981.

P. J. O'Rourke. Statistical properties and numerical implementation of a model for droplet dispersion in a turbulent gas. *Journal of Computational Physics*, 83(2):345–360, 1989.

K. L. Pan, C. K. Law, and B. Zhou. Experimental and mechanistic description of merging and bouncing in head-on binary droplet collision. *Journal of Applied Physics*, 103(6):064901, 2008.

K. L. Pan, Y. H. Tseng, J. C. Chen, K. L. Huang, C. H. Wang, and M. C. Lai. Controlling droplet bouncing and coalescence with surfactant. *Journal of Fluid Mechanics*, 799:603–636, 2016.

Y. Pan and K. Suga. Numerical simulation of binary liquid droplet collision. *Physics of Fluids*, 17(8):082105, 2005.

L. Pasternak and M. Sommerfeld. Experimental investigation of size effects in colliding droplet. In *Ilass Europe. 28th european conference on Liquid Atomization and Spray Systems*, pages 710–715. Editorial Universitat Politècnica de València, 2017.

L. Pasternak and M. Sommerfeld. Spray characterisation for modelling the tablet coating process. *International Conference on Liquid Atomization and Spray Systems (ICLASS)*, 1: 343, 2021.

L. Pasternak, J. M. Mañas, and M. Sommerfeld. Influence of droplet properties on the coating of free-falling spherical particles. *Atomization and Sprays*, 31(2):37–61, 2021.

C. Planchette, E. Lorenceau, and G. Brenn. Binary collisions of immiscible liquid drops for liquid encapsulation. *Fluid Dynamics & Materials Processing*, 7(3):279–301, 2011.

C. Planchette, H. Hinterbichler, M. Liu, D. Bothe, and G. Brenn. Colliding drops as coalescing and fragmenting liquid springs. *Journal of Fluid Mechanics*, 814:277–300, 2017.

S. L. Post and J. Abraham. Modeling the outcome of drop–drop collisions in Diesel sprays. *International Journal of Multiphase Flow*, 28(6):997–1019, 2002.

J. Qian and C. Law. Effects of liquid and ambient gas properties on droplet collision. In *32nd Aerospace Sciences Meeting and Exhibit*. American Institute of Aeronautics and Astronautics, 1994.

J. Qian, G. Tryggvason, and C. Law. An experimental and computational study of bouncing and deformation in droplet collision. In *In 35th Aerospace Sciences Meeting and Exhibit*, 1997.

C. Rabe, J. Malet, and F. Feuillebois. Experimental investigation of water droplet binary collisions and description of outcomes with a symmetric Weber number. *Physics of Fluids*, 22(4):047101, 2010.

A. H. Rajkotwala, H. Mirsandi, E. a. J. F. Peters, M. W. Baltussen, C. W. M. van der Geld, J. G. M. Kuerten, and J. a. M. Kuipers. Extension of local front reconstruction method with controlled coalescence model. *Physics of Fluids*, 30(2):022102, 2018.

G. A. Ricardo and Martin Sommerfeld. Experimental evaluation of surface roughness variation of ductile materials due to solid particle erosion. *Advanced Powder Technology*, 31(9):3790–3816, 2020.

I. V. Roisman, C. Planchette, E. Lorenceau, and G. Brenn. Binary collisions of drops of immiscible liquids. *Journal of Fluid Mechanics*, 690:512–535, 2012.

M. Ruger, S. Hohmann, M. Sommerfeld, and G. Kohnen. Euler/Lagrange calculations of turbulent sprays: the effect of droplet collisions and coalescence. *Atomization and Sprays*, 10(1), 2000.

M. D. Saroka and N. Ashgriz. Separation Criteria for Off-Axis Binary Drop Collisions. *Journal of Fluids*, 2015:1–15, 2015.

M. D. Saroka, N. Ashgriz, and M. Movassat. Numerical Investigation of Head-on Binary Drop Collisions in a Dynamically Inert Environment. *Journal of Applied Fluid Mechanics*, 5(1), 2012.

L. Schiller. A Drag Coefficient Correlation. *VDI Zeitung*, 77:318–320, 1933.

G. Schuch and F. Löffler. Über die Abscheidewahrscheinlichkeit von Feststoffpartikeln an Tropfen in einer Gasströmung durch Trägheitseffekte. *Verfahrenstechnik*, 12(5):302–306, 1978.

P. K. Senecal, E. Pomraning, K. J. Richards, and S. Som. An investigation of grid convergence for spray simulations using an LES turbulence model. Technical report, SAE Technical Paper 2013-01-1083, 2013.

O. L. Sgrott and M. Sommerfeld. Influence of inter-particle collisions and agglomeration on cyclone performance and collection efficiency. *The Canadian Journal of Chemical Engineering*, 97(2):511–522, 2019.

N. E. Shlegel, P. P. Tkachenko, and P. A. Strizhak. Collision of water droplets with different initial temperatures. *Powder Technology*, 367:820–830, 2020.

M. Sommerfeld. Some open questions and inconsistencies of Lagrangian particle dispersion models. In *9th. Symposium on Turbulent Shear Flows. Kyoto, Japan.*, volume 15, 1993.

M. Sommerfeld. *Modellierung und numerische Berechnung von partikelbeladenen turbulenten Strömungen mit Hilfe des Euler-Lagrange-Verfahrens.* Berichte aus der Strömungstechnik. Shaker, 1996.

M. Sommerfeld. Validation of a stochastic Lagrangian modelling approach for inter-particle collisions in homogeneous isotropic turbulence. *International Journal of Multiphase Flow*, 27(10):1829–1858, 2001.

M. Sommerfeld. Numerical Methods for Dispersed Multiphase Flows. In Tomáš Bodnár, Giovanni P. Galdi, and Šárka Nečasová, editors, *Particles in flows*, pages 327–396. Springer International Publishing, Cham,

M. Sommerfeld and M. Kuschel. Modelling droplet collision outcomes for different substances and viscosities. *Experiments in Fluids*, 57(12), 2016.

M. Sommerfeld and L. Pasternak. Advances in modelling of binary droplet collision outcomes in Sprays: A review of available knowledge. *International Journal of Multiphase Flow*, 117: 182–205, 2019.

M. Sommerfeld, B. van Wachem, and R. Oliemans. *Best Practice Guidelines for Computational Fluid Dynamics of Dispersed Multiphase Flows.* ERCOFTAC (European Research Community on Flow, Turbulence and Combustion, 2008.

M. Sommerfeld, O. L. Sgrott, M. A. Taborda, P. Koullapis, K. Bauer, and S. Kassinos. Analysis of flow field and turbulence predictions in a lung model applying RANS and implications for particle deposition. *European Journal of Pharmaceutical Sciences*, 166:105959, 2021a.

M. Sommerfeld, M. Sui, and L. Santiago. Euler/Lagrange Computations of Sprays Produced by Different Liquids using a Generalised Stochastic Droplet Collision Model. In *15th Triennial International Conference on Liquid Atomization and Spray Systems*, volume 1, Edinburgh, UK, 2021.

M. Sui, M. Sommerfeld, and L. Pasternak. Modelling the occurrence of bouncing in droplet collision for different liquids. In *29th European Conference on Liquid Atomization and Spray Systems*, Paris, France, 2019.

M. Sui, M. Sommerfeld, and L. Pasternak. Experimental studies on binary water droplet collisions considering size ratio effects. In *15th Triennial International Conference on Liquid Atomization and Spray Systems*, volume 1, Edinburgh, UK, 2021.

M. Sui, M. Sommerfeld, and L. Pasternak. Extended model of bouncing boundary for droplet collisions considering numerous different liquids. *International Journal of Multiphase Flow*, 162:104418, 2023.

S. Sundaram and L. R. Collins. Numerical Considerations in Simulating a Turbulent Suspension of Finite-Volume Particles. *Journal of Computational Physics*, 124(2):337–350, 1996.

S. Suo and M. Jia. Correction and improvement of a widely used droplet–droplet collision outcome model. *Physics of Fluids*, 32(11):111705, 2020.

MA. Taborda, M. Sommerfeld, and M. Muniz. LES-Euler/Lagrange modelling of bubble columns considering mass transfer, chemical reactions and effects of bubble dynamics. *Chemical Engineering Science*, 229:116121, 2021.

Manuel A. Taborda and Martin Sommerfeld. Modelling the Influence of Bubble Dynamics on Motion, Mass Transfer and Chemical Reaction in LES-Euler/Lagrange Computations. In Michael Schlüter, Dieter Bothe, Sonja Herres-Pawlis, and Ulrich Nieken, editors, *Reactive Bubbly Flows: Final Report of the DFG Priority Program 1740*, Fluid Mechanics and Its Applications, pages 379–411. Springer International Publishing, Cham, 2021.

C. Tang, P. Zhang, and C. K. Law. Bouncing, coalescence, and separation in head-on collision of unequal-size droplets. *Physics of Fluids*, 24(2):022101, 2012.

S. Tanguy and A. Berlemont. Application of a level set method for simulation of droplet collisions. *International Journal of Multiphase Flow*, 31(9):1015–1035, 2005.

A. Wehrfritz, V. Vuorinen, O. Kaario, and M. Larmi. Large eddy simulation of high-velocity fuel sprays: Studying mesh resolution and breakup model effects for spray A. *Atomization and Sprays*, 23(5), 2013.

K. Willis and M. Orme. Experiments on the dynamics of droplet collisions in a vacuum. *Experiments in Fluids*, 29(4):347–358, 2000.

K. Willis and M. Orme. Binary droplet collisions in a vacuum environment: an experimental investigation of the role of viscosity. *Experiments in Fluids*, 34(1):28–41, 2003.

M. Yoshino, J. Sawada, and K. Suzuki. Numerical simulation of head-on collision dynamics of binary droplets with various diameter ratios by the two-phase lattice kinetic scheme. *Computers & Fluids*, 168:304–317, 2018.

L. I. Zaichik and V Alipchenkov, M. Pair dispersion and preferential concentration of particles in isotropic turbulence. *Physics of Fluids*, 15(6):1776, 2003.

H. Zhang, Y. Li, J. Li, and Q. Liu. Study on separation abilities of moisture separators based on droplet collision models. *Nuclear Engineering and Design*, 325:135–148, 2017.

P. Zhang and C. K. Law. An analysis of head-on droplet collision with large deformation in gaseous medium. *Physics of Fluids*, 23(4):042102, 2011.

Z. Zhang and P. Zhang. Kinetic energy recovery and interface hysteresis of bouncing droplets after inelastic head-on collision. *Physics of Fluids*, 29(10):103306, 2017.

G. Zivkovic and M. Sommerfeld. Simulation of pneumatic transport in horizontal channels. In *In Second International Forum on Expert Systems and Computer Simulation in Energy Engineering*. Begel House Inc., 1992.

Appendix A

For completeness, the relevant properties of the liquids considered in this study are summarised, including those in the article.

Species	Oh [-]	ρ [kg/m^3]	σ [mN/m]	μ [mPa·s]	d [μm]
Nonanol [1]	0.141	828	28	12.9	361
Dodecanol [1]	0.166	831	30.4	15.9	363
Heptanol [1]	0.081	820	27.7	7.4	367
Hexanol [1]	0.049	814	25.9	4.3	365
Propanol [1]	0.024	803	23.7	1.95	347
Ethanol [1]	0.015	790	22.6	1.2	358
FVA 23C [1]	0.282	858.5	30.3	28.2	384
FVA 45*C [1]	0.152	842.9	28.1	14.5	384
FVA 60*C [1]	0.072	832.2	27.2	6.7	385
FVA 70C [1]	0.058	825	26.2	5.3	385
FVA 90*C [1]	0.042	810.8	23.9	3.6	385
FVA 100*C [1]	0.036	803.7	22.6	3.04	393
Decane 300 um [2]	0.013	730	23.8	0.92	302
Decane 600 pum [2]	0.009	730	23.8	0.92	601
Dodecane 300 pm [2]	0.018	750	25.3	1.34	302
Dodecane 600 um [2]	0.013	750	25.3	1.34	596
Tetradecane 300 um [2]	0.029	764	27	2.3	305
Tetradecane 600 um [2]	0.021	764	27	2.3	600
Hexadecane 300 um [2]	0.044	770	28	3.5	300
Hexadecane 600 um [2]	0.031	770	28	3.5	600
n-Decane [3]	0.012	730	23.83	0.921	339
Diesel/10% Biodiesel (B10) [4]	0.033	830	27.5	4.9	966
Diesel/60% Biodiesel (B60) [4]	0.1	870	31.5	15.4	865
Diesel/10% Water (W10) [4]	0.035	840	27.5	4.6	744
Diesel/30% Water (W30) [4]	0.105	876	27.5	15	847
HPMC 2% [5]	0.021	998	46	2.8	387
HPMC 4% [5]	0.063	998	45.8	8.2	371
HPMC 8% [5]	0.216	997	45.7	28.4	379
MEG [3]	0.155	1113.4	50.77	21.81	350

Table A.1: Summary of the liquid properties classified as **non-water-like** liquids of experimental studies on binary droplet collision including the resulting Ohnesorge number considered in the present analysis: [1] Sommerfeld and Kuschel (2016); [2] Huang and Pan (2015); [3] Gotaas et al. (2007); [4] Chen et al. (2016); [5] Al-Dirawi and Bayly (2019)

Species	Oh [-]	ρ [kg/m^3]	σ [mN/m]	μ [mPa·s]	d [μm]
Foissac 300um Water [1]	0.005	998.2	72.5	1	300
Kuschel 381pum Water [2]	0.005	998.2	72.7	1	381
Sui 601um Water [3]	0.005	998.2	72	1	601
Sui 404um Water [3]	0.006	998.2	72	1	404
Sucrose 40% [4]	0.032	1176.5	75.1	6	391
Sucrose 50% [4]	0.082	1229.7	76	15.5	380
Sucrose 54% [4]	0.01	1252	76.4	19.4	382
Sucrose 58% [4]	0.219	1274.9	76.9	42.2	380
Sucrose 60% [4]	0.295	1286.8	77.1	57.3	381
PVP K17 5% [4]	0.009	1044.6	69.7	1.45	357
PVP K17 10% [4]	0.015	1044.6	69.1	2.5	385
PVP K17 20% [4]	0.047	1044.6	67.4	7.6	371
PVP K17 30% [4]	0.139	1063.2	66.3	22.7	380
PVP K17 35% [4]	0.243	1067.9	64.8	39.4	380
PVP K17 560um [5]	0.03	1043.2	62.2	5.5	518
PVP K17 350pm [4]	0.037	1043.2	62.2	5.5	341
PVP K30 5% [4]	0.016	1009.8	70.5	2.6	371
PVP K30 10% [4]	0.035	1021.5	69.7	5.7	379
PVP K30 15% [4]	0.076	1033.1	68.9	12.5	380
PVP K30 20% [4]	0.167	1044	68	27.4	379
PVP K30 23% [4]	0.267	1051.7	67.5	43.9	381
PVP K30 25% [4]	0.365	1056.3	67.2	60	381
Glycerol 40% [6]	0.021	1104	68.5	5.01	753
Glycerol 60% [6]	0.064	1158	67.9	15.5	746
Glycerol 80% [6]	0.38	1211	65.1	88.8	693

Table A.2: Summary of the liquid properties classified as **water-like** liquids of experimental studies on binary droplet collision including the resulting Ohnesorge number considered in the present analysis: [1] Foissac et al. (2010); [2] Sommerfeld and Kuschel (2016); [3] Sui et al. (2021); [4] Kuschel and Sommerfeld (2013); [5] Sommerfeld and Pasternak (2019); [6] Finotello et al. (2019);